Search and Observation of the Decay $D_s^{*+} \to D_s^+ e^+ e^-$ and Measurement of the Ratio of Branching Fractions $B(D_s^{*+} \to D_s^+ e^+ e^-)/B(D_s^{*+} \to D_s^+ \gamma)$ at the CLEO-c Experiment

Souvik Das (*sd259@cornell.edu*)
Anders Ryd (*Anders.Ryd@cornell.edu*)

March 1, 2011

Abstract

The branching fraction for a previously unobserved decay $D_s^{*+} \to D_s^+ e^+ e^-$ is predicted theoretically in this document to be 0.65% of the branching fraction for the decay $D_s^{*+} \to D_s^+ \gamma$. We conduct a search for the $D_s^{*+} \to D_s^+ e^+ e^-$ in 586 pb^{-1} of e^+e^- collision data collected with the CLEO-c detector at the Cornell Electron Storage Ring (CESR) operating at a center of mass energy of 4170 MeV and observe it with a significance of 6.39σ over estimated backgrounds. The ratio of branching fractions $B(D_s^{*+} \to D_s^+ e^+ e^-)/B(D_s^{*+} \to D_s^+ \gamma)$ is measured to be $0.72 \pm 0.14(\text{stat}) \pm 0.06(\text{syst})\%$, which is within one standard deviation of uncertainty from the predicted value. The absolute branching fractions for $D_s^{*+} \to D_s^+ \gamma$, $D_s^{*+} \to D_s^+ \pi^0$ and $D_s^{*+} \to D_s^+ e^+ e^-$ are re-evaluated in light of this observation and measurement.

CBX2010-018
March 1, 2011

Contents

1 Introduction

In this note, we describe our search for a previously unobserved $D_s^{*+} \to D_s^+ e^+ e^-$ decay using data collected with the CLEO-c detector at the Cornell Electron Storage Ring (CESR) operating at a center of mass energy of $\sqrt{s}$=4,170 MeV. CLEO-c has collected 586 pb^{-1} of data at this energy which makes it possible for us to not only discover this decay but also try and measure the branching fraction for this decay within reasonable uncertainties.

A D_s^+ meson is the 0^- (L=0, S=0) bound state of a charm and strange quark system, while a D_s^{*+} is the 1^- (L=0, S=1) excited state of the same. Branching fractions for the known decays of the D_s^{*+} to the D_s^+, as recorded by the Review of Particle Physics 2008 [2], are tabulated in Table 1. It is important to note that the branching fractions listed in the table are derived from the ratio

$$\frac{\Gamma(D_s^{*+} \to D_s^+ \pi^0)}{\Gamma(D_s^{*+} \to D_s^+ \gamma)} = 0.062 \pm 0.008$$

assuming that the branching fractions of $D_s^{*+} \to D_s^+ \gamma$ and $D_s^{*+} \to D_s^+ \pi^0$ decays sum to 100%.

Our signal channel, a D_s^{*+} decaying to a D_s^+ via a virtual photon that manifests itself as an e^+e^- pair, does not violate any rigorous or semi-rigorous conservation principle. It is expected to occur at the rate of $D_s^{*+} \to D_s^+ \gamma$ suppressed by approximately a factor of the electromagnetic structure constant, α. Should we observe this decay and measure the ratio of rates

$$\frac{B(D_s^{*+} \to D_s^+ e^+ e^-)}{B(D_s^{*+} \to D_s^+ \gamma)}, \tag{1}$$

it would lead to a re-evaluation of the branching fractions in the table.

The S=1 structure of the quarks in the D_s^{*+} could perhaps be probed using this decay. We do not make such an attempt.

Table 1: Branching fractions of the known decays of the D_s^{*+}.

Mode	Branching Fraction
$B(D_s^{*+} \to D_s^+ \gamma)$	$(94.2 \pm 0.7)\%$
$B(D_s^{*+} \to D_s^+ \pi^0)$	$(5.8 \pm 0.7)\%$

2 Theory

The electromagnetic decay $D_s^{*+} \to D_s^+\gamma$ supercedes the strong decay $D_s^{*+} \to D_s^+\pi^0$ in rate because the latter is suppressed by isospin violation of the strong interaction. The currently known branching fractions of the D_s^{*+} are listed in Table 1 of the Introduction 1. In this section, we propose the hitherto unobserved electromagnetic decay $D_s^{*+} \to D_s^+e^+e^-$. It is separated from the $D_s^{*+} \to D_s^+\gamma$ process by one vertex of the electromagnetic interaction, as seen on comparing Fig. 2.1 and 2.2, and does not violate any known symmetry.

In this section, we estimate the ratio of branching fractions $B(D_s^{*+} \to D_s^+e^+e^-)/B(D_s^{*+} \to D_s^+\gamma)$ through a prediction of the ratio of rates for the $D_s^{*+} \to D_s^+e^+e^-$ and $D_s^{*+} \to D_s^+\gamma$ processes.

$$\frac{B(D_s^{*+} \to D_s^+e^+e^-)}{B(D_s^{*+} \to D_s^+\gamma)} = \frac{\Gamma(D_s^{*+} \to D_s^+e^+e^-)}{\Gamma(D_s^{*+} \to D_s^+\gamma)} \tag{2}$$

With reference to Fig. 2.1, the amplitude for the $D_s^{*+} \to D_s^+\gamma$ process may be written schematically as:

$$\mathcal{M}(D_s^{*+} \to D_s^+\gamma) = \varepsilon^{\mu}_{D_s^*}\varepsilon^{*\nu}_{\gamma}T_{\mu\nu}(P,k), \tag{3}$$

where $\varepsilon^{\mu}_{D_s^*}$ is the polarization vector of the decaying D_s^{*+} meson with three degrees of freedom indexed by μ, $\varepsilon^{*\nu}_{\gamma}$ is the polarization vector of the photon with two degrees of freedom indexed by ν, P is the four-momentum of the D_s^{*+}, k is the four-momentum of the photon and $T_{\mu\nu}(P,k)$ encodes the coupling between the meson and the photon.

$T_{\mu\nu}(P,k)$ may be expressed, most generally, in the form:

$$T_{\mu\nu}(P,k) = Ag_{\mu\nu} + Bk_{\mu}P_{\nu} + C\epsilon_{\mu\nu\alpha\beta}P^{\alpha}k^{\beta}. \tag{4}$$

The D_s^{*+} meson has $J^P = 1^-$, the D_s^+ has $J^P = 0^-$ and the emitted γ has spin $s = 1$ with intrinsic odd parity. The angular momentum of the $D_s^+\gamma$ state, L, could be $0, 1$ or 2 depending on the projection of the spin of the photon on the J_z of the D_s^{*+}. If $s_z = J_z$, then $L = 0$. If $s_z = 0$ then $L = 1, L_z = J_z$. And if $s_z = -J_z$, then $L = 2, L_z = 2J_z$. However, in order to conserve the odd parity of the initial state, given $P = -1$ for both the D_s^+ and the γ, L must be equal to 1. This narrows down the kind of terms that may constitute $T_{\mu\nu}(P,k)$ to

$$T_{\mu\nu}(P,k) = C\epsilon_{\mu\nu\alpha\beta}P^{\alpha}k^{\beta}, \tag{5}$$

where α and β keep track of the four-momentum components of the D_s^{*+} and photon respectively.

In order to model the $D_s^{*+} \to D_s^+e^+e^-$ process, we change the final state photon to a virtual photon and couple it to a e^+e^- pair as depicted in Fig. 2.2. We may then write the invariant amplitude as

$$\mathcal{M}(D_s^{*+} \to D_s^+e^+e^-) = \varepsilon^{\mu}_{D_s^*}T_{\mu\nu}(P,k)\frac{-ig^{\nu\alpha}}{k^2}\langle\bar{u}(p)|ie\gamma_{\alpha}|v(p')\rangle, \tag{6}$$

where $u(p)$ and $v(p')$ are the spinors of the electron and positron respectively as functions of their four-momenta, k is the four-momentum of the virtual photon and $g^{\nu\alpha}$ is the metric

tensor of flat spacetime. Below we will also use the notion q for the virtual photon four-momentum, or q^2 for the invariant mass squared of the electron positron pair.

2.1 Rate for $D_s^{*+} \to D_s^+ \gamma$

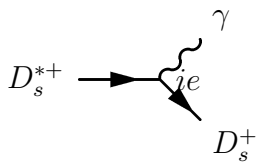

Figure 1: A Feynman diagram for the $D_s^{*+} \to D_s^+ \gamma$ process.

Now we proceed to express the rate for $D_s^{*+} \to D_s^+ \gamma$ in terms of the normalization constant C used to express $T_{\mu\nu}(P,k)$ in Eq. 5 and other constants in this process such as the masses of the D_s^{*+} and D_s^+ which we denote by $m_{D_s^{*+}}$ and $m_{D_s^+}$ respectively.

Inserting the expression for the coupling in Eq. 5 into the expression for the invariant amplitude in Eq. 3, we may write:

$$\mathcal{M} = \varepsilon^{\mu}_{D_s^*} \varepsilon^{*\nu}_{\gamma} C \epsilon_{\mu\nu\alpha\beta} P^{\alpha} k^{\beta}. \tag{7}$$

This may be squared to get

$$|\mathcal{M}^2| = |C^2| \varepsilon^{\mu}_{D_s^*} \varepsilon^{*\nu}_{\gamma} \epsilon_{\mu\nu\alpha\beta} P^{\alpha} k^{\beta} \varepsilon^{*\mu'}_{D_s^*} \varepsilon^{\nu'}_{\gamma} \epsilon_{\mu'\nu'\alpha'\beta'} P^{\alpha'} k^{\beta'}, \tag{8}$$

where μ', ν', α' and β' are indices of four momentum distinguished from their un-primed cousins.

We now sum over final state polarizations and average over initial state polarizations, recalling for photons that

$$\sum_{\lambda=1,2} \varepsilon^{*\nu}_{\gamma_\lambda} \varepsilon^{\nu'}_{\gamma_\lambda} = -g^{\nu\nu'}, \tag{9}$$

and for massive vector bosons that

$$\frac{1}{3} \sum_{\lambda=1,3} \varepsilon^{*\nu}_{D_{s\lambda}^*} \varepsilon^{\nu'}_{D_{s\lambda}^*} = \frac{1}{3} \left(-g^{\nu\nu'} + \frac{P^{\mu} P^{\mu'}}{m^2_{D_s^*}} \right). \tag{10}$$

Thus, we get

$$\overline{|\mathcal{M}^2|} = \frac{|C^2|}{3} g^{\nu\nu'} \left(g^{\mu\mu'} - \frac{P^{\mu} P^{\mu'}}{m^2_{D_s^*}} \right) \epsilon_{\mu\nu\alpha\beta} P^{\alpha} k^{\beta} \epsilon_{\mu'\nu'\alpha'\beta'} P^{\alpha'} k^{\beta'} \tag{11}$$

which may be simplified to

$$\overline{|\mathcal{M}^2|} = \frac{2|C^2|}{3} (P \cdot k)^2 = \frac{2|C^2|}{3} m^2_{D_s^*} E^2_{\gamma} \tag{12}$$

where we have used the tensorial relationship $\epsilon^{\mu\nu}{}_{\alpha\beta}\epsilon_{\mu\nu\alpha'\beta'} = -2g_{\alpha\alpha'}g_{\beta\beta'} + 2g_{\alpha\beta'}g_{\alpha'\beta'}$ and E_γ is the energy component of the photon in the rest frame of the D_s^{*+}.

For a two-body decay, we may write the differential decay rate as

$$d\Gamma = \frac{1}{32\pi^2}\overline{|\mathcal{M}^2|}\frac{E_\gamma}{m_{D_s^*}^2}d\Omega \tag{13}$$

where $d\Omega$ is the differential element of the solid angle subtended from the point of decay of the D_s^{*+} in its rest frame. Since the invariant amplitude in the simplified expression of Eq. 12 does not have any angular dependence, our expression for the rate of $D_s^{*+} \to D_s^+\gamma$ simplifies to

$$\Gamma = \frac{|C^2|}{12\pi}E_\gamma^3. \tag{14}$$

2.2 Rate for $D_s^{*+} \to D_s^+e^+e^-$

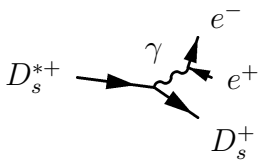

Figure 2: A Feynman diagram for the $D_s^{*+} \to D_s^+e^+e^-$ process.

The rate for $D_s^{*+} \to D_s^+e^+e^-$ is a bit more involved as it is a three-body decay. We will proceed in the same way. First we will calculate $\overline{|\mathcal{M}^2|}$. We start with the amplitude which is given by

$$A(D_s^{*+} \to D_s^+e^+e^-) = \varepsilon^\mu_{D_s^*}C\epsilon_{\mu\nu\alpha\beta}P^\alpha k^\beta\frac{-ig^{\nu\rho}}{k^2}\bar{u}(p)ie\gamma_\rho v(p'). \tag{15}$$

Next we square this

$$|\mathcal{M}^2| = |C^2|\varepsilon^\mu_{D_s^*}\varepsilon^{*\mu'}_{D_s^*}\epsilon_{\mu\nu\alpha\beta}P^\alpha k^\beta\epsilon_{\mu'\nu'\alpha'\beta'}P^{\alpha'}k^{\beta'}\frac{g^{\nu\rho}g^{\nu'\rho'}}{k^4}\bar{u}(p)e\gamma_\rho v(p')\bar{v}(p')e\gamma_{\rho'}u(p).$$

Summing over final states and averaging over initial states allow us to write

$$\begin{aligned}
\overline{|\mathcal{M}^2|} &= -\frac{4e^2|C^2|}{3k^4}\epsilon^\mu{}_{\nu\alpha\beta}\epsilon_{\mu\nu'\alpha'\beta'}P^\alpha k^\beta P^{\alpha'}k^{\beta'}\left[p^\nu p'^{\nu'} + p'^\nu p^{\nu'} - g^{\nu\nu'}(p\cdot p' + m^2)\right] \\
&= -\frac{4e^2|C^2|}{3k^4}\left[M_{D_s^*}^2k^4 - k^2(P\cdot k)^2 - 2X^2\right] \\
&= \frac{4e^2|C^2|}{3k^4}\left[k^2(P\cdot k)^2 + 2X^2 - M_{D_s^*}^2k^4\right],
\end{aligned}$$

where

$$X^\mu \equiv \epsilon^\mu{}_{\nu\alpha\beta}P^\alpha p'^\beta p^\nu$$

and we have used

$$\begin{aligned}
\sum_{s,r} \bar{u}_s \gamma_\rho v_r \bar{v}_r \gamma_{\rho'} u_s &= \sum_{s,r} \mathrm{Tr}[\bar{u}_s \gamma_\rho v_r \bar{v}_r \gamma_{\rho'} u_s] \\
&= \sum_{s,r} \mathrm{Tr}[u_s \bar{u}_s \gamma_\rho v_r \bar{v}_r \gamma_{\rho'}] \\
&= \mathrm{Tr}[(\not{p} + m)\gamma_\rho (\not{p}' - m)\gamma_{\rho'}] \\
&= \mathrm{Tr}[\not{p}\gamma_\rho \not{p}'\gamma_{\rho'} - m^2 \gamma_\rho \gamma_{\rho'}] \\
&= 4(p_\rho p'_{\rho'} + p_{\rho'} p'_\rho - g_{\rho\rho'}(p \cdot p' + m^2)
\end{aligned}$$

The evaluate this we use

$$\begin{aligned}
\epsilon^{\mu\alpha\beta\gamma}\epsilon_{\mu\alpha'\beta'\gamma'} &= -g^\alpha_{\alpha'} g^\beta_{\beta'} g^\gamma_{\gamma'} - g^\alpha_{\beta'} g^\beta_{\gamma'} g^\gamma_{\alpha'} - g^\alpha_{\gamma'} g^\beta_{\alpha'} g^\gamma_{\beta'} \\
&\quad + g^\alpha_{\alpha'} g^\beta_{\gamma'} g^\gamma_{\beta'} + g^\alpha_{\gamma'} g^\beta_{\beta'} g^\gamma_{\alpha'} + g^\alpha_{\beta'} g^\beta_{\alpha'} g^\gamma_{\gamma'}
\end{aligned}$$

This then gives

$$\begin{aligned}
X^2 &= -P^2 p'^2 p^2 - 2P \cdot p' p' \cdot p P \cdot p + P^2 (p \cdot p')^2 + m^2((P \cdot p')^2 + (P \cdot p)^2) \\
&= -M^2_{D^*_s} m^4 - (q^2 - 2m^2)(P \cdot p')(P \cdot p) + M^2_{D^*_s}(q^2/2 - m^2)^2 + m^2[(P \cdot p)^2 + (P \cdot p')^2] \\
&= -q^2 (P \cdot p')(P \cdot p) + M^2_{D^*_s}(q^4/2 - q^2 m^2) + \frac{m^2}{4}(M^2_{D^*_s} - M^2_{D_s} + q^2)^2
\end{aligned}$$

where I have used

$$p \cdot p' = q^2/2 - m^2$$

and

$$P \cdot k = (M^2_{D^*_s} - M^2_{D_s} + q^2)/2.$$

The next task is to express $P \cdot p'$ and $P \cdot p$ in a more convenient form. Denote by a * quantities evaluated in the e^+e^- restframe. Let θ^* be the angle the electron makes with the direction opposite to the D_s in the e^+e^- frame. This means that

$$\begin{aligned}
P \cdot p &= E^*_{D^*_s} E^*_e - |P^*_{D^*_s}||P^*_e| \cos\theta^*, \\
P \cdot p' &= E^*_{D^*_s} E^*_e + |P^*_{D^*_s}||P^*_e| \cos\theta^*.
\end{aligned}$$

But the energy in the e^+e^- restframe, $E^*_{D^*_s}$, can be written

$$E^*_{D^*_s} = \frac{P \cdot k}{\sqrt{q^2}}$$

as in this frame $k^\mu = (\sqrt{q^2}, 0, 0, 0)$. Similarly we can express the electron energy as

$$E^*_e = \frac{p \cdot k}{\sqrt{q^2}}$$

Putting this together we get

$$\begin{aligned} P\cdot p &= \frac{P\cdot k}{\sqrt{q^2}}\frac{p\cdot k}{\sqrt{q^2}}+\sqrt{\frac{(P\cdot k)^2}{q^2}-M_{D_s^*}^2}\sqrt{\frac{(p\cdot k)^2}{q^2}-m^2}\cos\theta^* \\ P\cdot p' &= \frac{P\cdot k}{\sqrt{q^2}}\frac{p\cdot k}{\sqrt{q^2}}-\sqrt{\frac{(P\cdot k)^2}{q^2}-M_{D_s^*}^2}\sqrt{\frac{(p\cdot k)^2}{q^2}-m^2}\cos\theta^* \end{aligned}$$

Using $p\cdot k = q^2/2$ gives

$$\begin{aligned} P\cdot p &= \frac{P\cdot k}{2}+\sqrt{\frac{(P\cdot k)^2}{q^2}-M_{D_s^*}^2}\sqrt{\frac{q^2}{2}-m^2}\cos\theta^* \\ P\cdot p' &= \frac{P\cdot k}{2}-\sqrt{\frac{(P\cdot k)^2}{q^2}-M_{D_s^*}^2}\sqrt{\frac{2^2}{2}-m^2}\cos\theta^* \\ (P\cdot p)(P\cdot p') &= (P\cdot k)^2/4-\left(\frac{(P\cdot k)^2}{q^2}-M_{D_s^*}^2\right)\left(\frac{q^2}{4}-m^2\right)\cos^2\theta^*. \end{aligned}$$

Putting this together we get

$$X^2 = -q^2\frac{(P\cdot k)^2}{4}+\left((P\cdot k)^2-q^2M_{D_s^*}^2\right)\left(\frac{q^2}{4}-m^2\right)\cos^2\theta^*-+M_{D_s^*}^2(\frac{q^4}{4}-q^2m^2)+\frac{m^2}{4}(M_{D_s^*}^2-M_{D_s}^2+q^2)^2.$$

Using $A\equiv M_{D_s^*}^2-M_{D_s}^2+q^2$ we get

$$\overline{|\mathcal{M}^2|} = \frac{4e^2|C^2|}{3q^4}\left[\frac{3A^2}{8}q^2-M_{D_s^*}^2\left(\frac{q^4}{2}+2q^2m^2\right)+\frac{m^2}{2}A^2+\left(\frac{A^2}{4}-q^2M_{D_s^*}^2\right)\left(\frac{q^2}{2}-2m^2\right)\cos^2\theta^*\right]$$

For a three-body decay we can write

$$d\Gamma = \frac{1}{(2\pi)^3}\frac{1}{16M_{D_s^*}^2}\overline{|\mathcal{M}^2|}dE_e dq^2$$

We need to re-express dE_e in terms of $d\cos\theta^*$. To do this we use

$$E_e = \frac{P\cdot p}{M_{D_s^*}} = \frac{E_{D_s^*}^* E_e^*}{M_{D_s^*}}-\frac{|P_{D_s^*}^*||P_e^*|}{M_{D_s^*}}\cos\theta^*.$$

Note that in the expressions above, the quantities $E_{D_s^*}^*$, E_e^*, $|P_{D_s^*}^*|$, and $|P_e^*|$ depend only on q^2 and not on $\cos\theta^*$. This means we can diffrentiate this and obtain

$$dE_e = -\frac{|P_{D_s^*}^*||P_e^*|}{M_{D_s^*}}d\cos\theta^*.$$

Writing

$$E^*_{D^*_s} = \frac{q\cdot P}{q_0} = \frac{q\cdot P}{2|E^*_e|}$$

and

$$P^*_{D^*_s} = \sqrt{E^{*2}_{D^*_s} - M^2_{D^*_s}} = \sqrt{\frac{(q\cdot P)^2}{4E^{*2}_e} - M^2_{D^*_s}}$$

This allows us to obtain the simple result

$$\frac{|P^*_{D^*_s}||P^*_e|}{M_{D^*_s}} = \sqrt{\frac{(q\cdot P)^2}{4M^2_{D^*_s}} - E^{*2}_e} = \sqrt{\frac{q_0^2}{4} - E^{*2}_e} = \frac{1}{2}\sqrt{q_0^2 - q^2} = \frac{P_{D_s}}{2},$$

which gives

$$dE_e = \frac{P_{D_s}}{2} d\cos\theta^*.$$

Using this and integrating over $\cos\theta^*$ we get

$$\frac{d\Gamma}{dq^2} = \frac{P_{D_s}e^2|C^2|}{192\pi^3 M^2_{D^*_s}q^4}\left[\frac{3A^2}{4}q^2 - M^2_{D^*_s}\left(q^4+4q^2m^2\right) + m^2A^2 + \frac{2}{3}\left(\frac{A^2}{4} - q^2M^2_{D^*_s}\right)\left(\frac{q^2}{2} - 2m^2\right)\right] \quad (16)$$

$$= \frac{P_{D_s}\alpha|C^2|}{48\pi^2 M^2_{D^*_s}}\left[\frac{1}{q^4}\frac{2}{3}A^2m^2 + \frac{1}{q^2}\left(\frac{5}{6}A^2 + 4m^2M^2_{D^*_s}\right) - \frac{4}{3}M^2_{D^*_s}\right] \quad (17)$$

Numerical integration over q^2 gives

$$\frac{\Gamma(D^{*+}_s \to D^+_s e^+e^-)}{\Gamma(D^{*+}_s \to D^+_s\gamma)} = 0.89\alpha = 0.65\%, \quad (18)$$

which is remarkably close to the naive expectation that this ratio should be $\alpha = 0.730\%$.

3 Analysis Strategy for Measuring $B(D_s^{*+} \to D_s^+ e^+ e^-)/B(D_s^{*+} \to D_s^+ \gamma)$

As described in the Introduction, 1, this chapter documents a search and observation of the $D_s^{*+} \to D_s^+ e^+ e^-$ process along with a measurement of the ratio of branching fractions

$$\frac{B(D_s^{*+} \to D_s^+ e^+ e^-)}{B(D_s^{*+} \to D_s^+ \gamma)}$$

at the CLEO-c experiment. We chose to measure and present this ratio of branching fractions instead of an absolute branching fraction for the $D_s^{*+} \to D_s^+ e^+ e^-$ in order to minimize systematic uncertainties arising from the reconstruction and selection of D_s^+ mesons. When we refer to the positively charged D_s^{*+} or the D_s^+ in this document, we imply the negatively charged particle or the charge-conjugate process unless otherwise specified. This search and measurement was conducted in 586 pb^{-1} of e^+e^- collision data collected by the CLEO-c experiment at a center of mass energy of 4,170 MeV. At this energy, the total charm cross section is known to be $\simeq$ 9 nb, of which about 10% produces $D_s^{\pm} D_s^{*\mp}$ events. More accurately, the cross section for producing $D_s^{\pm} D_s^{*\mp}$ at this energy has been experimentally measured in [4] and [1] that we average to quote 948 $\pm$ 36 pb. How we arrive at this number is covered in more detail in Section 7 on the datasets we have used. Using the quoted values of integrated luminosity and production cross section, we conclude that approximately 556 thousand events were at our disposal for this analysis.

In our search and measurement, we employ a blind-analysis technique to search for our signal process, the $D_s^{*+} \to D_s^+ e^+ e^-$, where we reconstruct the D_s^{*+} through the D_s^+ on the same side as the D_s^{*+} and the soft e^+e^- pair. The D_s^+ is reconstructed exclusively through the nine hadronic decay channels outlined in Eq. 19 - 27. Selection criteria are optimized, their efficiencies noted and the background levels estimated from data outside the signal region before we proceed to unblind data within the signal region.

$$D_s^+ \to K^+ K^- \pi^+ \tag{19}$$
$$D_s^+ \to K_S K^+ \tag{20}$$
$$D_s^+ \to \eta \pi^+; \eta \to \gamma\gamma \tag{21}$$
$$D_s^+ \to \eta' \pi^+; \eta' \to \pi^+\pi^- \eta; \eta \to \gamma\gamma \tag{22}$$
$$D_s^+ \to K^+ K^- \pi^+ \pi^0 \tag{23}$$
$$D_s^+ \to K^{*+} K^{*0} \tag{24}$$
$$D_s^+ \to \pi^+ \pi^- \pi^+ \tag{25}$$
$$D_s^+ \to \eta \rho^+; \eta \to \gamma\gamma; \rho^+ \to \pi^+ \pi^0 \tag{26}$$
$$D_s^+ \to \eta' \pi^+; \eta' \to \rho^0 \gamma \tag{27}$$

Selection criteria on the reconstructed D_s^{*+}, D_s^+ and soft e^+e^- candidates are designed to reject background events described in Section 4. These selection criteria are described in

Section 5. Of note are the criteria on the helix parameters of the soft e^+e^- tracks that are used to discriminate our signal against backgrounds that come from $D_s^{*+} \to D_s^+\gamma$ where the γ converted to an e^+e^- pair in material. These selection criteria are optimized for each of the nine hadronic decay modes of the D_s^+ using Monte Carlo simulations of the signal and backgrounds as described in Section 10.

The e^+e^- pair from the D_s^{*+} decay share ~ 144 MeV of energy and are hence anticipated to be very soft. The Kalman-filter based track fitter used in CLEO-c did not, by default, store track fits with the electron mass hypothesis, storing tracks fitted to the charged pion mass hypothesis instead. Section 10 that documents our effort to converge on optimal sets of parameters for our selection criteria also documents our realization that tracks fitted to the electron hypothesis offers us considerably higher signal significances for observing the $D_s^{*+} \to D_s^+e^+e^-$ than tracks fitted to the pion hypothesis. Therefore, a campaign to reprocess several datasets to include track fits with the electron mass hypothesis was launched and this is described in Section 8. Henceforth, the analysis focusses on electron mass fitted data in searching for the $D_s^{*+} \to D_s^+e^+e^-$.

Having narrowed down on a signal region for each of the hadronic decay modes of the D_s^+ in the course of our optimization procedure, we estimate the expected number of background events within this region for each mode by extrapolating Monte Carlo simulation and data points from the sideband regions. This is described in Section 12. Before we unblind data within the signal regions, we establish that our predicted signal and estimated background levels are adequate to obtain maximal signal significance if we are to unblind data in all the modes.

Thereafter, we measure the efficiencies of our selection criteria for $D_s^{*+} \to D_s^+e^+e^-$ reconstruction in each of the hadronic decay channels in Section 13. We could at this point, in principle, proceed to unblind data and used the number of observed events in conjuction with the selection efficiencies to present a measurement for the absolute branching fraction of $D_s^{*+} \to D_s^+e^+e^-$. Such a measurement, however, would have large systematic errors from the reconstruction of the D_s^+ and we choose not to follow this route.

Using criteria similar to those used to select $D_s^{*+} \to D_s^+e^+e^-$ events except without the track helix criteria for the e^+e^- and including criteria on the photon from the D_s^{*+}, we reconstruct $D_s^{*+} \to D_s^+\gamma$ events where the D_s^+ decays in the hadronic modes specified in Eq. 19 - 27. The efficiency of our selection criteria is noted, as is our signal yield for each of the channels. This is described in Section 14.

We then unblind data in the signal regions of the $D_s^{*+} \to D_s^+e^+e^-$ reconstruction in each of the chosen decay modes of the D_s^+, taking into account the background for each mode estimated in Section 12. Using the number of observed signal events, the efficiencies for our selection criteria and the signal yields and efficiencies for the $D_s^{*+} \to D_s^+\gamma$ reconstruction, we proceed to compute the ratio of branching fractions we seek to measure. This is described in Section 15 of the document. Also motivated in this section is our requirement for estimating the systematic uncertainty, in the form of deviations between data and Monte Carlo simulations, in the reconstruction of soft e^+e^- pairs.

The systematic uncertainties associated with the selection and reconstruction efficiencies

of soft e^+e^- pairs in $D_s^{*+} \to D_s^+e^+e^-$ and the photon in $D_s^{*+} \to D_s^+\gamma$ is measured in Section 16. We estimate the systematic deviation between reconstruction efficiencies in Monte Carlo simulation and data by measuring the ratio of the numbers of events where one of the π^0 Dalitz decays to γe^+e^- to the number of events where both π^0 decay to $\gamma\gamma$ and comparing this to the ratio expected from currently accepted branching fractions for $\pi^0 \to \gamma e^+e^-$ and $\pi^0 \to \gamma\gamma$. This uncertainty is propagated into the ratio of branching fractions reported in Section 15.

4 Backgrounds for $D_s^{*+} \to D_s^+e^+e^-$

A significant background to the observation of this decay is expected from $D_s^{*+} \to D_s^+\gamma$ where the γ converts in the material of the apparatus or the beam-pipe to form an e^+e^- pair. The material of the beam-pipe is known to have been approximately 1% of a radiation length thick for photons incident on it closest to the interaction region and higher for photons incident at steeper angles. If we accept the theoretical estimate of the rate of the $D_s^{*+} \to D_s^+e^+e^-$ process with respect to the $D_s^{*+} \to D_s^+\gamma$ as described in Section 2, we conclude that this conversion process occurred at roughly the same rate as the signal. This background is called the *conversion background* in this document. The electrons from such conversions will have the same range of energies as those from signal processes. However, their tracks would appear to originate at a distance away from the primary interaction point. Selection criteria for selecting and reconstructing the $D_s^{*+} \to D_s^+e^+e^-$ are designed to exploit this fact.

Another source of background, also seen to be significant from Monte Carlo simulation studies, arises from π^0 mesons that were produced at the primary interaction point which then decayed through the Dalitz channel: $\pi^0 \to \gamma e^+e^-$. Such e^+e^- pairs would typically have had the same range of energies as those expected from the signal process and would seem to have originated from the primary interaction point. Though the rate of Dalitz decays of the π^0 is $\sim 1.2\%$ [2], the prodigious production of π^0 mesons makes this a significant background to our rare signal. We could veto events where the soft e^+e^- combined with a γ in the event to produce a π^0, but estimating the efficiency of such a veto from data would be difficult. Instead, we recognize that such a background would not peak in the variables of any of our selection criteria and estimate the frequency of its occurrence from the sidebands of the signal region in our data. We call this the *Dalitz decay background* in the rest of the document.

Combinatorial backgrounds necessarily result from combining candidate daughters of the D_s^+ and candidate e^-s and e^+s. We estimate these from the sidebands around the signal region in our data.

We also account for backgrounds that arise from light quark (u, d, s) production at the interaction point. These backgrounds are seen, from Monte Carlo simulations, to dominate, though not peak, in the $\pi^+\pi^-\pi^+$ and $\eta'\pi^+$; $\eta' \to \rho^0\gamma$ decay channels of the D_s^+ after applying our selection criteria. Therefore, we choose to estimate their contributions from the sidebands of the signal region in our data. They are collectively called the *continuum background* in the rest of this document.

5 Selection Criteria for Measuring $B(D_s^{*+} \to D_s^+ e^+ e^-)$

The entities directly measured by the CLEO-c detector that is relevant for our analysis are charged tracks and electromagnetic showers. Relatively stable particles, like the soft e^- and e^+ in the final state of our signal process or the π^+, K^+ and γ from decays of the D_s^+ could be detected directly by the detector. Short-lived particles like the D_s^+ and the D_s^{*+} must be reconstructed by analyzing the signatures of their decays into particles that left tracks or shower in the detector. As we have mentioned earlier, we choose to reconstruct the D_s^+ through 9 hadronic final states as listed in Eq. 19 - 27, and the D_s^{*+} through the D_s^+ and the soft e^+e^- pair.

We construct three kinematic variables from reconstructed D_s^+ and D_s^{*+} candidates, based on which we select events most likely to contain our signal. We also construct two combinations of track parameters of the e^- and e^+ which gave us criteria to powerfully reject conversion backgrounds.

5.1 Track Quality Requirements for the Soft e^+e^- Pair

Quality requirements are imposed on the soft e^+e^- tracks in order to reject poorly reconstructed tracks and tracks that cannot correspond to our signal process. These tracks are required to fit the hits in the drift chambers with χ^2 less than 100000. The measured energy, which is derived from the momentum, that in turn is inferred from the curvature of the track's helix in the 1 T magnetic field, is required to be between 10 MeV and 150 MeV. The upper limit is set by considering the mass difference between the D_s^{*+} and D_s^+ mesons, which is approximately 144 MeV. A single electron cannot carry more than that amount of energy. Below 10 MeV, electron tracks curl in a way that cannot be well reconstructed by the drift chamber. Next, we require that the tracks pass within 5 cm of the interaction point in the dimension parallel to the beam-axis and within 5 mm of the beam-axis in the transverse dimensions. Finally, in order to reject particles that are not electrons, we require the dE/dx as computed from the track fit to be within 3σ of that expected for electrons.

These criteria remain identical for all the hadronic decay modes of the D_s^+ as the e^+e^- pair is independent of the D_s^+.

5.2 $m_{D_s^+}$, the mass of the D_s^+ Meson

The D_s^+ meson is reconstructed using the tight D_s-tagging criteria outlined in [8]. We select events which have D_s^+ candidates with invariant mass within tens of MeV from 1.969 GeV. The current world standard for its mass as recorded in the Review of Particle Physics 2008 [2] is 1.96849 ± 0.00034 GeV. This criterion rejects most false combinations of D_s^+ daughters. The exact width of this criterion was optimized individually for each mode.

5.3 m_{BC} of the D_s^{*+}

The energy of a D_s^{*+} meson produced from the e^+e^- collisions in CESR may be determined with higher precision from the measured energy of the beam than from the sum of the energies of its decay constituents as measured by the CLEO-c detector. It may be calculated from:

$$E_{D_s^{*+}}(\text{beam}) = \frac{4s - m^2_{D_s^+}(\text{RPP}) + m^2_{D_s^{*+}}(\text{RPP})}{4\sqrt{s}}, \tag{28}$$

where $E_{D_s^{*+}}(\text{beam})$ is the energy of the D_s^{*+} we calculated from the beam energy, s is the square of the center of mass energy of the beam, and $m_{D_s^+}(\text{RPP})$ and $m_{D_s^{*+}}(\text{RPP})$ are the current world standards for the D_s^+ and D_s^{*+} masses respectively as recorded in the Review of Particle Physics 2008.

Having thus calculated the energy of the D_s^{*+} meson, we can now define a more precise variant of the invariant mass of the D_s^{*+} as follows:

$$m_{BC} = \sqrt{E^2_{D_s^{*+}}(\text{beam}) - p^2_{D_s^{*+}}(\text{constituents})} \tag{29}$$

where $p_{D_s^{*+}}(\text{constituents})$ is the momentum of the D_s^{*+} calculated from the momenta of the daughters of its decay. m_{BC} is called the *beam constrained mass* in CLEO literature.

In this selection criterion, we accept events with candidates having m_{BC} within tens of MeV from 2.112 GeV. The current world standard for the D_s^{*+} mass as recorded in the Review of Particle Physics 2008 [2] is 2.1123 ± 0.0005 GeV. This criterion is meant to reject most false combinations of D_s^{*+} daughters.

5.4 δm between the D_s^{*+} and the D_s^+

We define δm as the mass difference between the reconstructed D_s^{*+} and D_s^+ mesons.

$$\delta m = m_{D_s^{*+}} - m_{D_s^+} \tag{30}$$

This mass difference is known to be 143.8 MeV [2]. By accepting events with δm within a narrow range of this values around 143.8 MeV, we reject most combinations where the e^- or e^+ that we use to reconstruct the D_s^{*+} did not, in fact, come from decays of the D_s^{*+}.

5.5 Δd_0

In CLEO, the d_0 of a track is defined as the distance of closest approach of the track to the z-axis. It is a signed quantity, whose sign depends on the charge of the track (inferred from the sense of the track helix) and whether the origin of the $x-y$ plane falls within the circle made by the track in that plane. For more details, one may see Section 6 of [6].

Now, for e^- and e^+ tracks that come from the origin, as they do for our signal, it may be seen from Fig. 3 that $d_0^{e^-} - d_0^{e^+}$ is 0. Hence, in data, our signal will have Δd_0 centered around 0.

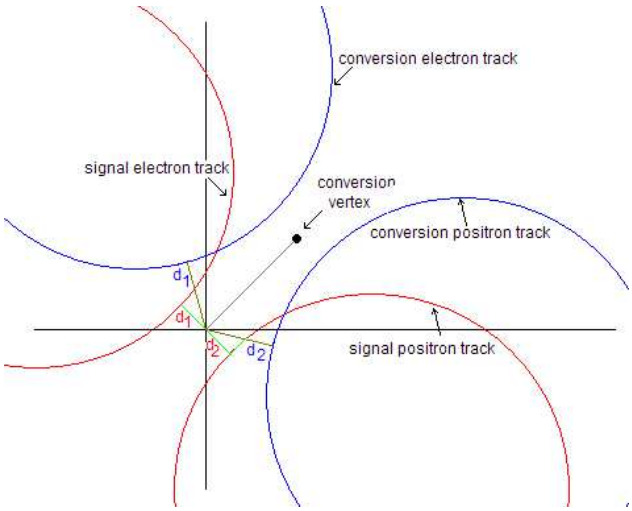

Figure 3: An illustration of Δd_0 between the soft electron tracks of the signal and conversion events.

However, for e^- and e^+ tracks that come from a point away from the origin, as they do for the conversion background, it is clear from Fig. 3 that $d_0^{e^-} - d_0^{e^+}$ will be negative.

For our selection criterion, we define:

$$\Delta d_0 = d_0^{e^-} - d_0^{e^+} \tag{31}$$

and require Δd_0 to be greater than -5 mm. This rejects conversion background events.

5.6 $\Delta\phi_0$

The azimuthal angle of the e^- and e^+ tracks measured at the point of closest approach of the track to the z-axis, denoted by ϕ_0, appears to be very effective in rejecting conversion background events.

For events where the e^- and e^+ tracks come from the origin, as they do for our signal, it may be noted from Fig. 4 that if we define:

$$\Delta\phi_0 = \phi_0^{e^-} - \phi_0^{e^+}, \tag{32}$$

$\Delta\phi_0$ will be centered around 0 for the signal. However, for conversion events where the tracks do not emanate from the origin, it may be inferred from 4 that $\Delta\phi_0$ will always be positive.

Requiring $\Delta\phi_0$ to be less than 0.12 in this selection criterion rejects a significant portion of our conversion background events.

5.7 Interdependence of Kinematic variables

We may construct yet another kinematic variable for a selection criterion:

$$\delta E = E_{D_s^{*+}}(\text{constituents}) - E_{D_s^{*+}}(\text{beam}), \tag{33}$$

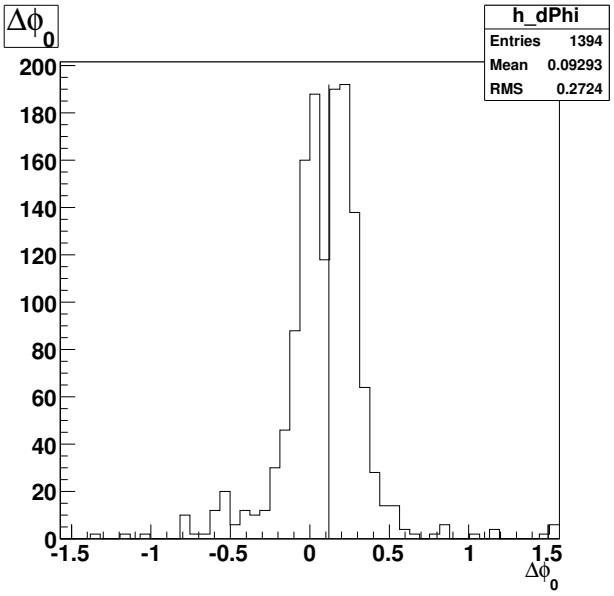

Figure 4: An illustration of $\Delta\phi_0$ between the soft electron tracks of the signal and conversion events.

where $E_{D_s^{*+}}(\text{constituents})$ is the energy of the D_s^{*+} as reconstructed from its decay constituents and $E_{D_s^{*+}}(\text{beam})$ is the energy of the D_s^{*+} as calculated from the beam energy. However, δE would not be independent of $m_{D_s^+}(\text{constituents})$ and m_{BC}. This is because we can combine the expressions for δE and m_{BC} to get:

$$(\delta E)^2 + 2E_{D_s^{*+}}(\text{beam})\delta E + m_{BC}^2 = m_{D_s^{*+}}^2(\text{constituents}) \tag{34}$$

This means if we shape δE to be 0, m_{BC} will be shaped towards $m_{D_s^{*+}}^2(\text{constituents})$. So now, if we shape m_{BC} around $m_{D_s^{*+}}(\text{RPP})$, we are shaping $m_{D_s^{*+}}(\text{constituents})$. If we shape that, and also shape $m_{D_s^+}(\text{constituents})$ in our first selection criterion, we are shaping δm. An equation with just the kinematic quantities that we shape and a constant, $E_{D_s^{*+}}(\text{beam})$, is:

$$(\delta E)^2 + 2E_{D_s^{*+}}(\text{beam})\delta E + m_{BC}^2 = (\delta m + m_{D_s^+}(\text{constituents}))^2 \tag{35}$$

6 Selection Criteria for Measuring $B(D_s^{*+} \to D_s^+\gamma)$

As mentioned, we seek to measure the ratio of branching fractions $B(D_s^{*+} \to D_s^+e^+e^-)/B(D_s^{*+} \to D_s^+\gamma)$ in order to minimize systematics arising from the reconstructing of D_s^+ mesons, and therefore we must have a way to measure yields and efficiencies for a $B(D_s^{*+} \to D_s^+\gamma)$ measurement. We do this, again, by reconstructing the D_s^{*+} through the D_s^+ on the same side and the γ. The D_s^+ is reconstructed exclusively through the nine hadronic decay channels listed in Eq. 19 - 27.

Selection criteria used to separate the $D_s^{*+} \to D_s^+\gamma$ signal from backgrounds are similar to those used for the $D_s^{*+} \to D_s^+e^+e^-$. The kinematic variables $m_{D_s^+}$, m_{BC} and δm retain their definitions from the previous section, except the four-momenta of the e^+e^- pair is replaced by that of a γ. Selection criteria on the e^+e^- pair are obviously inapplicable and are replaced by criteria on the γ. This is described in the following section. Furthermore, we plot the distribution of m_{BC} after applying all other criteria, and the large rate of this channel that translates to a large number of data points allows us to compute the signal yields and efficiencies from a fit instead of cutting and counting within a range.

6.1 Shower Criteria on the γ

Photons are reconstructed in CLEO-c from electromagnetic showers in the calorimeter that distribute their energies over multiple crystals. The direction of the photon is determined by interpolating between crystals and the total energy is determined by summing the energy deposited in the region identified as part of an electromagnetic shower. The shower is required to have total energy between 10 MeV and 2 GeV. No part of the shower may deposit its energy in a known noisy, i.e. "hot", crystal or an under-performing one. The shower may not lie in the path of a track since such a shower would almost certainly have been produced by a charged particle and therefore cannot be a photon candidate. Electromagnetic showers tend to deposit a narrower distribution of energy than a hadronic shower. The collimation of energy deposition is measured by a quantity known as $E9/E25$. It is the ratio of energy in the 3×3 block of crystal surrounding the cluster-center of the shower energy to the energy deposited in the 5×5 block. $E9/E25$ is required to be close to 1 for a photon shower. We also require that energies in this 5×5 block that are associated with any other photon are removed and this procedure is called "unfolding" in this context. We select on a range for this unfolded $E9/E25$ variable, limited by 1, such that 99% of showers are accepted. And finally, the shower must be from a region of the barrel or endcap calorimeter known to be good.

Table 2: Integrated luminosity corresponding to the CLEO-c datasets used in this analysis. The statistical uncertainties are added in quadrature, while the systematic uncertainties are added linearly. Thereafter, these two forms of uncertainties are added in quadrature to give us the total uncertainty we use for the analysis and the remainder of this document.

Dataset	Integrated Luminosity ± stat ± syst (pb^{-1})
39	55.1 ± 0.03 ± 0.56
40	123.9 ± 0.05 ± 1.3
41	119.1 ± 0.05 ± 1.3
47	109.8 ± 0.05 ± 1.1
48	178.3 ± 0.06 ± 1.9
Total	586.2 ± 0.11 ± 6.1

7 Datasets Used

Data taken at $\sqrt{s}$ = 4,170 MeV by the CLEO-c detector used for this analysis correspond to the datasets enumerated in Table 2. We add the integrated luminosities of each of the datasets to converge on the value of 586 ± 6 pb^{-1} as the total luminosity of our data. This value is used for the rest of this document.

Electron-positron collisions at a center of mass energy of $\sqrt{s}$= 4,170 MeV have been measured to produce $D_s^{\pm}D_s^{*\mp}$ pairs with a cross section of 916 ± 11(statistical) ± 49(systematic) pb in [4] and 983 ± 46(statistical) ± 21(systematics of measurement) ± 10 (systematics of luminosity) in [1]. These being independent measurements, we use the uncertainty-weighted average value of 948 ± 36 pb for the cross section in this analysis.

Dataset 42 containing 48.1 pb^{-1} of data collected at the $\psi(2S)$ resonance energy was used to measure the systematic uncertainty in the electron tracking and reconstruction for this analysis.

Monte Carlo samples modeling known physical processes expected in these datasets had been produced and are available as the *Generic* and *Continnum* samples described in the following sections.

7.1 Generic Monte Carlo

By *Generic Monte Carlo*, we mean a Monte Carlo (MC) simulation of all known physics processes that follow from the production of charm quarks at 4,170 MeV e^+e^- collisions. The $D_s^{*+} \to D_s^+e^+e^-$ process which we are searching for, consequently, is not a part of this simulation. In order to decrease statistical uncertainties, the Generic MC was created with approximately 20 events for every 1 event of data. This scale factor of 20 was aimed for, but not necessarily achieved due to computational errors. We re-evaluate the scale factor achieved as follows:

According to

`https://www.lepp.cornell.edu/~c3mc/private/genmc_decs/20080404_MCGEN_1/ddmix_4170_isr.dec`,

which is the EVTGEN decay file used to set the branching fractions of the various charm

quark states possible at 4,170 MeV, the branching fraction of producing $D_s^{\pm} D_s^{*\mp}$ is 0.1014. Also, from the "Samples" section of
`https://wiki.lepp.cornell.edu/lepp/bin/view/CLEO/Private/SW/CLEOcMCstatus`,
the total number of produced events is 105.2 million. Therefore, we may write:

$$\frac{(586 \pm 3)\text{pb}^{-1} \times (948 \pm 36)\text{pb}}{0.1014} \times \text{scale} = (105.2 \pm 0.1) \times 10^6 \tag{36}$$

From this, we deduce that the achieved scale factor for the Generic MC sample has been 19.2 ± 0.8. The uncertainty in the luminosity contributes most to the uncertainty in this scale. Since we will be mostly dividing the number of events in Generic MC with this scale, it is useful to record the inverse of this scale: 0.052 ± 0.002.

7.2 Continuum Monte Carlo

By *Continuum Monte Carlo*, we mean a Monte Carlo simulation of all physics processes that follow from the production of up, down and strange quarks at $\sqrt{s} = 4{,}170$ MeV e^+e^- collisions. The scale factor for this MC sample is read off as 5 from the website:
`https://wiki.lepp.cornell.edu/lepp/bin/view/CLEO/Private/SW/CLEOcMCstatus`

8 Reprocessing for Electron-fitted Tracks

Tracks in CLEO are fitted to various particle mass hypotheses with a Kalman filter. In order to conserve disk-space, however, CLEO has chosen to not store fits made with the electron mass hypothesis in the reconstruction process. Electrons are reconstructed using track fits made with the charged pion mass hypothesis. This works fine for energies above a few hundred MeVs, but not in our analysis which deals with average electron energies of 70 MeV and goes down to 40 MeV. A plot of the difference between the reconstructed and Monte Carlo generated electron energy against the generated energy using the pion mass hypothesis is presented in Fig. 5. A significant over-estimation of the energy is observed for true energies less than 80 MeV.

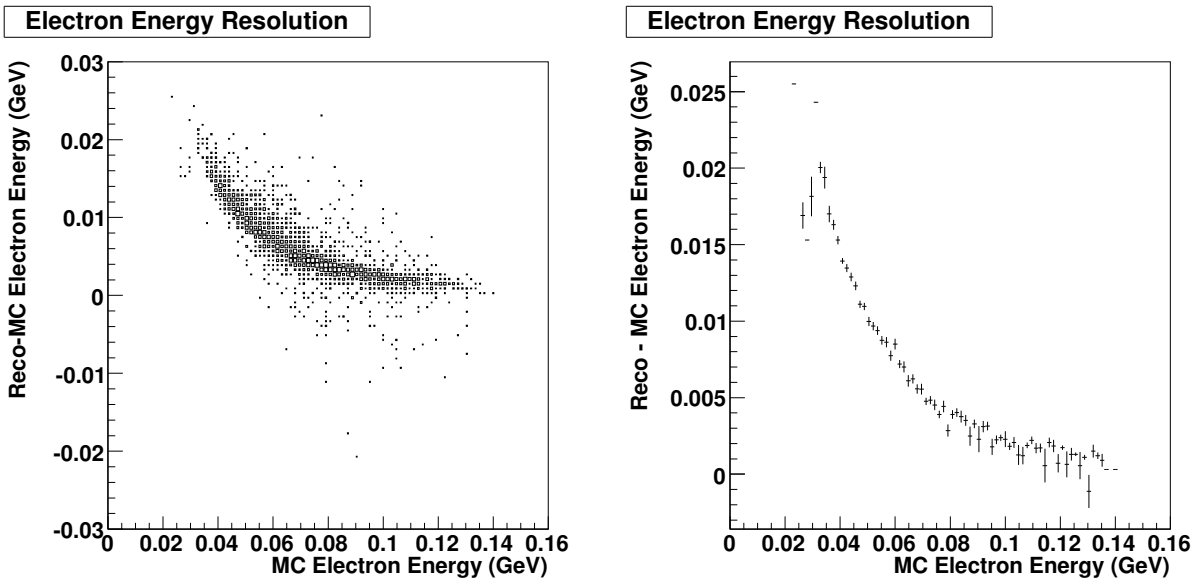

Figure 5: (Left) A scatter plot between the reconstructed and Monte Carlo generated electron energy against the generated energy using the pion mass hypothesis. (Right) The y-profile of the scatter plot.

This is seen to be corrected when we use the electron mass hypothesis for our track fits as presented in Fig. 6. Simply re-parameterizing the energy of the tracks using a fit to the profile plot in Fig. 5 did not improve our results as significantly as reconstructing tracks with the electron mass fit.

To carry out this reprocessing procedure, we observed the following steps:

1. We staged in the raw events of the datasets in Table 2 and dataset 42 to disk,

2. We recognized that we do not need the electron mass hypothesis fit, shortened to *electron-fit* in the rest of the document, in all events. Our analysis only requires events that have a D_s candidate which decayed in one of the nine hadronic modes specified in Eq. 19 - 27 to be electron-fitted. To that end, we produced an Indexed Ascii (IDXA)

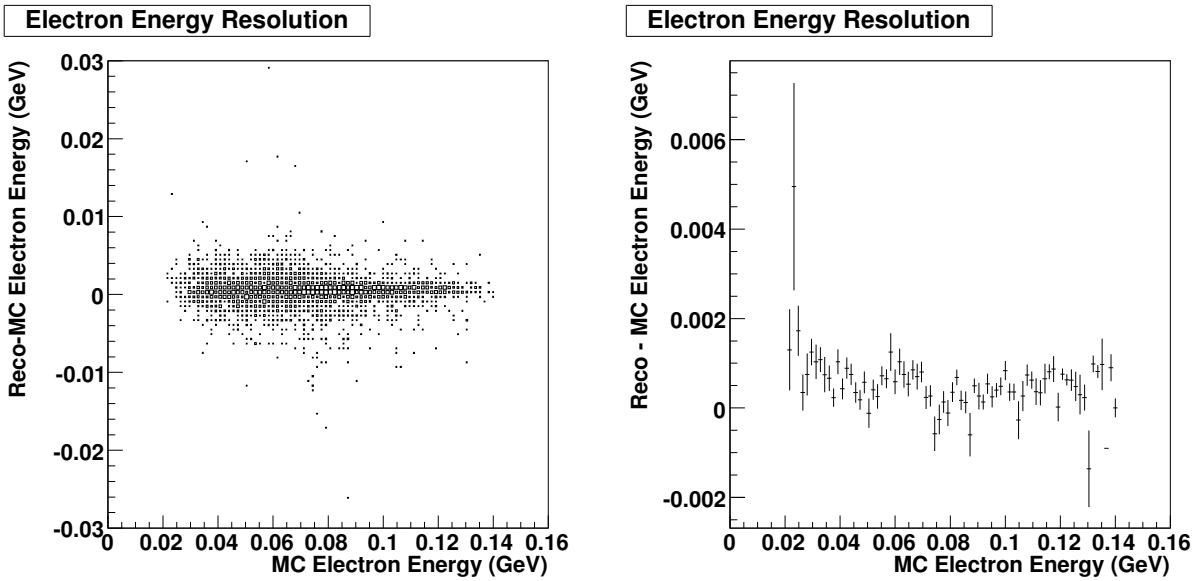

Figure 6: (Left) A scatter plot between the reconstructed and Monte Carlo generated electron energy against the generated energy using the electron mass hypothesis. (Right) The y-profile of the scatter plot.

file containing the run and event numbers of all such events in each of the datasets we used. This IDXA file was used to skim the events of interest from the staged-in datasets and write them out in PDS format to a local disk. For dataset 42, we skimmed events that contained a reconstructed J/ψ, a π^0, an e^- and a γ for reconstruction.

3. We ran the *pass2* reconstruction procedure on the PDS file, taking care to use the Suez versions and the constants versions originally used to process the datasets as recorded at:
`https://wiki.lepp.cornell.edu/lepp/bin/view/CLEO/Private/SW/FederationDetails`,
We kept the electron track information `FATable<TRHelixElectronFit>` and `FATable<TRElectronQuality>` for datasets in Table 2. For dataset 42, we kept the electron track information as well as photon decay information for π^0 mesons: `FATable<PhdPi0>`. This reconstruction procedure was carried out exclusively on the Cornell solaris batch farm that was used to originally *pass2* these datasets. It wrote out another set of PDS files.

4. After *pass2*, the PDS files corresponding to the datasets in Table 2 were run through the D_s-tagging procedure on the Cornell linux farm. Once again, care was taken to use the same Suez and constants versions originally used for this procedure. The PDS files written out at the end of this process contained the data with electron-fitted tracks relevant for our analysis.

5. The number of D_s candidates that decayed in one of the nine hadronic decay modes

of our analysis should not have changed in the course of our reprocessing. However, we noticed a tendency for our procedure to miss and create new D_s candidates once in roughly 1,000 events. On inspection, these missed or new candidates were found to occur when the momentum of a single track in the event somehow got tweaked. It could be attributed to a subtle filter or processor that we may have missed in our *pass2* or D_s-tagging procedures. Since this effect is at the per-mill level, we concluded that it would not affect the results of our analysis gravely. The fraction of missed and newly created D_s tags are used to quantify the veracity of our reprocessing technique in the subsequent sections.

8.1 Dataset 39

Dataset 39 contains 55.1 pb^{-1} of data, which originally had 3,560,069 D_s-tags. It was reconstructed on the solaris farm using Suez version `20060117_P2` and constants version `PASS2-C_5`. D_s-tagging was done on the linux farm using Suez version `20060224_FULL_1` and constants version `Analysis-C_5`. Our procedure missed 6,451 tags and created 3,825 new tags. Therefore, we missed $\sim 0.18\%$ and created $\sim 0.1\%$ new D_s-tags in this dataset.

8.2 Dataset 40

Dataset 40 contains 123.9 pb^{-1} of data, which originally had 7,995,036 D_s-tags. It was reconstructed on the solaris farm using Suez version `20060802_P2` and constants version `PASS2-C_6`. D_s-tagging was done on the linux farm using Suez version `20060224_FULL_1` and constants version `Analysis-C_6`. Our procedure missed 11,594 tags and created 6,960 new tags. Therefore, we missed $\sim 0.15\%$ and created $\sim 0.09\%$ new D_s-tags in this dataset.

8.3 Dataset 41

Dataset 41 contains 119.1 pb^{-1} of data, which originally had 7,680,344 D_s-tags. It was reconstructed on the solaris farm using Suez version `20060802_P2` and constants version `PASS2-C_6`. D_s-tagging was done on the linux farm using Suez version `20060224_FULL_1/3` and constants version `Analysis-C_6`. Our procedure missed 10,424 tags and created 6,431 new tags. Therefore, we missed $\sim 0.14\%$ and created $\sim 0.08\%$ new D_s-tags in this dataset.

8.4 Dataset 42

Dataset 42 contains 48.1 pb^{-1} of data collected at the $\psi(2S)$ resonance energy. It was re-reconstructed in order to have electron-fitted tracks for our low energy electron tracking efficiency study. It was reconstructed on the solaris farm using Suez version `20060802_P2` and constants version `PASS2-C_6`.

8.5 Dataset 47

Dataset 47 contains 109.8 pb^{-1} of data, which originally had 7,184,618 D_s-tags. It was reconstructed on the solaris farm using Suez version `20071023_P2` and constants version `PASS2-C_6`. D_s-tagging was done on the linux farm using Suez version `20060224_FULL_A_3` and constants version `Analysis-C_6`. Our procedure missed 13,036 tags and created 8,377 new tags. Therefore, we missed $\sim 0.18\%$ and created $\sim 0.11\%$ new D_s-tags in this dataset.

8.6 Dataset 48

Dataset 48 contains 178.3 pb^{-1} of data, which originally had 11,560,602 D_s-tags. It was reconstructed on the solaris farm using Suez version `20071023_P2` and constants version `PASS2-C_6`. D_s-tagging was done on the linux farm using Suez version `20060224_FULL_A_3` and constants version `Analysis-C_6`. Our procedure missed 17,151 tags and created 9,541 new tags. Therefore, we missed $\sim 0.15\%$ and created $\sim 0.08\%$ new D_s-tags in this dataset.

9 Validation of Generated Signal Monte Carlo

We have arrived at an analytical form for $d\Gamma/dq^2$ in Eq. 17 that we've integrated over q^2 and divided by Eq. 14 to compute $\Gamma(D_s^{*+} \to D_s^+ e^+ e^-)/\Gamma(D_s^{*+} \to D_s^+ \gamma)$ in Eq. 18. However, we have simply inserted the form of the matrix element for our process, Eq. 15, as a module in `EVTGEN`. Therefore, we must check if the $d\Gamma/dq^2$ in our Monte Carlo distribution follows the analytical form we arrived at.

To do so, we plot $d\Gamma/dq^2$ as a function of q^2 that was written down in Eq. 17 overlaid with an appropriately normalized histogram of the q^2 recovered from the generator level invariant mass of the e^+e^- pair in Fig. 7.

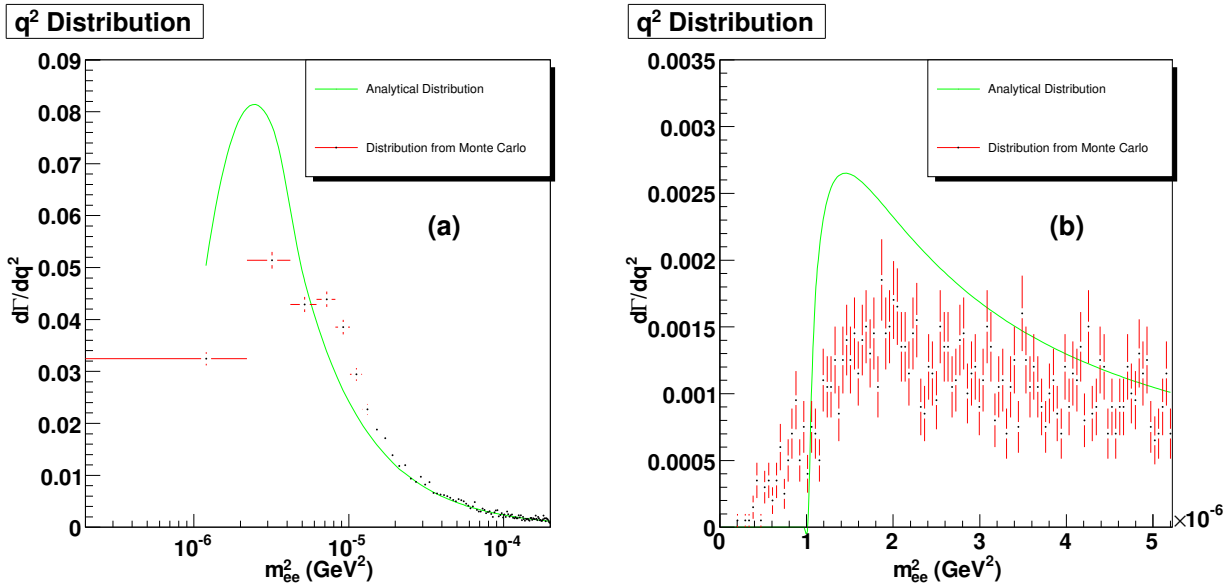

Figure 7: (a) The analytical expression for the distribution of q^2 overlaid with the distribution of m_{ee}^2 from our generated Monte Carlo. The discrepancy is explained in the text. (b) The same plot zoomed in between 0 GeV and $20m_e^2$ to illustrate the discrepancy better.

This discrepancy was tracked down to the insufficient precision with which the values of electron energy and momentum at generator level Monte Carlo are stored in CLEO-c software. This causes a smearing in the invariant mass of a single electron calculated from the stored values of its energy and momentum, as shown in Fig. 8. It gets worse as one goes to higher energies, as seen in Fig. 8b.

Henceforth, we decided to re-calculate the energy of each electron from its momentum. The distribution of m_{ee}^2 now matches our analytical calculation, as shown in Fig. 9.

This discrepancy is not expected to be a problem in reconstructed data as the energy of electron tracks are recomputed from the reconstructed track momentum by assuming the electron mass. Also, discrepancies in the range of MeVs, as suggested by Fig. 7 and 8 would be washed away by the resolution of the detector.

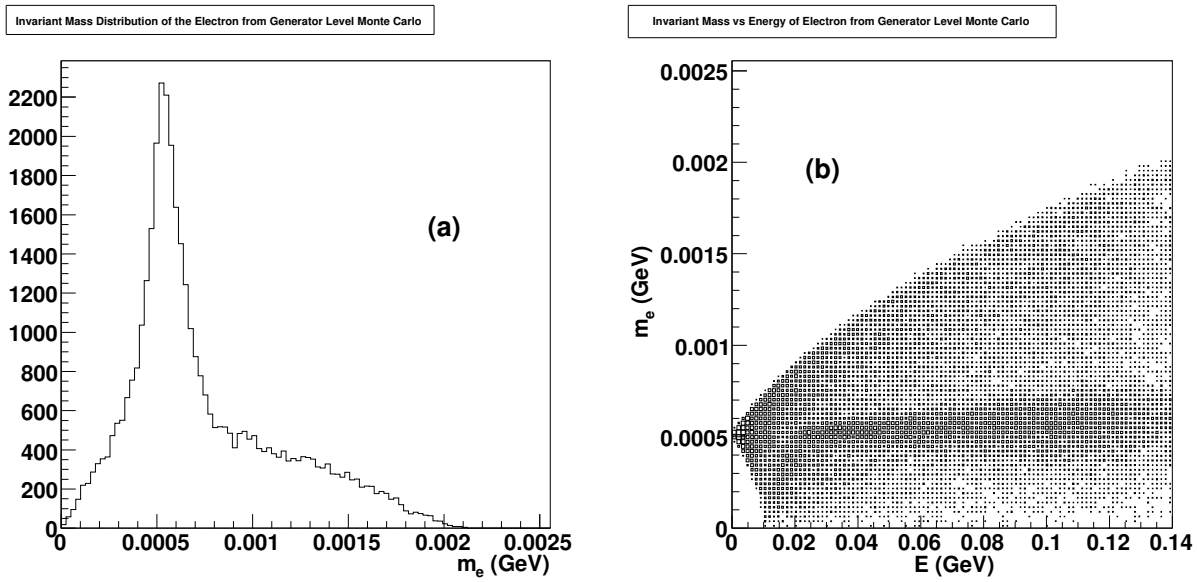

Figure 8: (a) Invariant mass distribution of an electron from the values of energy and momentum stored at generator level Monte Carlo. (b) The same plotted against the energy of the electron.

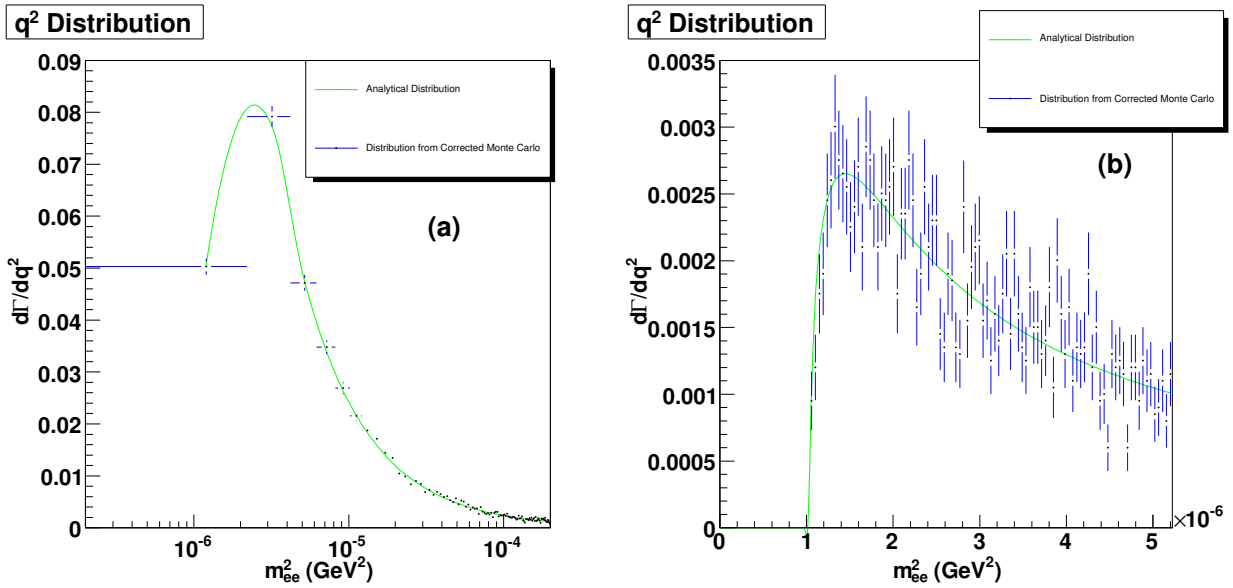

Figure 9: (a) The analytical expression for the distribution of q^2 overlaid with the distribution of the corrected m_{ee}^2 from the Monte Carlo. (b) A zoom into the region betweeen 0 GeV and $20m_e^2$ to illustrate the close match near the peak.

10 Optimization of Selection Criteria for Measuring $B(D_s^{*+} \to D_s^+ e^+ e^-)$

We optimize the selection criteria for each of the 9 hadronic decay modes of the D_s^+ used in this analysis, for both the pion-fitted and electron-fitted samples. Improvements in the signal yields and significances are noted as we go from the pion-fitted to the electron-fitted samples, and this is tabulated in Tables 6, 8, 10, 12, 14, 16, 18, 20 and 22.

A problem arises in making optimization plots for the electron-fitted samples because the generic Monte Carlo and the continuum Monte Carlo are not electron-fitted. To get around this, we recognize that electron-fitting tracks is most important for separating conversion events from signal. It does not change distributions of the Dalitz decay or other combinatoric backgrounds appreciably for the purposes of this analysis. Therefore, we privately produce electron-fitted Monte Carlo samples of $D_s^{*+} \to D_s^+ \gamma$ events where the D_s^+ decays generically, and use them in place of Generic Monte Carlo events which have $D_s^{*+} \to D_s^+ \gamma$ at their generator level.

To create the plots in the following sub-sections for each hadronic decay of the D_s^+, it is assumed that:

- $D_s^{\pm} D_s^{*\mp}$ pairs are produced at $\sqrt{s}$= 4170 MeV with a cross section of 948 $\pm$ 36 pb,
- the branching fraction of $D_s^{*+} \to D_s^+ \gamma$ is 94.2%,
- the branching fraction of $D_s^{*+} \to D_s^+ e^+ e^-$ is 0.65%,
- the scale of generic Monte Carlo is 1/19.2,
- the scale of continuum Monte Caro is 1/5.

A summary of the number of signal and background events expected after optimization for each mode with pion-fitted samples is tabulated in Table 3. A similar summary for electron-fitted samples is presented in Table 4. They are a compilation of results obtained in the following sub-sections that deals with the optimization of the modes individually. The numbers in these tables are, by no means, used as final expectations of the background in data. A data driven method is used to achieve that in Section 12 and summarized in Section 12.12. The numbers here are merely representative and were used to converge on an optimized set of parameters for our selection criteria.

10.1 $D_s^+ \to K^+ K^- \pi^+$

Given that the branching fraction of $D_s^+ \to K^+ K^- \pi^+$ is 5.50%, we studied the plots in 10, 12, 14, 16 and 18 to arrive at the selection criteria for pion-fitted data, and the plots in 11, 13, 15, 17 and 19 to arrive at the selection criteria for electron-fitted data. These are summarized in Table 5.

The result of these selection criteria, applied to the pion and electron-fitted samples, are presented in terms of the signal and background yields we can expect in 586 pb^{-1} of data

Table 3: Number of signal and background events expected from Monte Carlo in pion mass fitted data.

Mode	Signal	Generic Background	Continuum Background	Total Background	$s/\sqrt{b}$
$K^+K^-\pi^+$	11.7	2.03	0.00	2.03	8.2
K_SK^+	3.12	0.78	0.00	0.78	3.5
$\eta\pi^+$	1.57	0.21	0.20	0.41	6.3
$\eta'\pi^+;\eta'\to\pi^+\pi^-\eta$	1.02	0.47	0.00	0.47	1.5
$K^+K^-\pi^+\pi^0$	4.62	3.49	0.40	3.89	2.3
$\pi^+\pi^-\pi^+$	2.99	0.73	0.60	1.33	2.6
$K^{*+}K^{*0}$	1.78	1.35	0.00	1.35	1.5
$\eta\rho^+$	5.54	2.40	3.60	6.00	2.3
$\eta'\pi^+;\eta'\to\rho^0\gamma$	2.17	0.83	1.60	2.43	1.4
Total	36.94	12.29	6.4	18.69	8.6

Table 4: Number of signal and background events expected from Monte Carlo in electron mass fitted data.

Mode	Signal	Conversion Background	Generic Background Conversions Vetoed	Continuum Background	Total Background	$s/\sqrt{b}$
$K^+K^-\pi^+$	13.36	1.04	0.42	0.00	1.45	11.1
K_SK^+	3.05	0.34	0.21	0.00	0.54	4.13
$\eta\pi^+$	1.79	0.17	0.10	0.20	0.47	6.6
$\eta'\pi^+;\eta'\to\pi^+\pi^-\eta$	0.74	0.00	0.00	0.00	0.00	∞
$K^+K^-\pi^+\pi^0$	4.86	0.63	1.46	0.20	2.29	3.2
$\pi^+\pi^-\pi^+$	3.67	0.28	0.21	1.60	2.09	2.5
$K^{*+}K^{*0}$	2.02	0.23	0.63	0.20	1.05	2.0
$\eta\rho^+$	5.71	0.85	0.99	1.00	2.84	3.4
$\eta'\pi^+;\eta'\to\rho^0\gamma$	2.41	0.34	0.21	1.80	2.35	1.6
Total	40.36	3.88	4.23	5.00	13.08	11.2

in Table 6. A signal significance, defined for now simply as $\frac{N_SignalEvents}{\sqrt{N_BackgroundEvents}}$, serves as a measure of comparison between the two sets of criteria and samples.

Optimization plots for the $m_{D_s^+}$ selection criterion in the $D_s^+ \to K^+K^-\pi^+$ decay mode having applied all other selection criteria. All plots are normalized to 586 pb^{-1} of data. The top left plots, for both the pion and electron-fitted sets of data, are the distributions of $m_{D_s^+}$ in the signal MC sample. The top right plot is the signal MC sample accepted by the criterion as we increase the cut width plotted on the x-axis. For the pion-fitted samples on the left, the plots in the second and third rows correspond to the generic and continuum MC samples, respectively. For the electron-fitted samples on the right, the plots in the second, third and fourth rows correspond to the conversion, generic and continuum MC samples, respectively. For both sets of plots, the bottom left shows the significance of the signal over background. The bottom right plot shows the precision of the signal.

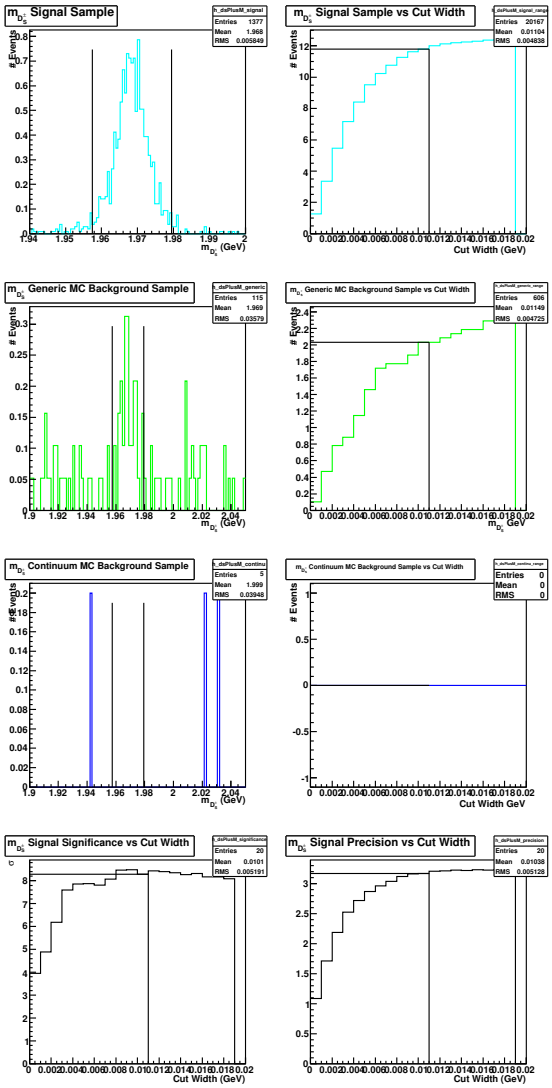

Figure 10: Optimization plots for the $m_{D_s^+}$ selection criterion in the $D_s^+ \to K^+K^-\pi^+$ decay mode for pion-fitted data.

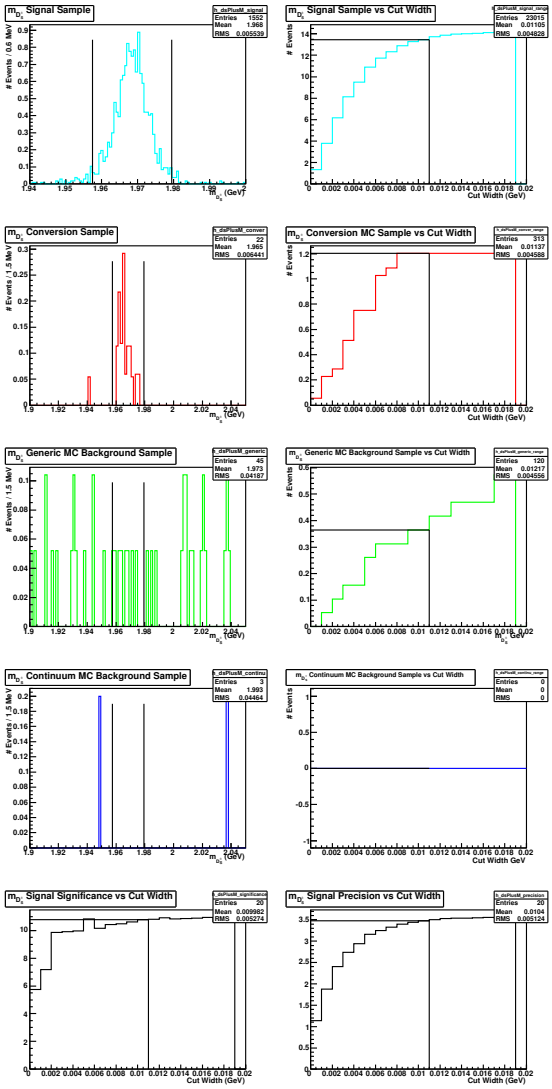

Figure 11: Optimization plots for the $m_{D_s^+}$ selection criterion in the $D_s^+ \to K^+K^-\pi^+$ decay mode for electron-fitted data.

Optimization plots for the m_{BC} selection criterion in the $D_s^+ \to K^+K^-\pi^+$ decay mode having applied all other selection criteria. All plots are normalized to 586 pb^{-1} of data.

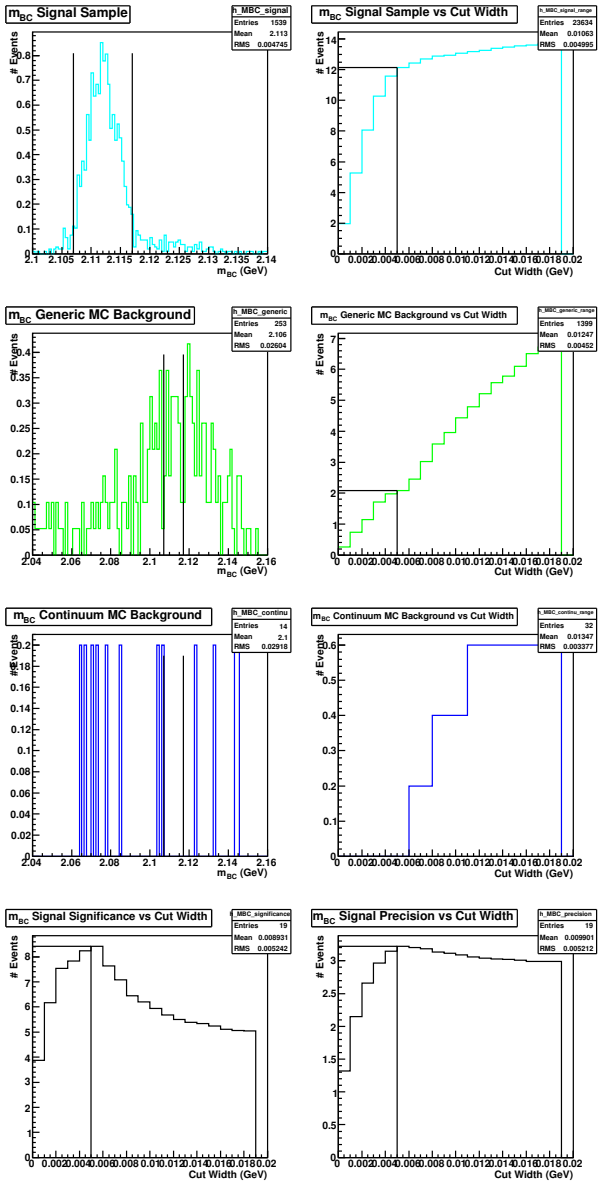

Figure 12: Optimization plots for the m_{BC} selection criterion in the $D_s^+ \to K^+K^-\pi^+$ decay mode for pion-fitted data.

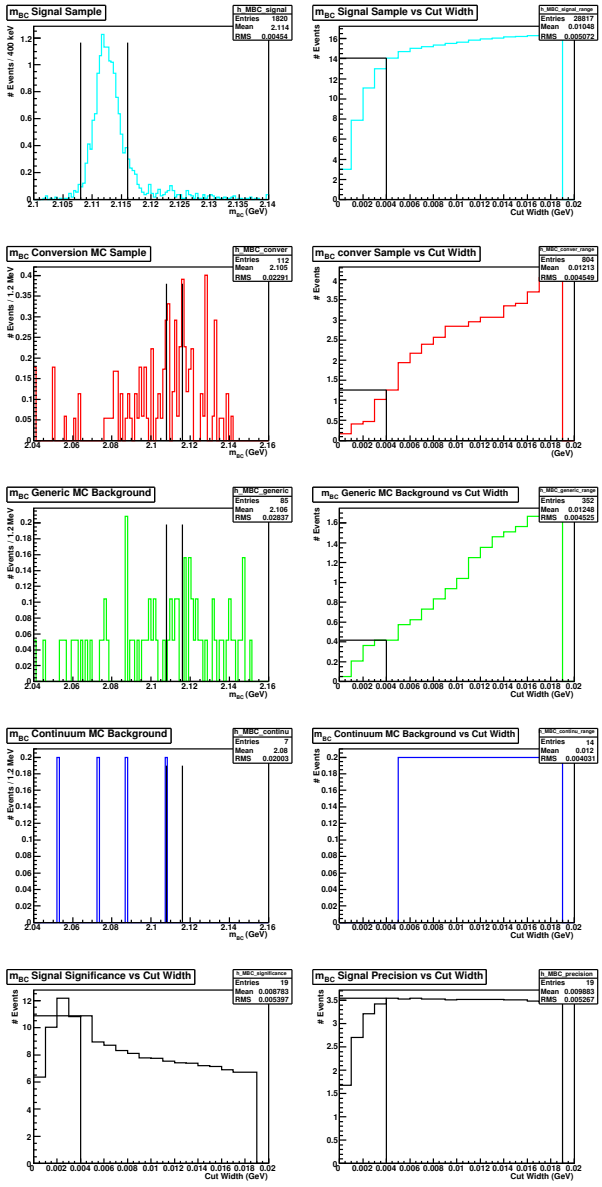

Figure 13: Optimization plots for the m_{BC} selection criterion in the $D_s^+ \to K^+K^-\pi^+$ decay mode for electron-fitted data.

Optimization plots for the δm selection criterion in the $D_s^+ \to K^+K^-\pi^+$ decay mode having applied all other selection criteria. All plots are normalized to 586 pb^{-1} of data.

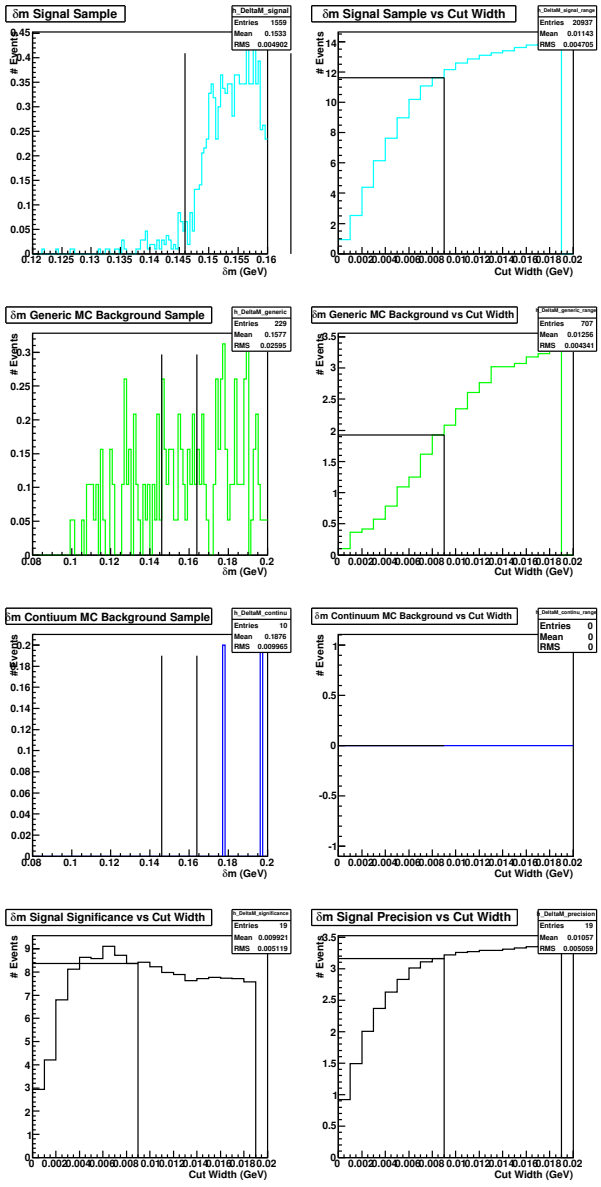

Figure 14: Optimization plots for the δm selection criterion in the $D_s^+ \to K^+K^-\pi^+$ decay mode for pion-fitted data.

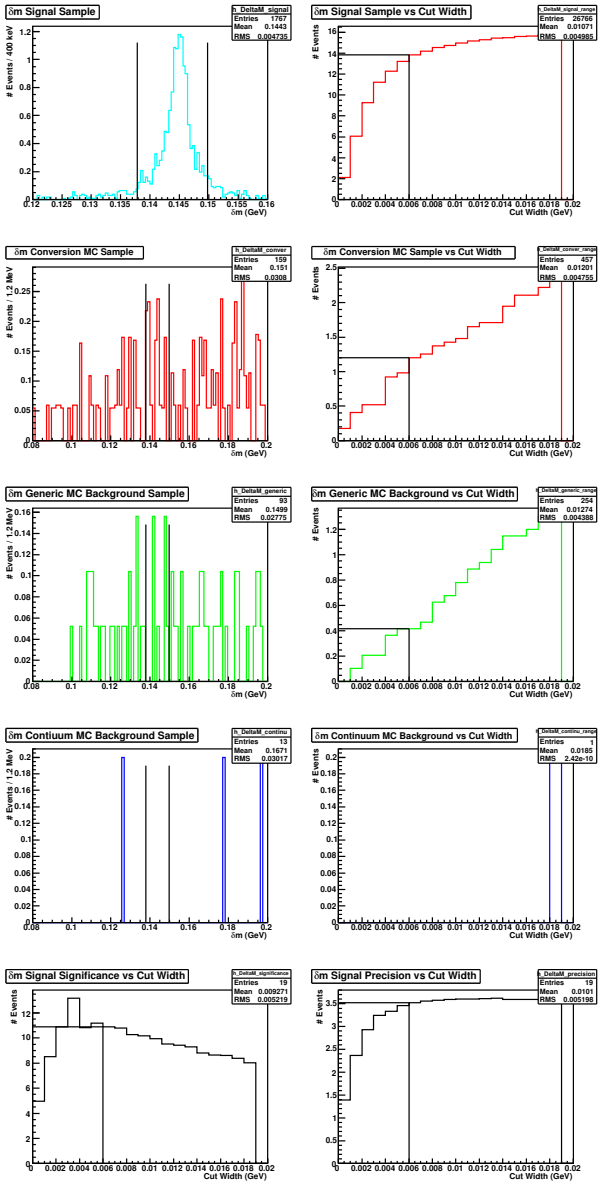

Figure 15: Optimization plots for the δm selection criterion in the $D_s^+ \to K^+K^-\pi^+$ decay mode for electron-fitted data.

Optimization plots for the selection criterion on the Δd_0 of the e^+e^- in the $D_s^+ \to K^+K^-\pi^+$ decay mode having applied all other selection criteria. All plots are normalized to 586 pb^{-1} of data.

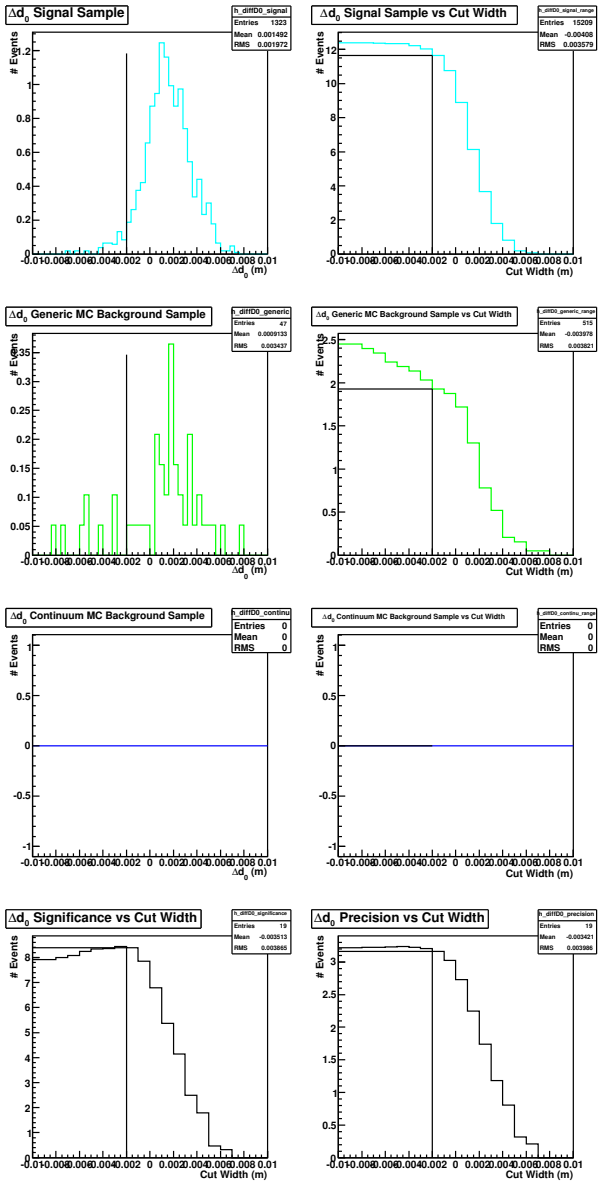

Figure 16: Optimization plots for the selection criterion on Δd_0 in the $D_s^+ \to K^+K^-\pi^+$ for pion-fitted data.

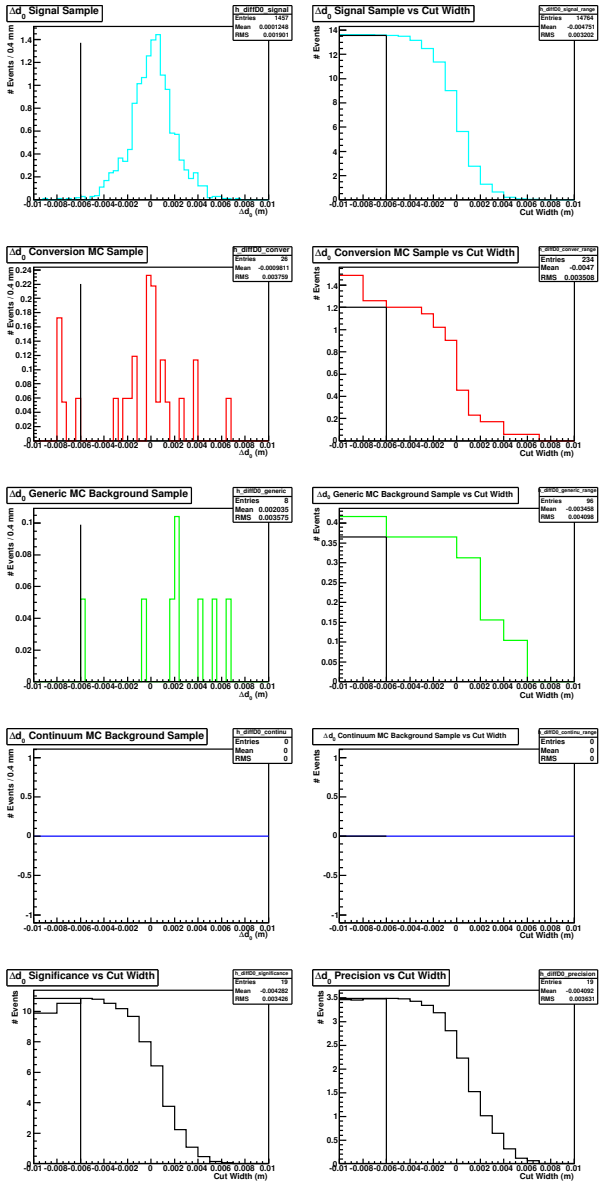

Figure 17: Optimization plots for the selection criterion on Δd_0 in the $D_s^+ \to K^+K^-\pi^+$ for electron-fitted data.

Optimization plots for the selection criterion on the $\Delta\phi_0$ of the e^+e^- in the $D_s^+ \to K^+K^-\pi^+$ decay mode having applied all other selection criteria. All plots are normalized to 586 pb^{-1} of data.

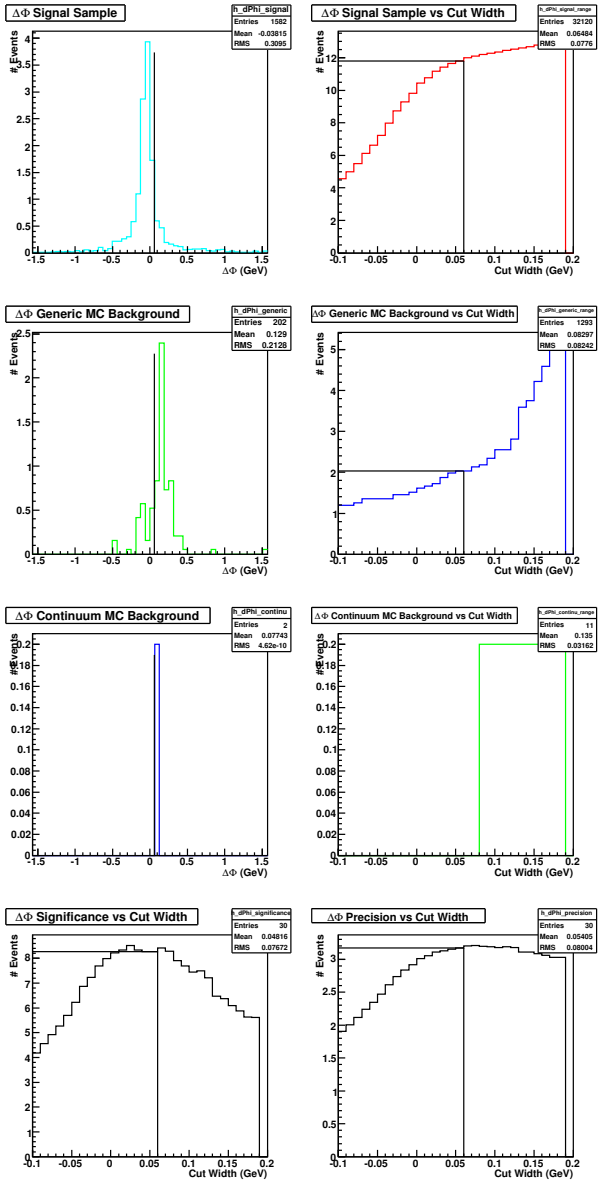

Figure 18: Optimization plots for the selection criterion on the $\Delta\phi_0$ of the e^+e^- in the $D_s^+ \to K^+K^-\pi^+$ decay mode for pion-fitted data.

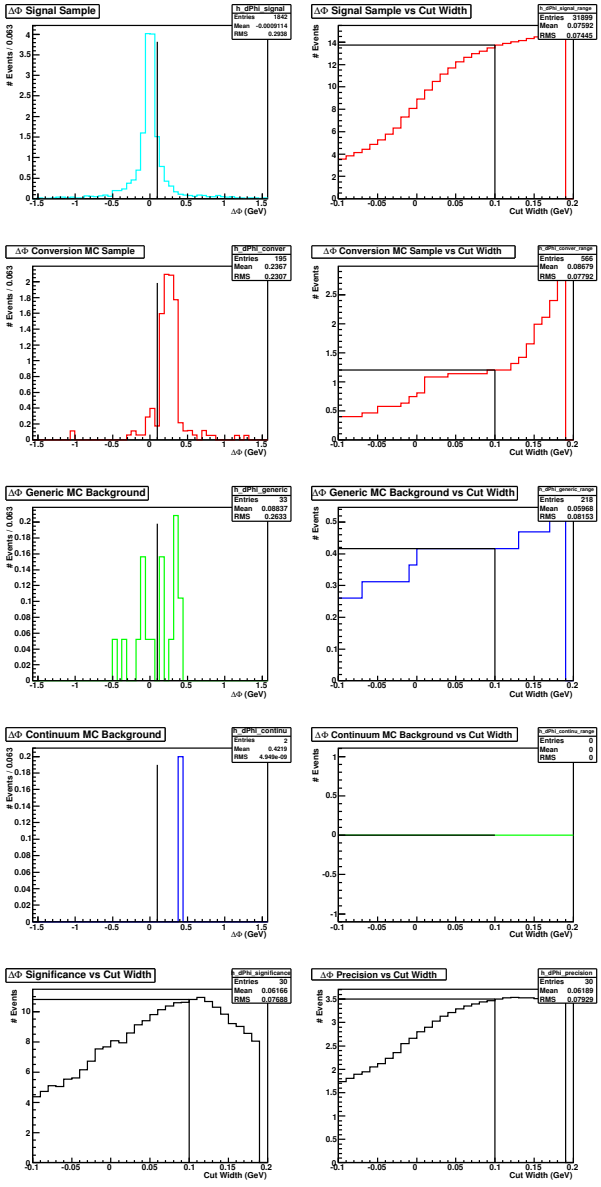

Figure 19: Optimization plots for the selection criterion on the $\Delta\phi_0$ of the e^+e^- in the $D_s^+ \to K^+K^-\pi^+$ decay mode for electron-fitted data.

Table 5: Selection criteria for pion-fitted and electron-fitted data in the $D_s^+ \to K^+K^-\pi^+$ decay mode.

Selection Criterion	Pion-Fitted Data Cut Center ± Width	Electron-Fitted Data Cut Center ± Width
$m_{D_s^+}$	1.969 ± 0.011 GeV	1.969 ± 0.011 GeV
m_{BC}	2.112 ± 0.005 GeV	2.112 ± 0.004 GeV
δm	0.155 ± 0.009 GeV	0.144 ± 0.006 GeV
Δd_0	-0.002 m	-0.006 m
$\Delta\phi_0$	0.06	0.1

Table 6: Number of signal and background events expected in pion and electron-fitted data in the $D_s^+ \to K^+K^-\pi^+$ decay mode.

Expected Number of Events in 586 pb^{-1}	Pion-Fitted Samples and Criteria	Electron-Fitted Samples and Criteria
Signal ($N_Ssignal Events$)	11.7	13.36
Conversion Background	-	1.04
Generic Background (without Conversions in e-fit)	2.03	0.42
Continuum Background	0.00	0.00
Total Background ($N_Background Events$)	2.03	1.45
$\frac{N_Signal Events}{\sqrt{N_Background Events}}$	8.2	11.1

10.2 $D_s^+ \to K_S K^+$

Given that the branching fraction of $D_s^+ \to K_S K^+$ is 1.49%, we studied the plots in 20, 22, 24, 26 and 28 to arrive at the selection criteria for pion-fitted data, and the plots in 21, 23, 25, 27 and 29 to arrive at the selection criteria for electron-fitted data. These are summarized in Table 7.

Table 7: Selection criteria for pion-fitted and electron-fitted data in the $D_s^+ \to K_S K^+$ decay mode.

Selection Criterion	Pion-Fitted Data Cut Center ± Width	Electron-Fitted Data Cut Center ± Width
$m_{D_s^+}$	1.969 ± 0.012 GeV	1.969 ± 0.008 GeV
m_{BC}	2.112 ± 0.006 GeV	2.112 ± 0.007 GeV
δm	0.158 ± 0.010 GeV	0.144 ± 0.006 GeV
Δd_0	-0.002 m	-0.004 m
$\Delta\phi_0$	0.09	0.14

The result of these selection criteria, applied to the pion and electron-fitted samples, are presented in terms of the signal and background yields we can expect in 586 pb^{-1} of data in Table 8. A signal significance, defined for now simply as $\frac{N_S ignal Events}{\sqrt{N_B ackground Events}}$, serves as a measure of comparison between the two sets of criteria and samples.

Table 8: Number of signal and background events expected in pion and electron-fitted data in the $D_s^+ \to K_S K^+$ decay mode.

Expected Number of Events in 586 pb^{-1}	Pion-Fitted Samples and Criteria	Electron-Fitted Samples and Criteria
Signal ($N_S ignal Events$)	3.12	3.05
Conversion Background	-	0.34
Generic Background (without Conversions in e-fit)	0.78	0.21
Continuum Background	0.00	0.00
Total Background ($N_B ackground Events$)	0.78	0.54
$\frac{N_S ignal Events}{\sqrt{N_B ackground Events}}$	3.5	4.13

Optimization plots for the $m_{D_s^+}$ selection criterion in the $D_s^+ \to K_S K^+$ decay mode having applied all other selection criteria. All plots are normalized to 586 pb^{-1} of data. The top left plots, for both the pion and electron-fitted sets of data, are the distributions of $m_{D_s^+}$ in the signal MC sample. The top right plot is the signal MC sample accepted by the criterion as we increase the cut width plotted on the x-axis. For the pion-fitted samples on the left, the plots in the second and third rows correspond to the generic and continuum MC samples, respectively. For the electron-fitted samples on the right, the plots in the second, third and fourth rows correspond to the conversion, generic and continuum MC samples, respectively. For both sets of plots, the bottom left shows the significance of the signal over background. The bottom right plot shows the precision of the signal.

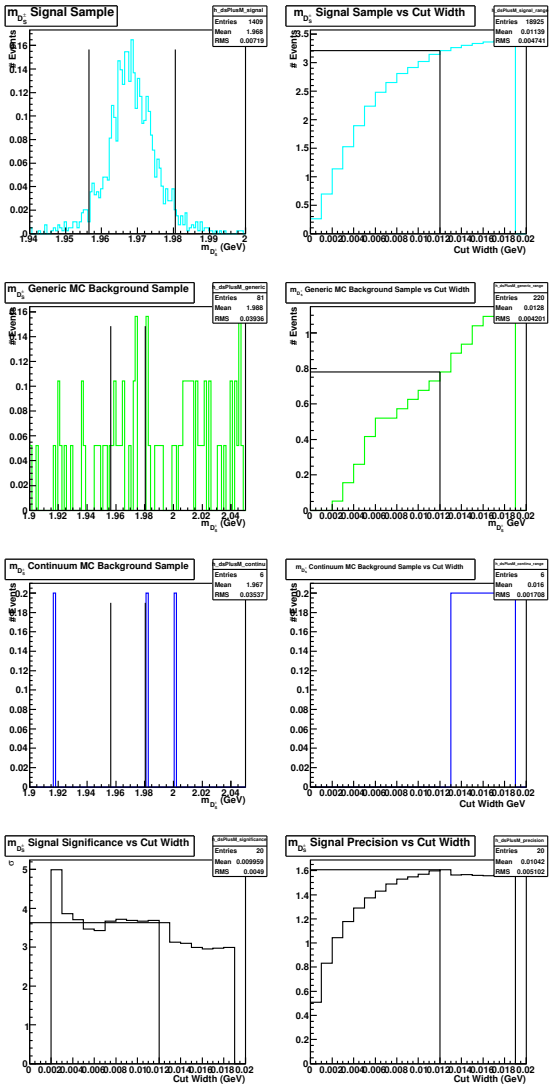

Figure 20: Optimization plots for the $m_{D_s^+}$ selection criterion in the $D_s^+ \to K_S K^+$ decay mode for pion-fitted data.

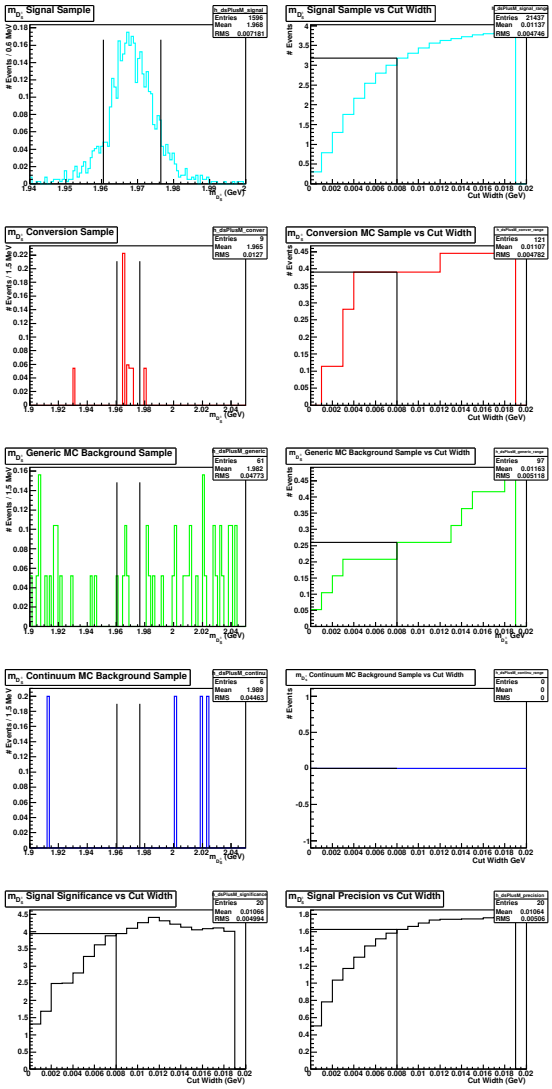

Figure 21: Optimization plots for the $m_{D_s^+}$ selection criterion in the $D_s^+ \to K_S K^+$ decay mode for electron-fitted data.

Optimization plots for the m_{BC} selection criterion in the $D_s^+ \to K_S K^+$ decay mode having applied all other selection criteria. All plots are normalized to 586 pb^{-1} of data.

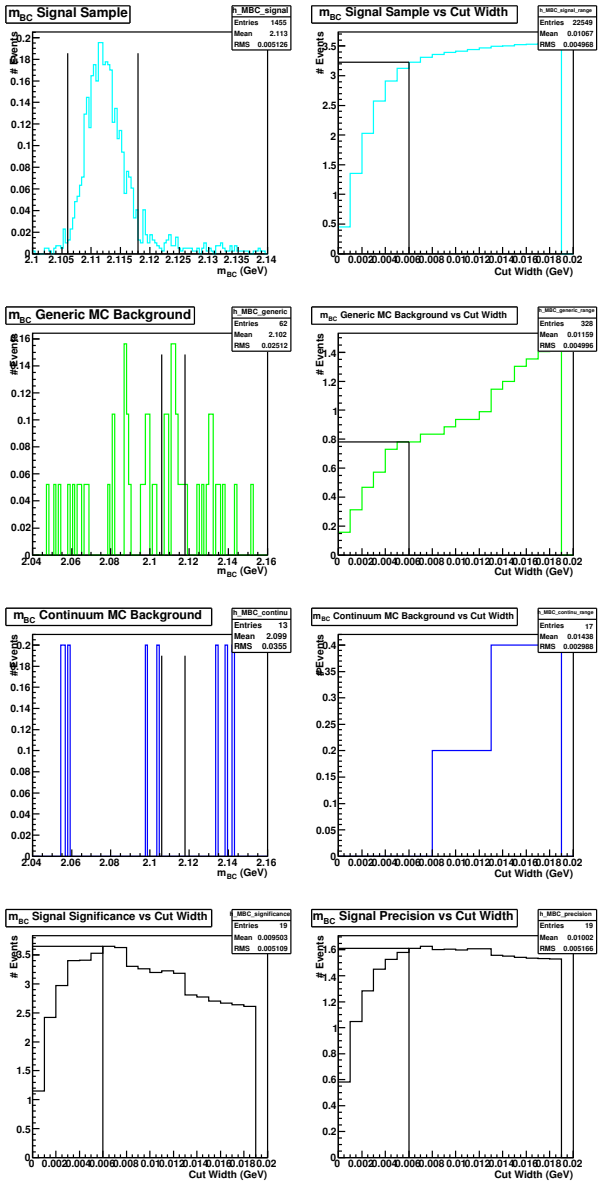

Figure 22: Optimization plots for the m_{BC} selection criterion in the $D_s^+ \to K_S K^+$ decay mode for pion-fitted data.

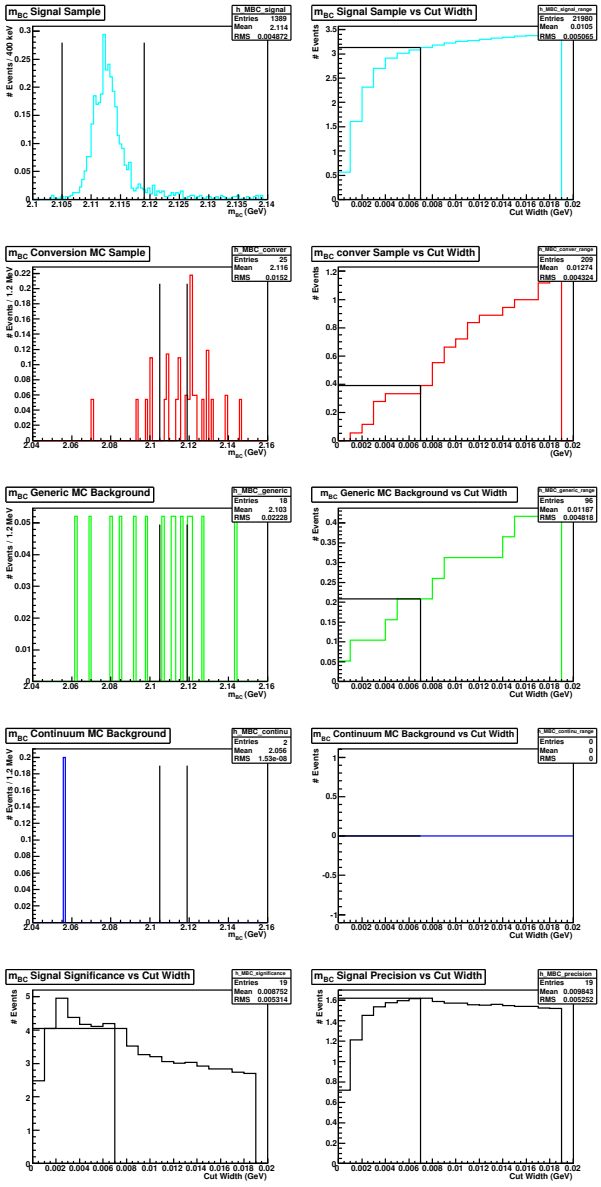

Figure 23: Optimization plots for the m_{BC} selection criterion in the $D_s^+ \to K_S K^+$ decay mode for electron-fitted data.

Optimization plots for the δm selection criterion in the $D_s^+ \to K_S K^+$ decay mode having applied all other selection criteria. All plots are normalized to 586 pb^{-1} of data.

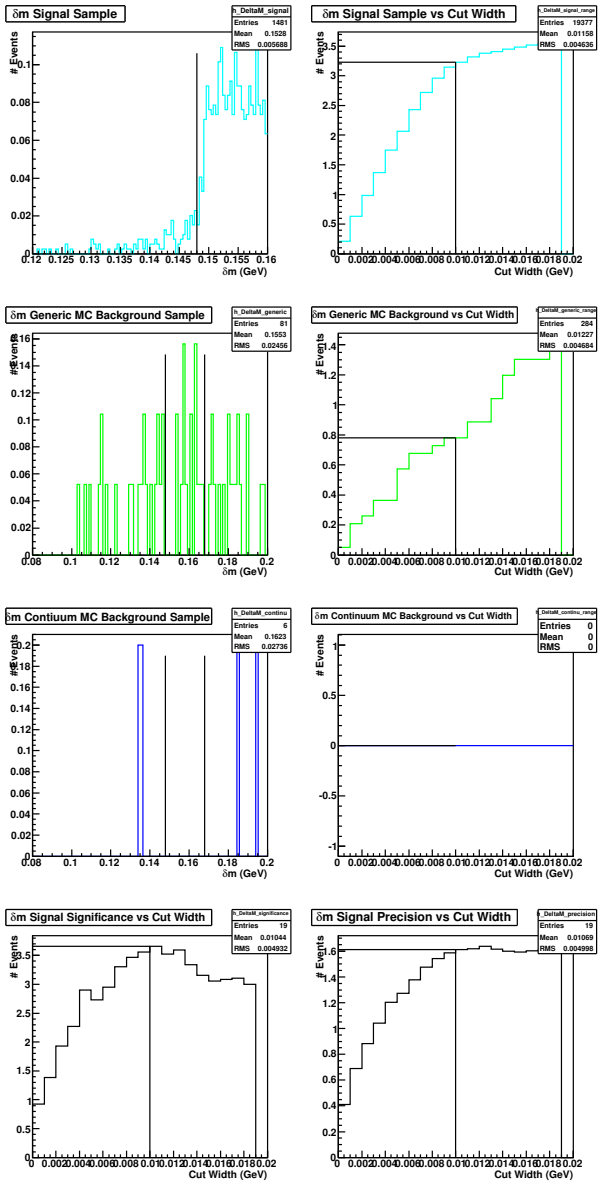

Figure 24: Optimization plots for the δm selection criterion in the $D_s^+ \to K_S K^+$ decay mode for pion-fitted data.

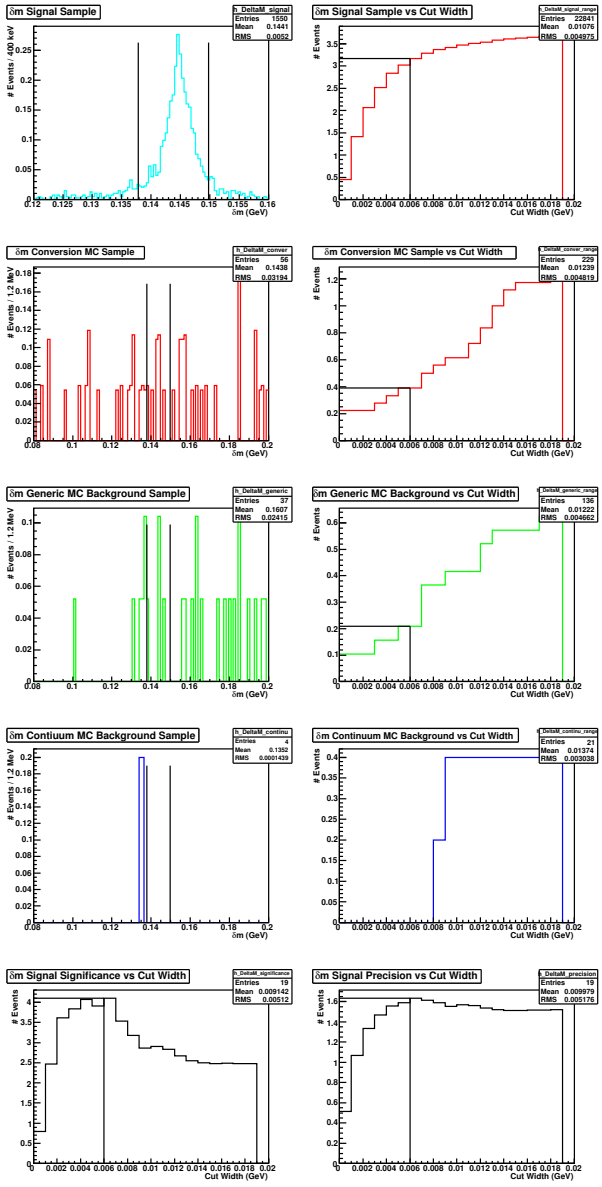

Figure 25: Optimization plots for the δm selection criterion in the $D_s^+ \to K_S K^+$ decay mode for electron-fitted data.

Optimization plots for the selection criterion on the Δd_0 of the e^+e^- in the $D_s^+ \to K_S K^+$ decay mode having applied all other selection criteria. All plots are normalized to 586 pb^{-1} of data.

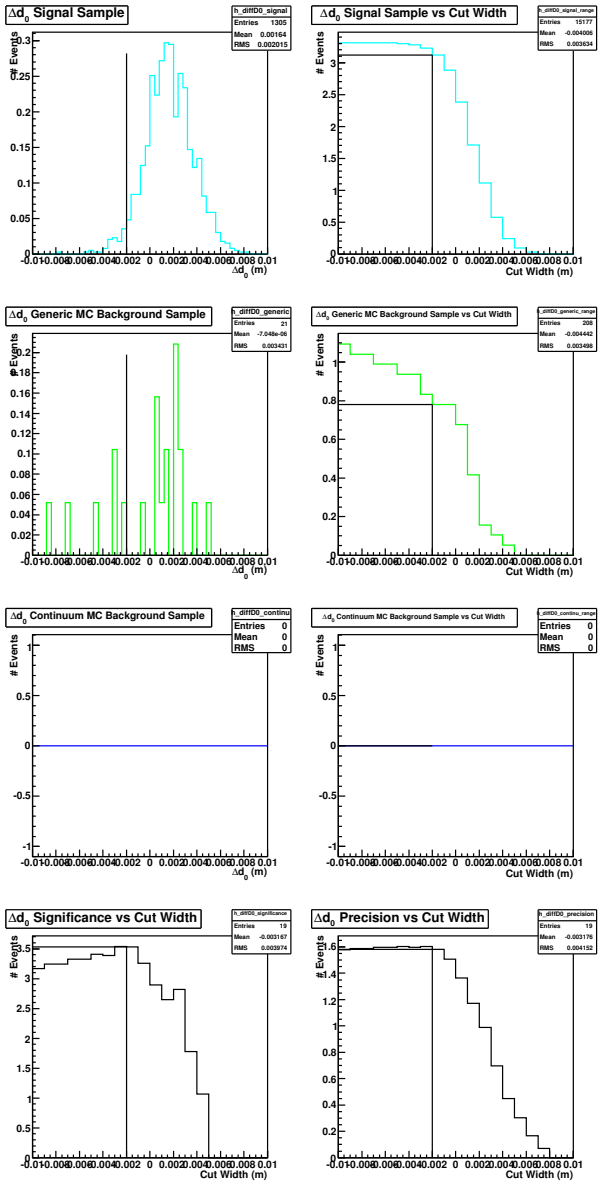

Figure 26: Optimization plots for the selection criterion on Δd_0 in the $D_s^+ \to K_S K^+$ for pion-fitted data.

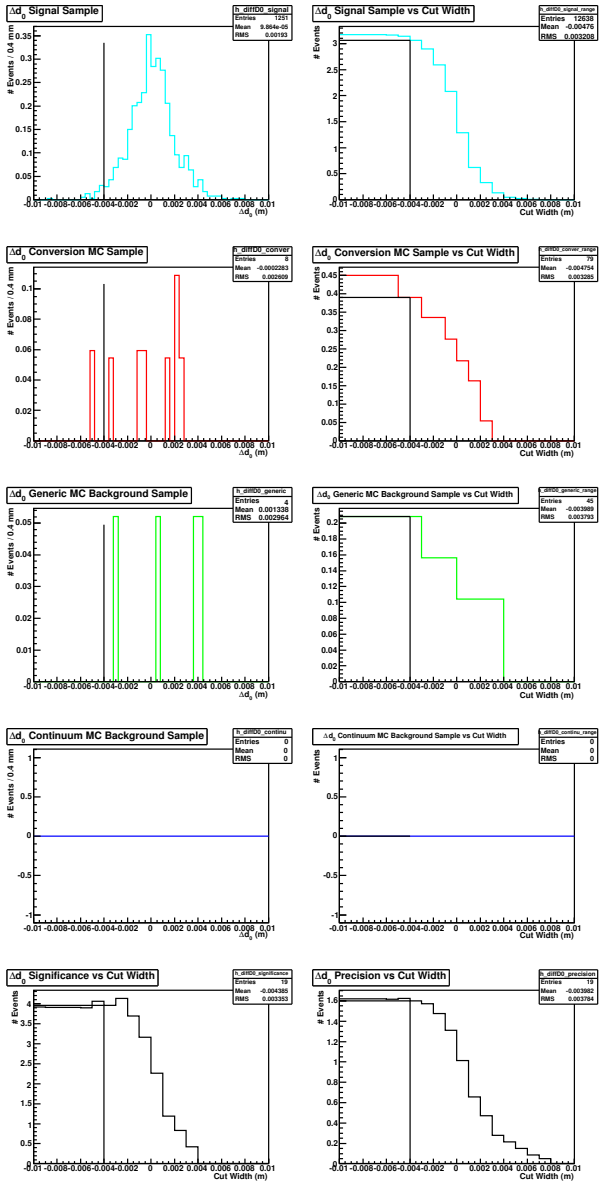

Figure 27: Optimization plots for the selection criterion on Δd_0 in the $D_s^+ \to K_S K^+$ for electron-fitted data.

Optimization plots for the selection criterion on the $\Delta\phi_0$ of the e^+e^- in the $D_s^+ \to K_S K^+$ decay mode having applied all other selection criteria. All plots are normalized to 586 pb^{-1} of data.

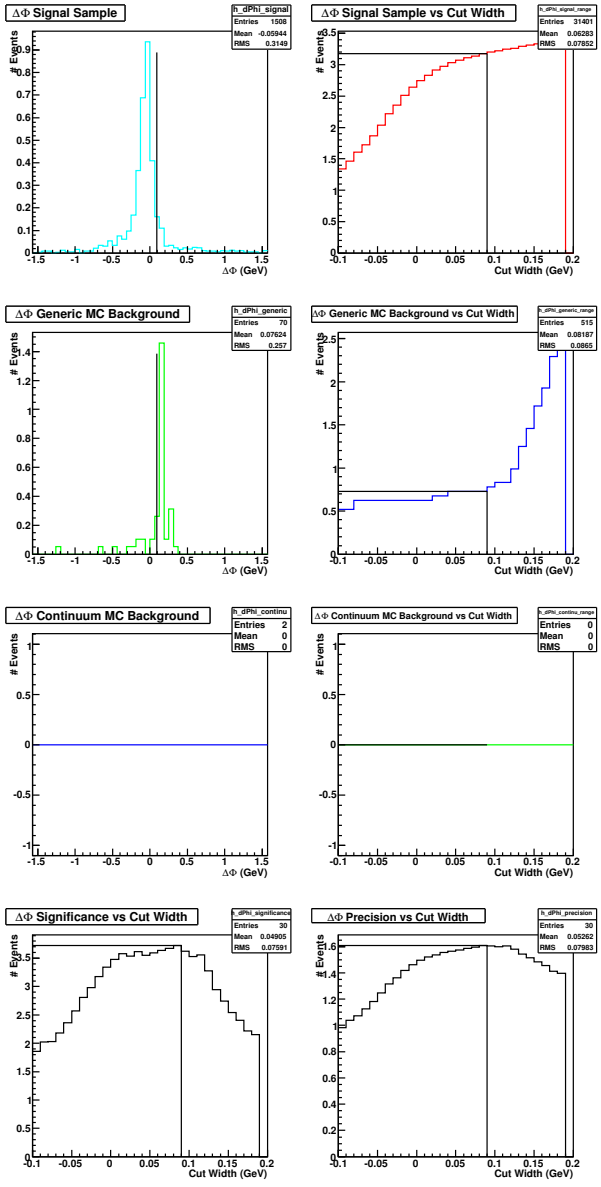

Figure 28: Optimization plots for the selection criterion on the $\Delta\phi_0$ of the e^+e^- in the $D_s^+ \to K_S K^+$ decay mode for pion-fitted data.

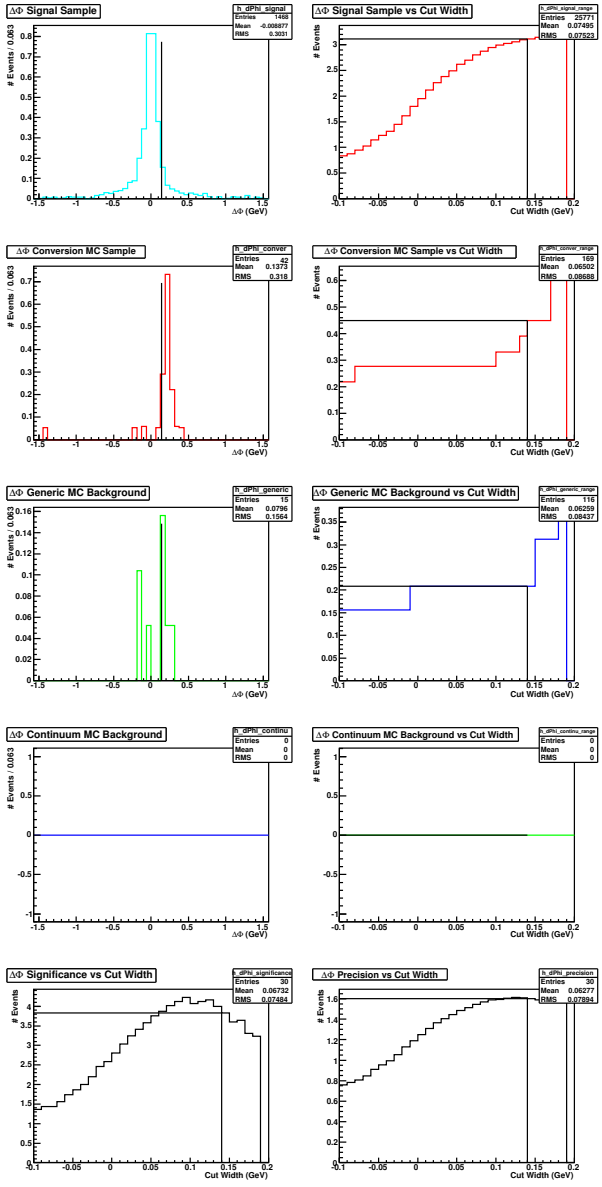

Figure 29: Optimization plots for the selection criterion on the $\Delta\phi_0$ of the e^+e^- in the $D_s^+ \to K_S K^+$ decay mode for electron-fitted data.

10.3 $D_s^+ \to \eta\pi^+; \eta \to \gamma\gamma$

Given that:

- the branching fraction of $D_s^+\eta\pi^+$ is $\simeq 1.58\%$, and
- the branching fraction of $\eta \to \gamma\gamma$ is $\simeq 39.31\%$,

, we studied the plots in 30, 32, 34, 36 and 38 to arrive at the selection criteria for pion-fitted data, and the plots in 31, 33, 35, 37 and 39 to arrive at the selection criteria for electron-fitted data. These are summarized in Table 9.

Table 9: Selection criteria for pion-fitted and electron-fitted data in the $D_s^+ \to \eta\pi^+; \eta \to \gamma\gamma$ decay mode.

Selection Criterion	Pion-Fitted Data Cut Center ± Width	Electron-Fitted Data Cut Center ± Width
$m_{D_s^+}$	1.969 ± 0.015 GeV	1.969 ± 0.016 GeV
m_{BC}	2.112 ± 0.007 GeV	2.112 ± 0.008 GeV
δm	0.155 ± 0.013 GeV	0.144 ± 0.008 GeV
Δd_0	-0.007 m	-0.004 m
$\Delta\phi_0$	0.07	0.12

The result of these selection criteria, applied to the pion and electron-fitted samples, are presented in terms of the signal and background yields we can expect in 586 pb^{-1} of data in Table 10. A signal significance, defined for now simply as $\frac{N_SignalEvents}{\sqrt{N_BackgroundEvents}}$, serves as a measure of comparison between the two sets of criteria and samples.

Table 10: Number of signal and background events expected in pion and electron-fitted data in the $D_s^+ \to \eta\pi^+; \eta \to \gamma\gamma$ decay mode.

Expected Number of Events in 586 pb^{-1}	Pion-Fitted Samples and Criteria	Electron-Fitted Samples and Criteria
Signal ($N_SignalEvents$)	1.57	1.79
Conversion Background	-	0.17
Generic Background (without Conversions in e-fit)	0.21	0.10
Continuum Background	0.20	0.20
Total Background ($N_BackgroundEvents$)	0.41	0.47
$\frac{N_SignalEvents}{\sqrt{N_BackgroundEvents}}$	6.3	6.6

Optimization plots for the $m_{D_s^+}$ selection criterion in the $D_s^+ \to \eta\pi^+; \eta \to \gamma\gamma$ decay mode having applied all other selection criteria. All plots are normalized to 586 pb^{-1} of data. The top left plots, for both the pion and electron-fitted sets of data, are the distributions of $m_{D_s^+}$ in the signal MC sample. The top right plot is the signal MC sample accepted by the criterion as we increase the cut width plotted on the x-axis. For the pion-fitted samples on the left, the plots in the second and third rows correspond to the generic and continuum MC samples, respectively. For the electron-fitted samples on the right, the plots in the second, third and fourth rows correspond to the conversion, generic and continuum MC samples, respectively. For both sets of plots, the bottom left shows the significance of the signal over background. The bottom right plot shows the precision of the signal.

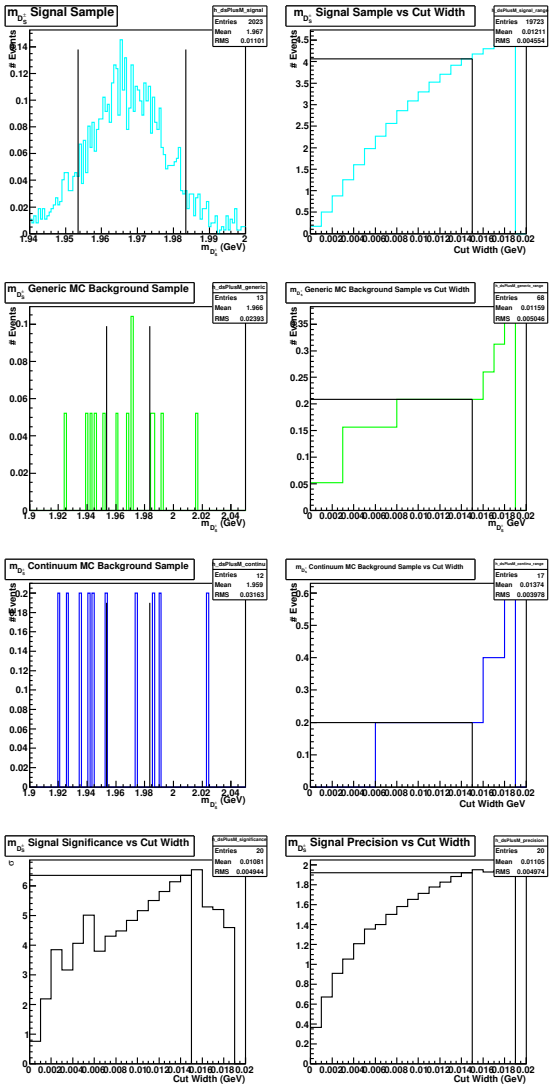

Figure 30: Optimization plots for the $m_{D_s^+}$ selection criterion in the $D_s^+ \to \eta\pi^+; \eta \to \gamma\gamma$ decay mode for pion-fitted data.

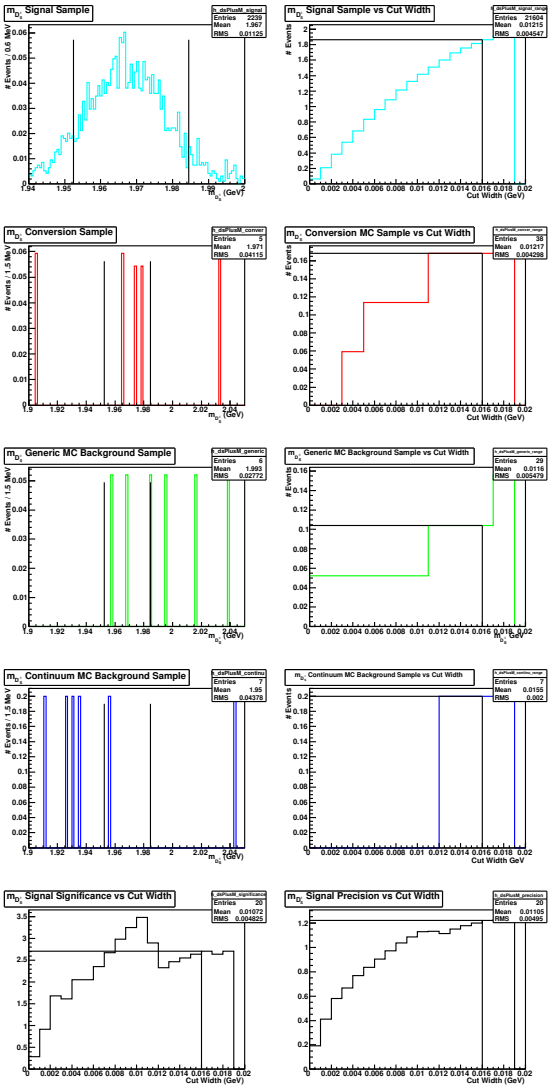

Figure 31: Optimization plots for the $m_{D_s^+}$ selection criterion in the $D_s^+ \to \eta\pi^+; \eta \to \gamma\gamma$ decay mode for electron-fitted data.

Optimization plots for the m_{BC} selection criterion in the $D_s^+ \to \eta\pi^+; \eta \to \gamma\gamma$ decay mode having applied all other selection criteria. All plots are normalized to 586 pb^{-1} of data.

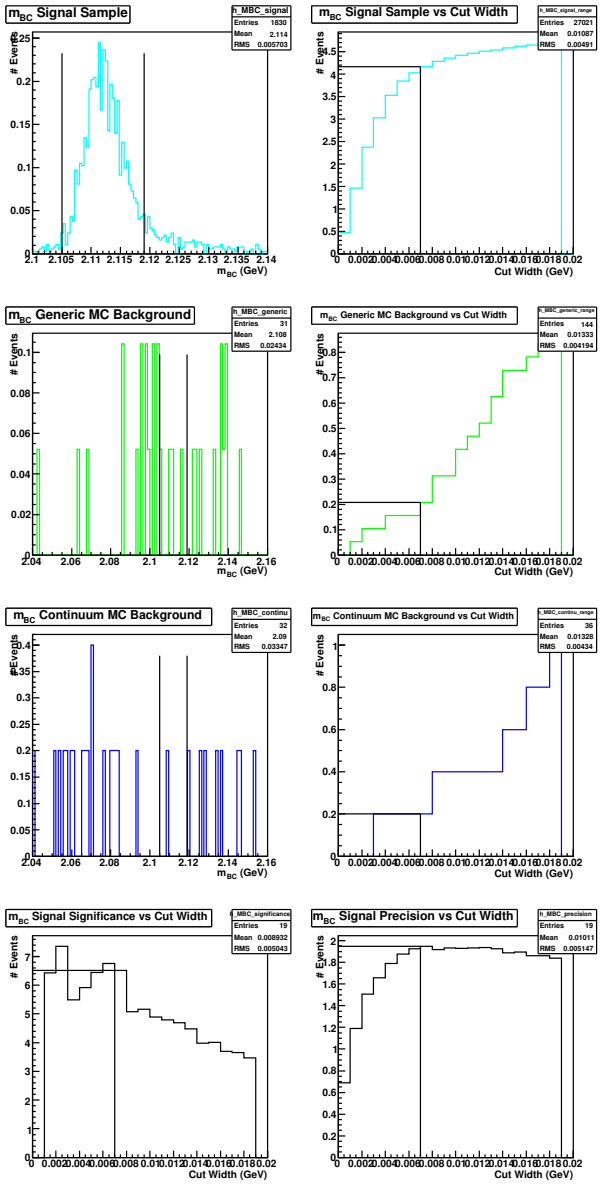

Figure 32: Optimization plots for the m_{BC} selection criterion in the $D_s^+ \to \eta\pi^+; \eta \to \gamma\gamma$ decay mode for pion-fitted data.

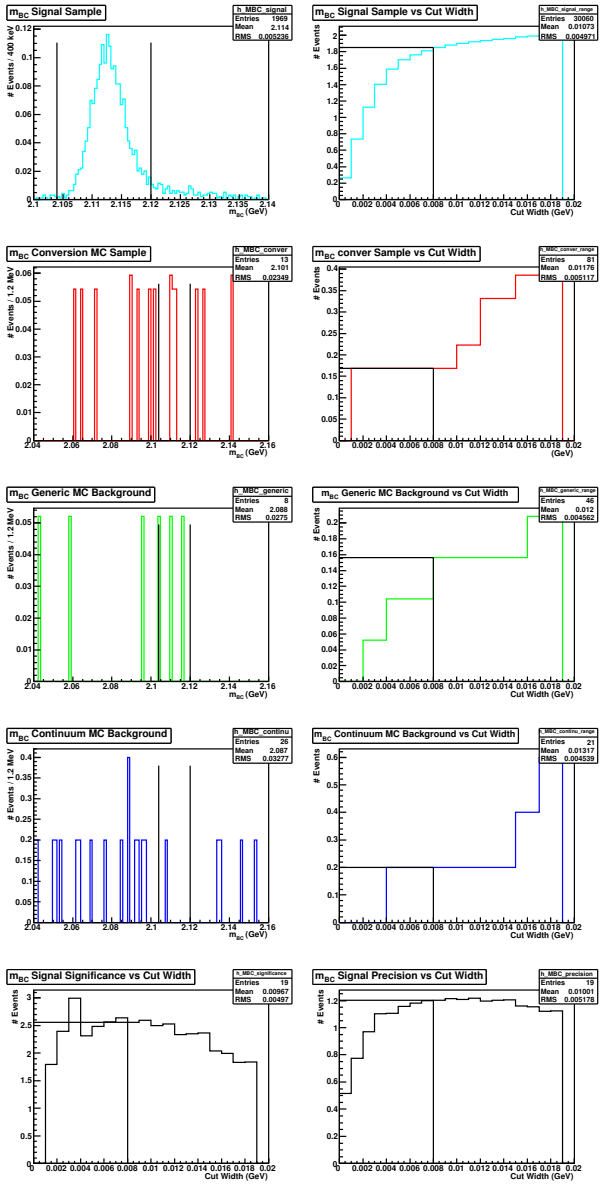

Figure 33: Optimization plots for the m_{BC} selection criterion in the $D_s^+ \to \eta\pi^+; \eta \to \gamma\gamma$ decay mode for electron-fitted data.

Optimization plots for the δm selection criterion in the $D_s^+ \to \eta\pi^+; \eta \to \gamma\gamma$ decay mode having applied all other selection criteria. All plots are normalized to 586 pb^{-1} of data.

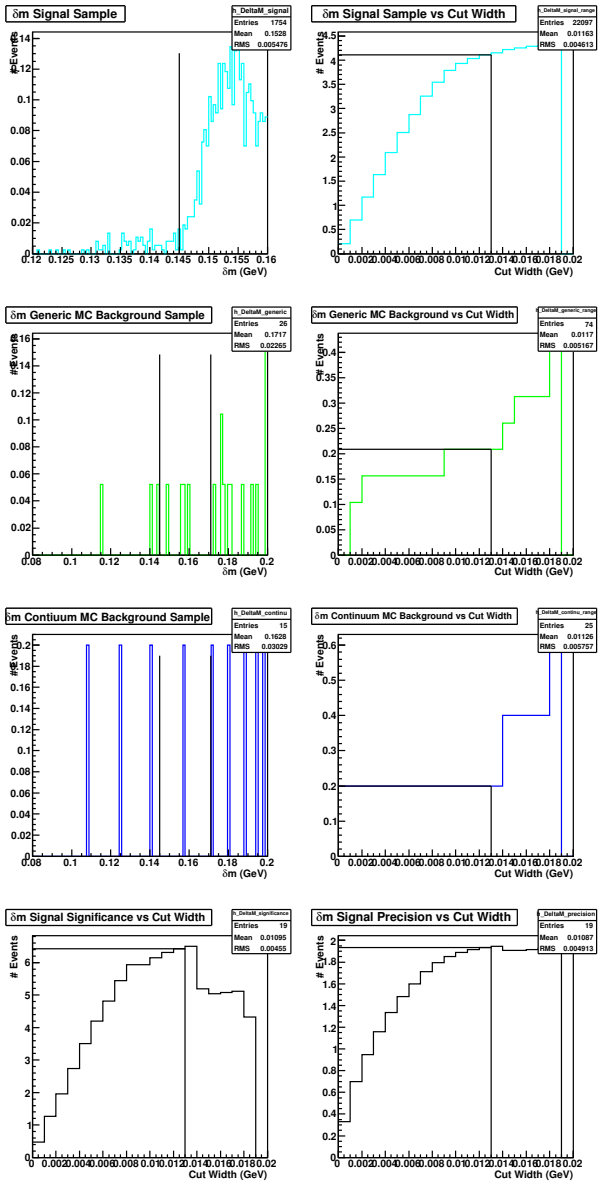

Figure 34: Optimization plots for the δm selection criterion in the $D_s^+ \to \eta\pi^+; \eta \to \gamma\gamma$ decay mode for pion-fitted data.

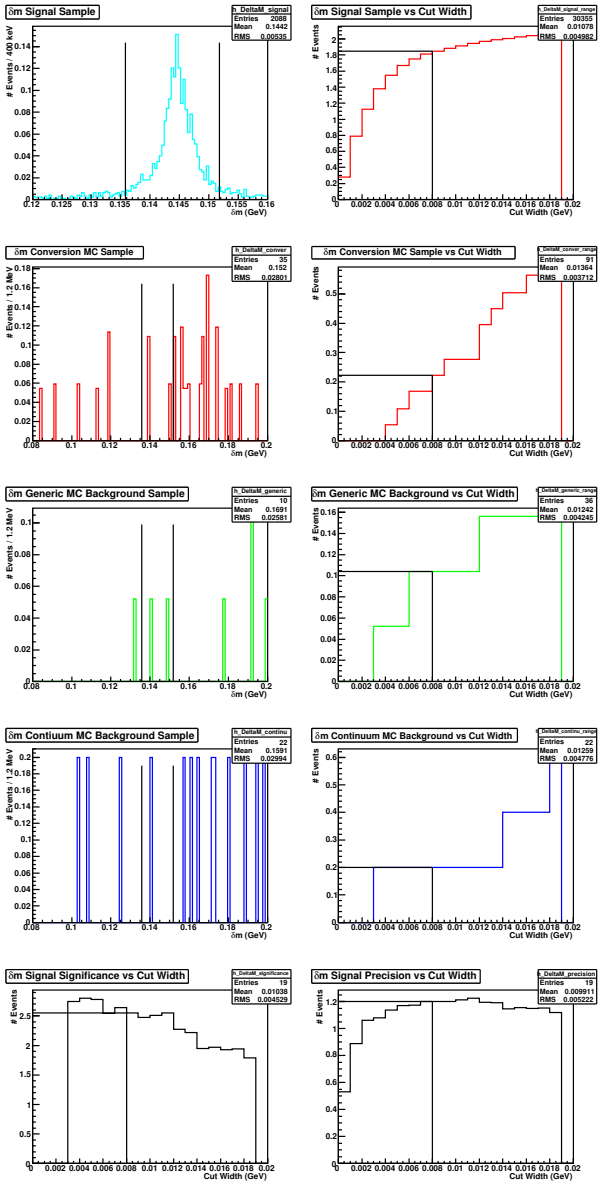

Figure 35: Optimization plots for the δm selection criterion in the $D_s^+ \to \eta\pi^+; \eta \to \gamma\gamma$ decay mode for electron-fitted data.

Optimization plots for the selection criterion on the Δd_0 of the e^+e^- in the $D_s^+ \to \eta\pi^+; \eta \to \gamma\gamma$ decay mode having applied all other selection criteria. All plots are normalized to 586 pb^{-1} of data.

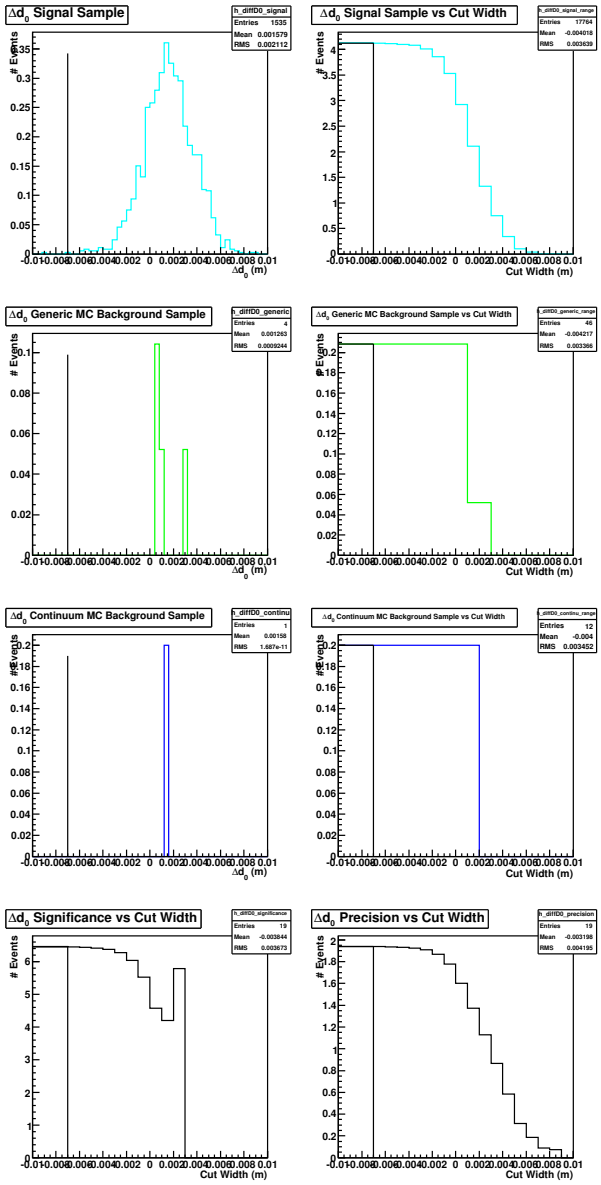

Figure 36: Optimization plots for the selection criterion on Δd_0 in the $D_s^+ \to \eta\pi^+; \eta \to \gamma\gamma$ for pion-fitted data.

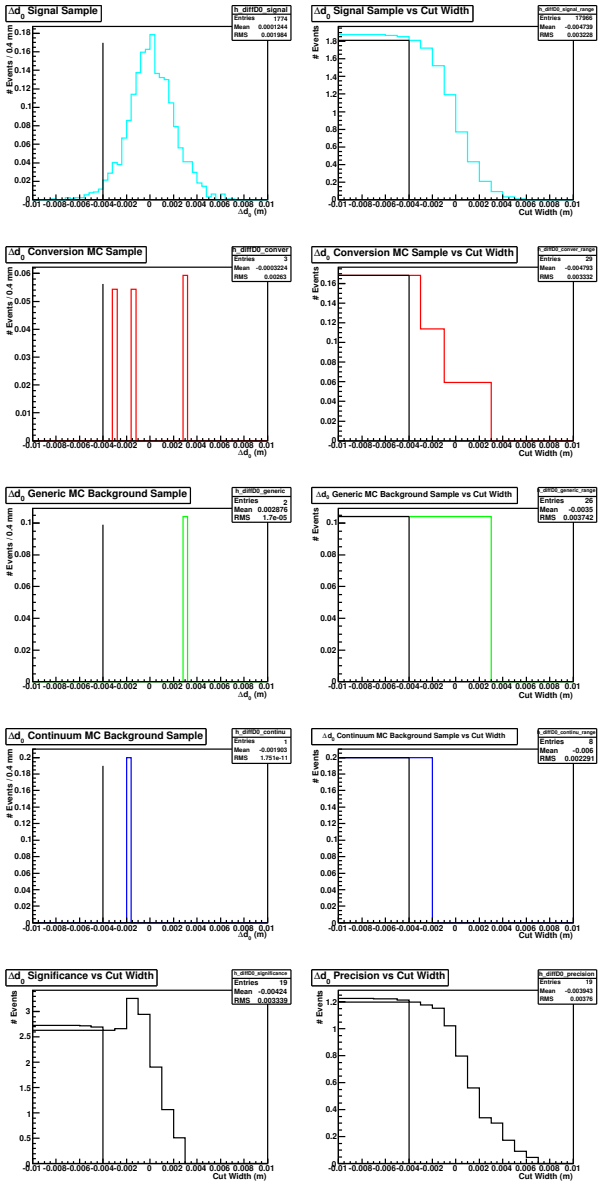

Figure 37: Optimization plots for the selection criterion on Δd_0 in the $D_s^+ \to \eta\pi^+; \eta \to \gamma\gamma$ for electron-fitted data.

Optimization plots for the selection criterion on the $\Delta\phi_0$ of the e^+e^- in the $D_s^+ \to \eta\pi^+; \eta \to \gamma\gamma$ decay mode having applied all other selection criteria. All plots are normalized to 586 pb^{-1} of data.

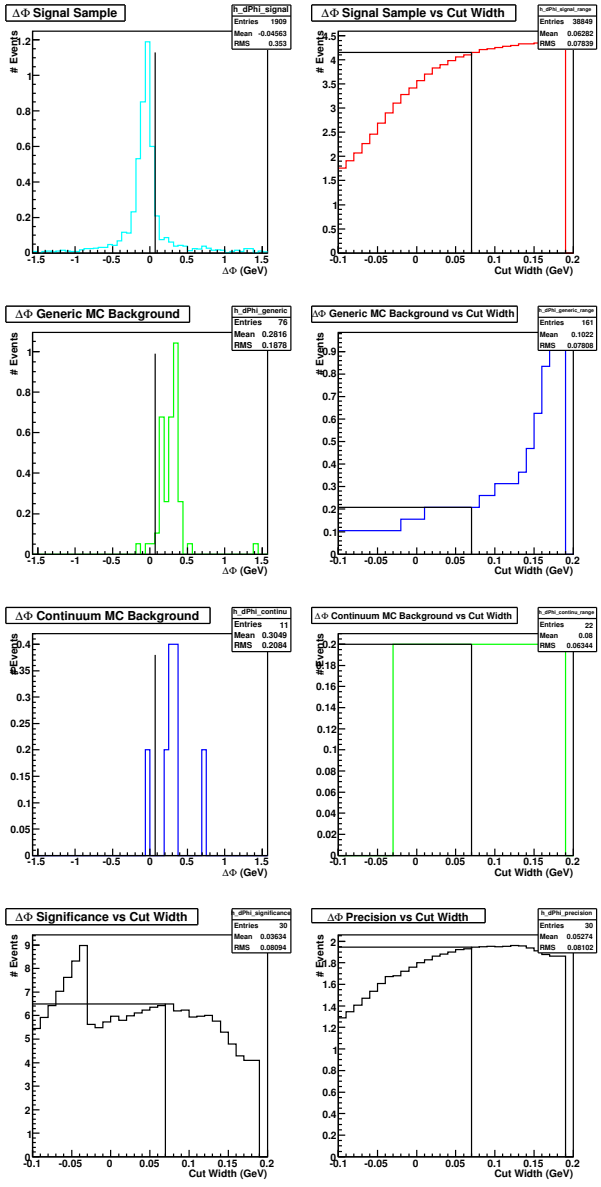

Figure 38: Optimization plots for the selection criterion on the $\Delta\phi_0$ of the e^+e^- in the $D_s^+ \to \eta\pi^+; \eta \to \gamma\gamma$ decay mode for pion-fitted data.

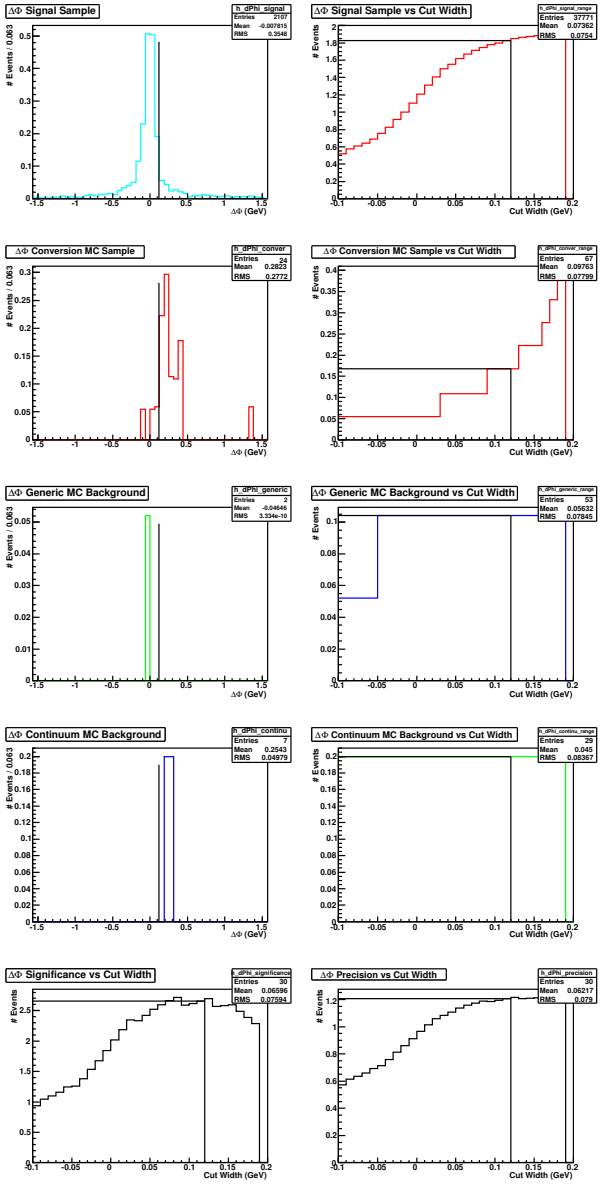

Figure 39: Optimization plots for the selection criterion on the $\Delta\phi_0$ of the e^+e^- in the $D_s^+ \to \eta\pi^+; \eta \to \gamma\gamma$ decay mode for electron-fitted data.

10.4 $D_s^+ \to \eta'\pi^+; \eta' \to \pi^+\pi^-\eta; \eta \to \gamma\gamma$

Given that

- the branching fraction of $D_s^+ \to \eta'\pi^+$ is $\simeq 3.8\%$, and
- the branching fraction of $\eta' \to \pi^+\pi^-\eta$ is $\simeq 44.6\%$,
- the branching fraction of $\eta \to \gamma\gamma$ is 39.31%,

we studied the plots in 40, 42, 44, 46 and 48 to arrive at selection criteria for pion-fitted data, and the plots in 41, 43, 45, 47 and 49 to arrive at the selection criteria for electron-fitted data. These are tabulated in Table 11

Table 11: Selection criteria for pion-fitted and electron-fitted data in the $D_s^+ \to \eta'\pi^+; \eta' \to \pi^+\pi^-\eta; \eta \to \gamma\gamma$ decay mode.

Selection Criterion	Pion-Fitted Data Cut Center ± Width	Electron-Fitted Data Cut Center ± Width
$m_{D_s^+}$	1.969 ± 0.011 GeV	1.969 ± 0.008 GeV
m_{BC}	2.112 ± 0.011 GeV	2.112 ± 0.004 GeV
δm	0.155 ± 0.013 GeV	0.144 ± 0.008 GeV
Δd_0	-0.003 m	-0.004 m
$\Delta\phi_0$	0.07	0.1

The result of these selection criteria, applied to the pion and electron-fitted samples, are presented in terms of the signal and background yields we can expect in 586 pb^{-1} of data in Table 12. A signal significance, defined for now simply as $\frac{N_S ignal Events}{\sqrt{N_B ackground Events}}$, serves as a measure of comparison between the two sets of criteria and samples.

Table 12: Number of signal and background events expected in pion and electron-fitted data in the $D_s^+ \to \eta'\pi^+; \eta' \to \pi^+\pi^-\eta; \eta \to \gamma\gamma$ decay mode.

Expected Number of Events in 586 pb^{-1}	Pion-Fitted Samples and Criteria	Electron-Fitted Samples and Criteria
Signal ($N_S ignal Events$)	1.02	0.74
Conversion Background	-	0.00
Generic Background (without Conversions in e-fit)	0.47	0.00
Continuum Background	0.00	0.00
Total Background ($N_B ackground Events$)	0.47	0.00
$\frac{N_S ignal Events}{\sqrt{N_B ackground Events}}$	1.50	∞

Optimization plots for the $m_{D_s^+}$ selection criterion in the $D_s^+ \to \eta'\pi^+; \eta' \to \pi^+\pi^-\eta; \eta \to \gamma\gamma$ decay mode having applied all other selection criteria. All plots are normalized to 586 pb^{-1} of data. The top left plots, for both the pion and electron-fitted sets of data, are the distributions of $m_{D_s^+}$ in the signal MC sample. The top right plot is the signal MC sample accepted by the criterion as we increase the cut width plotted on the x-axis. For the pion-fitted samples on the left, the plots in the second and third rows correspond to the generic and continuum MC samples, respectively. For the electron-fitted samples on the right, the plots in the second, third and fourth rows correspond to the conversion, generic and continuum MC samples, respectively. For both sets of plots, the bottom left shows the significance of the signal over background. The bottom right plot shows the precision of the signal.

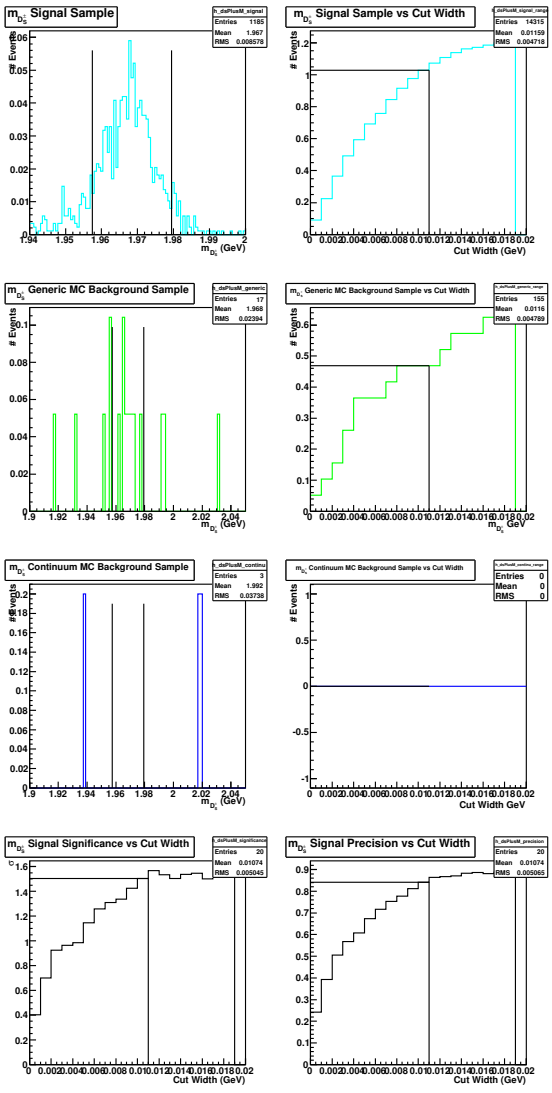

Figure 40: Optimization plots for the $m_{D_s^+}$ selection criterion in the $D_s^+ \to \eta'\pi^+; \eta' \to \pi^+\pi^-\eta; \eta \to \gamma\gamma$ decay mode for pion-fitted data.

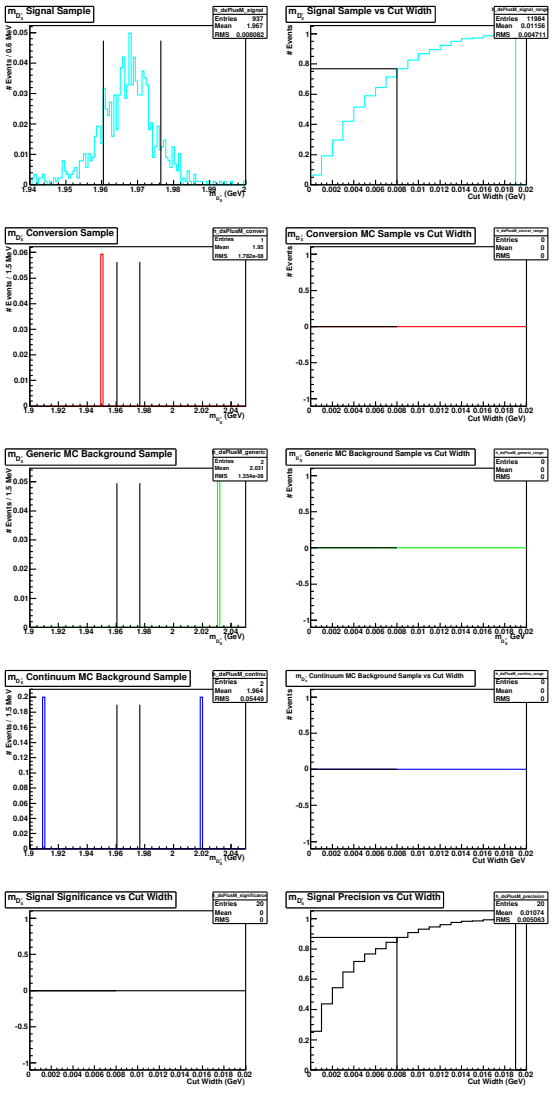

Figure 41: Optimization plots for the $m_{D_s^+}$ selection criterion in the $D_s^+ \to \eta'\pi^+; \eta' \to \pi^+\pi^-\eta; \eta \to \gamma\gamma$ decay mode for electron-fitted data.

Optimization plots for the m_{BC} selection criterion in the $D_s^+ \to \eta'\pi^+; \eta' \to \pi^+\pi^-\eta; \eta \to \gamma\gamma$ decay mode having applied all other selection criteria. All plots are normalized to 586 pb^{-1} of data.

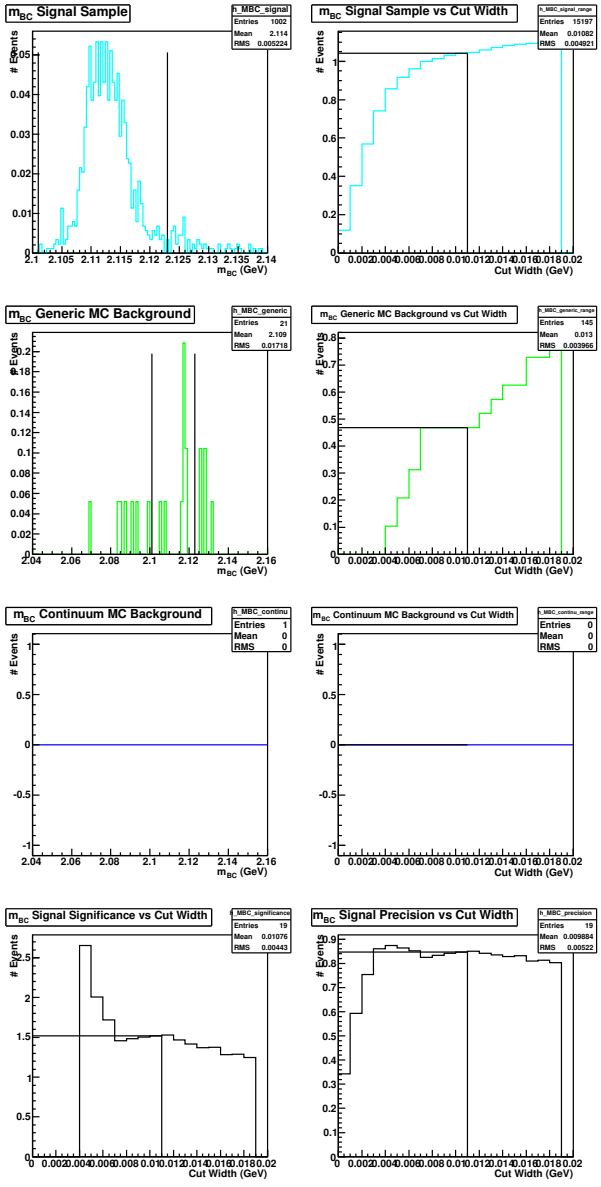

Figure 42: Optimization plots for the m_{BC} selection criterion in the $D_s^+ \to \eta'\pi^+; \eta' \to \pi^+\pi^-\eta; \eta \to \gamma\gamma$ decay mode for pion-fitted data.

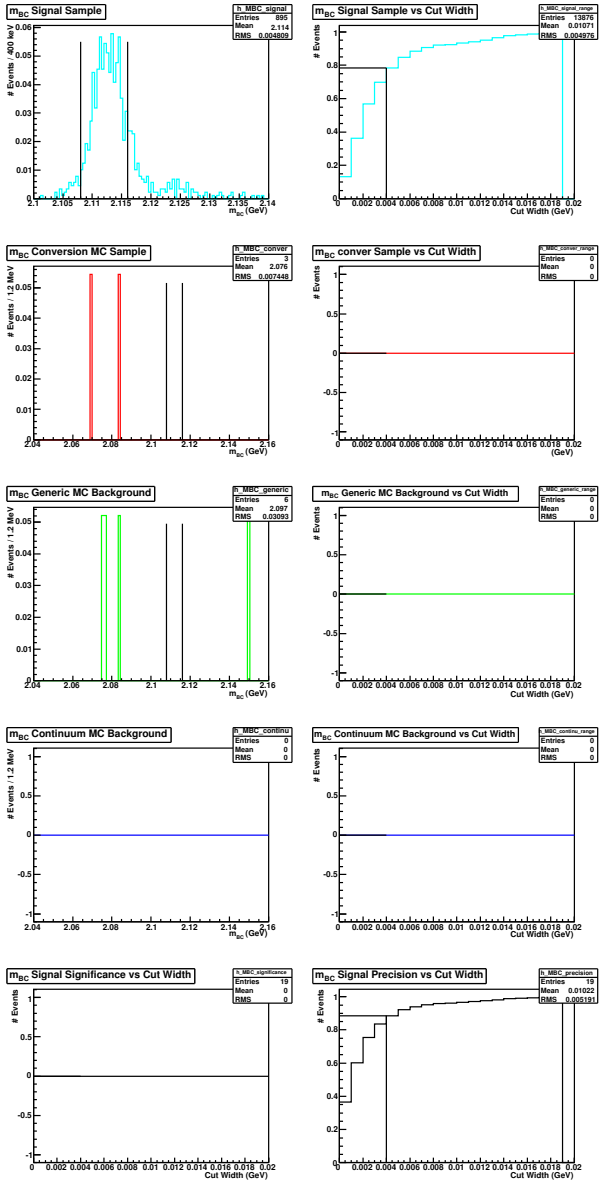

Figure 43: Optimization plots for the m_{BC} selection criterion in the $D_s^+ \to \eta'\pi^+; \eta' \to \pi^+\pi^-\eta; \eta \to \gamma\gamma$ decay mode for electron-fitted data.

Optimization plots for the δm selection criterion in the $D_s^+ \to \eta'\pi^+; \eta' \to \pi^+\pi^-\eta$ decay mode having applied all other selection criteria. All plots are normalized to 586 pb^{-1} of data.

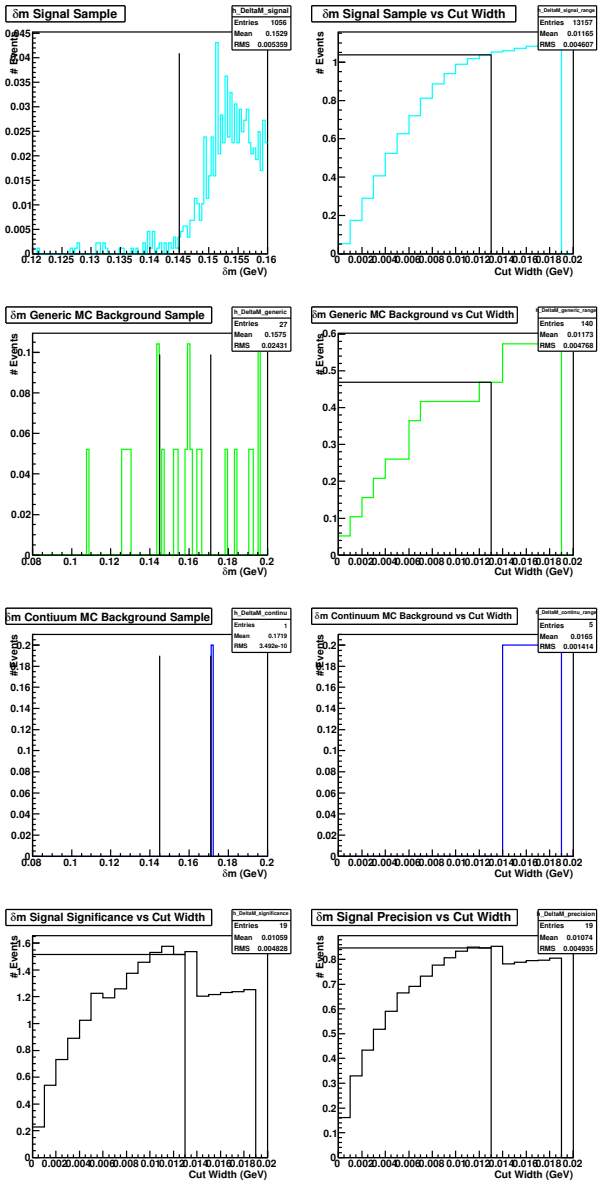

Figure 44: Optimization plots for the δm selection criterion in the $D_s^+ \to \eta'\pi^+; \eta' \to \pi^+\pi^-\eta$ decay mode for pion-fitted data.

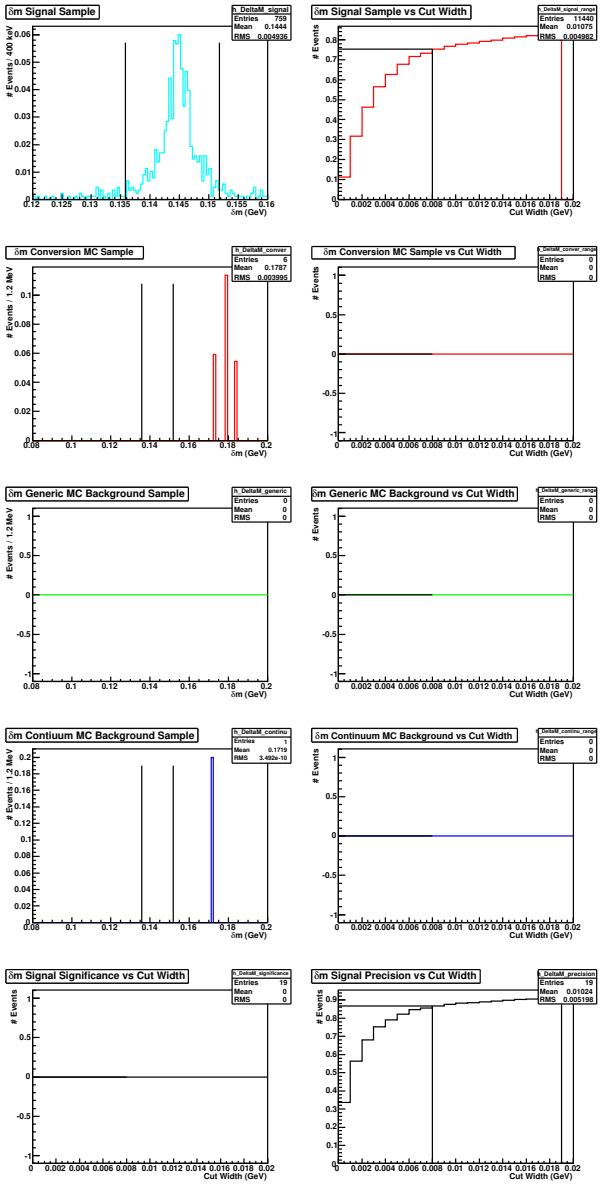

Figure 45: Optimization plots for the δm selection criterion in the $D_s^+ \to \eta'\pi^+; \eta' \to \pi^+\pi^-\eta$ decay mode for electron-fitted data.

Optimization plots for the selection criterion on the Δd_0 of the e^+e^- in the $D_s^+ \to \eta'\pi^+; \eta' \to \pi^+\pi^-\eta$ decay mode having applied all other selection criteria. All plots are normalized to 586 pb^{-1} of data.

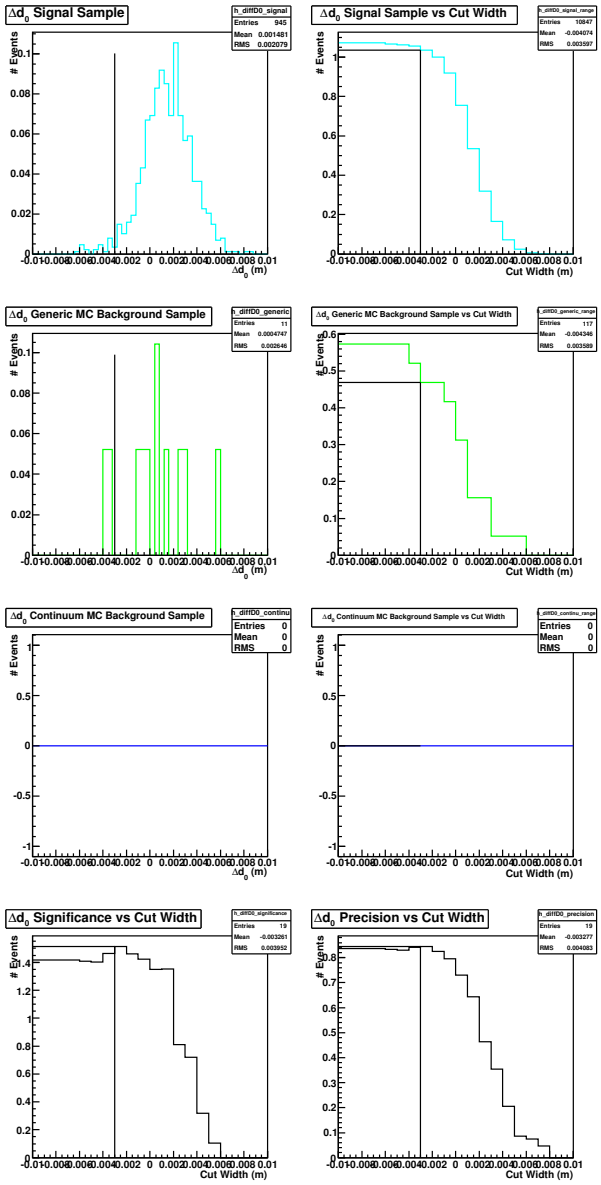

Figure 46: Optimization plots for the selection criterion on Δd_0 in the $D_s^+ \to \eta'\pi^+; \eta' \to \pi^+\pi^-\eta$ for pion-fitted data.

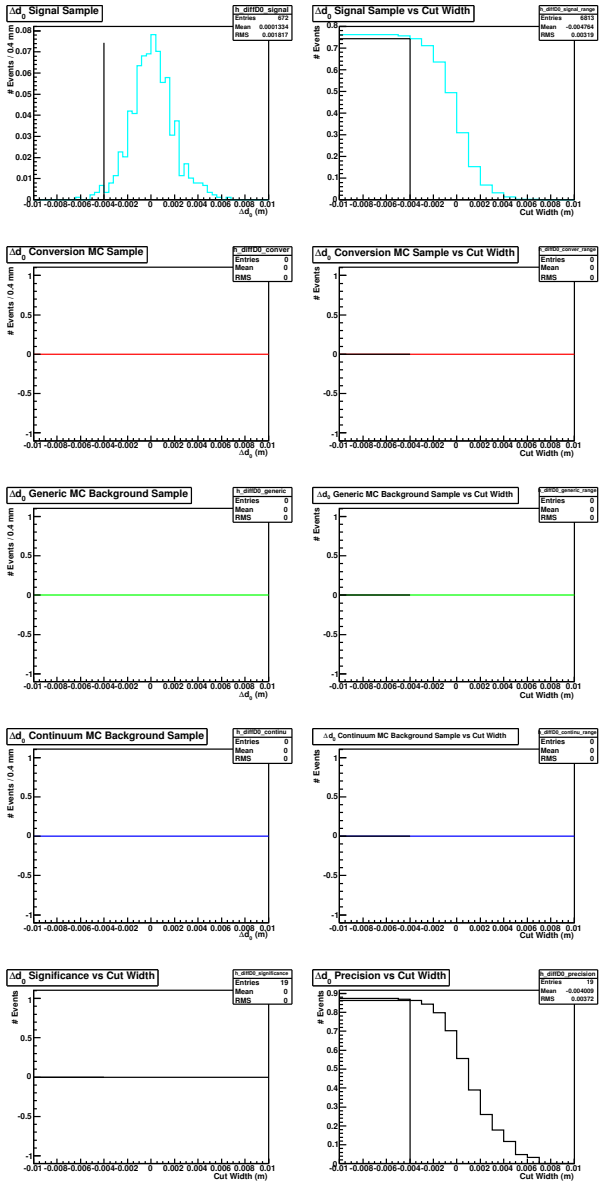

Figure 47: Optimization plots for the selection criterion on Δd_0 in the $D_s^+ \to \eta'\pi^+; \eta' \to \pi^+\pi^-\eta$ for electron-fitted data.

Optimization plots for the selection criterion on the $\Delta\phi_0$ of the e^+e^- in the $D_s^+ \to \eta'\pi^+; \eta' \to \pi^+\pi^-\eta$ decay mode having applied all other selection criteria. All plots are normalized to 586 pb^{-1} of data.

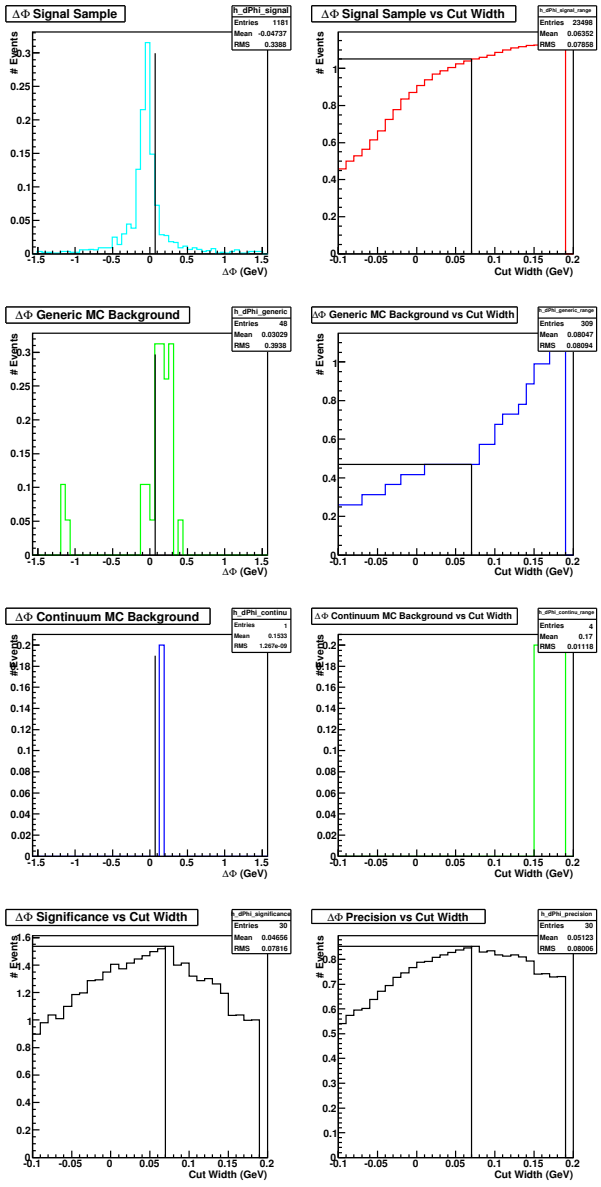

Figure 48: Optimization plots for the selection criterion on the $\Delta\phi_0$ of the e^+e^- in the $D_s^+ \to \eta' \to \pi^+\pi^-\eta; \eta \to \gamma\gamma$ decay mode for pion-fitted data.

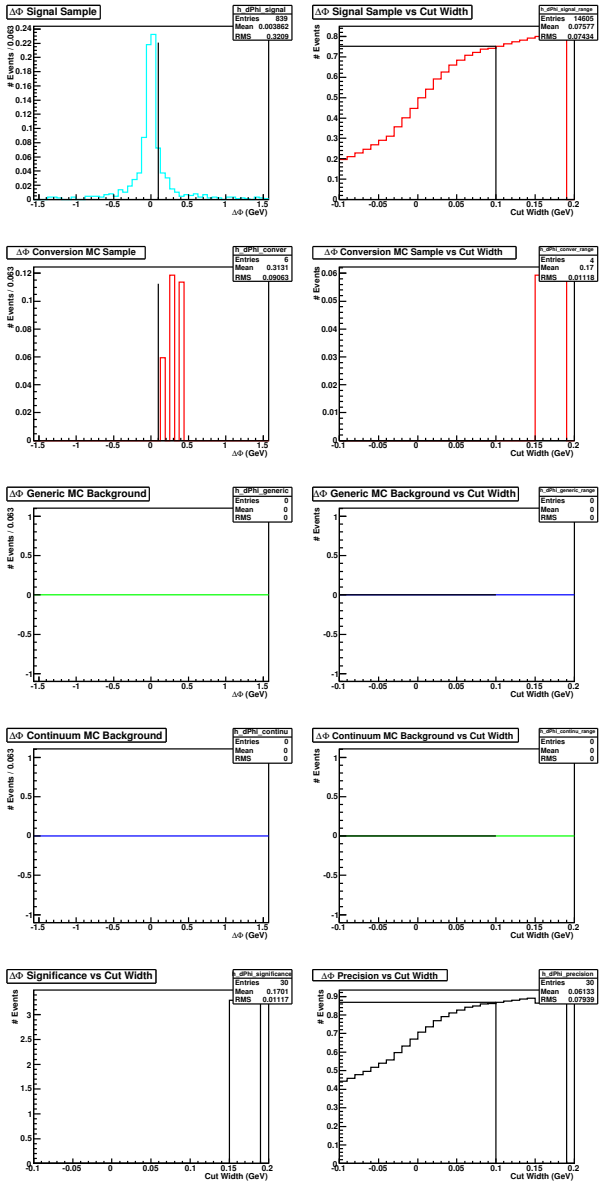

Figure 49: Optimization plots for the selection criterion on the $\Delta\phi_0$ of the e^+e^- in the $D_s^+ \to \eta' \to \pi^+\pi^-\eta; \eta \to \gamma\gamma$ decay mode for electron-fitted data.

10.5 $D_s^+ \to K^+K^-\pi^+\pi^0$

Given that the branching fraction of $D_s^+ \to K^+K^-\pi^+\pi^0$ is 5.6%, we studied the plots in 50, 52, 54, 56 and 58 to arrive at the selection criteria for pion-fitted data, and the plots in 51, 53, 55, 57 and 59 to arrive at the selection criteria for electron-fitted data. These are tabulated in Table 13

Table 13: Selection criteria for pion-fitted and electron-fitted data in the $D_s^+ \to K^+K^-\pi^+\pi^0$ decay mode.

Selection Criterion	Pion-Fitted Data Cut Center ± Width	Electron-Fitted Data Cut Center ± Width
$m_{D_s^+}$	1.969 ± 0.009 GeV	1.969 ± 0.010 GeV
m_{BC}	2.112 ± 0.007 GeV	2.112 ± 0.004 GeV
δm	0.155 ± 0.011 GeV	0.144 ± 0.006 GeV
Δd_0	-0.002 m	-0.006 m
$\Delta\phi_0$	0.07	0.12

The result of these selection criteria, applied to the pion and electron-fitted samples, are presented in terms of the signal and background yields we can expect in 586 pb^{-1} of data in Table 14. A signal significance, defined for now simply as $\frac{N_SignalEvents}{\sqrt{N_BackgroundEvents}}$, serves as a measure of comparison between the two sets of criteria and samples.

Table 14: Number of signal and background events expected in pion and electron-fitted data in the $D_s^+ \to K^+K^-\pi^+\pi^0$ decay mode.

Expected Number of Events in 586 pb^{-1}	Pion-Fitted Samples and Criteria	Electron-Fitted Samples and Criteria
Signal ($N_SignalEvents$)	4.62	4.86
Conversion Background	-	0.63
Generic Background (without Conversions in e-fit)	3.49	1.46
Continuum Background	0.40	0.20
Total Background ($N_BackgroundEvents$)	3.89	2.29
$\frac{N_SignalEvents}{\sqrt{N_BackgroundEvents}}$	2.3	3.2

Optimization plots for the $m_{D_s^+}$ selection criterion in the $D_s^+ \to K^+K^-\pi^+\pi^0$ decay mode having applied all other selection criteria. All plots are normalized to 586 pb^{-1} of data. The top left plots, for both the pion and electron-fitted sets of data, are the distributions of $m_{D_s^+}$ in the signal MC sample. The top right plot is the signal MC sample accepted by the criterion as we increase the cut width plotted on the x-axis. For the pion-fitted samples on the left, the plots in the second and third rows correspond to the generic and continuum MC samples, respectively. For the electron-fitted samples on the right, the plots in the second, third and fourth rows correspond to the conversion, generic and continuum MC samples, respectively. For both sets of plots, the bottom left shows the significance of the signal over background. The bottom right plot shows the precision of the signal.

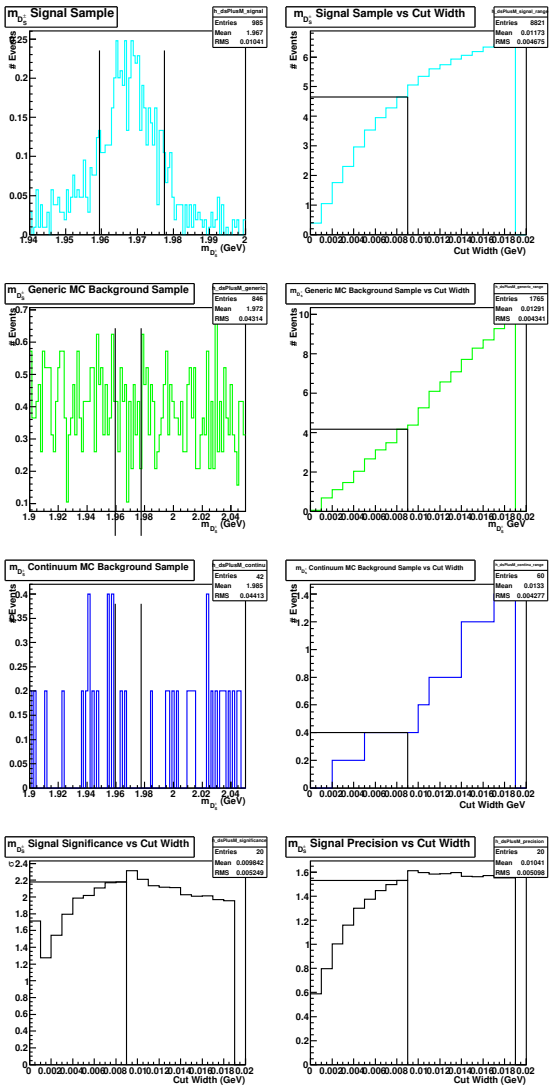

Figure 50: Optimization plots for the $m_{D_s^+}$ selection criterion in the $D_s^+ \to K^+K^-\pi^+\pi^0$ decay mode for pion-fitted data.

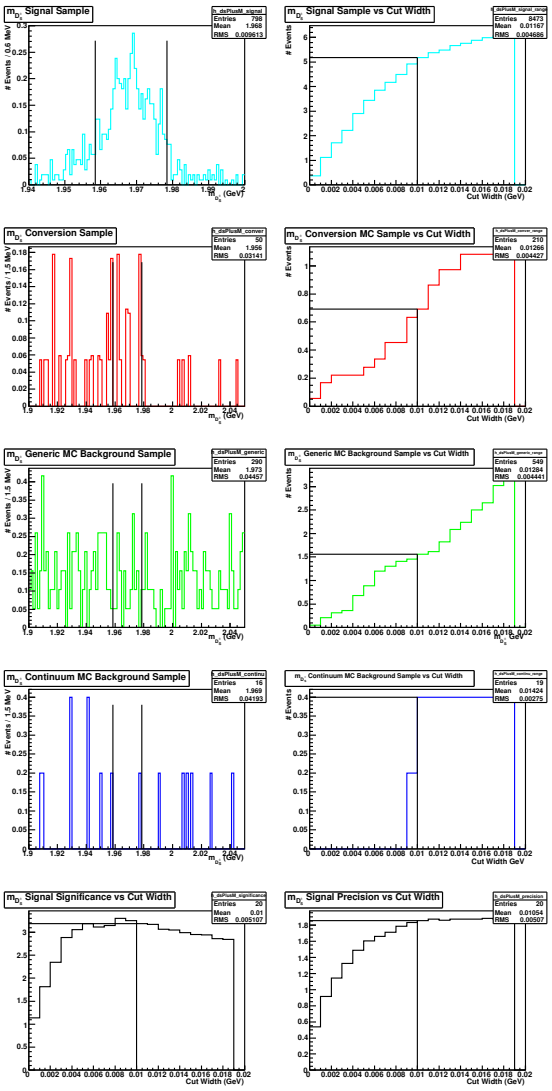

Figure 51: Optimization plots for the $m_{D_s^+}$ selection criterion in the $D_s^+ \to K^+K^-\pi^+\pi^0$ decay mode for electron-fitted data.

Optimization plots for the m_{BC} selection criterion in the $D_s^+ \to K^+K^-\pi^+\pi^0$ decay mode having applied all other selection criteria. All plots are normalized to 586 pb^{-1} of data.

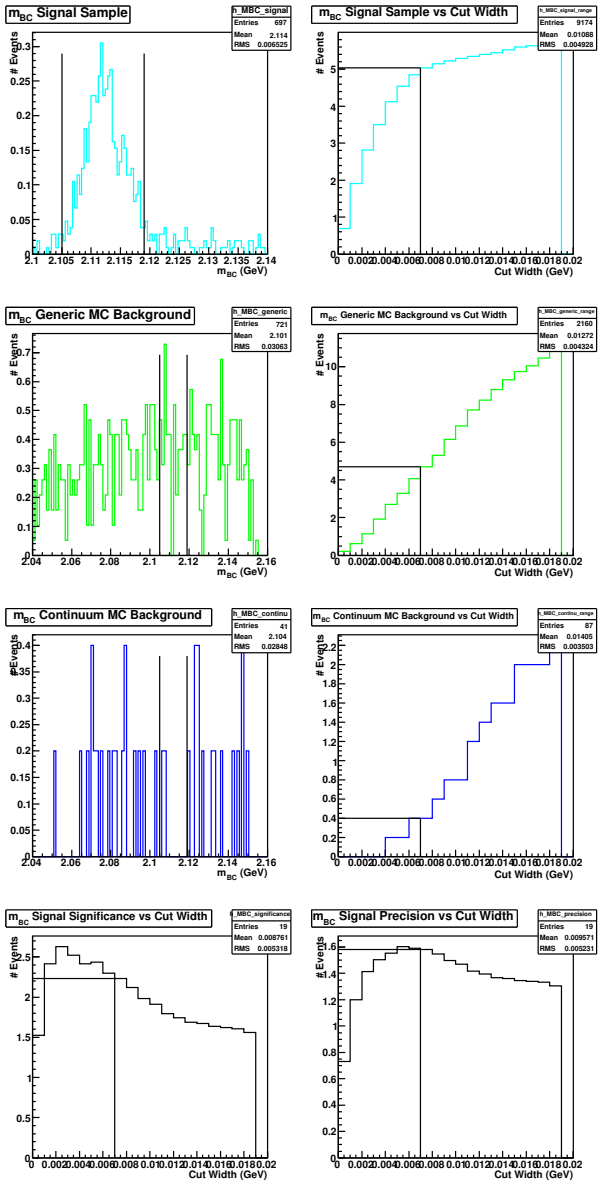

Figure 52: Optimization plots for the m_{BC} selection criterion in the $D_s^+ \to K^+K^-\pi^+\pi^0$ decay mode for pion-fitted data.

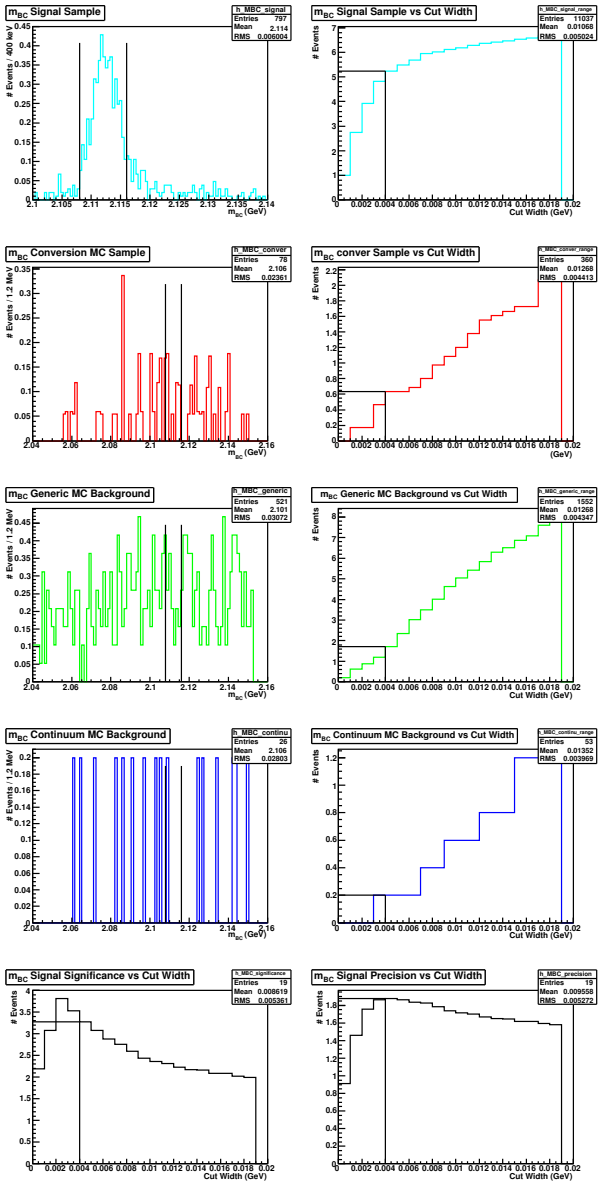

Figure 53: Optimization plots for the m_{BC} selection criterion in the $D_s^+ \to K^+K^-\pi^+\pi^0$ decay mode for electron-fitted data.

Optimization plots for the δm selection criterion in the $D_s^+ \to K^+K^-\pi^+\pi^0$ decay mode having applied all other selection criteria. All plots are normalized to 586 pb^{-1} of data.

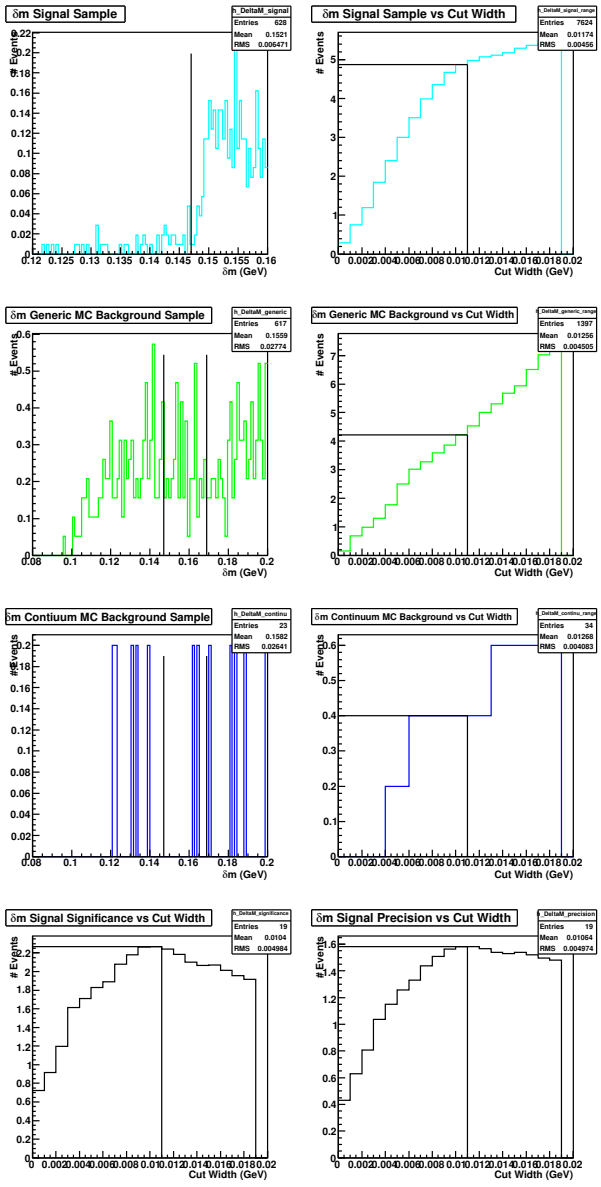

Figure 54: Optimization plots for the δm selection criterion in the $D_s^+ \to K^+K^-\pi^+\pi^0$ decay mode for pion-fitted data.

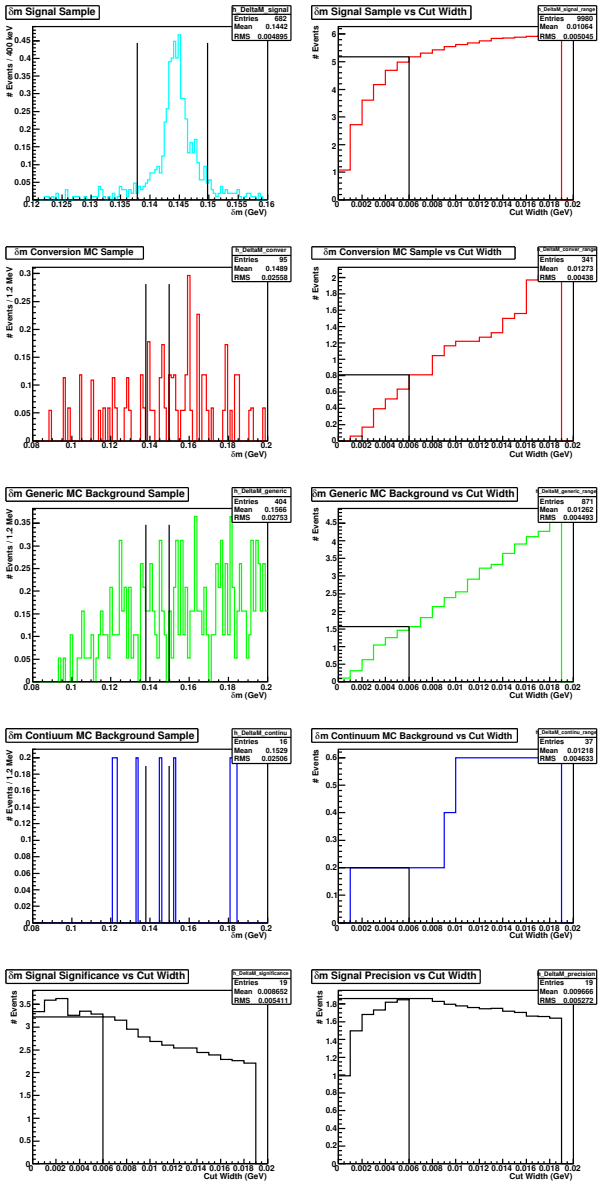

Figure 55: Optimization plots for the δm selection criterion in the $D_s^+ \to K^+K^-\pi^+\pi^0$ decay mode for electron-fitted data.

Optimization plots for the selection criterion on the Δd_0 of the e^+e^- in the $D_s^+ \to K^+K^-\pi^+\pi^0$ decay mode having applied all other selection criteria. All plots are normalized to 586 pb^{-1} of data.

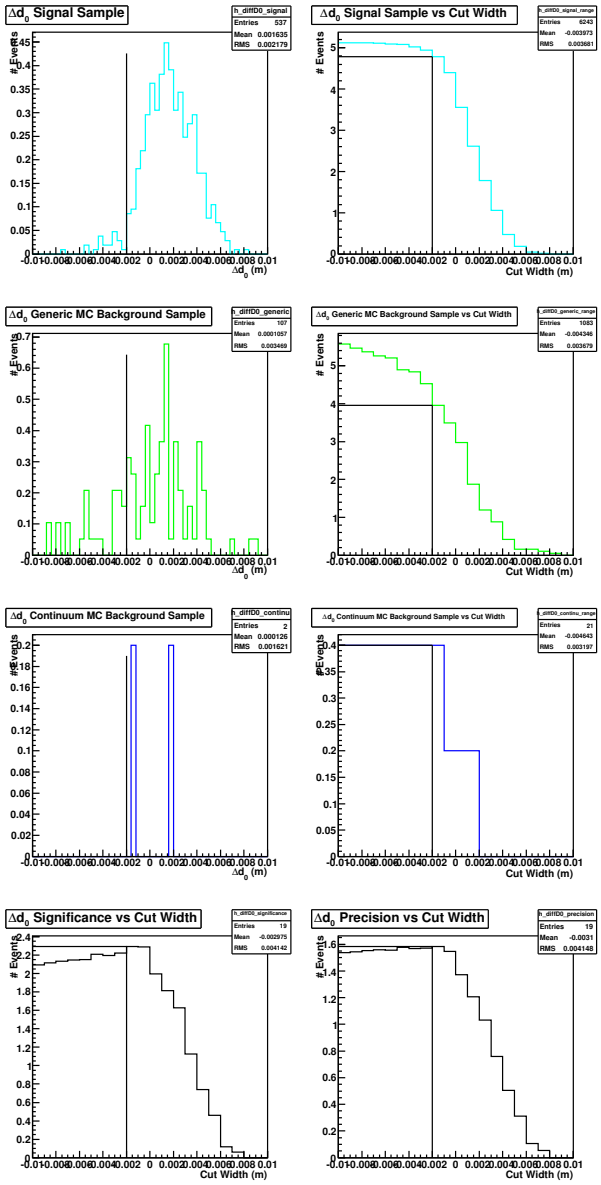

Figure 56: Optimization plots for the selection criterion on Δd_0 in the $D_s^+ \to K^+K^-\pi^+\pi^0$ for pion-fitted data.

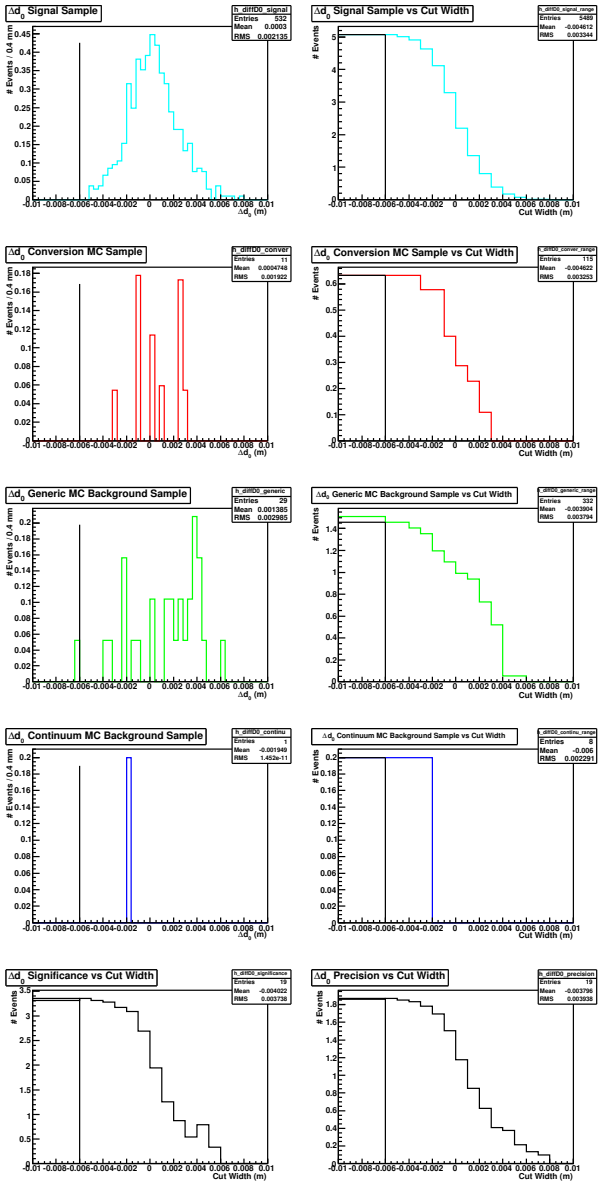

Figure 57: Optimization plots for the selection criterion on Δd_0 in the $D_s^+ \to K^+K^-\pi^+\pi^0$ for electron-fitted data.

Optimization plots for the selection criterion on the $\Delta\phi_0$ of the e^+e^- in the $D_s^+ \to K^+K^-\pi^+\pi^0$ decay mode having applied all other selection criteria. All plots are normalized to 586 pb^{-1} of data.

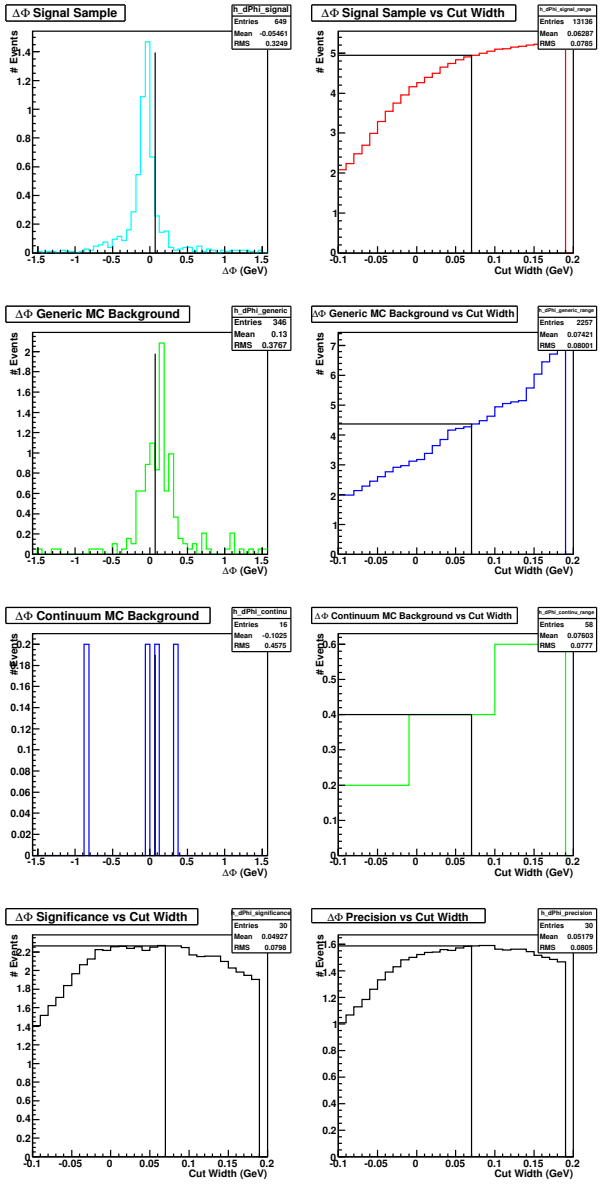

Figure 58: Optimization plots for the selection criterion on the $\Delta\phi_0$ of the e^+e^- in the $D_s^+ \to K^+K^-\pi^+\pi^0$ decay mode for pion-fitted data.

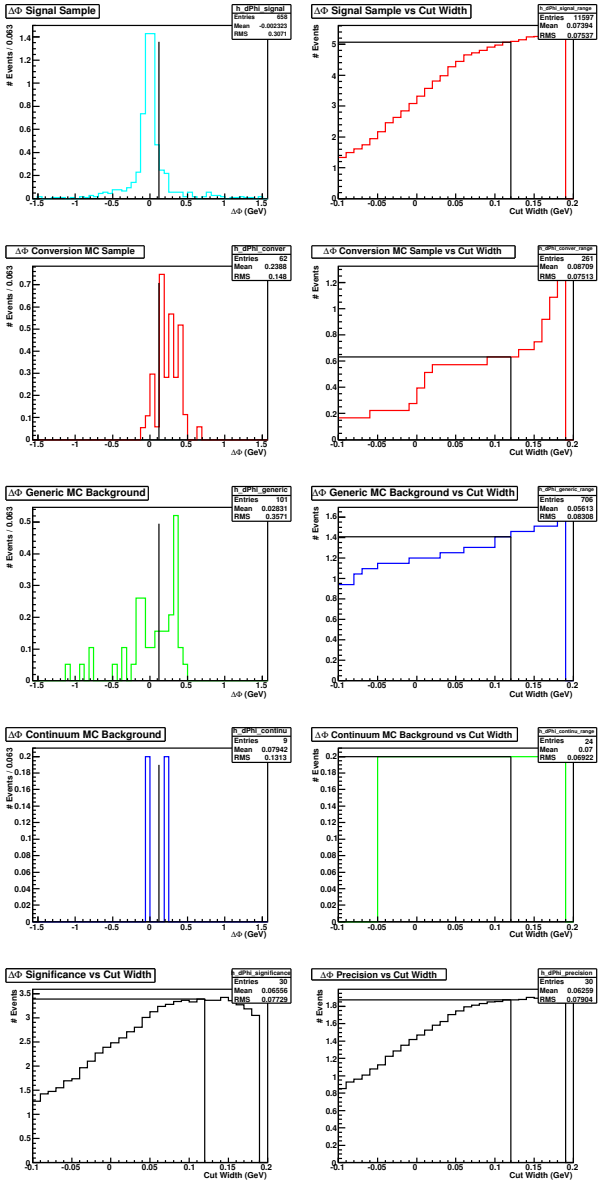

Figure 59: Optimization plots for the selection criterion on the $\Delta\phi_0$ of the e^+e^- in the $D_s^+ \to K^+K^-\pi^+\pi^0$ decay mode for electron-fitted data.

10.6 $D_s^+ \to \pi^+\pi^-\pi^+$

Given that the branching fraction of $D_s^+ \to \pi^+\pi^-\pi^+$ is 1.11%, we studied the plots in 60, 62, 64, 66 and 68 to arrive at the selection criteria for pion-fitted data, and the plots in 61, 63, 65, 67 and 69 to arrive at the selection criteria for electron-fitted data. These are tabulated in Table 15.

Table 15: Selection criteria for pion-fitted and electron-fitted data in the $D_s^+ \to \pi^+\pi^-\pi^+$ decay mode.

Selection Criterion	Pion-Fitted Data Cut Center ± Width	Electron-Fitted Data Cut Center ± Width
$m_{D_s^+}$	1.969 ± 0.013 GeV	1.969 ± 0.012 GeV
m_{BC}	2.112 ± 0.005 GeV	2.112 ± 0.004 GeV
δm	0.155 ± 0.009 GeV	0.144 ± 0.006 GeV
Δd_0	-0.001 m	-0.006 m
$\Delta\phi_0$	0.06	0.1

The result of these selection criteria, applied to the pion and electron-fitted samples, are presented in terms of the signal and background yields we can expect in 586 pb^{-1} of data in Table 16. A signal significance, defined for now simply as $\frac{N_S ignal Events}{\sqrt{N_B ackgroundEvents}}$, serves as a measure of comparison between the two sets of criteria and samples.

Table 16: Number of signal and background events expected in pion and electron-fitted data in the $D_s^+ \to \pi^+\pi^-\pi^+$ decay mode.

Expected Number of Events in 586 pb^{-1}	Pion-Fitted Samples and Criteria	Electron-Fitted Samples and Criteria
Signal ($N_S ignal Events$)	2.99	3.67
Conversion Background	-	0.28
Generic Background (without Conversions in e-fit)	0.73	0.21
Continuum Background	0.60	1.60
Total Background ($N_B ackground Events$)	1.33	2.09
$\frac{N_S ignal Events}{\sqrt{N_B ackgroundEvents}}$	2.6	2.5

Optimization plots for the $m_{D_s^+}$ selection criterion in the $D_s^+ \to \pi^+\pi^-\pi^+$ decay mode having applied all other selection criteria. All plots are normalized to 586 pb^{-1} of data. The top left plots, for both the pion and electron-fitted sets of data, are the distributions of $m_{D_s^+}$ in the signal MC sample. The top right plot is the signal MC sample accepted by the criterion as we increase the cut width plotted on the x-axis. For the pion-fitted samples on the left, the plots in the second and third rows correspond to the generic and continuum MC samples, respectively. For the electron-fitted samples on the right, the plots in the second, third and fourth rows correspond to the conversion, generic and continuum MC samples, respectively. For both sets of plots, the bottom left shows the significance of the signal over background. The bottom right plot shows the precision of the signal.

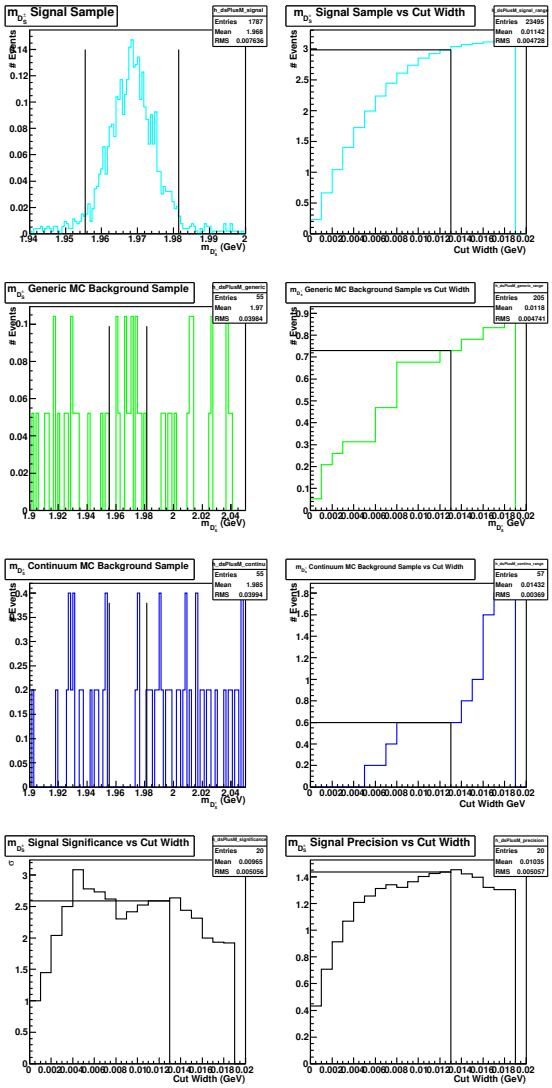

Figure 60: Optimization plots for the $m_{D_s^+}$ selection criterion in the $D_s^+ \to \pi^+\pi^-\pi^+$ decay mode for pion-fitted data.

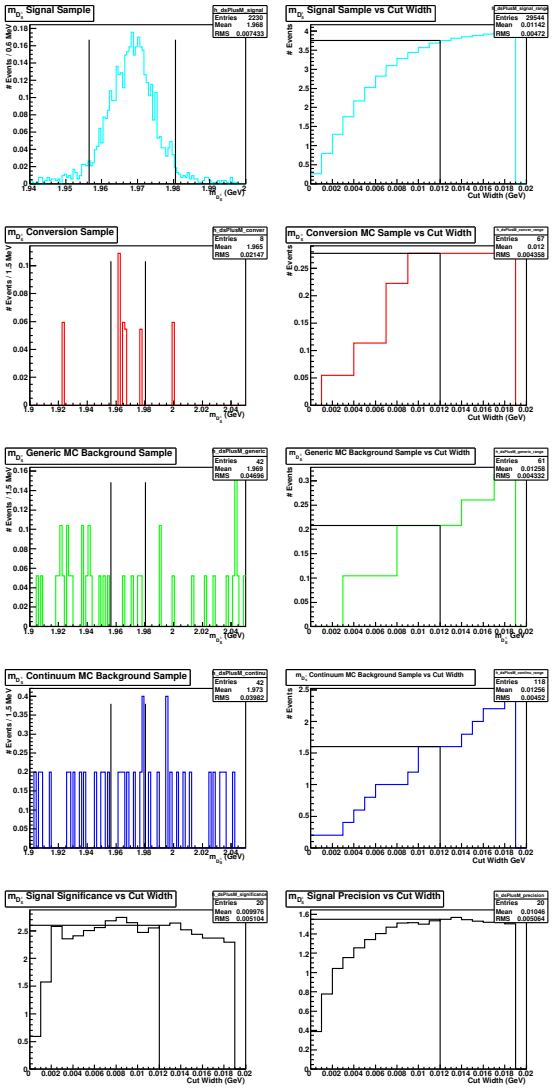

Figure 61: Optimization plots for the $m_{D_s^+}$ selection criterion in the $D_s^+ \to \pi^+\pi^-\pi^+$ decay mode for electron-fitted data.

Optimization plots for the m_{BC} selection criterion in the $D_s^+ \to \pi^+\pi^-\pi^+$ decay mode having applied all other selection criteria. All plots are normalized to 586 pb^{-1} of data.

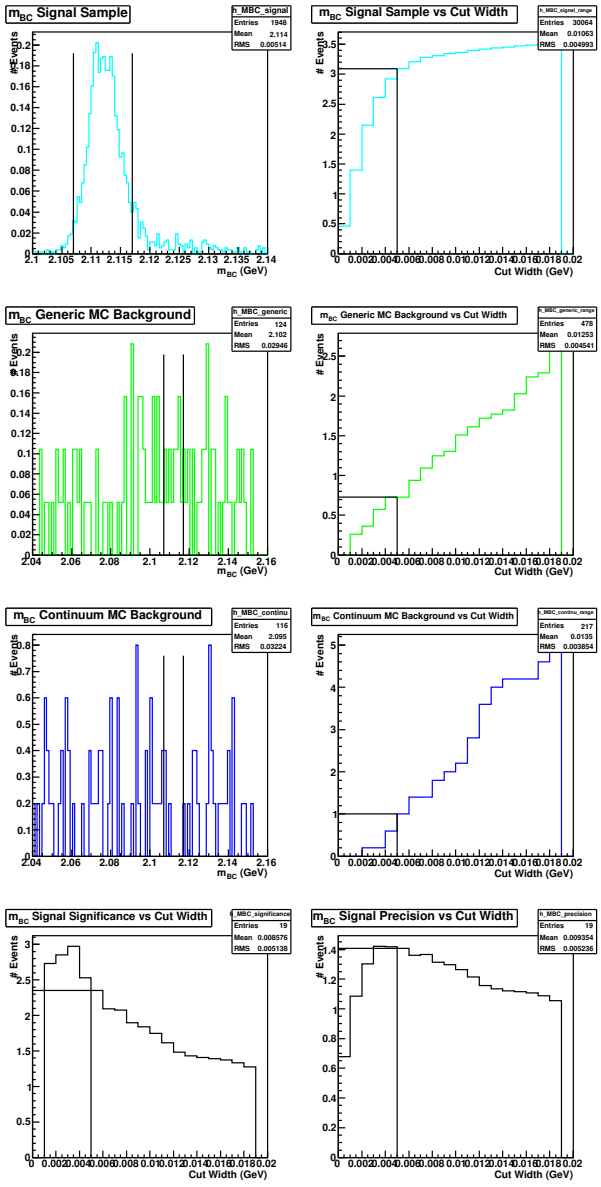

Figure 62: Optimization plots for the m_{BC} selection criterion in the $D_s^+ \to \pi^+\pi^-\pi^+$ decay mode for pion-fitted data.

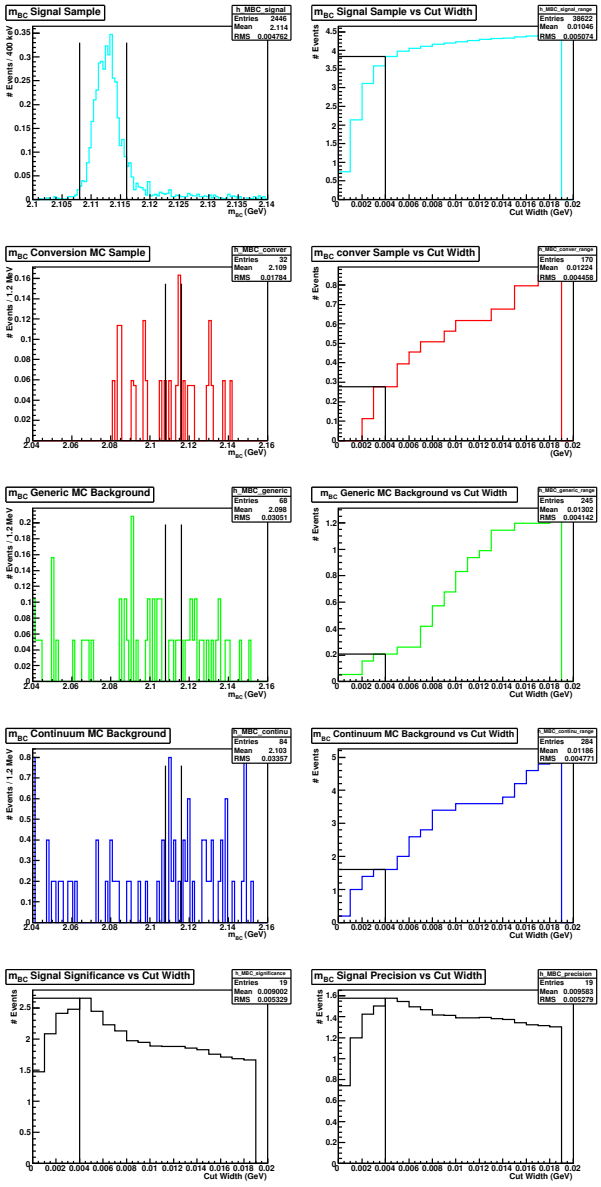

Figure 63: Optimization plots for the m_{BC} selection criterion in the $D_s^+ \to \pi^+\pi^-\pi^+$ decay mode for electron-fitted data.

Optimization plots for the δm selection criterion in the $D_s^+ \to \pi^+\pi^-\pi^+$ decay mode having applied all other selection criteria. All plots are normalized to 586 pb^{-1} of data.

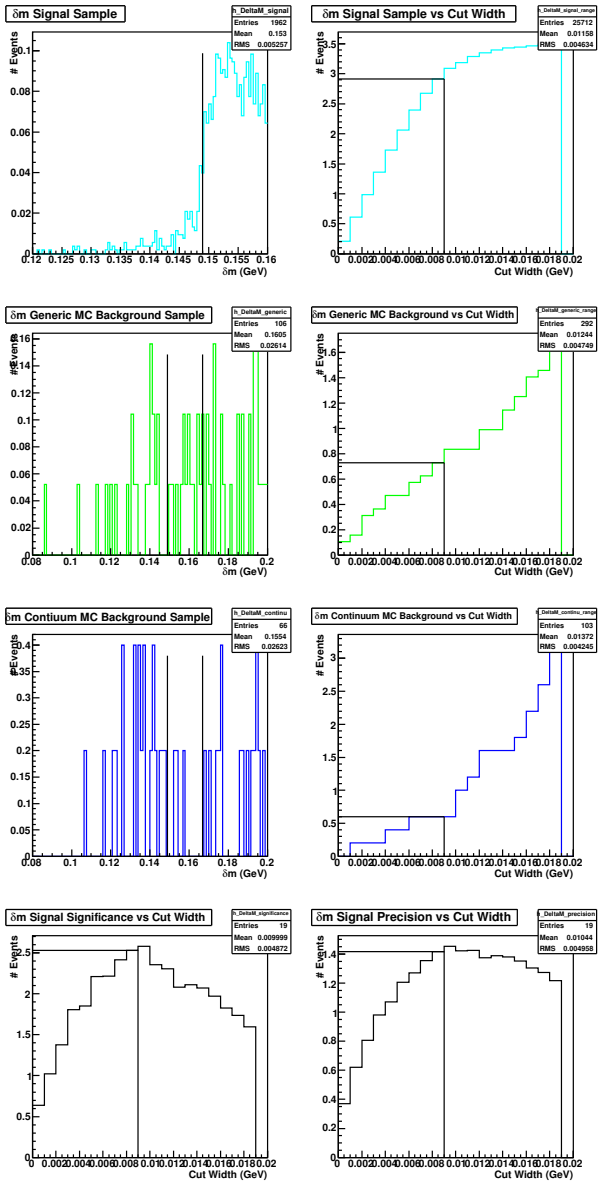

Figure 64: Optimization plots for the δm selection criterion in the $D_s^+ \to \pi^+\pi^-\pi^+$ decay mode for pion-fitted data.

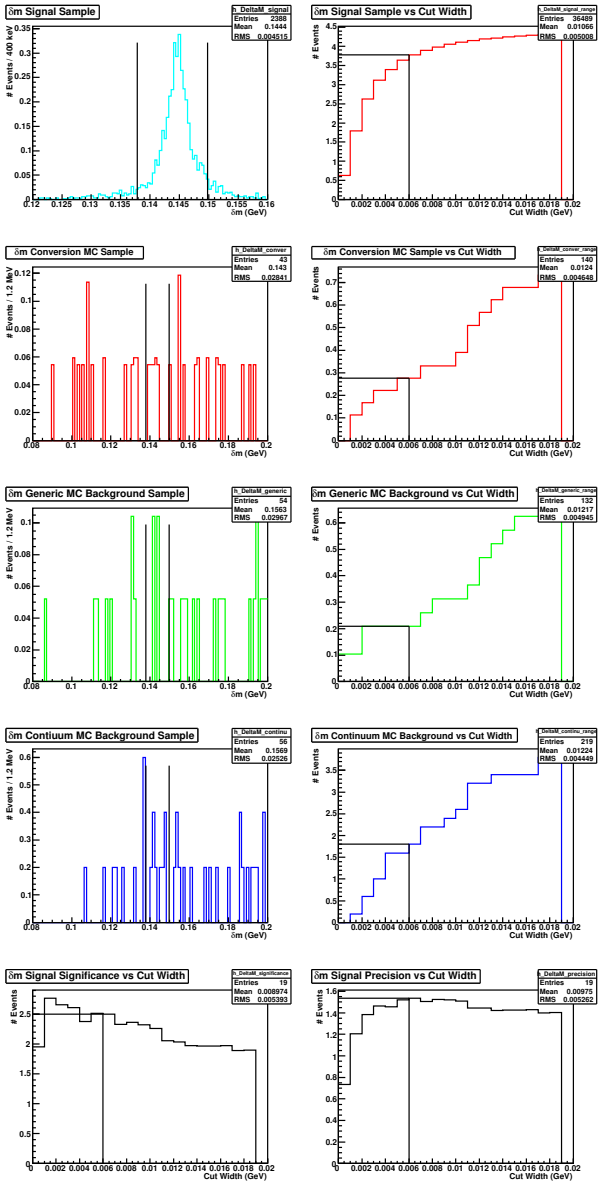

Figure 65: Optimization plots for the δm selection criterion in the $D_s^+ \to \pi^+\pi^-\pi^+$ decay mode for electron-fitted data.

Optimization plots for the selection criterion on the Δd_0 of the e^+e^- in the $D_s^+ \to \pi^+\pi^-\pi^+$ decay mode having applied all other selection criteria. All plots are normalized to 586 pb^{-1} of data.

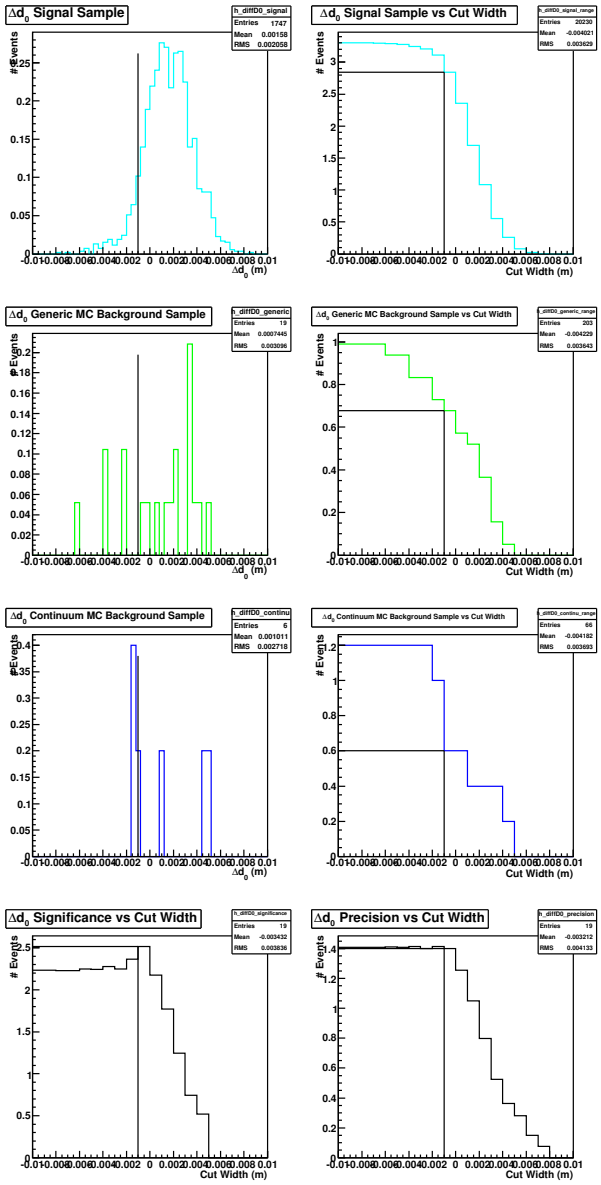

Figure 66: Optimization plots for the selection criterion on Δd_0 in the $D_s^+ \to \pi^+\pi^-\pi^+$ for pion-fitted data.

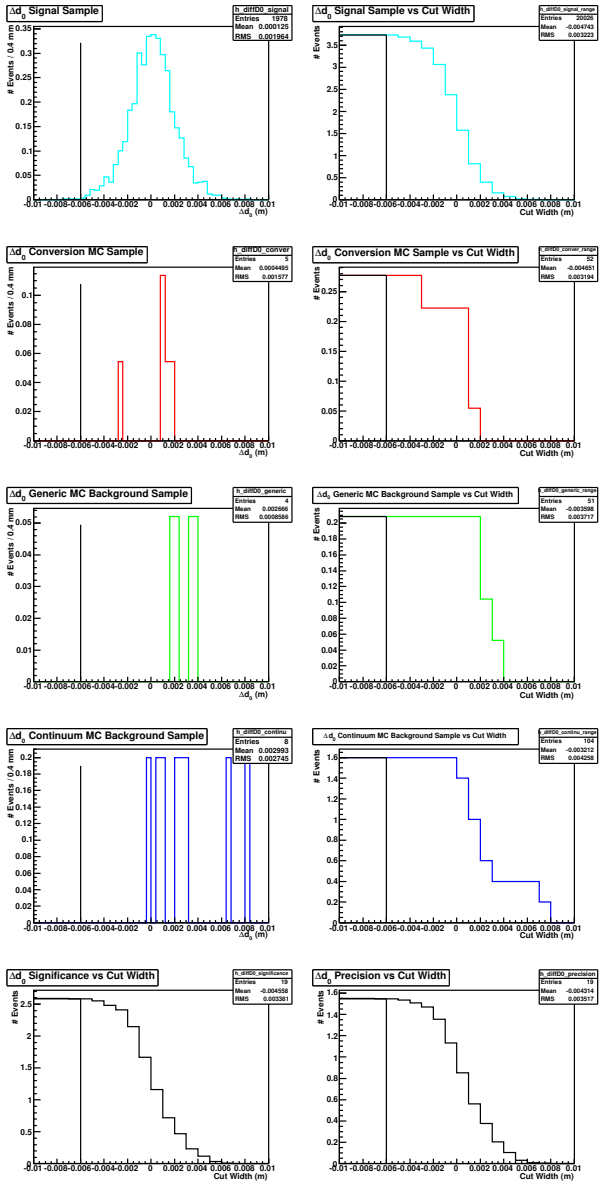

Figure 67: Optimization plots for the selection criterion on Δd_0 in the $D_s^+ \to \pi^+\pi^-\pi^+$ for electron-fitted data.

Optimization plots for the selection criterion on the $\Delta\phi_0$ of the e^+e^- in the $D_s^+ \to \pi^+\pi^-\pi^+$ decay mode having applied all other selection criteria. All plots are normalized to 586 pb^{-1} of data.

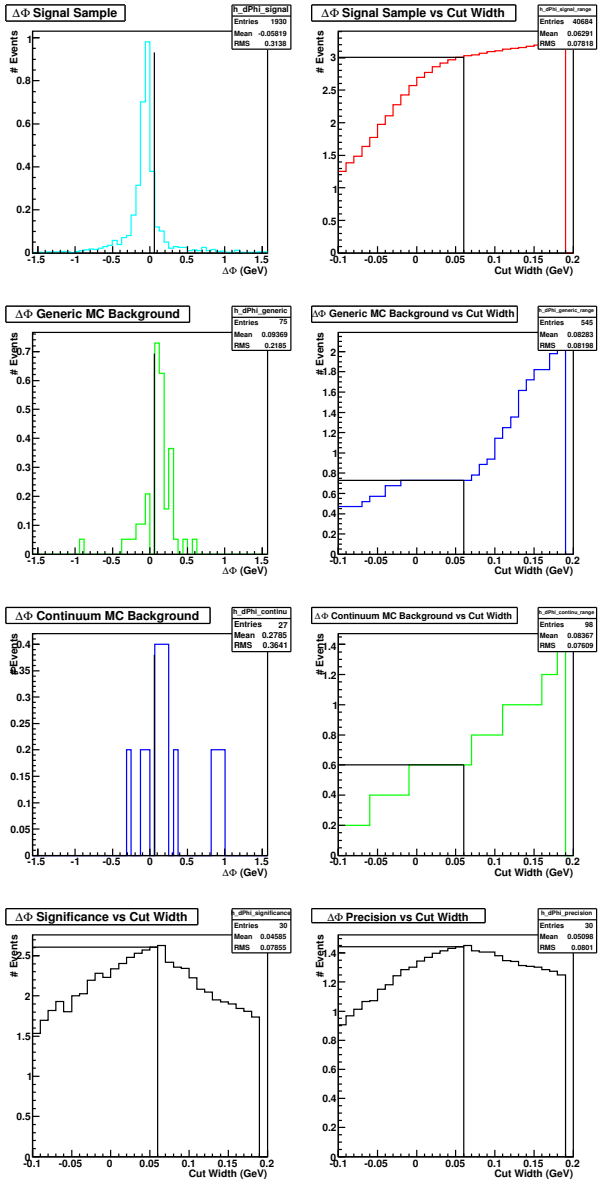

Figure 68: Optimization plots for the selection criterion on the $\Delta\phi_0$ of the e^+e^- in the $D_s^+ \to \pi^+\pi^-\pi^+$ decay mode for pion-fitted data.

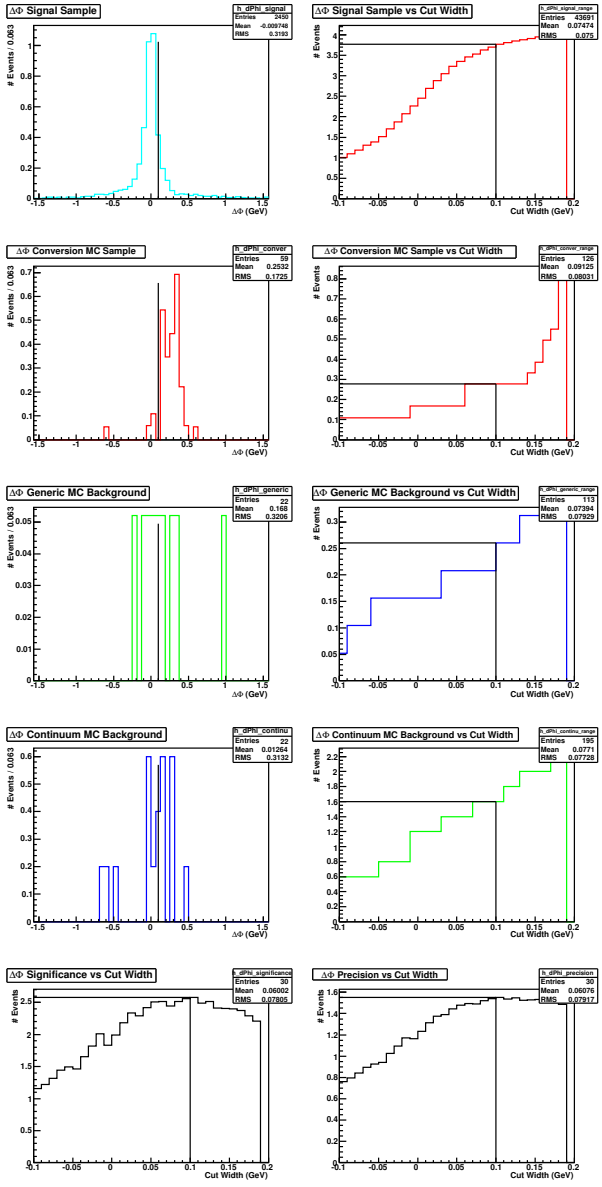

Figure 69: Optimization plots for the selection criterion on the $\Delta\phi_0$ of the e^+e^- in the $D_s^+ \to \pi^+\pi^-\pi^+$ decay mode for electron-fitted data.

10.7 $D_s^+ \to K^{*+}K^{*0}; K^{*+} \to K_S^0\pi^+, K^{*0} \to K^-\pi^+$)

Given that the branching fraction of $D_s^+ \to K^{*+}K^{*0}$ is $\simeq 1.64\%$, we studied the plots in 70, 72, 74, 76 and 78 to arrive the selection criteria tabulated for pion-fitted data, and the plots in 71, 73, 75, 77 and 79 to arrive at the selection criteria for electron-fitted data. These are tabulated in Table 17.

Table 17: Selection criteria for pion-fitted and electron-fitted data in the $D_s^+ \to K^{*+}K^{*0}$ decay mode.

Selection Criterion	Pion-Fitted Data Cut Center ± Width	Electron-Fitted Data Cut Center ± Width
$m_{D_s^+}$	1.969 ± 0.007 GeV	1.969 ± 0.006 GeV
m_{BC}	2.112 ± 0.007 GeV	2.112 ± 0.005 GeV
δm	0.155 ± 0.009 GeV	0.144 ± 0.008 GeV
Δd_0	-0.004 m	-0.005 m
$\Delta\phi_0$	0.07	0.13

The result of these selection criteria, applied to the pion and electron-fitted samples, are presented in terms of the signal and background yields we can expect in 586 pb^{-1} of data in Table 18. A signal significance, defined for now simply as $\frac{N_SignalEvents}{\sqrt{N_BackgroundEvents}}$, serves as a measure of comparison between the two sets of criteria and samples.

Table 18: Number of signal and background events expected in pion and electron-fitted data in the $D_s^+ \to K^{*+}K^{*0}$ decay mode.

Expected Number of Events in 586 pb^{-1}	Pion-Fitted Samples and Criteria	Electron-Fitted Samples and Criteria
Signal ($N_SignalEvents$)	1.78	2.02
Conversion Background	-	0.23
Generic Background (without Conversions in e-fit)	1.35	0.63
Continuum Background	0.00	0.20
Total Background ($N_BackgroundEvents$)	1.35	1.05
$\frac{N_SignalEvents}{\sqrt{N_BackgroundEvents}}$	1.5	2.0

Optimization plots for the $m_{D_s^+}$ selection criterion in the $D_s^+ \to K^{*+}K^{*0}$ decay mode having applied all other selection criteria. All plots are normalized to 586 pb^{-1} of data. The top left plots, for both the pion and electron-fitted sets of data, are the distributions of $m_{D_s^+}$ in the signal MC sample. The top right plot is the signal MC sample accepted by the criterion as we increase the cut width plotted on the x-axis. For the pion-fitted samples on the left, the plots in the second and third rows correspond to the generic and continuum MC samples, respectively. For the electron-fitted samples on the right, the plots in the second, third and fourth rows correspond to the conversion, generic and continuum MC samples, respectively. For both sets of plots, the bottom left shows the significance of the signal over background. The bottom right plot shows the precision of the signal.

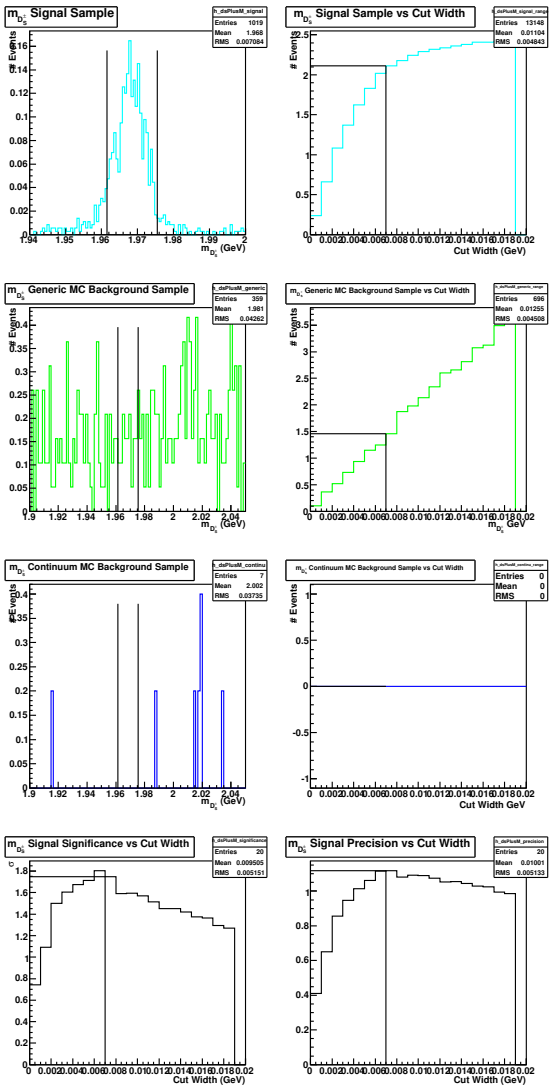

Figure 70: Optimization plots for the $m_{D_s^+}$ selection criterion in the $D_s^+ \to K^{*+}K^{*0}$ decay mode for pion-fitted data.

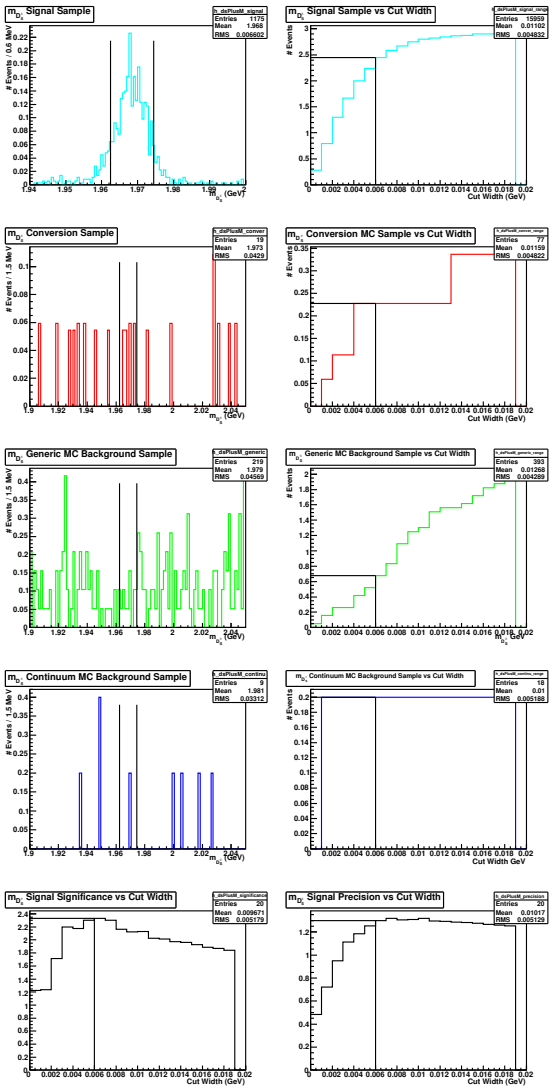

Figure 71: Optimization plots for the $m_{D_s^+}$ selection criterion in the $D_s^+ \to K^{*+}K^{*0}$ decay mode for electron-fitted data.

Optimization plots for the m_{BC} selection criterion in the $D_s^+ \to K^{*+}K^{*0}$ decay mode having applied all other selection criteria. All plots are normalized to 586 pb^{-1} of data.

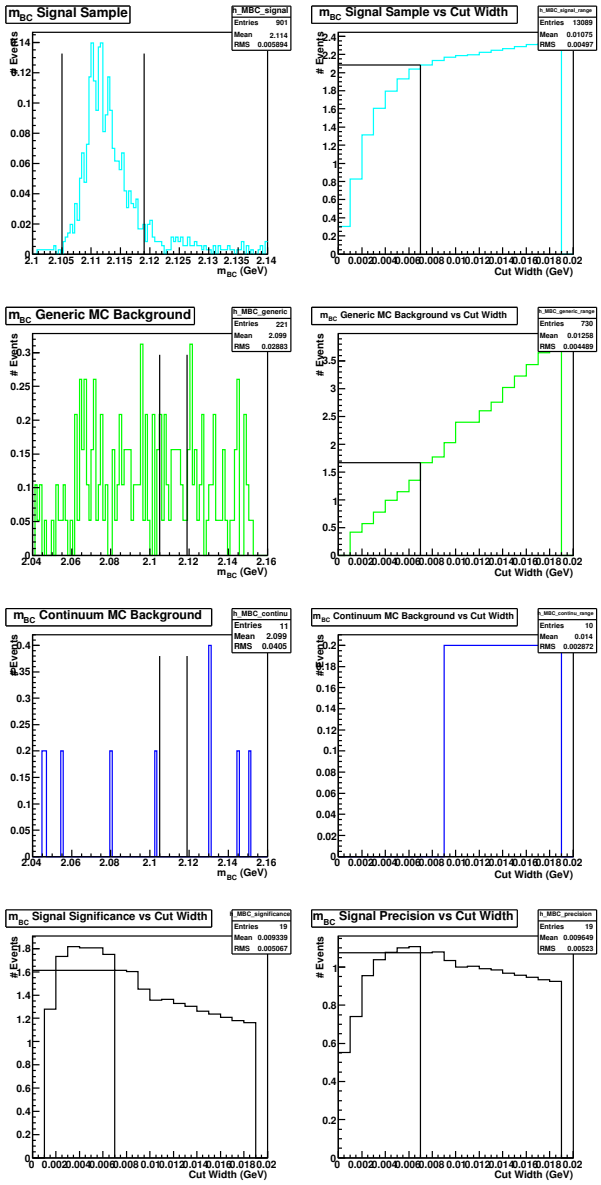

Figure 72: Optimization plots for the m_{BC} selection criterion in the $D_s^+ \to K^{*+}K^{*0}$ decay mode for pion-fitted data.

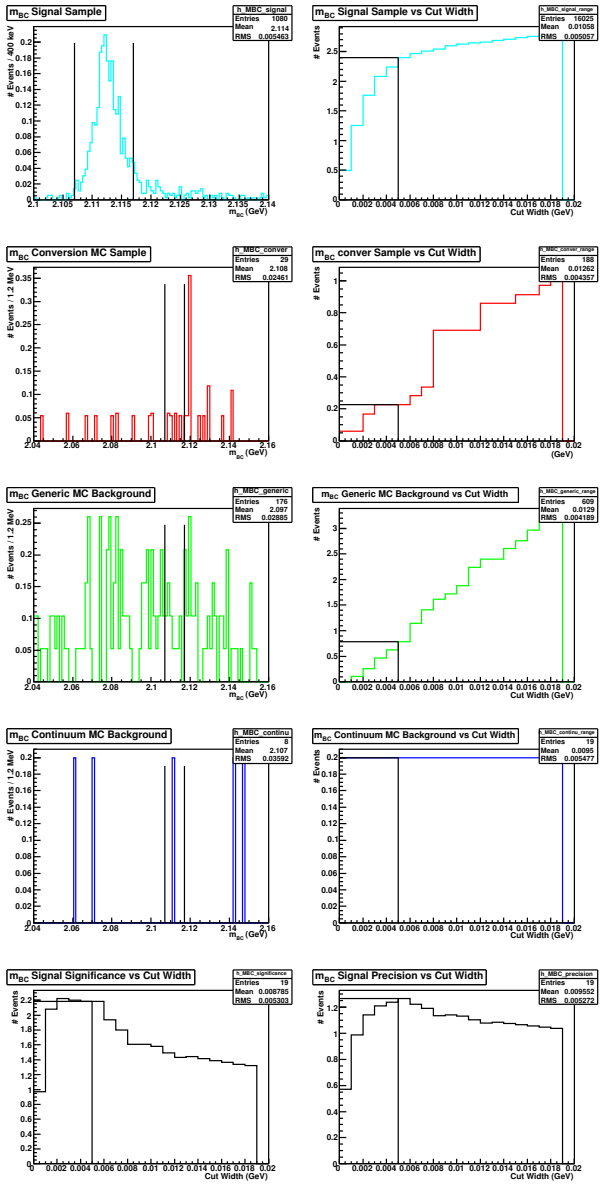

Figure 73: Optimization plots for the m_{BC} selection criterion in the $D_s^+ \to K^{*+}K^{*0}$ decay mode for electron-fitted data.

Optimization plots for the δm selection criterion in the $D_s^+ \to K^{*+}K^{*0}$ decay mode having applied all other selection criteria. All plots are normalized to 586 pb^{-1} of data.

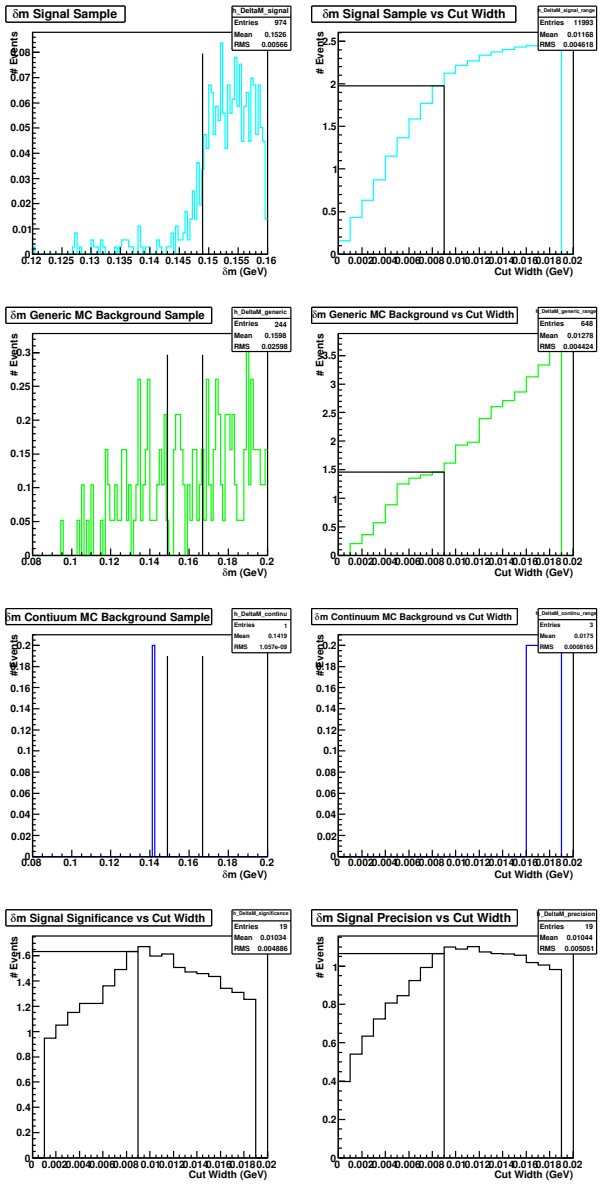

Figure 74: Optimization plots for the δm selection criterion in the $D_s^+ \to K^{*+}K^{*0}$ decay mode for pion-fitted data.

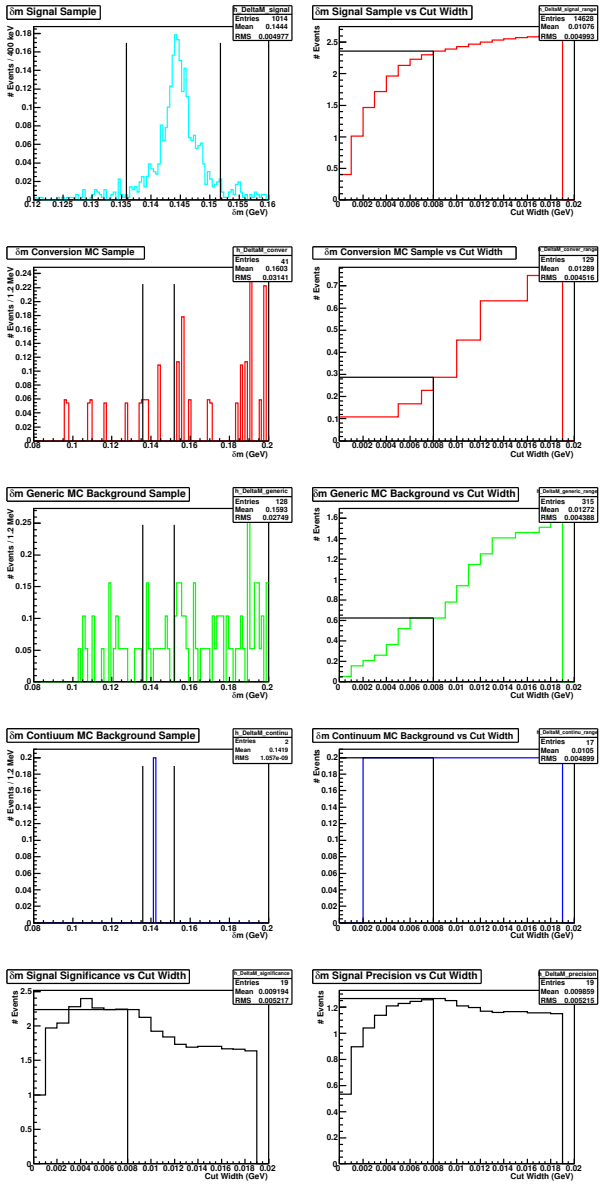

Figure 75: Optimization plots for the δm selection criterion in the $D_s^+ \to K^{*+}K^{*0}$ decay mode for electron-fitted data.

Optimization plots for the selection criterion on the Δd_0 of the e^+e^- in the $D_s^+ \to K^{*+}K^{*0}$ decay mode having applied all other selection criteria. All plots are normalized to 586 pb^{-1} of data.

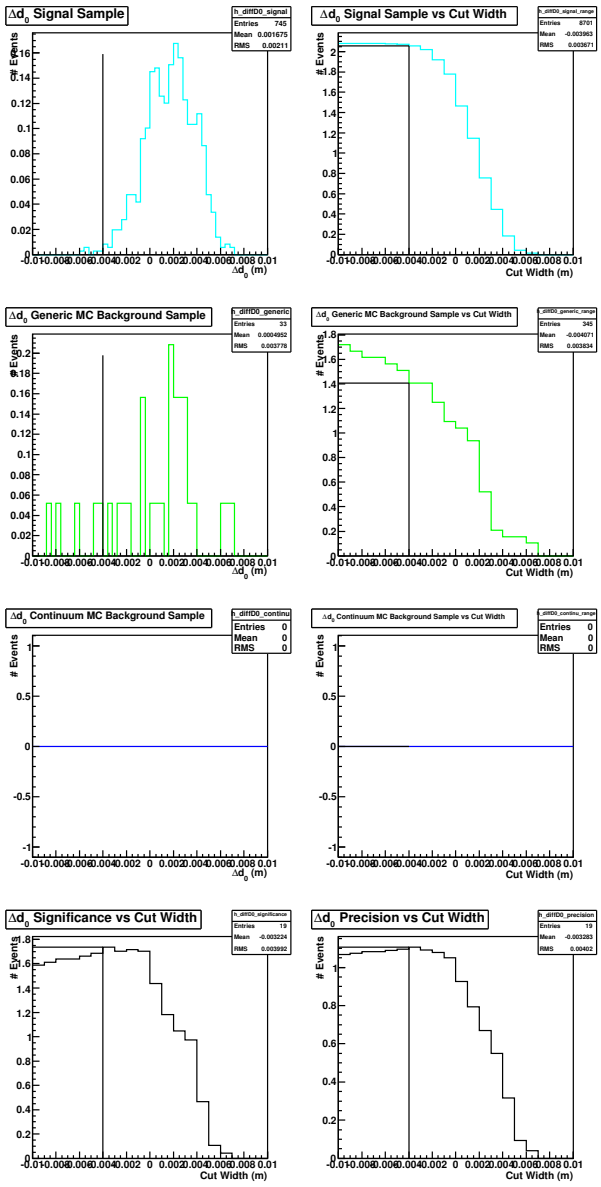

Figure 76: Optimization plots for the selection criterion on Δd_0 in the $D_s^+ \to K^{*+}K^{*0}$ for pion-fitted data.

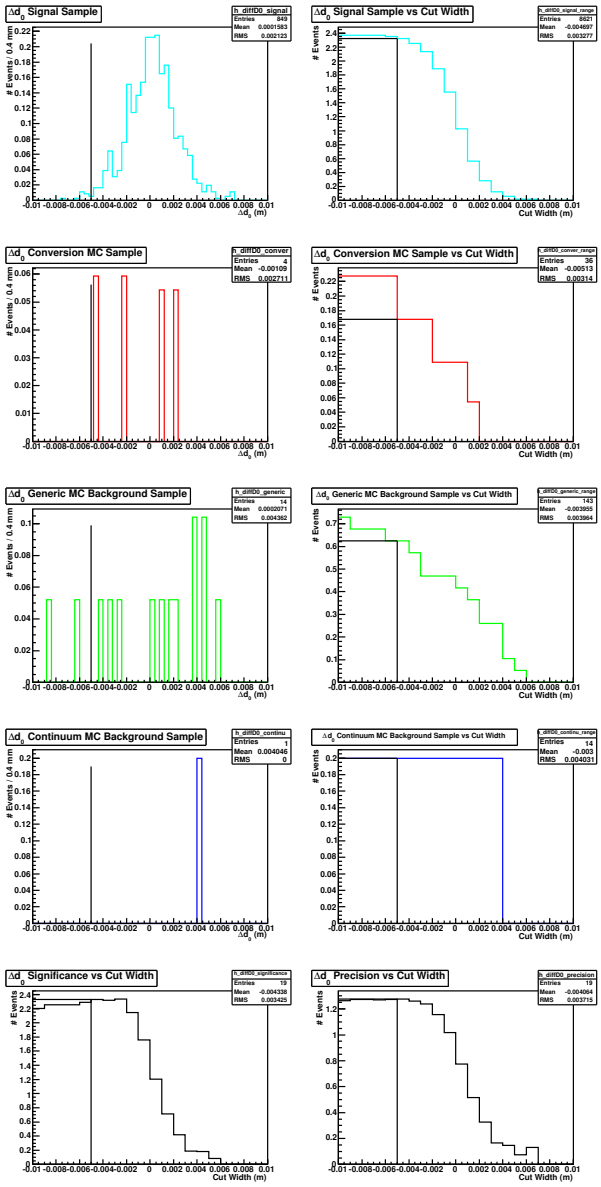

Figure 77: Optimization plots for the selection criterion on Δd_0 in the $D_s^+ \to K^{*+}K^{*0}$ for electron-fitted data.

Optimization plots for the selection criterion on the $\Delta\phi_0$ of the e^+e^- in the $D_s^+ \to K^{*+}K^{*0}$ decay mode having applied all other selection criteria. All plots are normalized to 586 pb^{-1} of data.

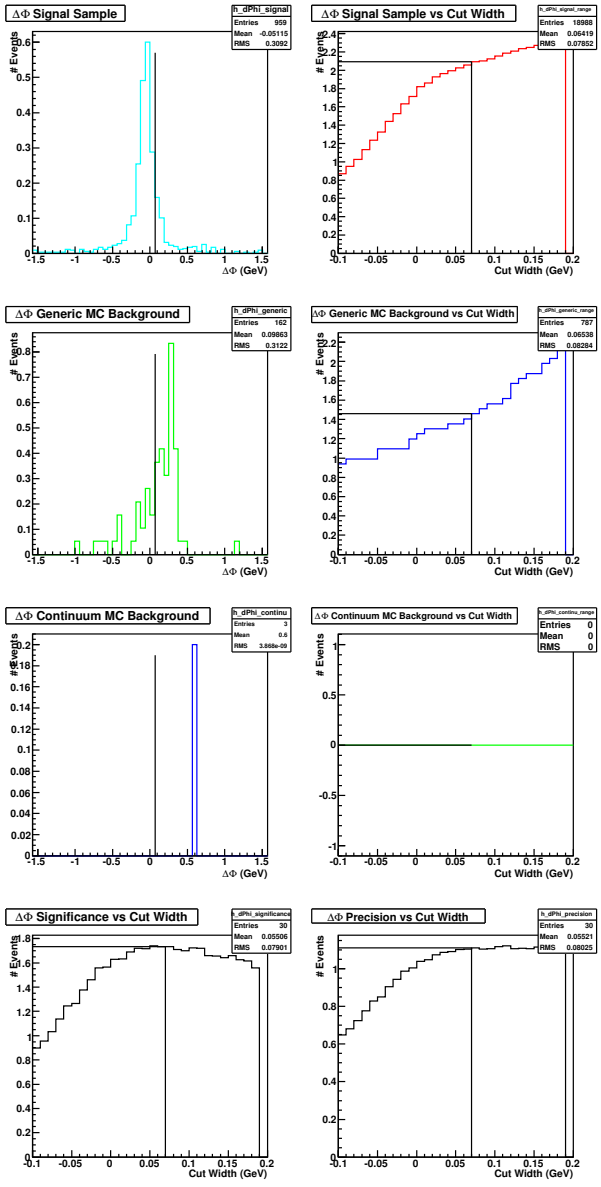

Figure 78: Optimization plots for the selection criterion on the $\Delta\phi_0$ of the e^+e^- in the $D_s^+ \to K^{*+}K^{*0}$ decay mode for pion-fitted data.

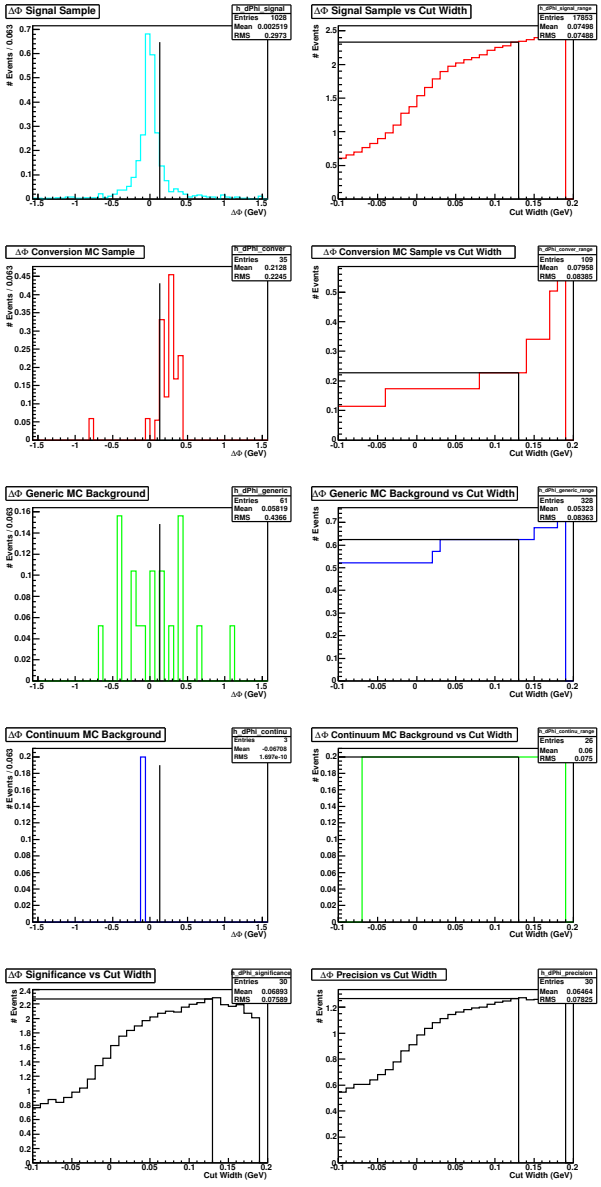

Figure 79: Optimization plots for the selection criterion on the $\Delta\phi_0$ of the e^+e^- in the $D_s^+ \to K^{*+}K^{*0}$ decay mode for electron-fitted data.

10.8 $D_s^+ \to \eta\rho^+; \eta \to \gamma\gamma; \rho^+ \to \pi^+\pi^0$

Given that:

- the branching fraction of $D_s^+ \to \eta\rho^+$ is $\simeq 13.1\%$, and
- the branching fraction of $\eta \to \gamma\gamma$ is $\simeq 99.95$ %,
- the branching fraction of $\rho^+ \to \pi^+\pi^0$ is $\simeq 39.31\%$,

we studied the plots in 80, 82, 84, 86 and 88 to arrive at the selection criteria for pion-fitted data, and the plots in 81, 83, 85, 87 and 89 to arrive at the selection criteria for electron-fitted data. These are tabulated in Table 19.

Table 19: Selection criteria for pion-fitted and electron-fitted data in the $D_s^+ \to \eta\rho^+; \eta \to \gamma\gamma; \rho^+ \to \pi^+\pi^0$ decay mode.

Selection Criterion	Pion-Fitted Data Cut Center ± Width	Electron-Fitted Data Cut Center ± Width
$m_{D_s^+}$	1.969 ± 0.014 GeV	1.969 ± 0.015 GeV
m_{BC}	2.112 ± 0.006 GeV	2.112 ± 0.004 GeV
δm	0.155 ± 0.009 GeV	0.144 ± 0.005 GeV
Δd_0	-0.003 m	-0.007 m
$\Delta\phi_0$	0.07	0.13

The result of these selection criteria, applied to the pion and electron-fitted samples, are presented in terms of the signal and background yields we can expect in 586 pb^{-1} of data in Table 20. A signal significance, defined for now simply as $\frac{N_S ignal Events}{\sqrt{N_B ackground Events}}$, serves as a measure of comparison between the two sets of criteria and samples.

Table 20: Number of signal and background events expected in pion and electron-fitted data in the $D_s^+ \to \eta\rho^+; \eta \to \gamma\gamma; \rho^+ \to \pi^+\pi^0$ decay mode.

Expected Number of Events in 586 pb^{-1}	Pion-Fitted Samples and Criteria	Electron-Fitted Samples and Criteria
Signal ($N_S ignal Events$)	5.54	5.71
Conversion Background	-	0.85
Generic Background (without Conversions in e-fit)	2.40	0.99
Continuum Background	3.60	1.00
Total Background ($N_B ackground Events$)	6.00	2.84
$\frac{N_S ignal Events}{\sqrt{N_B ackground Events}}$	2.3	3.4

Optimization plots for the $m_{D_s^+}$ selection criterion in the $D_s^+ \to \eta\rho^+; \eta \to \gamma\gamma; \rho^+ \to \pi^+\pi^0$ decay mode having applied all other selection criteria. All plots are normalized to 586 pb^{-1} of data. The top left plots, for both the pion and electron-fitted sets of data, are the distributions of $m_{D_s^+}$ in the signal MC sample. The top right plot is the signal MC sample accepted by the criterion as we increase the cut width plotted on the x-axis. For the pion-fitted samples on the left, the plots in the second and third rows correspond to the generic and continuum MC samples, respectively. For the electron-fitted samples on the right, the plots in the second, third and fourth rows correspond to the conversion, generic and continuum MC samples, respectively. For both sets of plots, the bottom left shows the significance of the signal over background. The bottom right plot shows the precision of the signal.

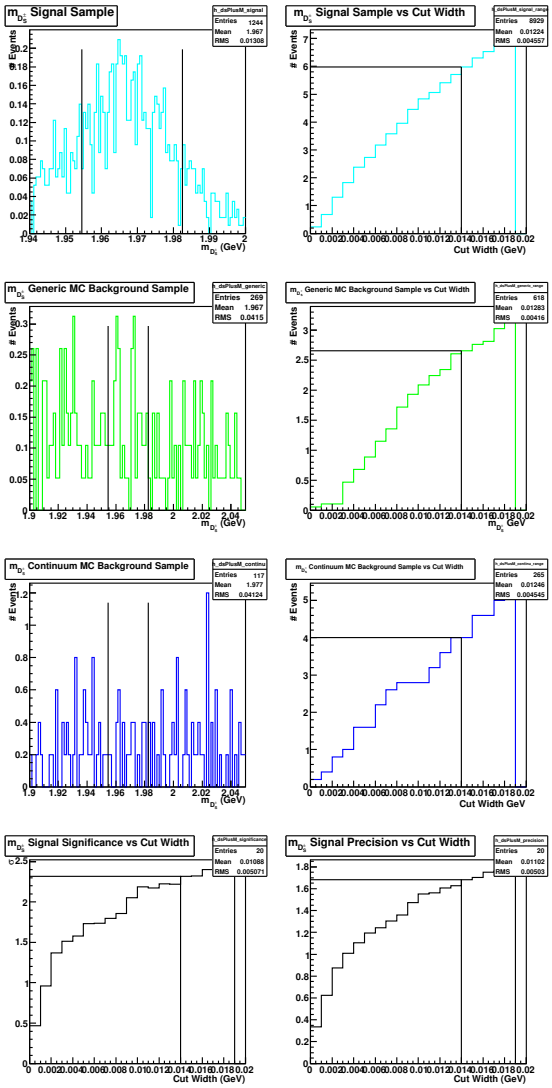

Figure 80: Optimization plots for the $m_{D_s^+}$ selection criterion in the $D_s^+ \to \eta\rho^+; \eta \to \gamma\gamma; \rho^+ \to \pi^+\pi^0$ decay mode for pion-fitted data.

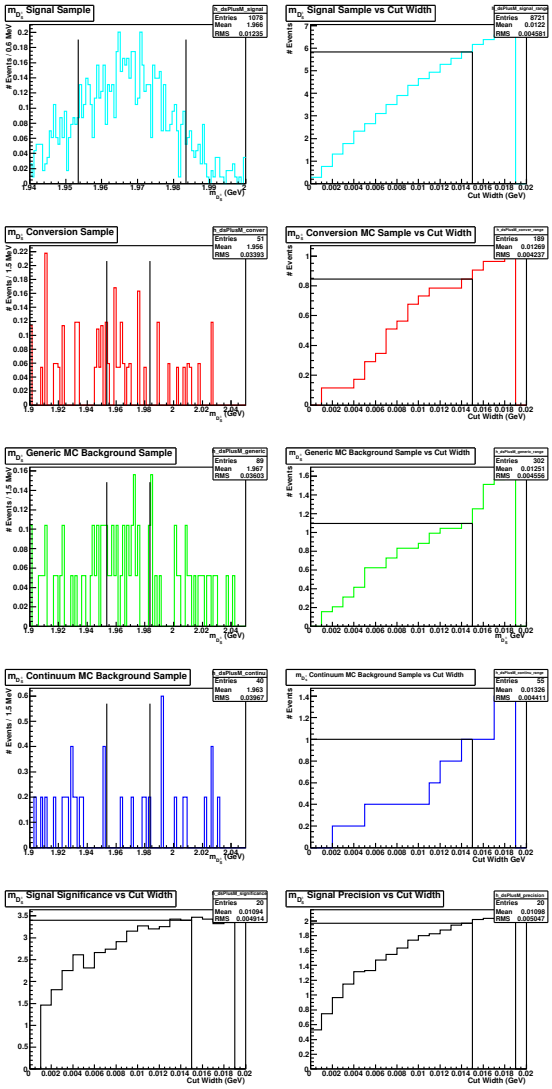

Figure 81: Optimization plots for the $m_{D_s^+}$ selection criterion in the $D_s^+ \to \eta\rho^+; \eta \to \gamma\gamma; \rho^+ \to \pi^+\pi^0$ decay mode for electron-fitted data.

Optimization plots for the m_{BC} selection criterion in the $D_s^+ \to \eta\rho^+; \eta \to \gamma\gamma; \rho^+ \to \pi^+\pi^0$ decay mode having applied all other selection criteria. All plots are normalized to 586 pb^{-1} of data.

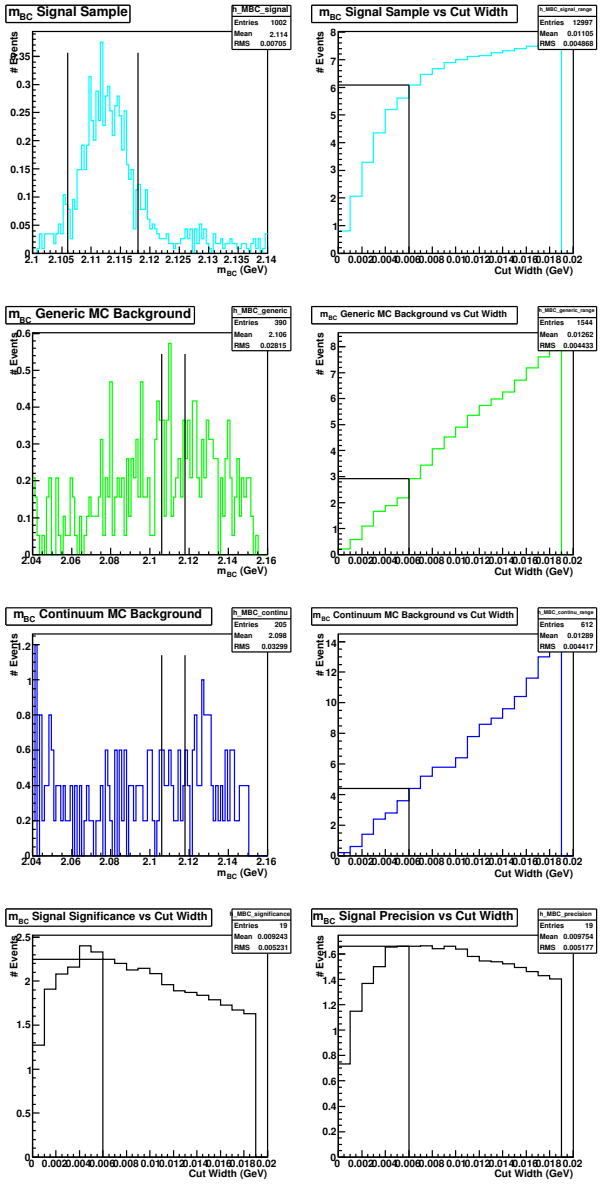

Figure 82: Optimization plots for the m_{BC} selection criterion in the $D_s^+ \to \eta\rho^+; \eta \to \gamma\gamma; \rho^+ \to \pi^+\pi^0$ decay mode for pion-fitted data.

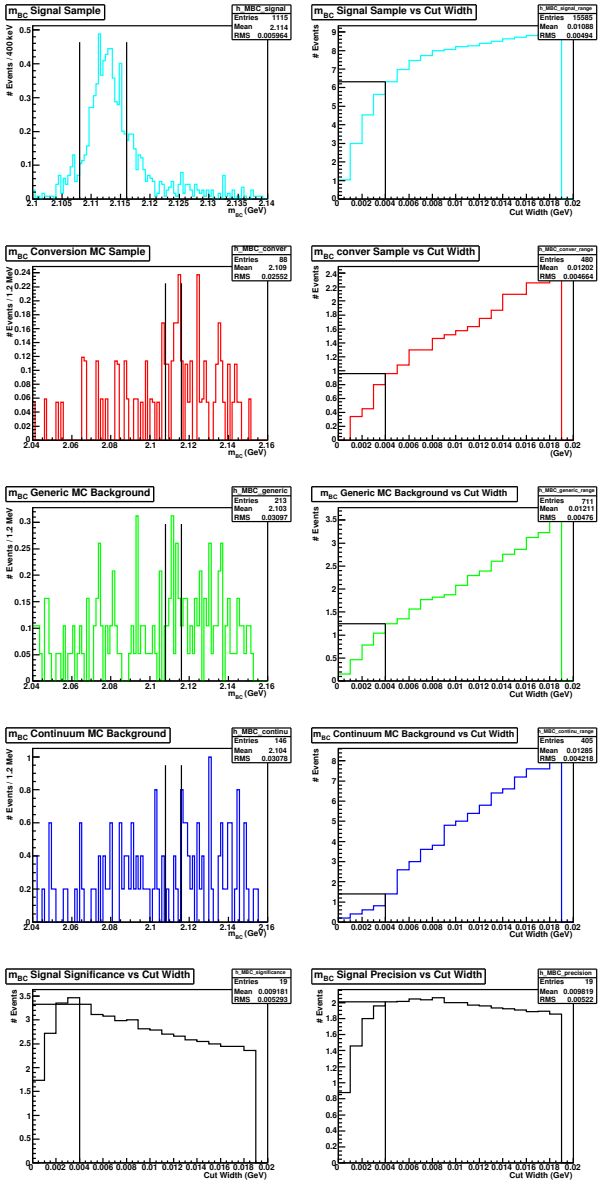

Figure 83: Optimization plots for the m_{BC} selection criterion in the $D_s^+ \to \eta\rho^+; \eta \to \gamma\gamma; \rho^+ \to \pi^+\pi^0$ decay mode for electron-fitted data.

Optimization plots for the δm selection criterion in the $D_s^+ \to \eta\rho^+; \eta \to \gamma\gamma; \rho^+ \to \pi^+\pi^0$ decay mode having applied all other selection criteria. All plots are normalized to 586 pb^{-1} of data.

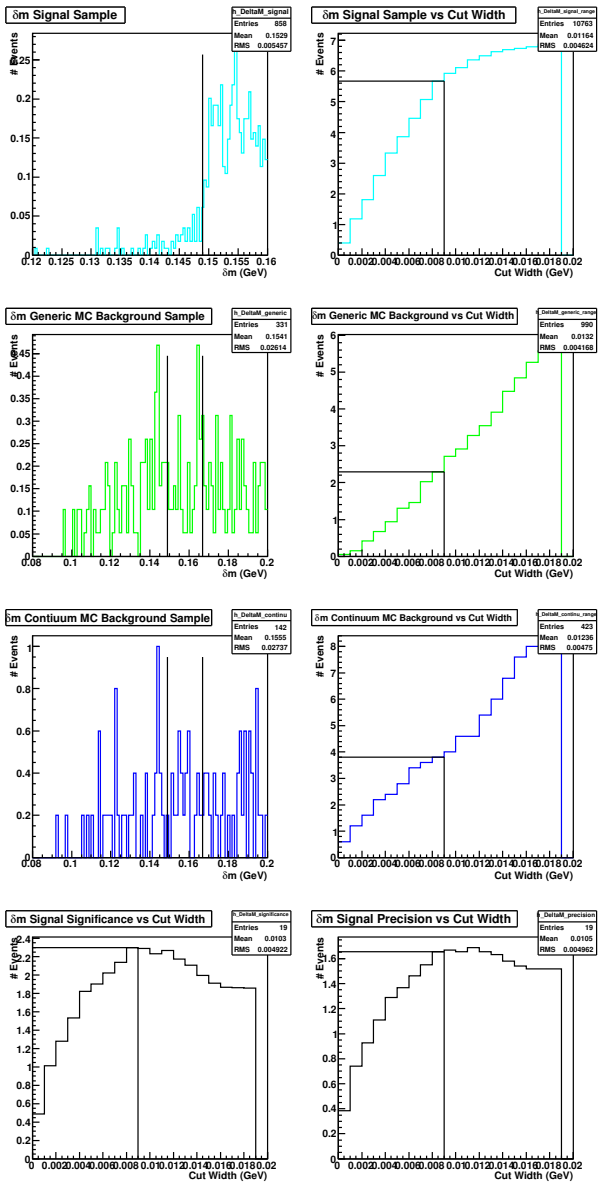

Figure 84: Optimization plots for the δm selection criterion in the $D_s^+ \to \eta\rho^+; \eta \to \gamma\gamma; \rho^+ \to \pi^+\pi^0$ decay mode for pion-fitted data.

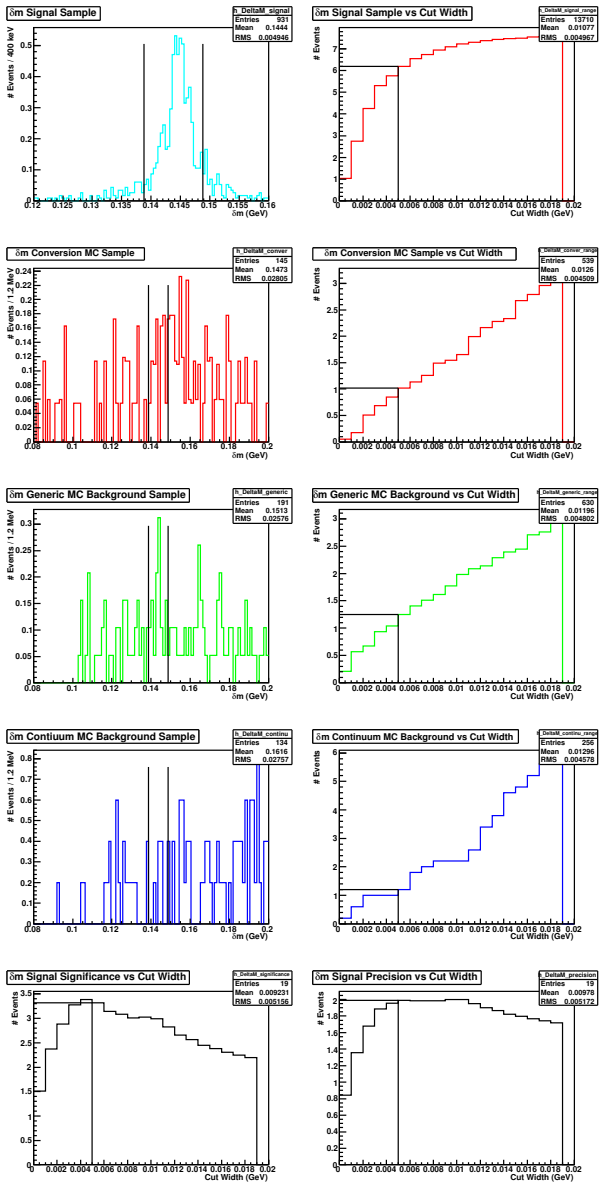

Figure 85: Optimization plots for the δm selection criterion in the $D_s^+ \to \eta\rho^+; \eta \to \gamma\gamma; \rho^+ \to \pi^+\pi^0$ decay mode for electron-fitted data.

Optimization plots for the selection criterion on the Δd_0 of the e^+e^- in the $D_s^+ \to \eta\rho^+; \eta \to \gamma\gamma; \rho^+ \to \pi^+\pi^0$ decay mode having applied all other selection criteria. All plots are normalized to 586 pb^{-1} of data.

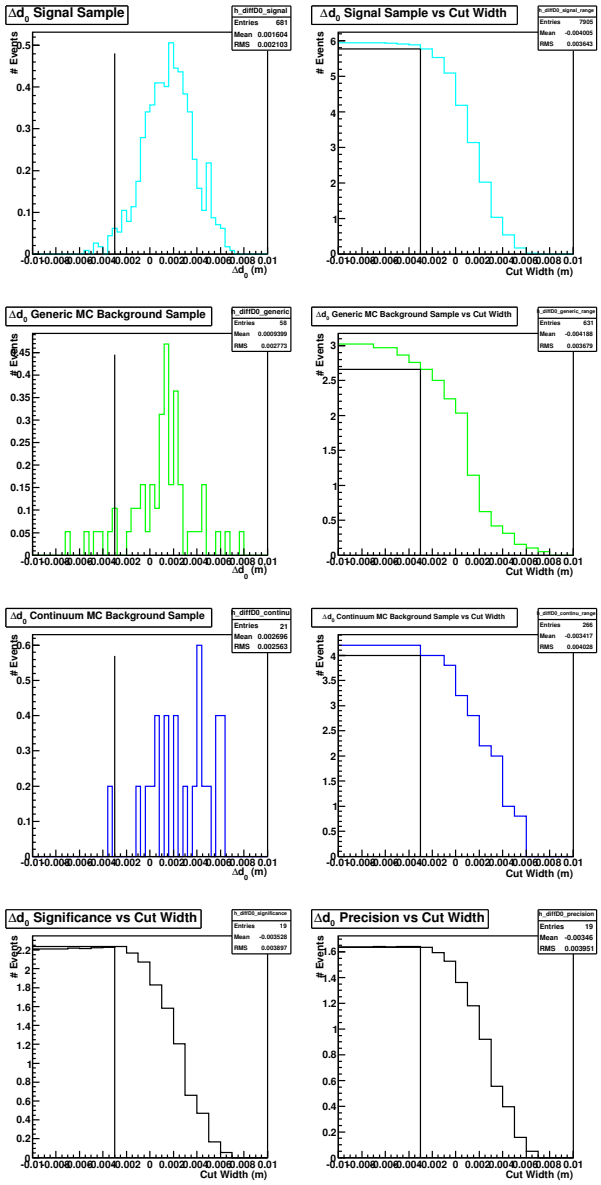

Figure 86: Optimization plots for the selection criterion on Δd_0 in the $D_s^+ \to \eta\rho^+; \eta \to \gamma\gamma; \rho^+ \to \pi^+\pi^0$ for pion-fitted data.

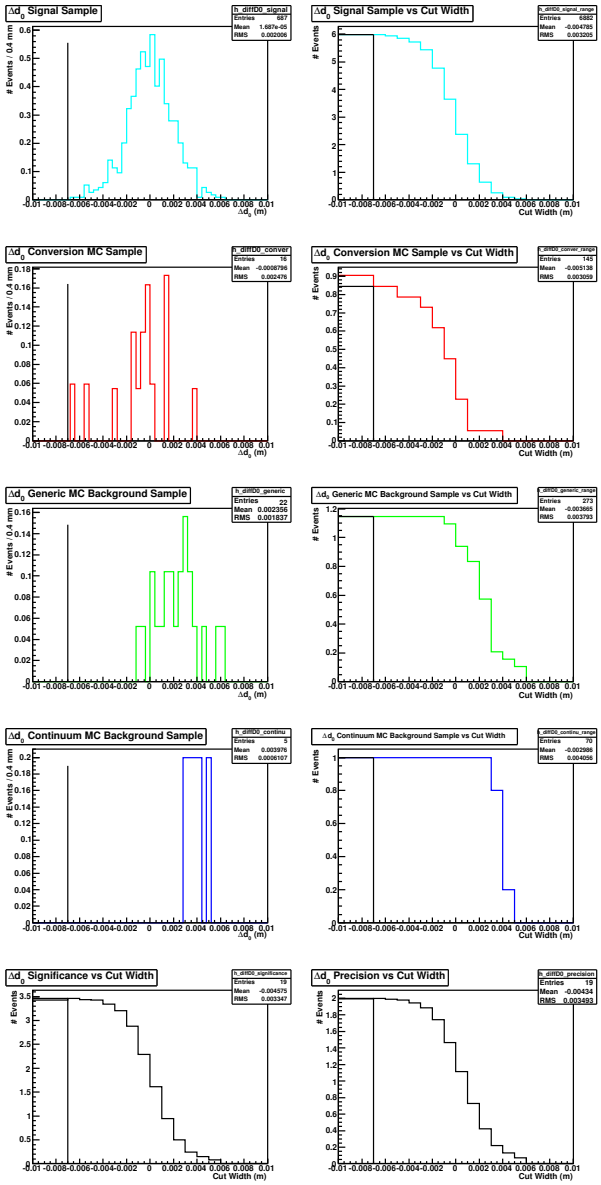

Figure 87: Optimization plots for the selection criterion on Δd_0 in the $D_s^+ \to \eta\rho^+; \eta \to \gamma\gamma; \rho^+ \to \pi^+\pi^0$ for electron-fitted data.

Optimization plots for the selection criterion on the $\Delta\phi_0$ of the e^+e^- in the $D_s^+ \to \eta\rho^+; \eta \to \gamma\gamma; \rho^+ \to \pi^+\pi^0$ decay mode having applied all other selection criteria. All plots are normalized to 586 pb^{-1} of data.

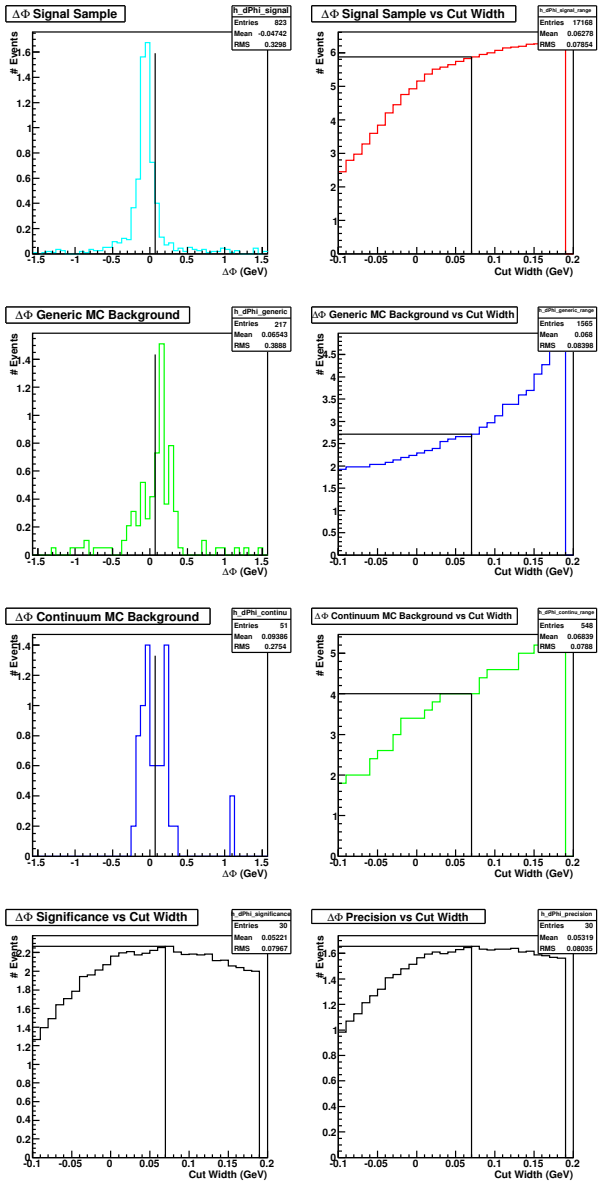

Figure 88: Optimization plots for the selection criterion on the $\Delta\phi_0$ of the e^+e^- in the $D_s^+ \to \eta\rho^+; \eta \to \gamma\gamma; \rho^+ \to \pi^+\pi^0$ decay mode for pion-fitted data.

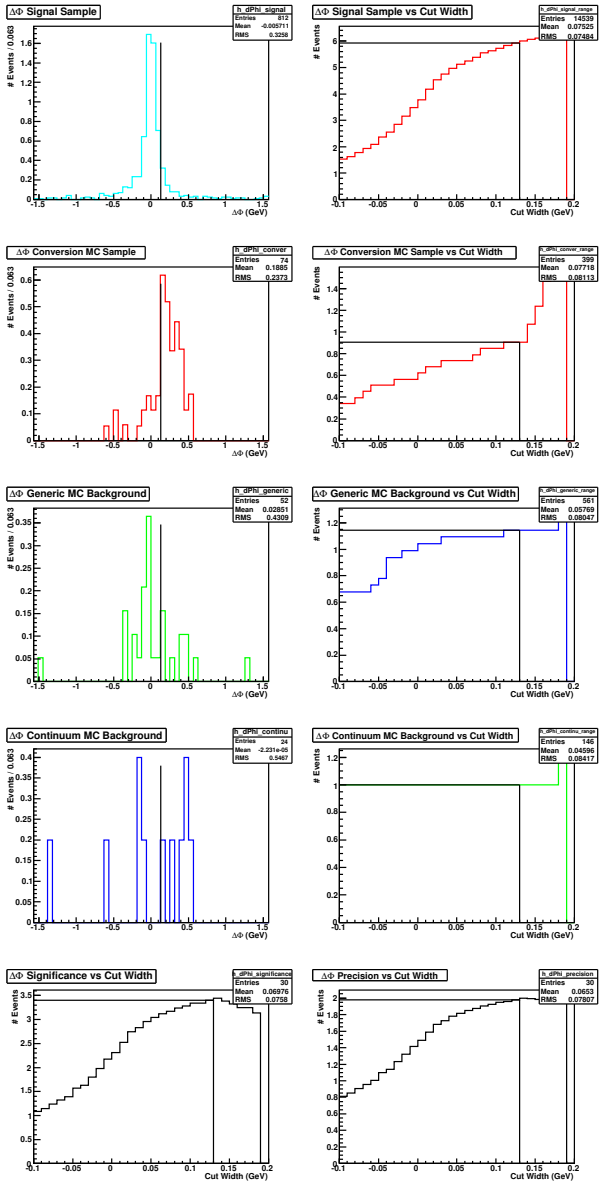

Figure 89: Optimization plots for the selection criterion on the $\Delta\phi_0$ of the e^+e^- in the $D_s^+ \to \eta\rho^+; \eta \to \gamma\gamma; \rho^+ \to \pi^+\pi^0$ decay mode for electron-fitted data.

10.9 $D_s^+ \to \eta'\pi^+; \eta' \to \rho^0\gamma$

Given that:

- the branching fraction of $D_s^+ \to \eta'\pi^+$ is $\simeq 3.8\%$, and
- the branching fraction of $\eta' \to \rho^0\gamma$ is $\simeq 29.4\%$,

we studied the plots in 90, 92, 94, 96 and 98 to arrive at the selection criteria for pion-fitted data, and we studied the plots in 91, 93, 95, 97 and 99 to arrive at the selection criteria for electron-fitted data. These are tabulated in Table 21.

Table 21: Selection criteria for pion-fitted and electron-fitted data in the $D_s^+ \to \eta'\pi^+; \eta' \to \rho^0\gamma$ decay mode.

Selection Criterion	Pion-Fitted Data Cut Center ± Width	Electron-Fitted Data Cut Center ± Width
$m_{D_s^+}$	1.969 ± 0.018 GeV	1.969 ± 0.012 GeV
m_{BC}	2.112 ± 0.004 GeV	2.112 ± 0.004 GeV
δm	0.155 ± 0.008 GeV	0.144 ± 0.007 GeV
Δd_0	-0.004 m	-0.006 m
$\Delta\phi_0$	0.09	0.11

The result of these selection criteria, applied to the pion and electron-fitted samples, are presented in terms of the signal and background yields we can expect in 586 pb^{-1} of data in Table 22. A signal significance, defined for now simply as $\frac{N_SignalEvents}{\sqrt{N_BackgroundEvents}}$, serves as a measure of comparison between the two sets of criteria and samples.

Table 22: Number of signal and background events expected in pion and electron-fitted data in the $D_s^+ \to \eta'\pi^+; \eta' \to \rho^0\gamma$ decay mode.

Expected Number of Events in 586 pb^{-1}	Pion-Fitted Samples and Criteria	Electron-Fitted Samples and Criteria
Signal ($N_SignalEvents$)	2.17	2.41
Conversion Background	-	0.34
Generic Background (without Conversions in e-fit)	0.83	0.21
Continuum Background	1.60	1.80
Total Background ($N_BackgroundEvents$)	2.43	2.35
$\frac{N_SignalEvents}{\sqrt{N_BackgroundEvents}}$	1.4	1.6

Optimization plots for the $m_{D_s^+}$ selection criterion in the $D_s^+ \to \eta'\pi^+; \eta' \to \rho^0\gamma$ decay mode having applied all other selection criteria. All plots are normalized to 586 pb^{-1} of data. The top left plots, for both the pion and electron-fitted sets of data, are the distributions of $m_{D_s^+}$ in the signal MC sample. The top right plot is the signal MC sample accepted by the criterion as we increase the cut width plotted on the x-axis. For the pion-fitted samples on the left, the plots in the second and third rows correspond to the generic and continuum MC samples, respectively. For the electron-fitted samples on the right, the plots in the second, third and fourth rows correspond to the conversion, generic and continuum MC samples, respectively. For both sets of plots, the bottom left shows the significance of the signal over background. The bottom right plot shows the precision of the signal.

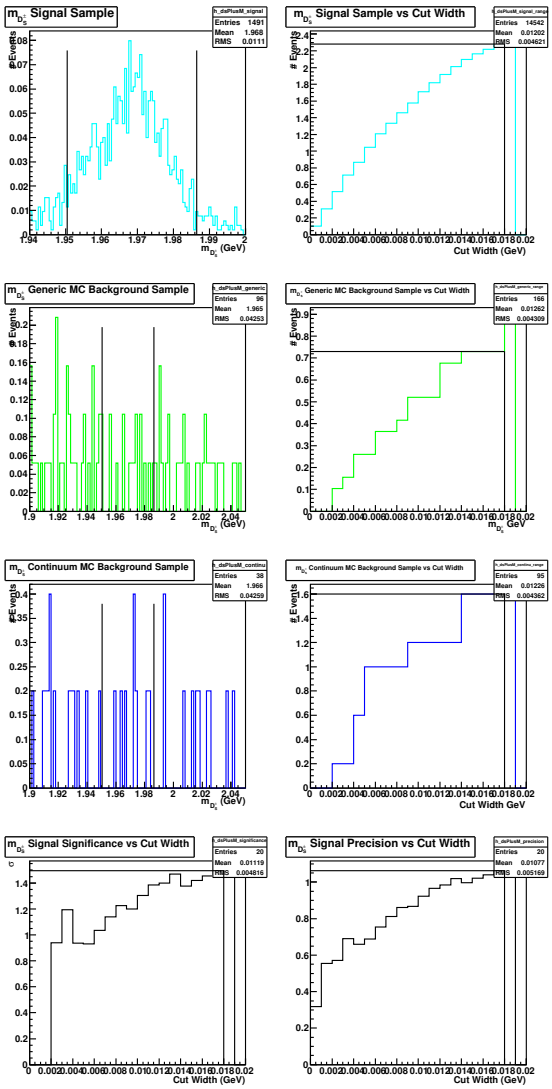

Figure 90: Optimization plots for the $m_{D_s^+}$ selection criterion in the $D_s^+ \to \eta'\pi^+; \eta' \to \rho^0\gamma$ decay mode for pion-fitted data.

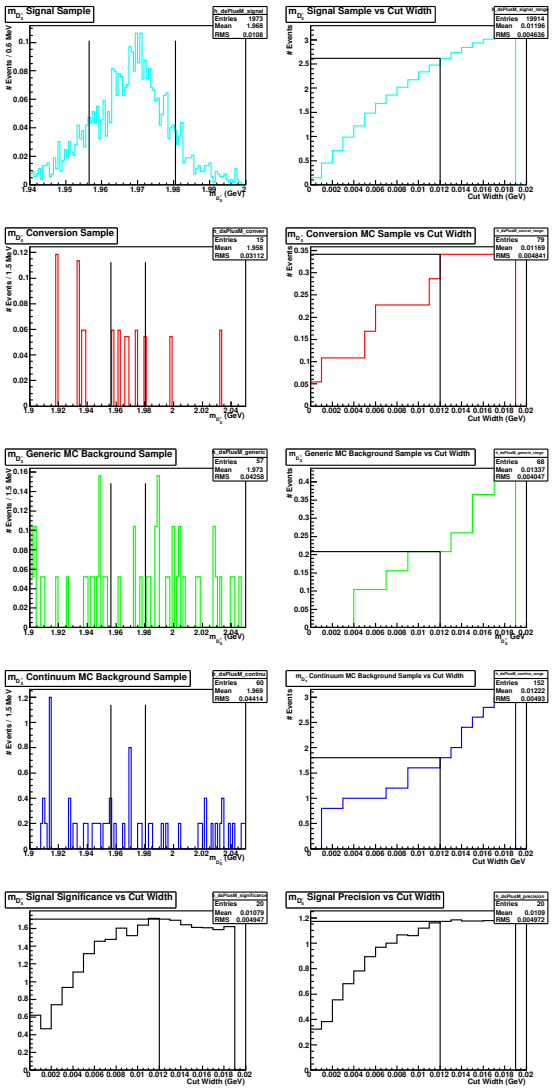

Figure 91: Optimization plots for the $m_{D_s^+}$ selection criterion in the $D_s^+ \to \eta'\pi^+; \eta' \to \rho^0\gamma$ decay mode for electron-fitted data.

Optimization plots for the m_{BC} selection criterion in the $D_s^+ \to \eta'\pi^+; \eta' \to \rho^0\gamma$ decay mode having applied all other selection criteria. All plots are normalized to 586 pb^{-1} of data.

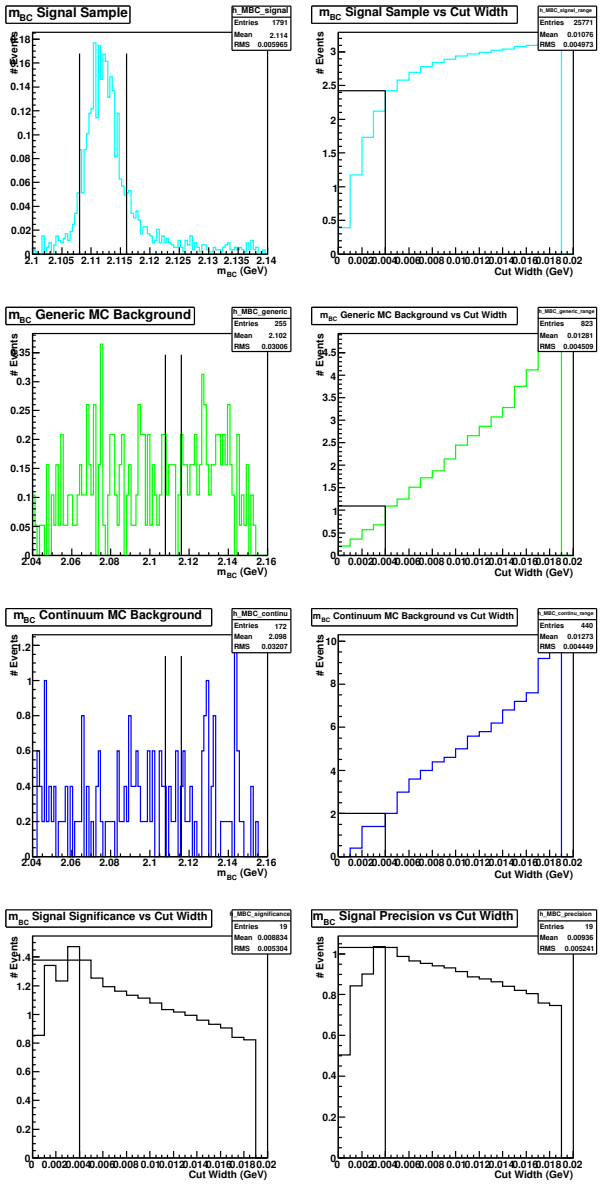

Figure 92: Optimization plots for the m_{BC} selection criterion in the $D_s^+ \to \eta'\pi^+; \eta' \to \rho^0\gamma$ decay mode for pion-fitted data.

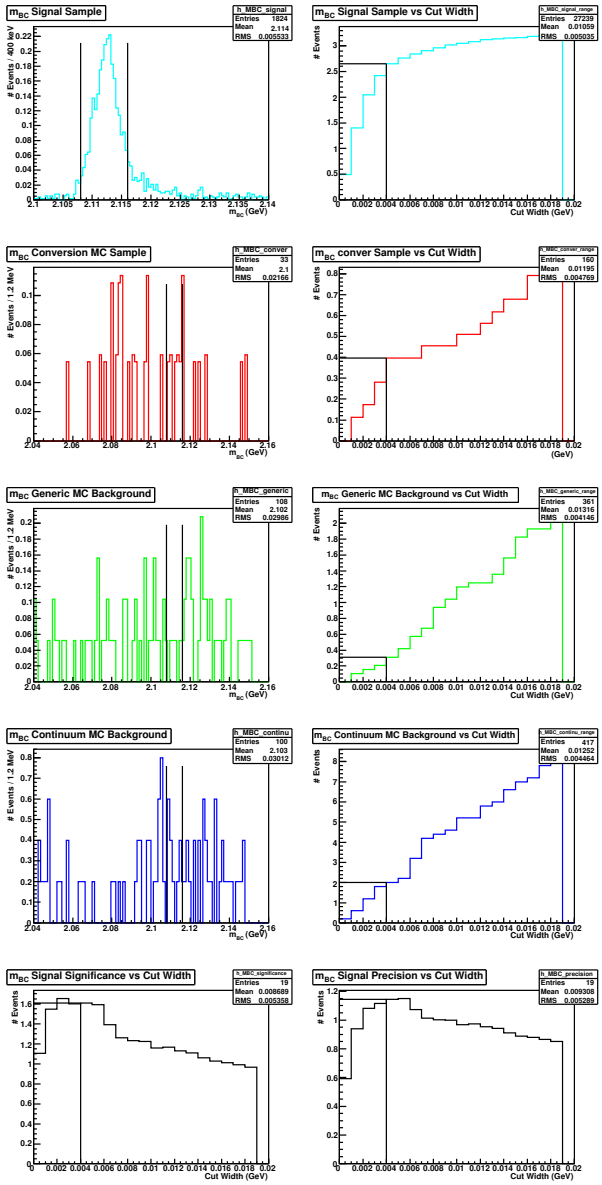

Figure 93: Optimization plots for the m_{BC} selection criterion in the $D_s^+ \to \eta'\pi^+; \eta' \to \rho^0\gamma$ decay mode for electron-fitted data.

Optimization plots for the δm selection criterion in the $D_s^+ \to \eta'\pi^+; \eta' \to \rho^0\gamma$ decay mode having applied all other selection criteria. All plots are normalized to 586 pb^{-1} of data.

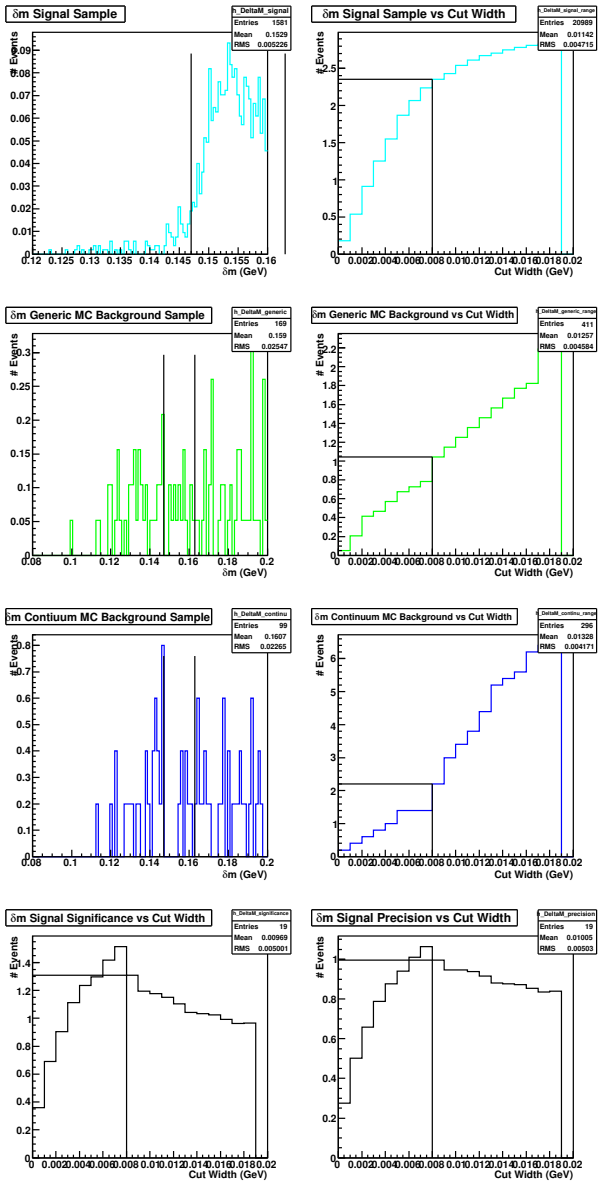

Figure 94: Optimization plots for the δm selection criterion in the $D_s^+ \to \eta'\pi^+; \eta' \to \rho^0\gamma$ decay mode for pion-fitted data.

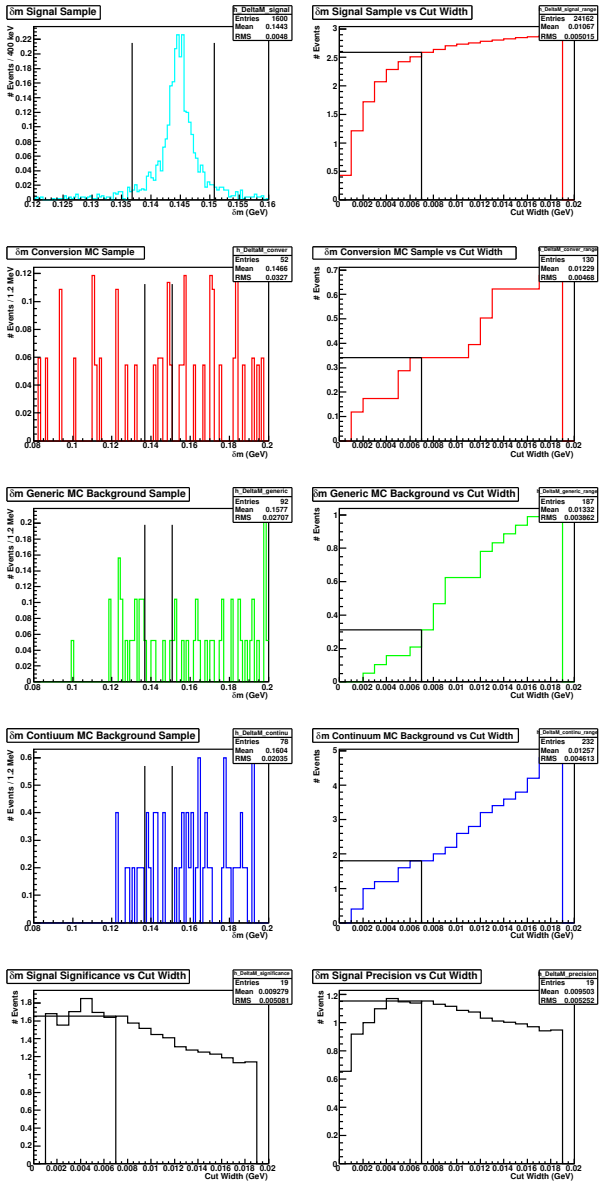

Figure 95: Optimization plots for the δm selection criterion in the $D_s^+ \to \eta'\pi^+; \eta' \to \rho^0\gamma$ decay mode for electron-fitted data.

Optimization plots for the selection criterion on the Δd_0 of the e^+e^- in the $D_s^+ \to \eta'\pi^+; \eta' \to \rho^0\gamma$ decay mode having applied all other selection criteria. All plots are normalized to 586 pb^{-1} of data.

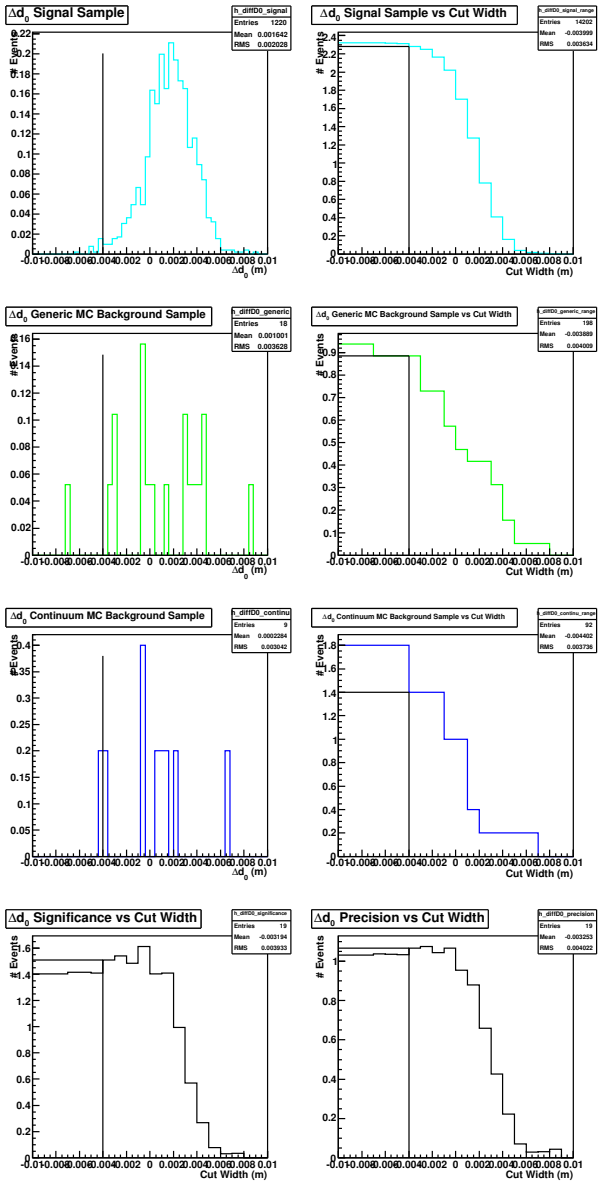

Figure 96: Optimization plots for the selection criterion on Δd_0 in the $D_s^+ \to \eta'\pi^+; \eta' \to \rho^0\gamma$ for pion-fitted data.

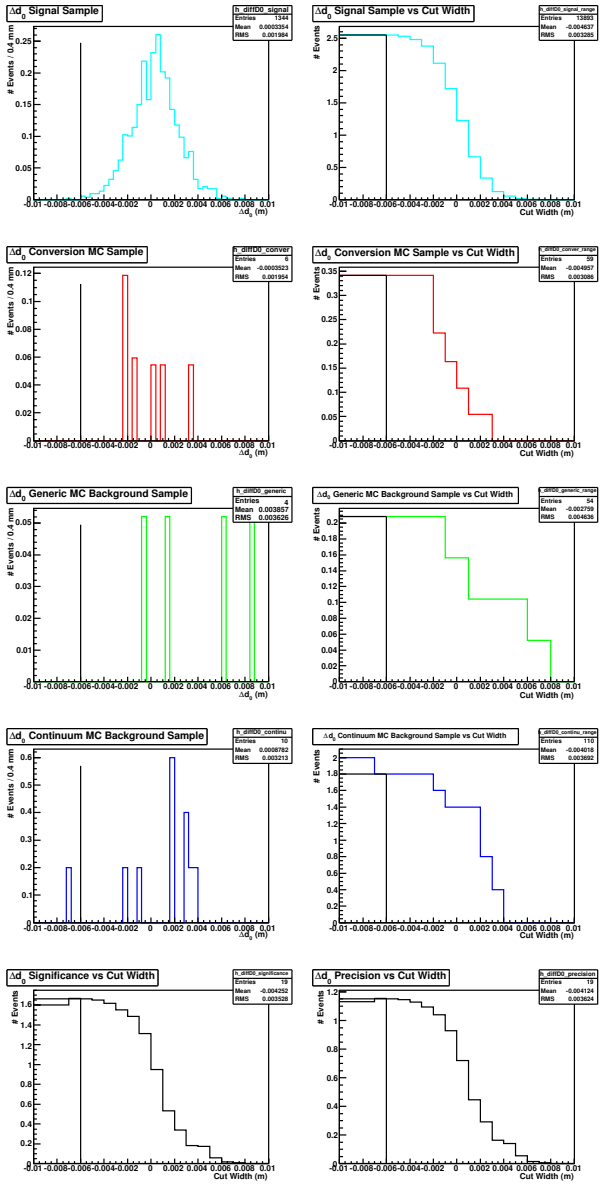

Figure 97: Optimization plots for the selection criterion on Δd_0 in the $D_s^+ \to \eta'\pi^+; \eta' \to \rho^0\gamma$ for electron-fitted data.

Optimization plots for the selection criterion on the $\Delta\phi_0$ of the e^+e^- in the $D_s^+ \to \eta'\pi^+; \eta' \to \rho^0\gamma$ decay mode having applied all other selection criteria. All plots are normalized to 586 pb^{-1} of data.

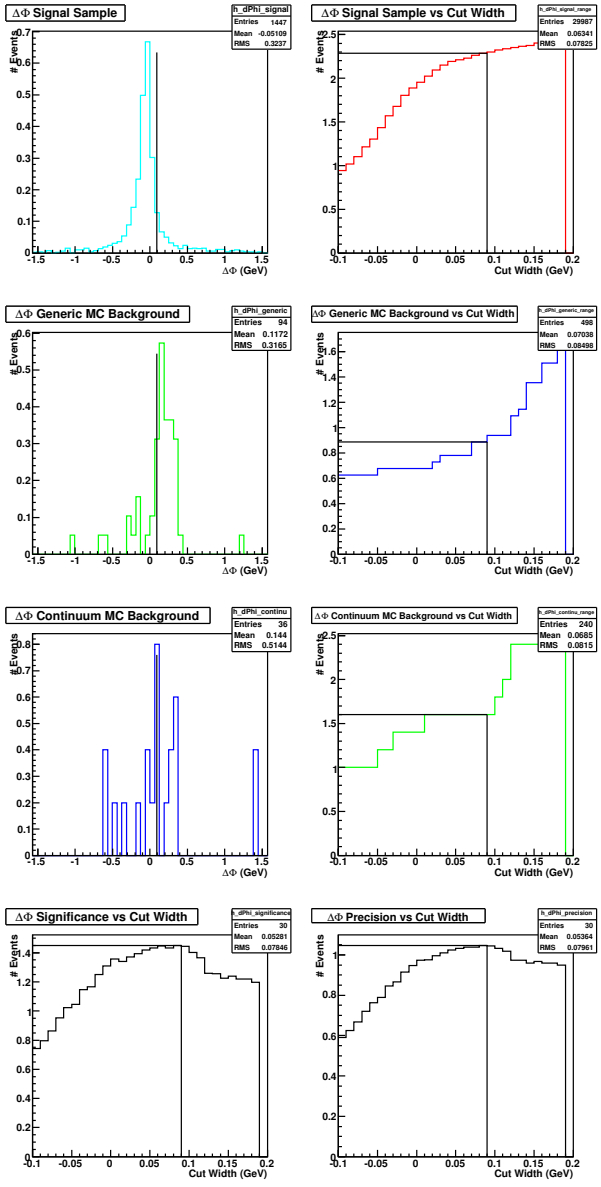

Figure 98: Optimization plots for the selection criterion on the $\Delta\phi_0$ of the e^+e^- in the $D_s^+ \to \eta'\pi^+; \eta' \to \rho^0\gamma$ decay mode for pion-fitted data.

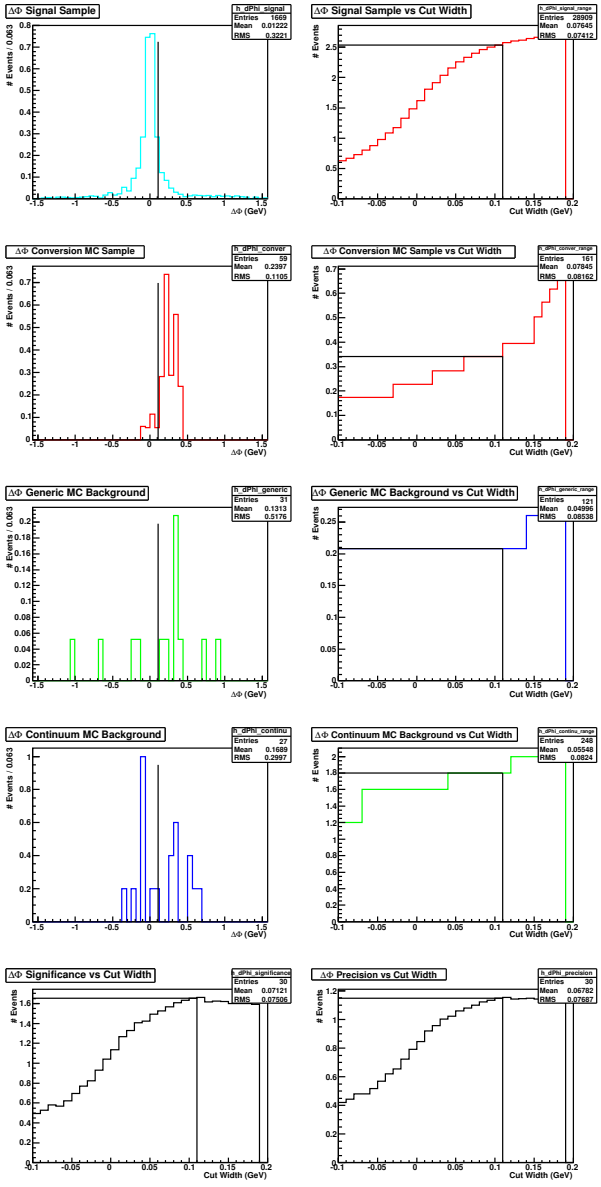

Figure 99: Optimization plots for the selection criterion on the $\Delta\phi_0$ of the e^+e^- in the $D_s^+ \to \eta'\pi^+; \eta' \to \rho^0\gamma$ decay mode for electron-fitted data.

11 The Effect of Vertex Fitting on Signal Significance

In this section, we describe three different approaches to increasing the signal significance of our selection criteria by vertex fitting tracks in our events. We are going to stick to the $K^+K^-\pi^+$ hadronic decay mode for this discussion, as that is the mode that suffers most from conversion backgrounds, which is what vertexing seeks to reject. First, we are going to see if vertexing all tracks from the decay of the D_s^{*+} improves the performance of our existing selection criteria. We will see if a cut on the invariant mass of the e^+e^- pair can offer a higher signal significance. Second, we will vertex constrain the origin of the soft e^+e^- tracks to see if the performance of the Δd_0 and $\Delta\phi_0$ can be improved. Third, we will vertex all tracks in the event with the beamspot in a somewhat more complicated procedure, that will be explained in the appropriate section, to see if a higher signal significance can be achieved. CLEO-c software has a package called `FitEvt` that is used, in our study, to constrain the tracks parameters to a single point in 3-D space. This is implemented using the error matrices of the fitted tracks and is described in [5]. We use the `FitEvt::k_VertexOnly` fit described in the document.

11.1 Vertex Fitting All Tracks From the D_s^+

The $K^+K^-\pi^+$ and e^+e^- tracks are constrained, using `FitEvt`, to originate from one vertex. We present a comparison of the optimization plots for our standard selection criteria applied on our electron-fitted sample alongside plots from the vertex constrained sample between Fig 100 and 108. A narrowing of the signal distribution of δm is noted with the vertex constraint and exploited towards attaining a higher significance. The width of the δm cut is shrunk from 6 MeV to 4 MeV as a consequence of this optimization, as recorded in Table 23. The change in signal significance is recorded in Table 24.

Table 23: Selection criteria for electron-fitted data with and without vertex fitting of tracks from the D_s^{*+} in the $D_s^+ \to K^+K^-\pi^+$ decay mode.

Selection Criterion	Electron-Fitted Samples Cut Center ± Width	Vertex-Fitted, Electron-Fitted Samples Cut Center ± Width
$m_{D_s^+}$	1.969 ± 0.011 GeV	1.969 ± 0.011 GeV
m_{BC}	2.112 ± 0.004 GeV	2.112 ± 0.004 GeV
δm	0.144 ± 0.006 GeV	0.144 ± 0.004 GeV
Δd_0	-0.006 m	-0.0005 m
$\Delta\phi_0$	0.1	0.1

Having achieved a small improvement in the signal significance at the cost of signal yield, we may ask if any improvement may be achieved by selecting on the invariant mass of the e^+e^- pair after vertexing. The idea here is that when we constrain to the interaction point e^+e^- tracks that in reality originate from the conversion of a photon away from the interaction point, we affect the Lorentz momenta of the e^+e^- tracks to produce a sharp peak

Optimization plots for the $m_{D_s^+}$ selection criterion in the $D_s^+ \to K^+K^-\pi^+$ decay mode having applied all other selection criteria. All plots are normalized to 586 pb^{-1} of data. Plots on the figure to the left correspond to simple electron-fitted samples. Plots on the figures to the right correspond to electron-fitted samples where all daughters of the D_s^{*+} have been vertex constrained to originate from a single point.

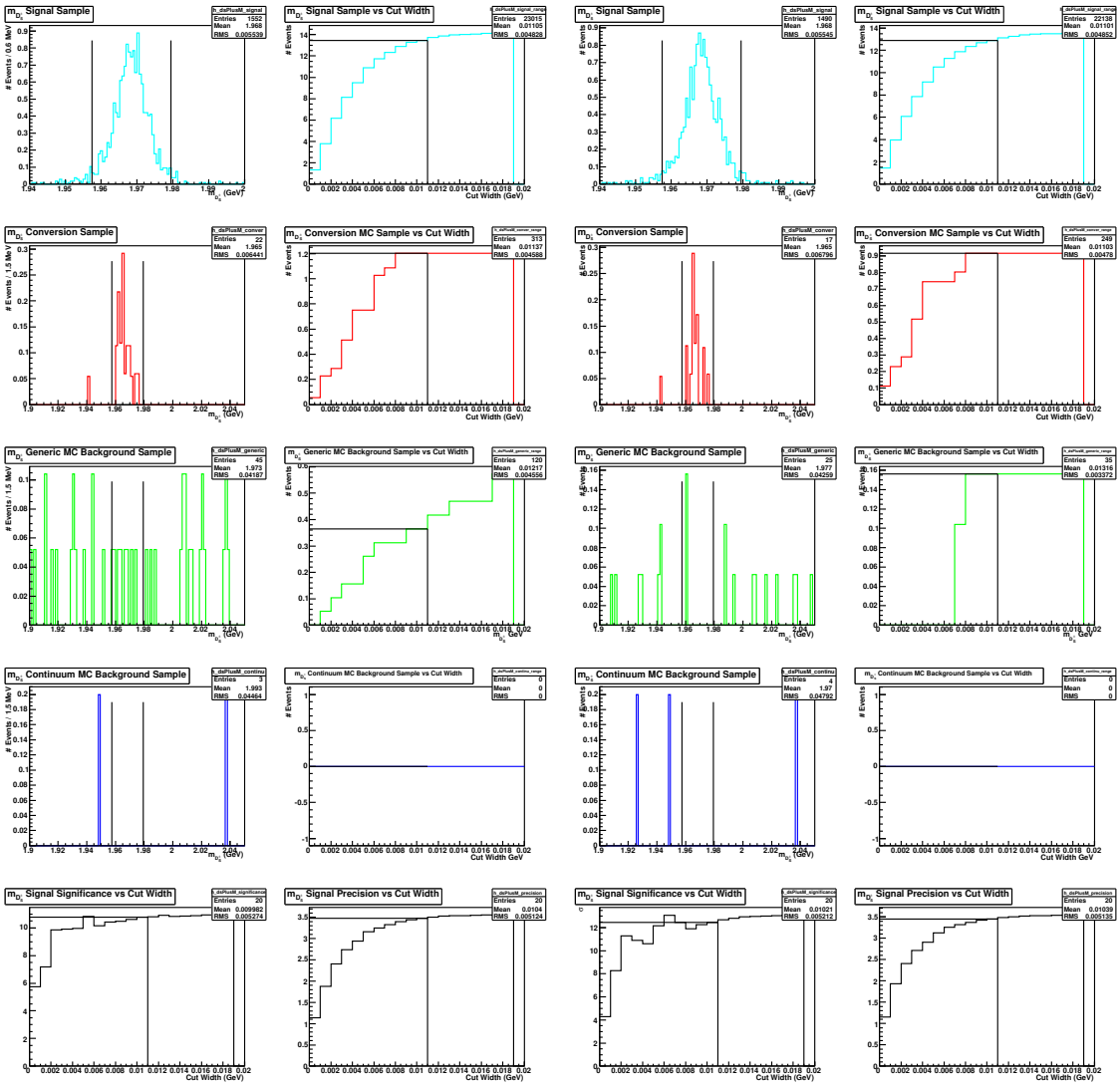

Figure 100: Optimization plots for the $m_{D_s^+}$ selection criterion in the $D_s^+ \to K^+K^-\pi^+$ decay mode for electron-fitted data.

Figure 101: Optimization plots for the $m_{D_s^+}$ selection criterion in the $D_s^+ \to K^+K^-\pi^+$ decay mode for electron-fitted data where all tracks in the event have been vertex constrained to a single point.

Optimization plots for the m_{BC} selection criterion in the $D_s^+ \to K^+K^-\pi^+$ decay mode having applied all other selection criteria. All plots are normalized to 586 pb^{-1} of data. Plots on the figure to the left correspond to simple electron-fitted samples. Plots on the figures to the right correspond to electron-fitted samples where all daughters of the D_s^{*+} have been vertex constrained to originate from a single point.

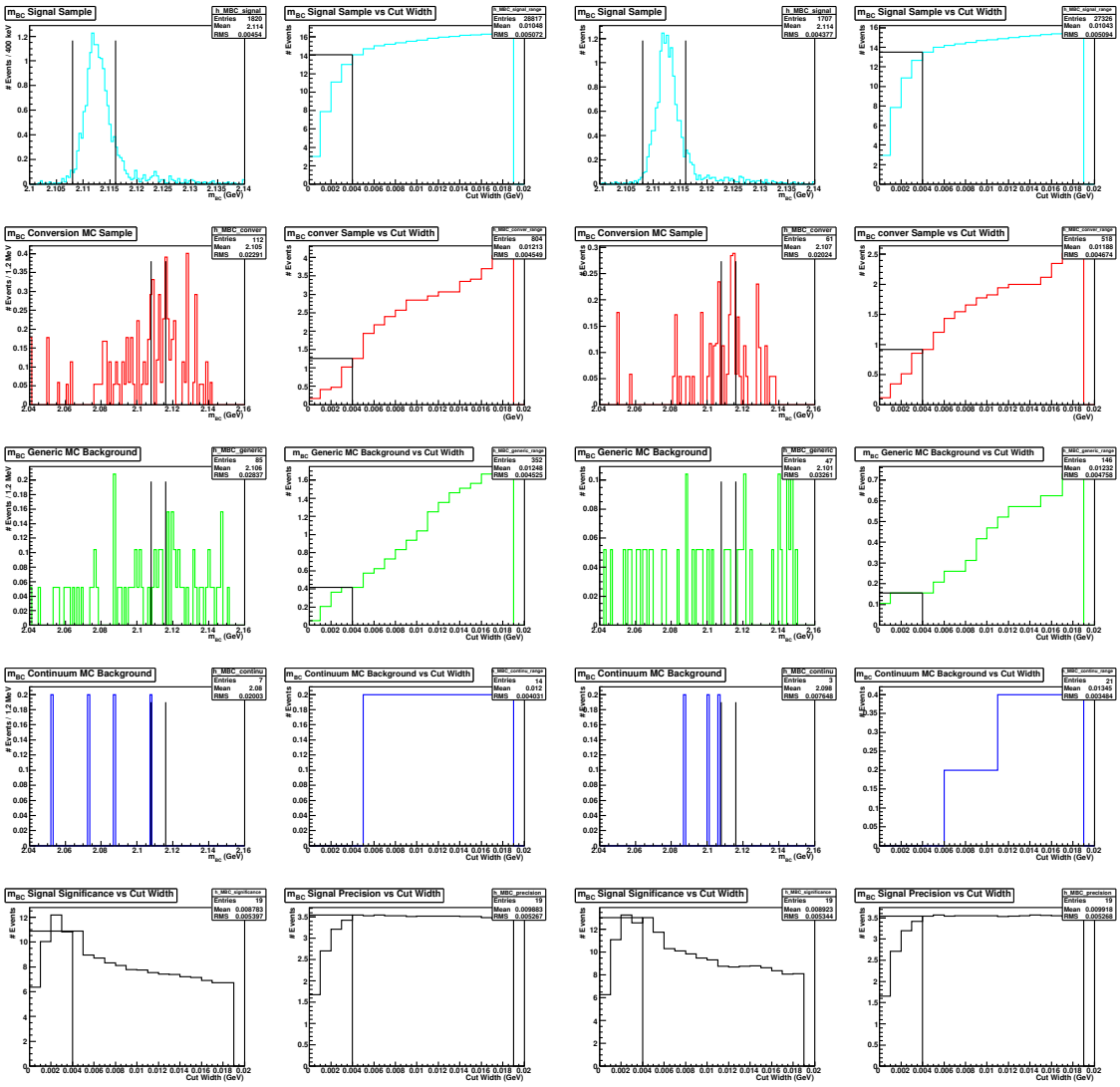

Figure 102: Optimization plots for the m_{BC} selection criterion in the $D_s^+ \to K^+K^-\pi^+$ decay mode for electron-fitted data.

Figure 103: Optimization plots for the m_{BC} selection criterion in the $D_s^+ \to K^+K^-\pi^+$ decay mode for electron-fitted data where all tracks in the event have been vertex constrained to a single point.

Optimization plots for the δm selection criterion in the $D_s^+ \to K^+K^-\pi^+$ decay mode having applied all other selection criteria. All plots are normalized to 586 pb^{-1} of data. Plots on the figure to the left correspond to simple electron-fitted samples. Plots on the figures to the right correspond to electron-fitted samples where all daughters of the D_s^{*+} have been vertex constrained to originate from a single point.

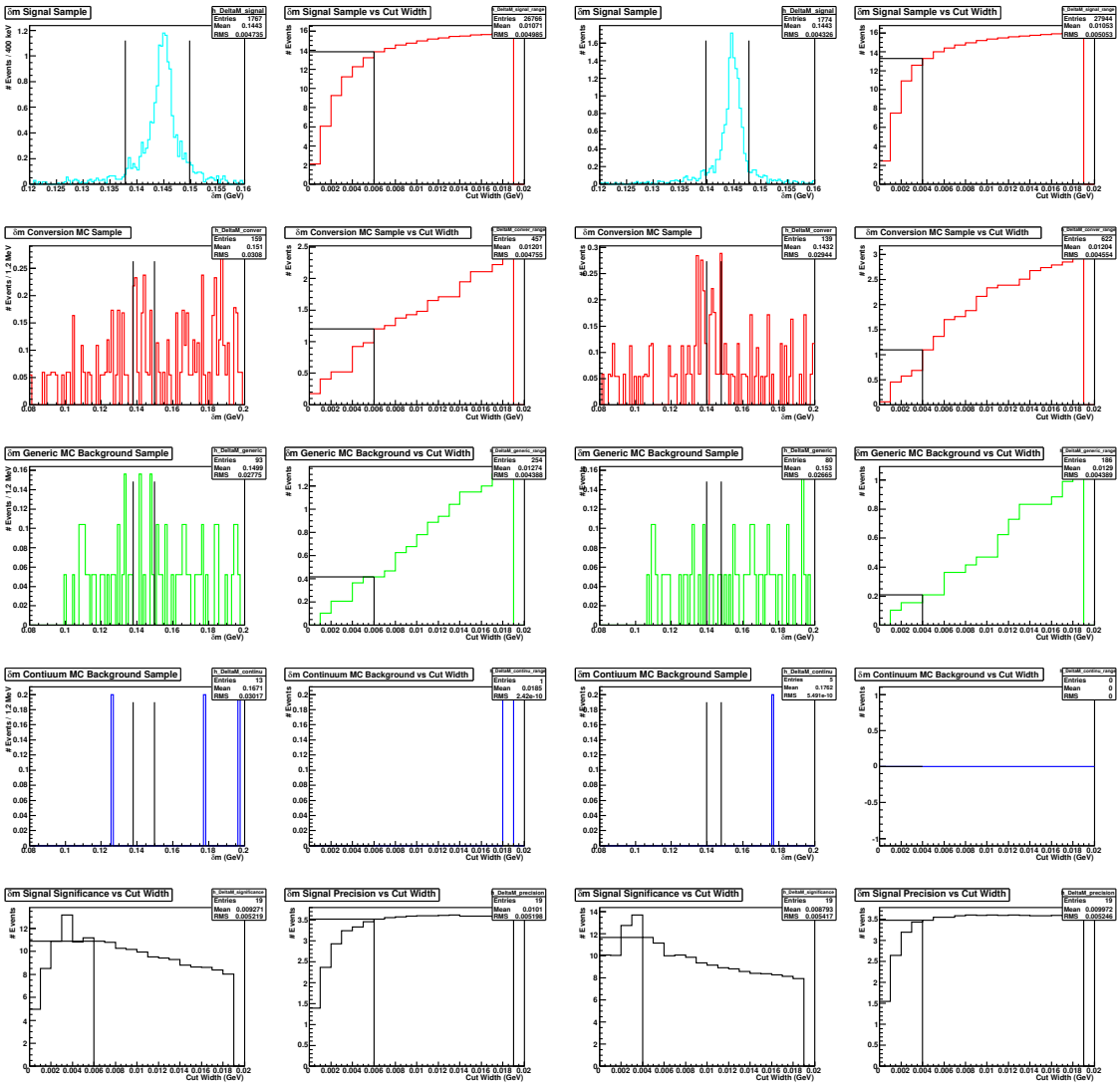

Figure 104: Optimization plots for the δm selection criterion in the $D_s^+ \to K^+K^-\pi^+$ decay mode for electron-fitted data.

Figure 105: Optimization plots for the δm selection criterion in the $D_s^+ \to K^+K^-\pi^+$ decay mode for electron-fitted data where all tracks in the event have been vertex constrained to a single point.

Optimization plots for the Δd_0 selection criterion in the $D_s^+ \to K^+K^-\pi^+$ decay mode having applied all other selection criteria. All plots are normalized to 586 pb^{-1} of data. Plots on the figure to the left correspond to simple electron-fitted samples. Plots on the figures to the right correspond to electron-fitted samples where all daughters of the D_s^{*+} have been vertex constrained to originate from a single point.

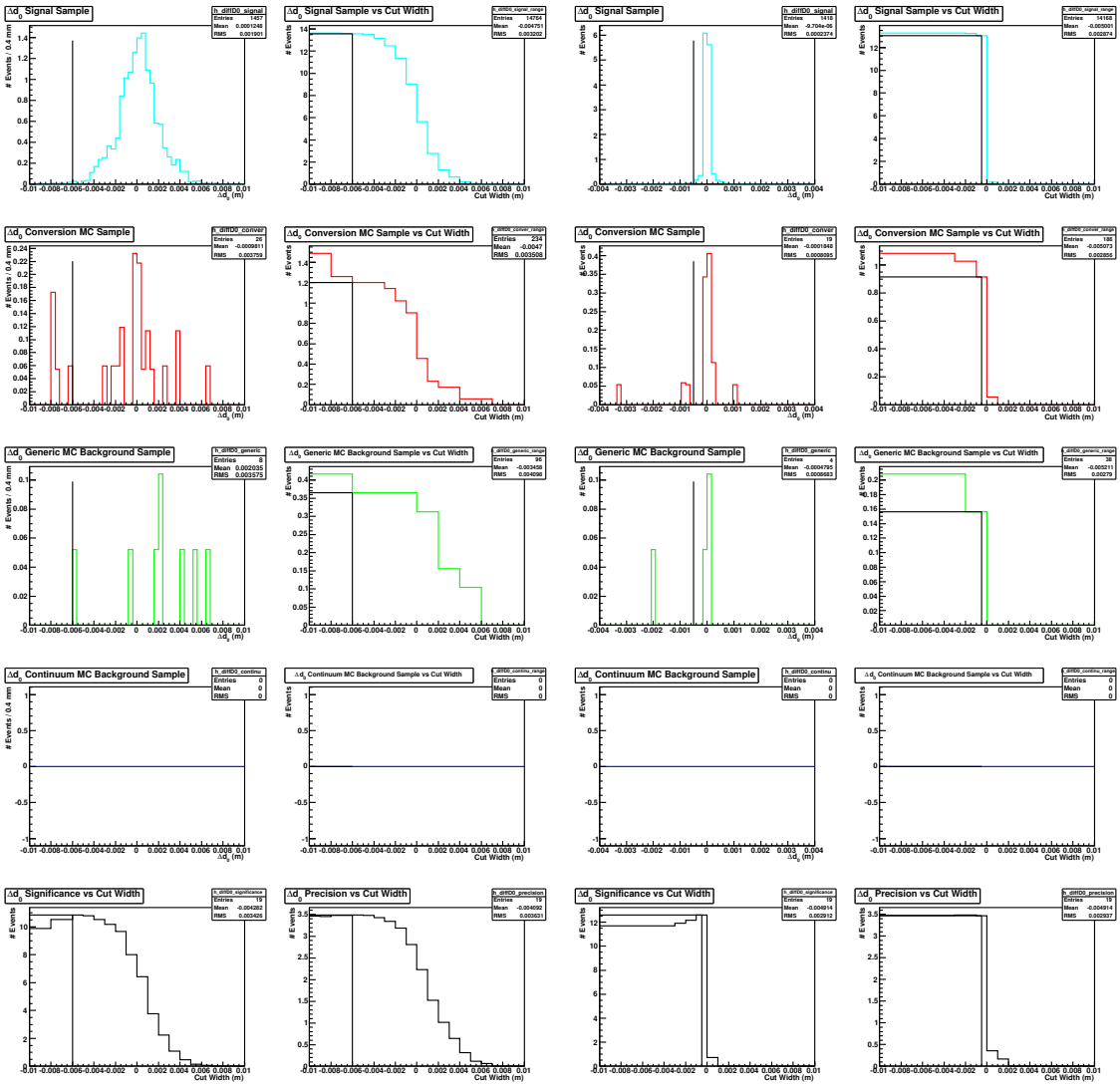

Figure 106: Optimization plots for the Δd_0 selection criterion in the $D_s^+ \to K^+K^-\pi^+$ decay mode for electron-fitted data.

Figure 107: Optimization plots for the Δd_0 selection criterion in the $D_s^+ \to K^+K^-\pi^+$ decay mode for electron-fitted data where all tracks in the event have been vertex constrained to a single point.

Optimization plots for the $\Delta\phi_0$ selection criterion in the $D_s^+ \to K^+K^-\pi^+$ decay mode having applied all other selection criteria. All plots are normalized to 586 pb^{-1} of data. Plots on the figure to the left correspond to simple electron-fitted samples. Plots on the figures to the right correspond to electron-fitted samples where all daughters of the D_s^{*+} have been vertex constrained to originate from a single point.

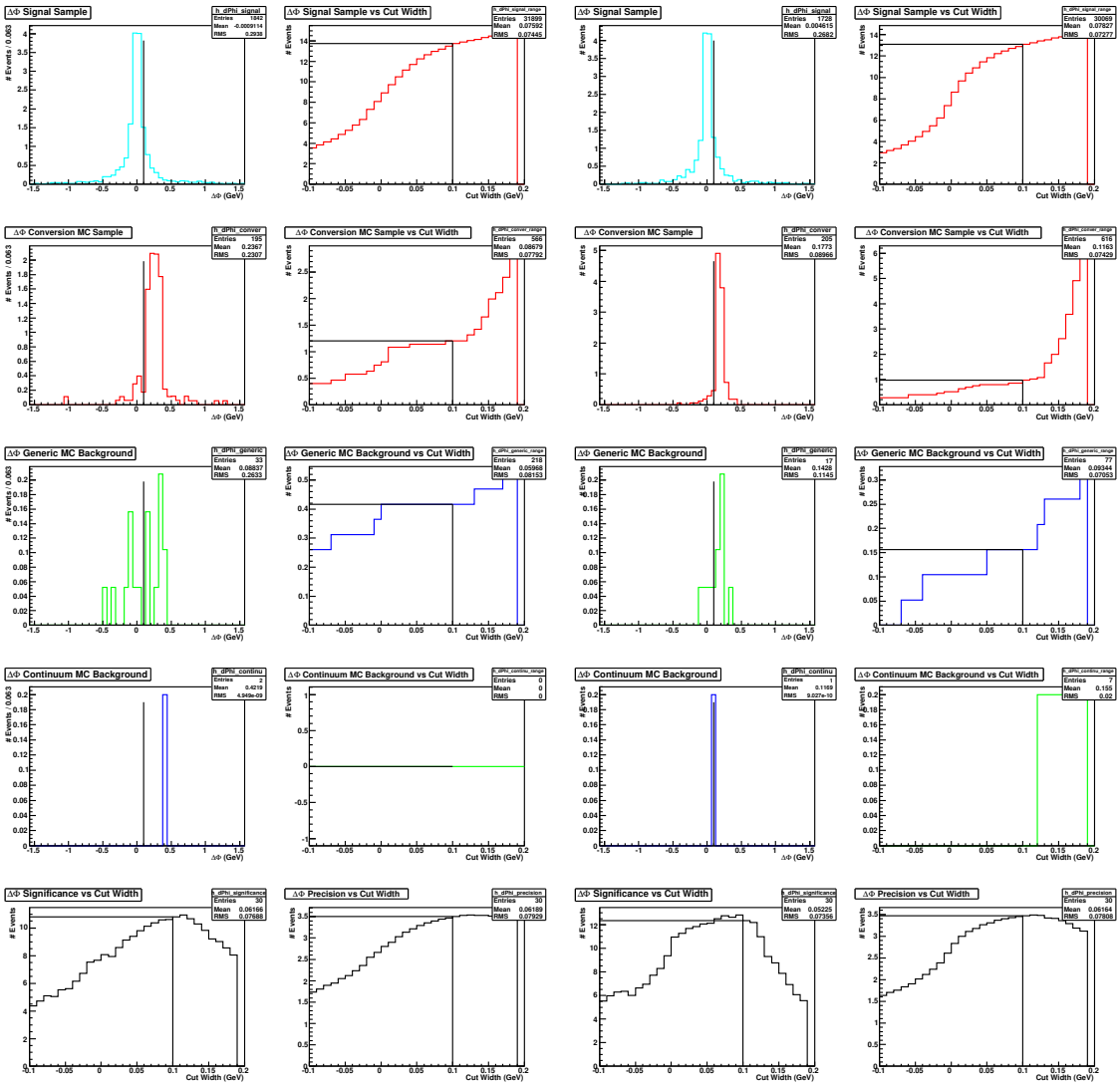

Figure 108: Optimization plots for the $\Delta\phi_0$ selection criterion in the $D_s^+ \to K^+K^-\pi^+$ decay mode for electron-fitted data.

Figure 109: Optimization plots for the $\Delta\phi_0$ selection criterion in the $D_s^+ \to K^+K^-\pi^+$ decay mode for electron-fitted data where all tracks in the event have been vertex constrained to a single point.

Table 24: Number of signal and background events expected in electron-fitted data with and without vertex fitting of tracks from the D_s^{*+} in the $D_s^+ \to K^+K^-\pi^+$ decay mode.

Expected Number of Events in 586 pb^{-1}	Electron-Fitted Samples and Criteria	Vertex-Fitted, Electron-Fitted Samples and Criteria
Signal ($N_Signal Events$)	13.36	12.84
Conversion Background	1.04	0.92
Generic Background (without Conversions in e-fit)	0.42	0.16
Continuum Background	0.00	0.00
Total Background ($N_Background Events$)	1.45	1.07
$\frac{N_Signal Events}{\sqrt{N_Background Events}}$	11.1	12.4

in the invariant mass m_{ee} at 13 MeV with a width of ~ 8 MeV as seen in Fig. 110. Having predominantly conversion events fall in this peak, we may now ask if rejecting these events offers us a higher overall signal significance than the application of $\Delta\phi_0$ and Δd_0 criteria. Table 25 summarizes the selection criteria for electron-fitted data with vertex fitting of tracks from the D_s^{*+} in the $D_s^+ \to K^+K^-\pi^+$ decay mode, with and without a replacement of Δd_0 and $\Delta\phi_0$ cuts by an m_{ee} cut. We accept events with the criterion: $|m_{ee} - 0.013| > 0.005 GeV$ in order to retain roughly similar signal yields. A comparison of the signal significance is presented in Table 26. Figure 110 depicts the distributions of m_{ee} in signal and background Monte Carlo samples without the vertex constraint, after all selection criteria for electron-fitted data we optimized in Section 10.1 have been applied to them. Figure 111 depicts the same distributions, but with the vertex constraint and without having applied the Δd_0 and $\Delta\phi_0$ selection criteria.

Table 25: Selection criteria for electron-fitted data with vertex fitting of tracks from the D_s^{*+} in the $D_s^+ \to K^+K^-\pi^+$ decay mode, with and without a replacement of Δd_0 and $\Delta\phi_0$ cuts by an m_{ee} cut.

Selection Criterion	D_s^{*+} Tracks Vertex-Fitted Samples Cut Center ± Width	D_s^{*+} Tracks Vertex-Fitted Samples with m_{ee} Cut Cut Center ± Width
$m_{D_s^+}$	1.969 ± 0.011 GeV	1.969 ± 0.011 GeV
m_{BC}	2.112 ± 0.004 GeV	2.112 ± 0.004 GeV
δm	0.144 ± 0.004 GeV	0.144 ± 0.004 GeV
Δd_0	-0.0005 m	
$\Delta\phi_0$	0.1	
m_{ee}		0.013 ± 0.005 GeV

Having thus established that rejecting conversion events based on the m_{ee} after vertex constraining does not fare better than the $\Delta\phi_0$ and Δd_0 selection criteria, we may ask whether it can significantly improve upon the latter. The distribution of m_{ee} after vertex constraining and all criteria is presented in Fig. 112. The results of such a comparison is presented in Table 27. We see that the signal significance doesn't improve much in spite of an 22% loss in the signal yield.

Studying the distribution of m_{ee} against χ^2 in Fig. 113, it seemed that one could also reject conversion background events by requiring $0 < \chi^2 < 11$. Doing so, we obtained the plot of m_{ee} shown in Fig. 114. Now we applied the criterion $|m_{ee} - 0.010| > 0.002$

Table 26: Number of signal and background events expected in electron-fitted samples with vertex fitting of tracks from the D_s^{*+} in the $D_s^+ \to K^+K^-\pi^+$ decay mode, with and without a replacement of Δd_0 and $\Delta\phi_0$ cuts by an m_{ee} cut.

Expected Number of Events in 586 pb^{-1}	D_s^{*+} Tracks Vertex-Fitted Samples and Criteria	D_s^{*+} Tracks Vertex-Fitted Samples with m_{ee} Cut without Δd_0 & $\Delta\phi_0$ Criteria
Signal ($N_S ignalEvents$)	12.84	12.68
Conversion Background	0.92	3.00
Generic Background (without Conversions in e-fit)	0.16	0.68
Continuum Background	0.00	0.2
Total Background ($N_B ackgroundEvents$)	1.07	3.88
$\frac{N_S ignalEvents}{\sqrt{N_B ackgroundEvents}}$	12.4	6.4

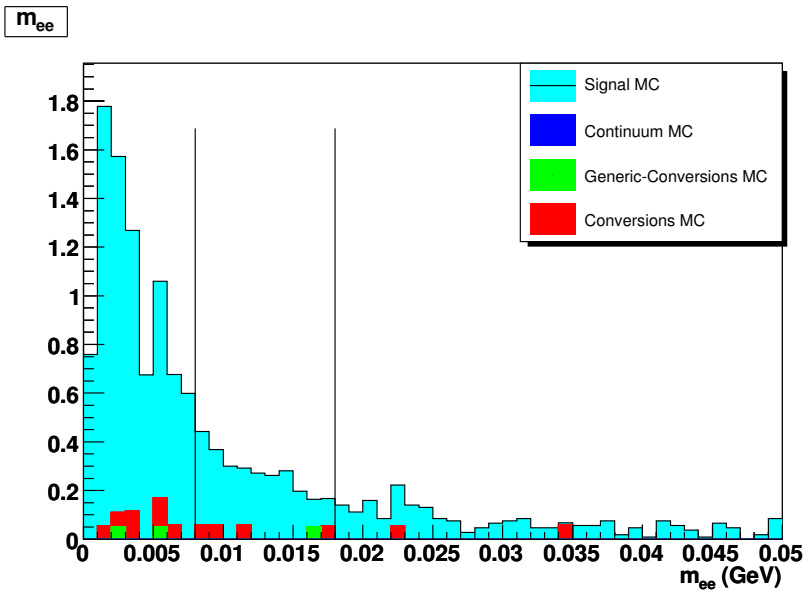

Figure 110: Distributions of the invariant mass of the e^+e^- pair after all selection criteria for electron-fitted data, optimized in Section 10.1, have been applied to the signal and various background Monte Carlo samples.

GeV to reject the peak in the conversion backgrounds. We obtained the signal yields and significances tabulated in Table 28. We conclude that such upper limits on the χ^2 does not help much either.

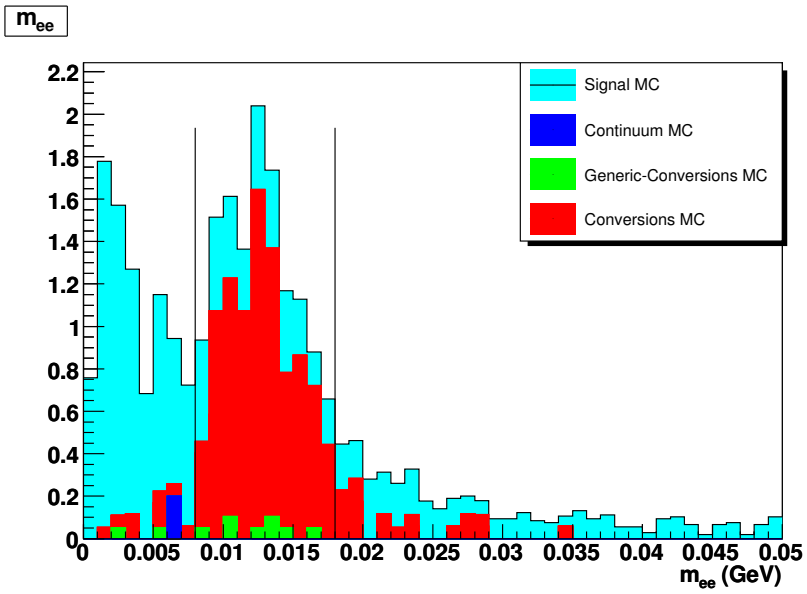

Figure 111: Distributions of the invariant mass of the e^+e^- pair where the daughters of the D_s^{*+} have been vertex constrained as described in the text. $\Delta\phi_0$ and Δd_0 cuts on the electrons have not been applied. Slightly different selection criteria, optimized for vertex constrained kinematic distributions as outlined in the text, are applied. Events within the marked region of m_{ee} are rejected.

Table 27: A comparison of signal and background events between samples with plain electron-fitted tracks, samples with the regular selection criteria optimized for vertex-fitted tracks and vertex-fitted samples where m_{ee} criteria have been added to the regular criteria.

Expected Number of Events in 586 pb^{-1}	Plain Electron-Fitted Samples with All Criteria	Vertex-Fitted Samples with All Criteria	Vertex-Fitted Samples with m_{ee} Cut and All Other Criteria
Signal ($N_SignalEvents$)	13.36	12.84	9.97
Conversion Background	1.04	0.92	0.69
Generic Background (without Conversions in e-fit)	0.42	0.16	0.10
Continuum Background	0.0	0.0	0.0
Total Background ($N_BackgroundEvents$)	1.45	1.07	0.79
$\frac{N_SignalEvents}{\sqrt{N_BackgroundEvents}}$	11.1	12.4	11.21

Table 28: Number of signal and background events expected in electron-fitted samples with vertex fitting of tracks from the D_s^{*+} in the $D_s^+ \to K^+K^-\pi^+$ decay mode, with and without a replacement of Δd_0 and $\Delta\phi_0$ cuts by an m_{ee} cut.

Expected Number of Events in 586 pb^{-1}	D_s^{*+} Tracks Vertex-Fitted Samples and Criteria	D_s^{*+} Tracks Vertex-Fitted Samples with m_{ee} Cut without Δd_0 & $\Delta\phi_0$ Criteria	D_s^{*+} Tracks Vertex-Fitted with $\chi^2 < 11$ m_{ee} Cut and without Δd_0 & $\Delta\phi_0$ criteria
Signal ($N_SignalEvents$)	12.84	12.68	7.48
Conversion Background	0.92	3.00	0.90
Generic Background (without Conversions in e-fit)	0.16	0.68	0.47
Continuum Background	0.00	0.2	0.0
Total Background ($N_BackgroundEvents$)	1.07	3.88	1.37
$\frac{N_SignalEvents}{\sqrt{N_BackgroundEvents}}$	12.4	6.4	6.4

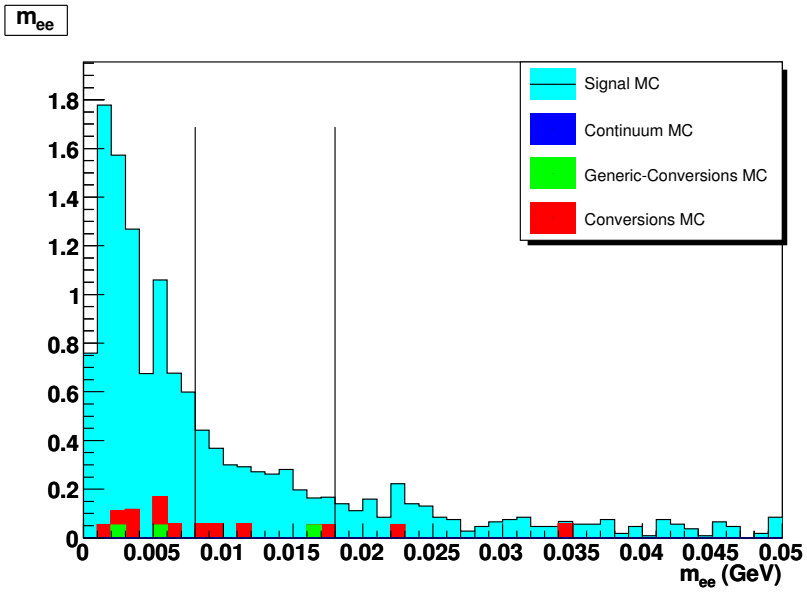

Figure 112: Distributions of the invariant mass of the e^+e^- pair where the daughters of the D_s^{*+} have been vertex constrained and all standard selection criteria applied. Events within the marked region of m_{ee} are rejected as part of the m_{ee} selection criterion.

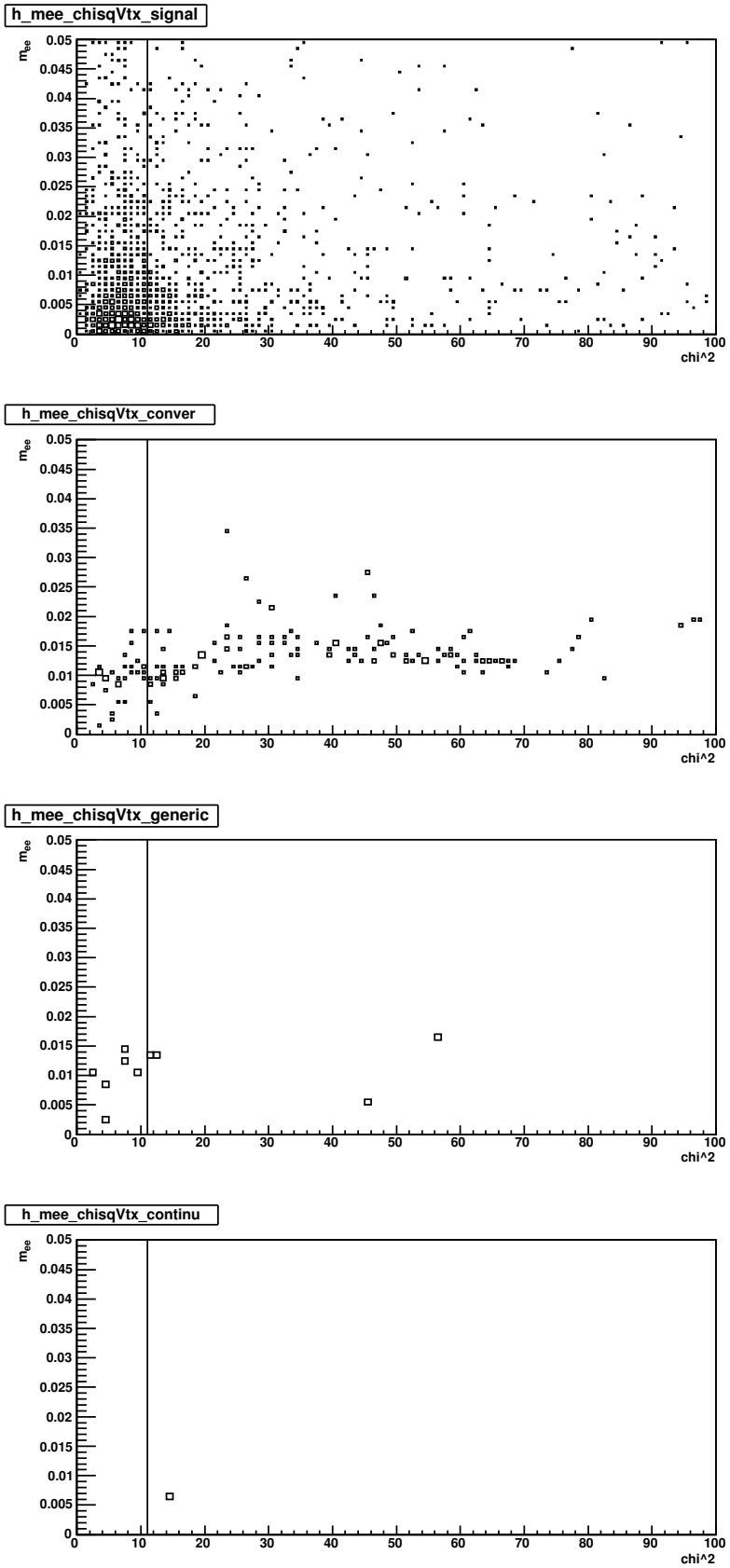

Figure 113: m_{ee} vs χ^2 for signal, conversion and generic Monte Carlo samples after all kinematic criteria, i.e. all except the $\Delta\phi_0$ and Δd_0 selection criteria, have been applied.

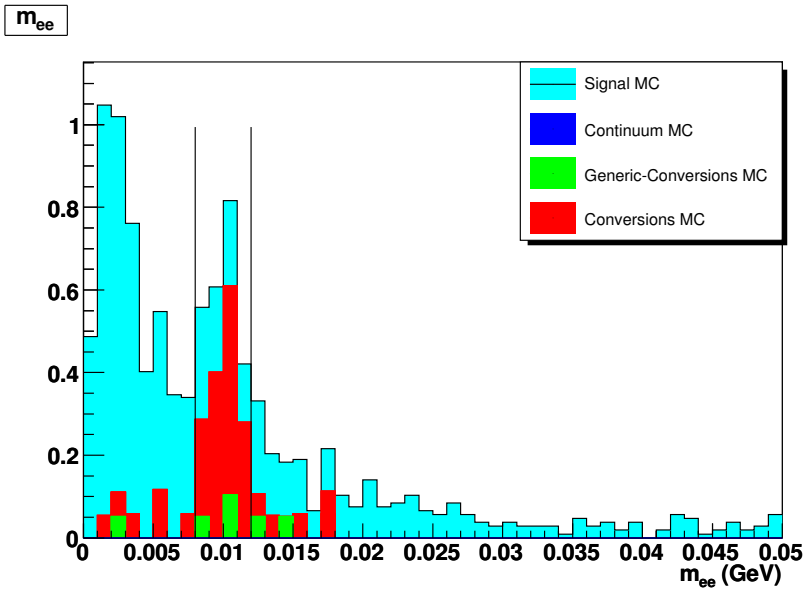

Figure 114: Distributions of the invariant mass of the e^+e^- pair where the daughters of the D_s^{*+} have been vertex constrained and all standard selection criteria applied. Events within the marked region of m_{ee} are rejected as part of the m_{ee} selection criterion.

11.2 Vertex Fitting e^+e^- Tracks

We may ask if the power of the Δd_0 and $\Delta\phi_0$ may be significantly improved by vertex constraining the e^+e^- tracks. Fig. 115 and 116 show the distributions of the Δd_0 and $\Delta\phi_0$ having vertex-fitted the e^+e^- pair for the signal and background Monte Carlo samples. They are to be compared with Fig. 106 and 108. The optimal parameters for the selection criteria are:

$$
\begin{aligned}
|m_{D_s^+} - 1.969| &< 0.011 GeV \\
|m_{BC} - 2.112| &< 0.004 GeV \\
|\delta m - 0.1438| &< 0.006 GeV \\
\Delta d_0 &> -0.006 m \\
\Delta\phi &< 0.1
\end{aligned}
$$

A comparison with the selection criteria without vertex-fitting is presented in Table 29. It is quite clear that this does not help in improving our signal significance or yield.

Table 29: Number of signal and background events expected in plain electron-fitted samples and samples where the electron-fitted e^+e^- tracks have been constrained to a common vertex.

Expected Number of Events in 586 pb^{-1}	Plain Electron-Fitted Samples with All Criteria	e^+e^- Vertex-Fitted Samples with All Criteria
Signal ($N_SignalEvents$)	13.36	8.31
Conversion Background	1.04	0.75
Generic Background (without Conversions in e-fit)	0.42	0.26
Continuum Background	0.0	0.0
Total Background ($N_BackgroundEvents$)	1.45	1.01
$\frac{N_SignalEvents}{\sqrt{N_BackgroundEvents}}$	11.1	8.29

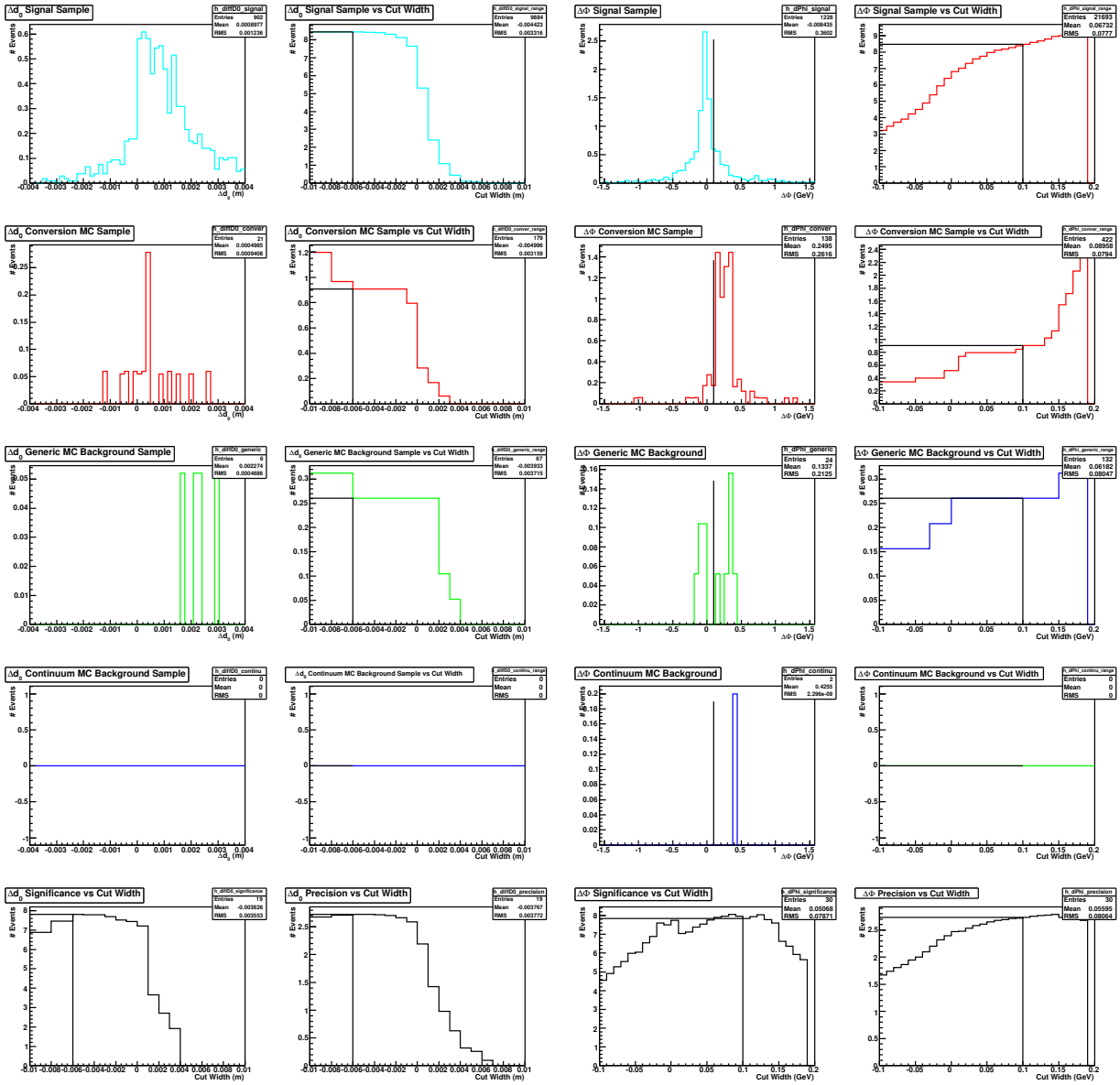

Figure 115: Optimization plots for the Δd_0 selection criterion in the $D_s^+ \to K^+K^-\pi^+$ decay mode for electron-fitted data where the candidate e^+e^- tracks in the event have been vertex constrained to a single point.

Figure 116: Optimization plots for the $\Delta\phi_0$ selection criterion in the $D_s^+ \to K^+K^-\pi^+$ decay mode for electron-fitted data where the candidate e^+e^- tracks in the event have been vertex constrained to a single point.

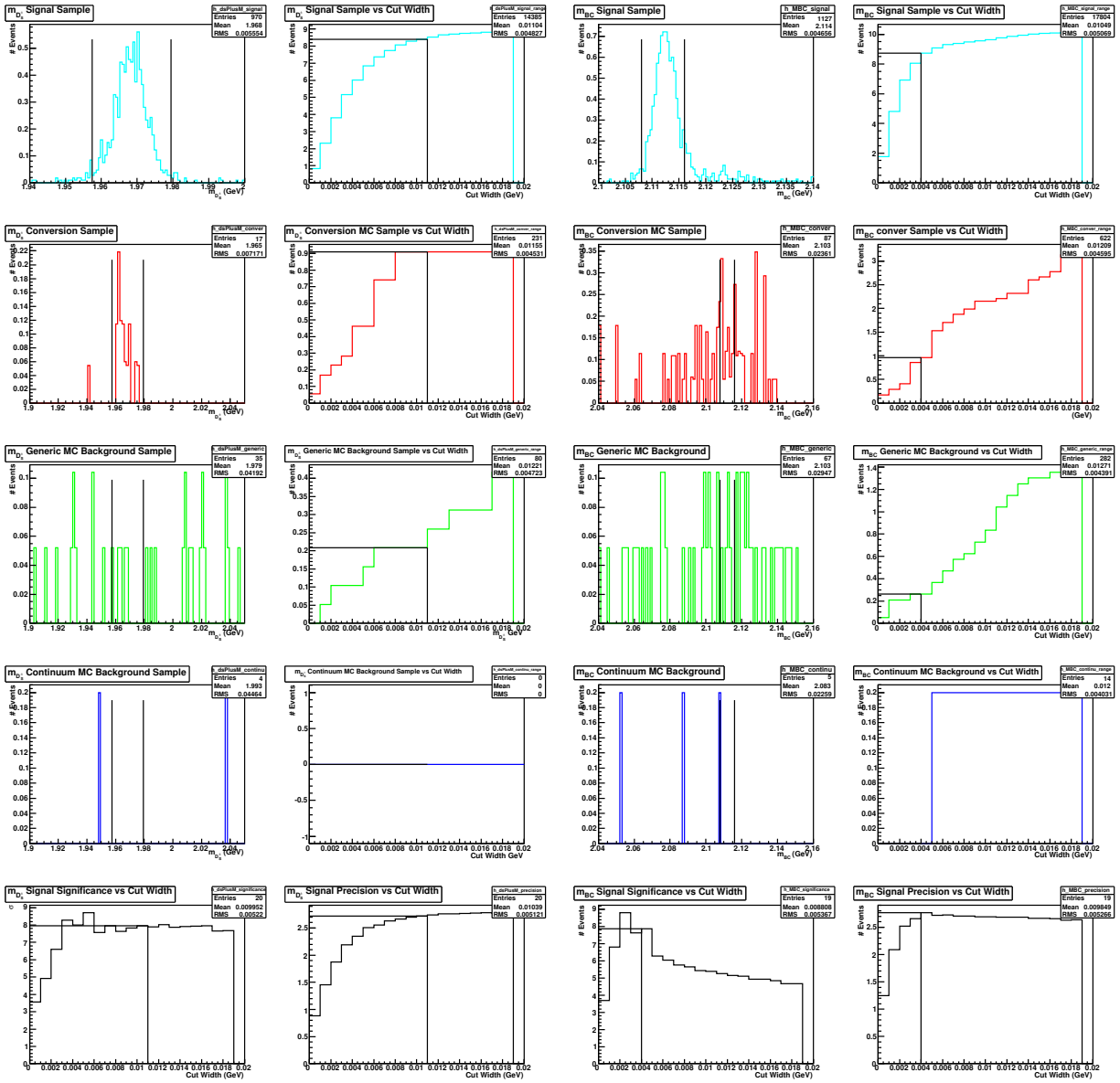

Figure 117: Optimization plots for the $m_{D_s^+}$ selection criterion in the $D_s^+ \to K^+K^-\pi^+$ decay mode for electron-fitted data where the candidate e^+e^- tracks in the event have been vertex constrained to a single point.

Figure 118: Optimization plots for the m_{BC} selection criterion in the $D_s^+ \to K^+K^-\pi^+$ decay mode for electron-fitted data where the candidate e^+e^- tracks in the event have been vertex constrained to a single point.

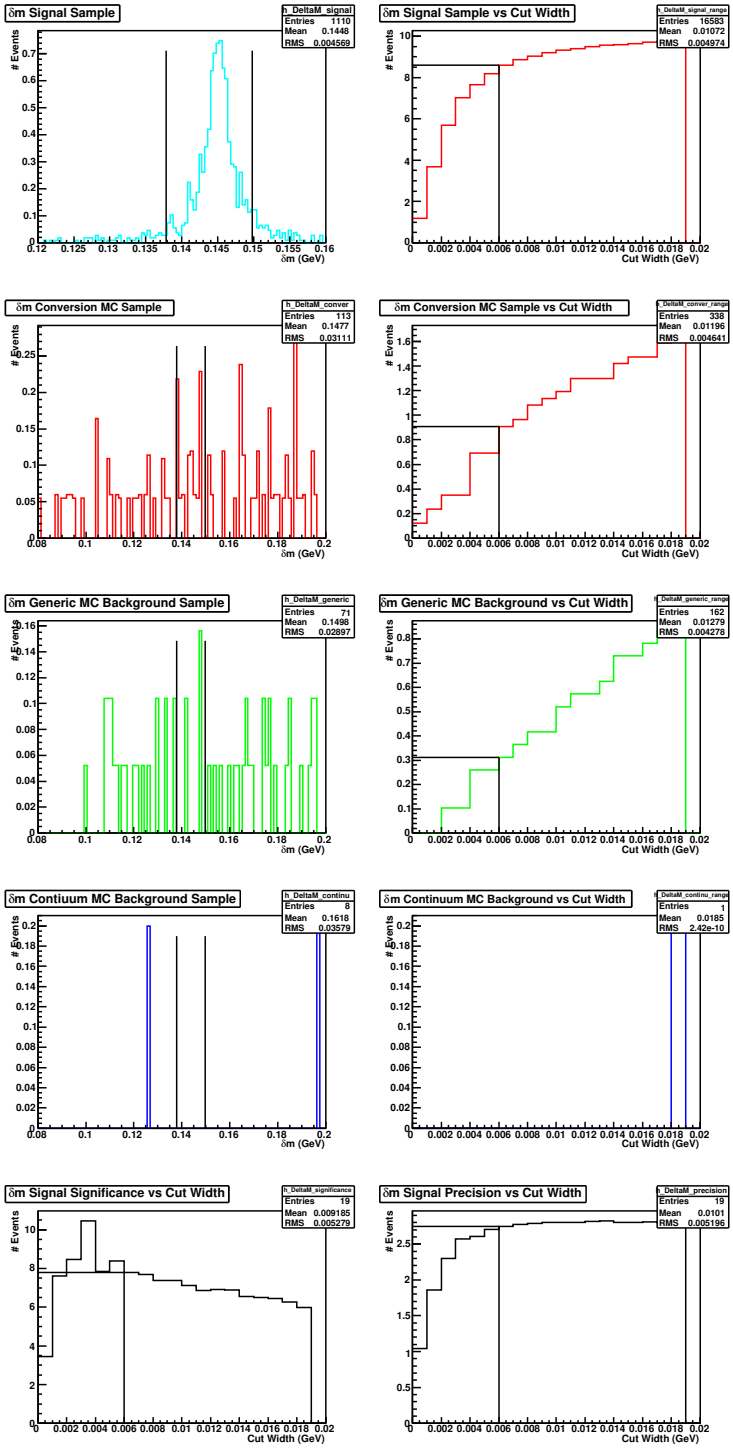

Figure 119: Optimization plots for the δm selection criterion in the $D_s^+ \to K^+K^-\pi^+$ decay mode for electron-fitted data where the candidate e^+e^- tracks in the event have been vertex constrained to a single point.

11.3 Vertex Fitted Tracks with the Beamspot

In this section, we include the beamspot in our vertex constraints. For every event, we create a fit where all daughters of the D_s^{*+} and the beampot are constrained to a vertex, and a fit where all daughters of the D_s^+ and the beamspot are constrained to a vertex. The Δd_0 and $\Delta\phi_0$ cuts are not applied as we are trying to see if our new scheme can replace them. The difference in the reduced χ^2, defined below, between the two fits are plotted in Fig. 120.

$$\chi^2_{red} = \chi^2/n$$

where n stands for the number of degrees of freedom in the fit. This difference allows us to discard clearly problematic fits, and looking at the distributions in Fig. 120 we choose to keep fits with values of χ^2_{red} between -4 and 1.5.

We optimize our selection criteria according to Fig. 121 - 125. The optimized selection criteria are tabulated in Table 30. Now we plot the invariant mass m_{ee} from the first vertex fit as shown in Fig. 126. In our rejection cut, we try to keep the signal yield roughly the same as the signal yield with vertexing just the daughters of the D_s^{*+} without the beamspot and compare the signal significance in Table 31.

Table 30: Selection criteria for electron-fitted data with vertex fitting of tracks from the D_s^{*+} and the beamspot, with a replacement of Δd_0 and $\Delta\phi_0$ cuts by $\delta\chi^2_{red}$ and m_{ee} cuts.

Selection Criterion	Beamspot-Vertex-Fitted Samples with m_{ee} replacing Δd_0 & $\Delta\phi_0$
$m_{D_s^+}$	1.969 ± 0.011 GeV
m_{BC}	2.112 ± 0.004 GeV
δm	0.144 ± 0.004 GeV
$\delta\chi^2_{red}$	0 ± 4
m_{ee}	0.013 ± 0.003 GeV

Table 31: Number of signal and background events expected with plain electron-fitted samples, and samples with vertex fitting of tracks from the D_s^{*+} and the beamspot, with a replacement of Δd_0 and $\Delta\phi_0$ cuts by $\delta\chi^2_{red}$ and m_{ee} cuts.

Expected Number of Events in 586 pb^{-1}	Plain Electron-Fitted Samples with All Criteria	Vertex-Fitted Samples with All Criteria	Beamspot-Vertex-Fitted Samples with m_{ee} replacing Δd_0 & $\Delta\phi_0$
Signal ($N_SignalEvents$)	13.36	12.84	12.45
Conversion Background	1.04	0.92	2.13
Generic Background (without Conversions in e-fit)	0.42	0.16	0.73
Continuum Background	0.0	0.0	0.2
Total Background ($N_BackgroundEvents$)	1.45	1.07	3.06
$\frac{N_SignalEvents}{\sqrt{N_BackgroundEvents}}$	11.1	12.4	7.1

Now, we may also ask if our $\delta\chi^2_{red}$ and m_{ee} cuts can help in addition to our Δd_0 and $\Delta\phi_0$ cuts. Fig. 127 presents the distribution of m_{ee} after having applied all the standard selection criteria, including $\Delta d_0 > -0.0005$ and $\Delta\phi_0 < 0.1$ as suggested by the optimization plots in Fig. 124 and 125. It seems clear than not much improvement can be achieved on the signal significance.

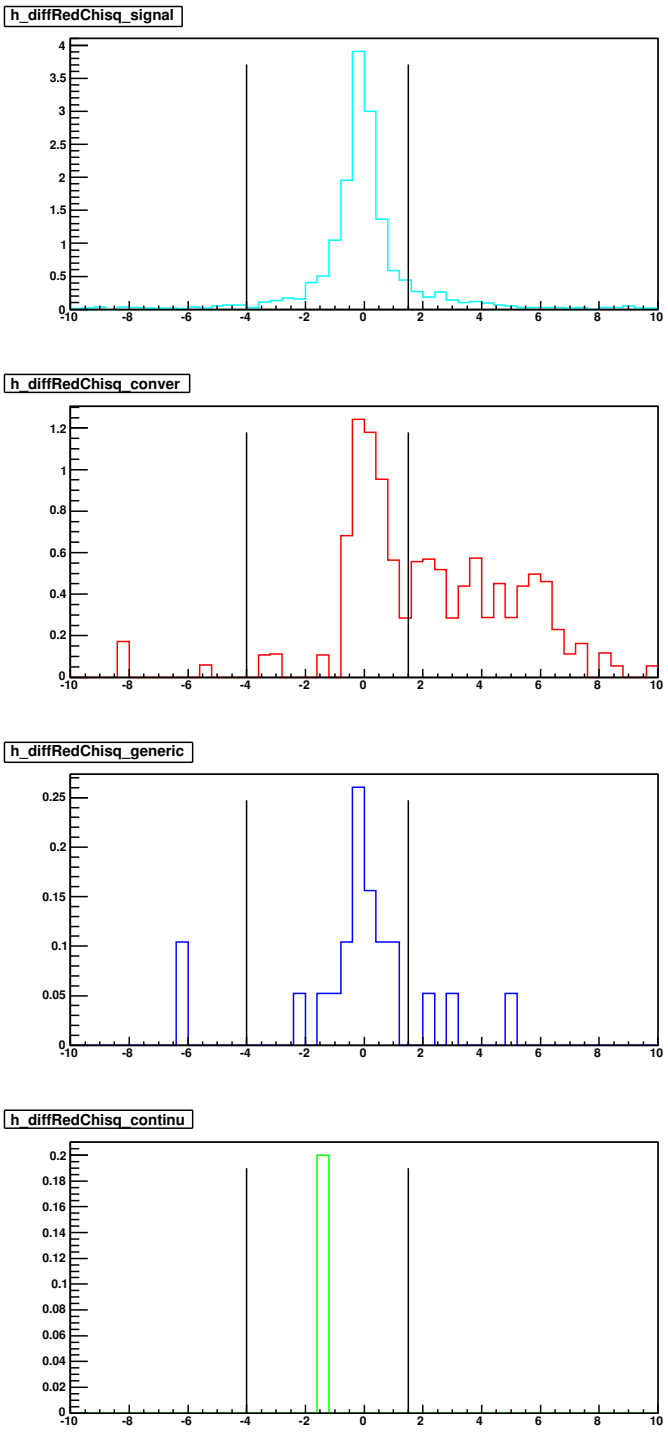

Figure 120: The difference in χ^2_{red} between the vertex fit with all D_s^{*+} tracks and the beamspot and the vertex fit with just the D_s^+ tracks and the beamspot. The top plot is the signal MC, the second is the conversion MC, the third is the generic MC with conversions excluded, and the lowest plot is the continuum MC.

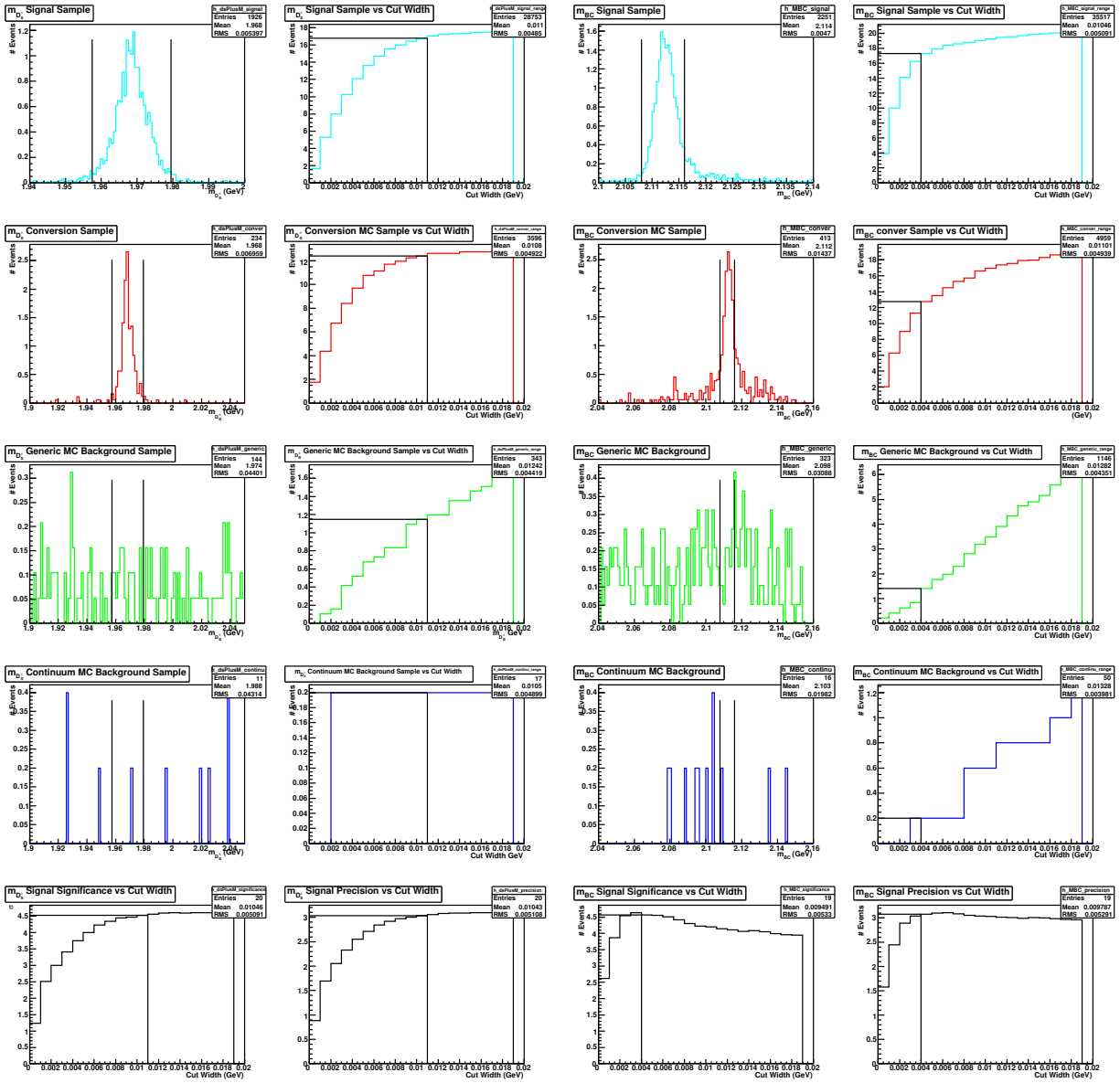

Figure 121: Optimization plots for the $m_{D_s^+}$ selection criterion in the $D_s^+ \to K^+K^-\pi^+$ decay mode for electron-fitted data where all tracks from the D_s^{*+} have been vertex constrained with the beamspot.

Figure 122: Optimization plots for the m_{BC} selection criterion in the $D_s^+ \to K^+K^-\pi^+$ decay mode for electron-fitted data where all tracks from the D_s^{*+} have been vertex constrained with the beamspot.

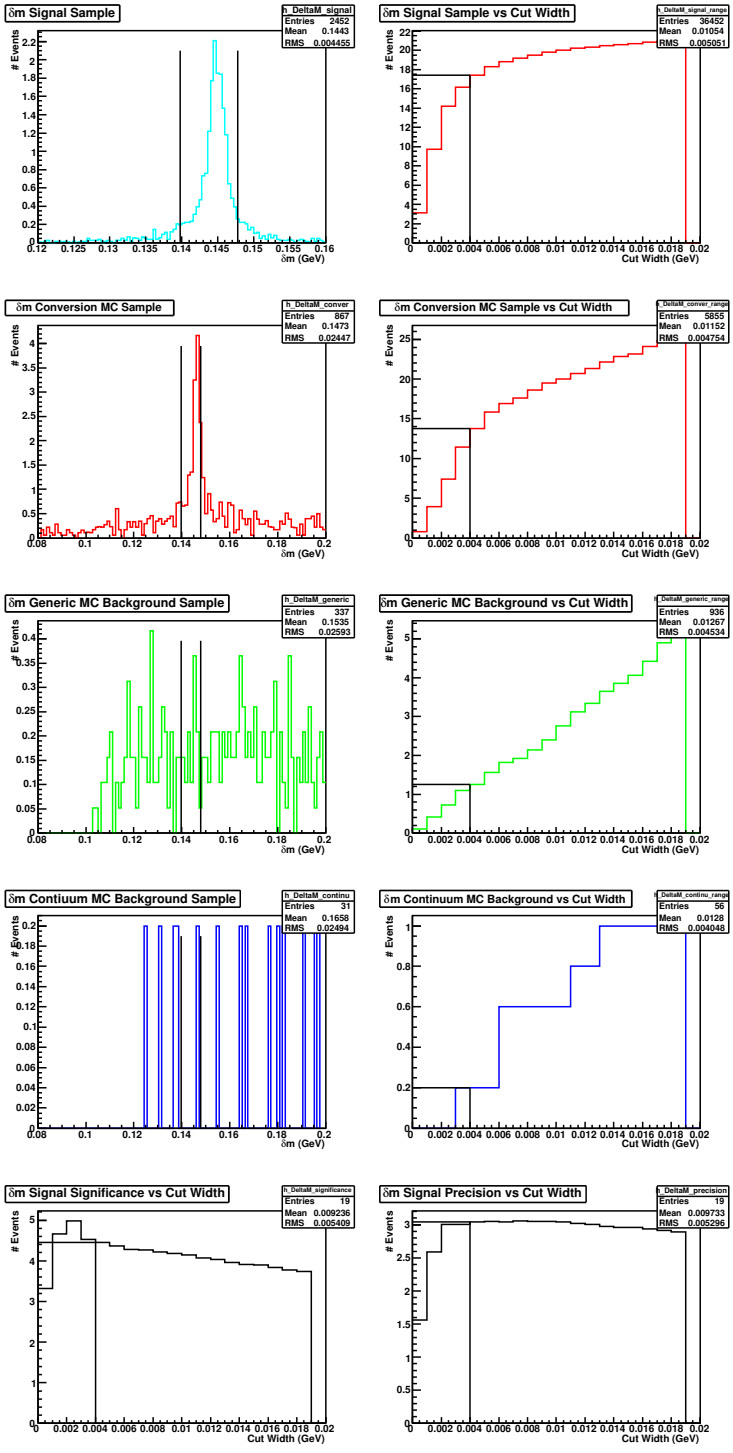

Figure 123: Optimization plots for the δm selection criterion in the $D_s^+ \to K^+K^-\pi^+$ decay mode for electron-fitted data where all tracks from the D_s^{*+} have been vertex constrained with the beamspot.

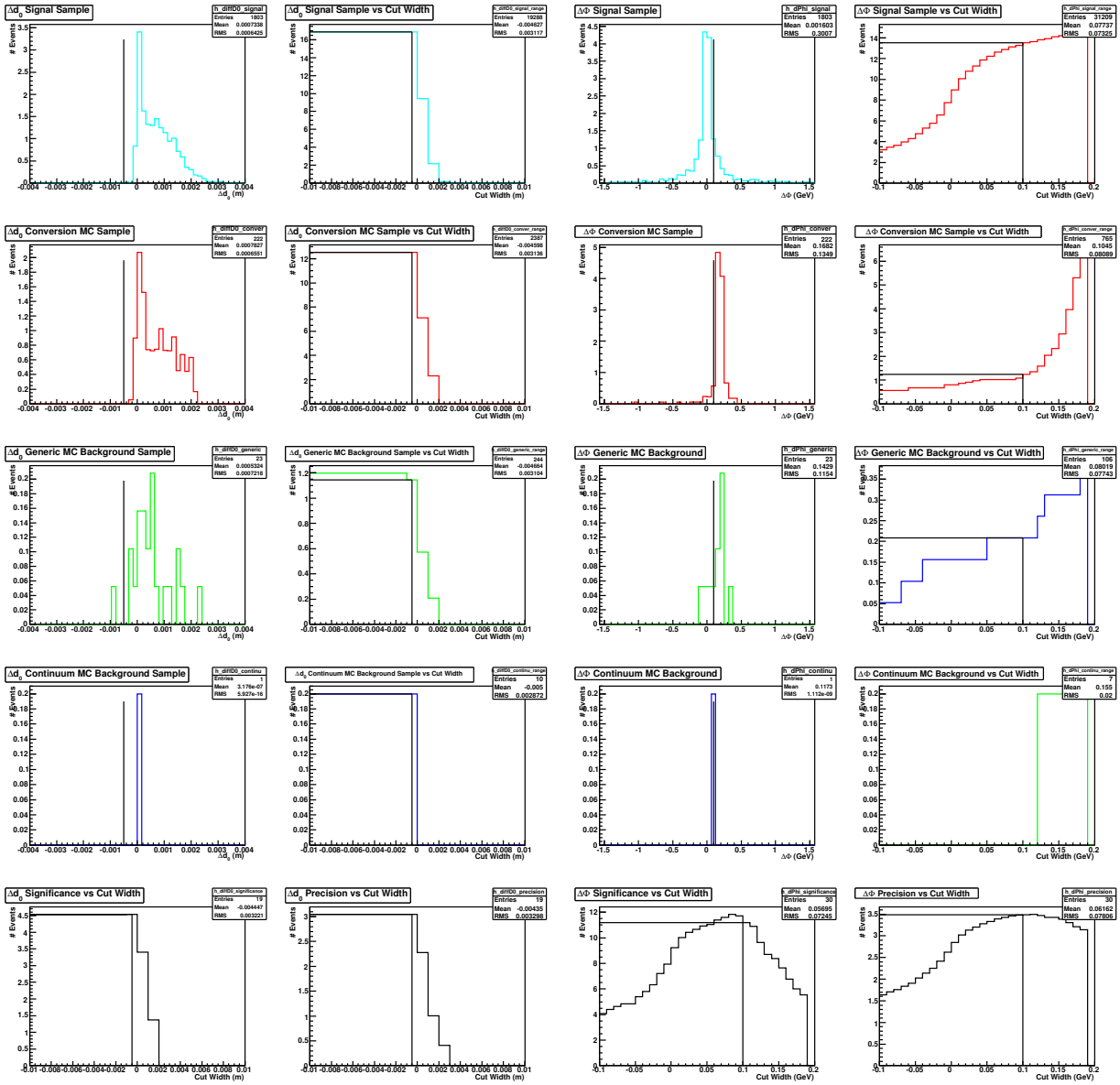

Figure 124: Optimization plots for the Δd_0 selection criterion in the $D_s^+ \to K^+K^-\pi^+$ decay mode for electron-fitted data where all tracks from the D_s^{*+} have been vertex constrained with the beamspot.

Figure 125: Optimization plots for the $\Delta\phi_0$ selection criterion in the $D_s^+ \to K^+K^-\pi^+$ decay mode for electron-fitted data where all tracks from the D_s^{*+} have been vertex constrained with the beamspot.

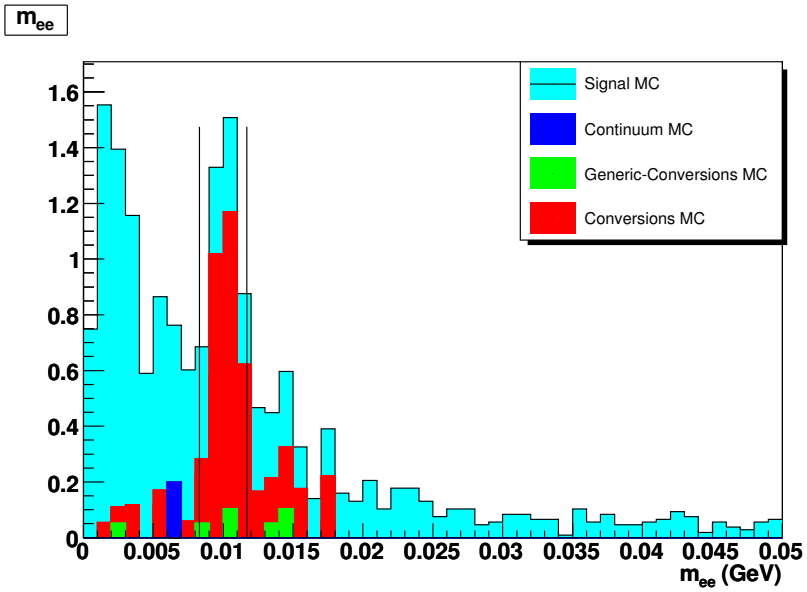

Figure 126: Distributions of the invariant mass of the e^+e^- pair where the daughters of the D_s^{*+} have been vertex constrained along with the beam-spot. The Δd_0 and $\Delta\phi_0$ cuts are replaced by a $\delta\chi^2_{red}$ and a rejection of the marked region in m_{ee}.

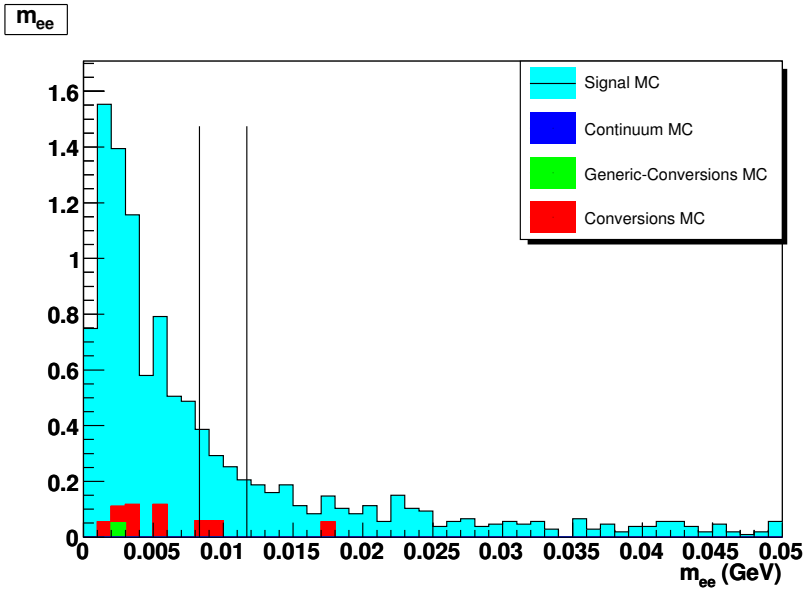

Figure 127: Distributions of the invariant mass of the e^+e^- pair where the daughters of the D_s^{*+} have been vertex constrained along with the beam-spot. All standard selection criteria have been applied, including $\Delta d_0 > -0.0005$ and $\Delta\phi_0 < 0.1$.

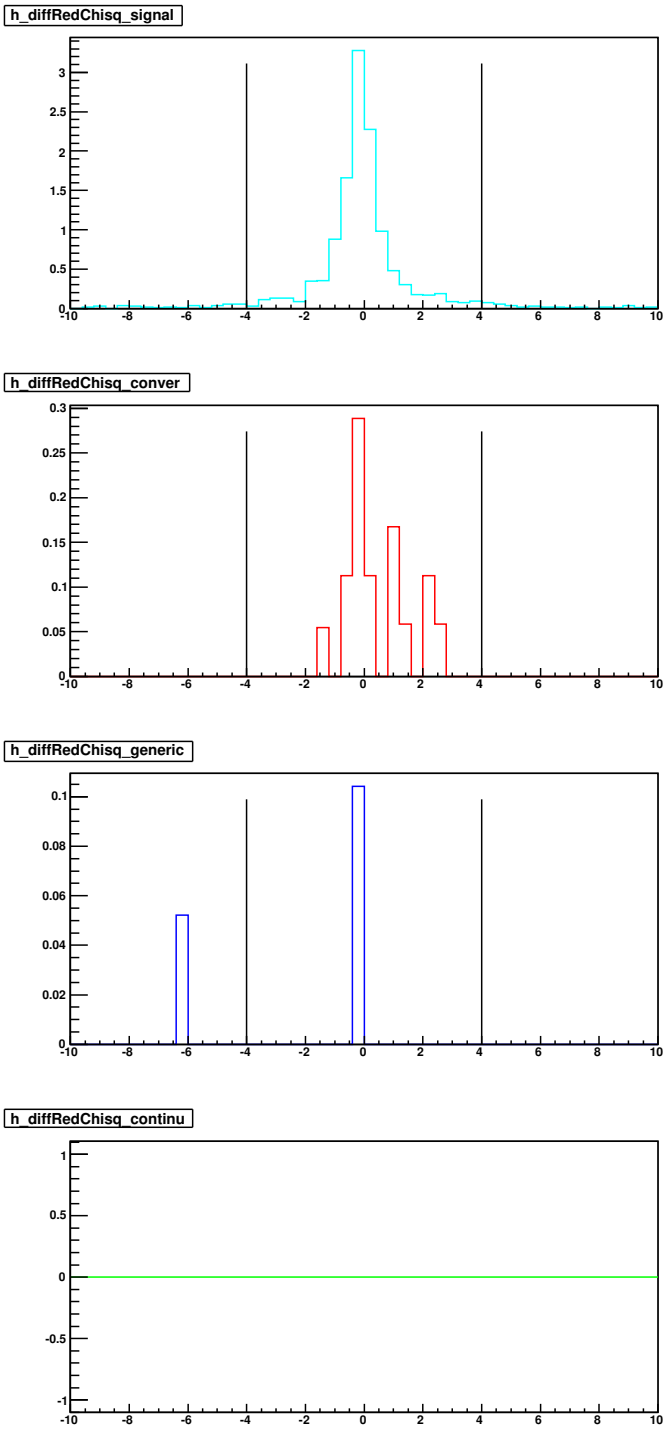

Figure 128: The difference in χ^2_{red} between the vertex fit with all D_s^{*+} tracks and the beamspot and the vertex fit with just the D_s^+ tracks and the beamspot. This is plotted after all the standard selection criteria, including the Δd_0 and $\Delta\phi_0$ have been applied.

12 Estimating Background Events in the Signal Region from Monte Carlo and Data in the Sidebands

In this section we estimate the number of background events expected in the signal region for each of the hadronic decay modes of the D_s^+. To do this, we study the sidebands of the signal regions in the m_{BC} and δm distributions of both Monte Carlo backgrounds and data in each of the modes. When we refer to either of the kinematic distributions, we imply that all other selection criteria have been applied before plotting the distribution.

The signal regions in the m_{BC} and δm distributions are kept blinded in data for this procedure. The regions in the distributions corresponding to values of the m_{BC} and δm greater than or less than the signal region are called the sideband regions. The distributions of the m_{BC} and δm in the sideband regions of data are extrapolated into the signal region using two pre-determined shapes to estimate the number of background events we expect there. The first shape is obtained by fitting the distributions of m_{BC} and δm in the simulated background Monte Carlo. We refer to this as the *MC shape* in the rest of this section. The second shape is determined by fitting the distributions of m_{BC} and δm in the sideband regions of data. This is referred to as the *data shape* in the rest of this section.

The backgrounds are estimated for each of the hadronic decay modes of the D_s^+. However, there are not enough data and Monte Carlo simulation points at the end our selection criteria in the distributions for each of the modes to make a meaningful fit that may be normalized to extract a shape. Therefore, we add the contributions from each mode to produce a summed distribution of m_{BC} and a summed distribution of δm. These distributions are used to determine the data and MC shapes for the m_{BC} and δm distributions as described in Sections 12.1 and 12.2 respectively.

The data and MC shapes are then scaled to fit the sideband regions of data in each of the individual modes, for both the m_{BC} and δm distributions. This is described, mode by mode, in the following sub-sections between 12.3 and 12.11. For each mode, we obtain four numbers for the estimated background from our fits extrapolating into the signal region – one for the data shape in the m_{BC} distribution, one for the MC shape in the m_{BC} distribution, one for the data shape in the δm distribution and one for the MC shape in the m_{BC} distribution. The average of the values and statistical uncertainties obtained from the the data and MC shapes in the m_{BC} distribution is used as the primary estimate for the background in each mode. The difference between this value and the average of the data and MC shape numbers for the δm distribution is quoted as the systematic uncertainty of our method for each mode. These numbers are summarized in Section 12.12.

Having thus obtained a summary of the background numbers expected for each of the modes, we are in a position to quantify the signal significance that can be achieved for a predicted number of signal events found in a given mode. This is described in Section 12.13.

The scale factors for the various Monte Carlo samples that constitute the simulation of background events are outlined below. It is important to get these scales correct as our determined MC shapes depend on it.

Generic MC This is known to have a scale factor $S_{gen} = 0.052 \pm 0.002$.

Continuum MC This is known to have a scale factor $S_{cont} = 0.2$.

Conversion MC As described earlier, given that our Generic MC sample is not electron-fitted, we veto events in the Generic MC that have $D_s^{*+} \to D_s^+\gamma$ and replace them with privately produced electron-fitted Monte Carlo events. We must first ensure that the number of $D_s^{*+} \to D_s^+\gamma$ events we expect in our Generic MC is within uncertainties of the number of such events we find. To do this, we first compute the efficiency of our n-tuplizer in keeping such events:

$$\epsilon_{D_s^+} = \frac{N^{afterNTuple}_{ConversionsD_s^+}}{N^{beforeNTuple}_{ConversionsD_s^+}} \tag{37}$$

$$\epsilon_{D_s^-} = \frac{N^{afterNTuple}_{ConversionsD_s^-}}{N^{beforeNTuple}_{ConversionsD_s^-}} \tag{38}$$

$$\Delta\epsilon_{D_s^+}(stat) = \sqrt{\frac{(1-\epsilon_{D_s^+})\epsilon_{D_s^+}}{N^{beforeNTuple}_{ConversionsD_s^+}}} \tag{39}$$

$$\Delta\epsilon_{D_s^-}(stat) = \sqrt{\frac{(1-\epsilon_{D_s^-})\epsilon_{D_s^-}}{N^{beforeNTuple}_{ConversionsD_s^+}}} \tag{40}$$

where $N^{beforeNTuple}_{ConversionsD_s^+}$ and $N^{beforeNTuple}_{ConversionsD_s^-}$ are the number of sample events of $D_s^{*+} \to D_s^+\gamma$ and $D_s^{*-} \to D_s^-\gamma$ respectively we started with, and $N^{afterNTuple}_{ConversionsD_s^+}$ and $N^{afterNTuple}_{ConversionsD_s^-}$ are the number of events that remained in those samples after the n-tuplizer.

Given that $N^{beforeNTuple}_{ConversionsD_s^+}$=4511222, $N^{beforeNTuple}_{ConversionsD_s^-}$=4896941, $N^{afterNTuple}_{ConversionsD_s^+}$=106893, and $N^{afterNTuple}_{ConversionsD_s^-}$=115969, we evaluate:

$$\epsilon_{D_s^+} = 0.02370 \pm 0.00007(stat) \tag{41}$$

$$\epsilon_{D_s^-} = 0.02368 \pm 0.00007(stat) \tag{42}$$

Then the number of $D_s^{*+} \to D_s^+\gamma$ and $D_s^{*-} \to D_s^-\gamma$ events in 586 ± 6 pb^{-1} of Generic MC expected to be seen after the n-tuplizer are:

$$N^{afterNTuple}_{expD_s^{*+}\to D_s^+\gamma} = L\sigma_{D_s^{*\pm}D_s^{\mp}} B(D_s^{*+} \to D_s^+\gamma)\frac{\epsilon_{D_s^+}}{2} \tag{43}$$

$$N^{afterNTuple}_{expD_s^{*-}\to D_s^-\gamma} = L\sigma_{D_s^{*\pm}D_s^{\mp}} B(D_s^{*-} \to D_s^-\gamma)\frac{\epsilon_{D_s^-}}{2} \tag{44}$$

$$\Delta N^{afterNTuple}_{expD_s^{*+}\to D_s^+\gamma} = N_{expD_s^{*+}\to D_s^+\gamma}\sqrt{\left(\frac{\Delta L}{L}\right)^2 + \left(\frac{\Delta\sigma}{\sigma}\right)^2 + \left(\frac{\Delta B}{B}\right)^2 + \left(\frac{\Delta\epsilon_{D_s^+}}{\epsilon_{D_s^+}}\right)^2} \tag{45}$$

$$\Delta N^{afterNTuple}_{expD_s^{*-}\to D_s^-\gamma} = N_{expD_s^{*-}\to D_s^-\gamma}\sqrt{\left(\frac{\Delta L}{L}\right)^2 + \left(\frac{\Delta\sigma}{\sigma}\right)^2 + \left(\frac{\Delta B}{B}\right)^2 + \left(\frac{\Delta\epsilon_{D_s^+}}{\epsilon_{D_s^+}}\right)^2} \tag{46}$$

$$\tag{47}$$

where $L = 586 \pm 6$ pb^{-1} is the luminosity of the sample, $\sigma_{D_s^{*\pm}D_s^{\mp}} = 948 \pm 36$ pb is the production cross section of $D_s^{*\pm}D_s^{\mp}$ at 4170 MeV, and $B(D_s^{*+} \to D_s^+\gamma) = 0.942 \pm 0.007$ is the branching fraction of $D_s^{*+} \to D_s^+\gamma$. With these values, we calculate:

$$N^{afterNTuple}_{expD_s^{*+}\to D_s^+\gamma} = 6200 \pm 250 \tag{48}$$

$$N^{afterNTuple}_{expD_s^{*-}\to D_s^-\gamma} = 6200 \pm 250 \tag{49}$$

Now, the number of $D_s^{*-} \to D_s^-\gamma$ surviving in the Generic MC after the n-tuplizer are:

$$N^{afterNTuple}_{seenD_s^{*+}\to D_s^+\gamma} = N^{afterNTuple}_{D_s^{*+}\to D_s^+\gamma} S_{gen} \tag{50}$$

$$N^{afterNTuple}_{seenD_s^{*-}\to D_s^-\gamma} = N^{afterNTuple}_{D_s^{*-}\to D_s^-\gamma} S_{gen} \tag{51}$$

$$\Delta N^{afterNTuple}_{seenD_s^{*+}\to D_s^+\gamma} = N^{afterNTuple}_{seenD_s^{*+}\to D_s^+\gamma} \left(\frac{\Delta S_{gen}}{S_{gen}}\right) \tag{52}$$

$$\Delta N^{afterNTuple}_{seenD_s^{*-}\to D_s^-\gamma} = N^{afterNTuple}_{seenD_s^{*-}\to D_s^-\gamma} \left(\frac{\Delta S_{gen}}{S_{gen}}\right) \tag{53}$$

where $N_{D_s^{*+}\to D_s^+\gamma}$ is the number of events left over after the n-tuplizer in the Generic MC sample and $N_{seenD_s^{*+}\to D_s^+\gamma}$ is that number divided by S_{gen}. This is found to be:

$$N^{afterNTuple}_{seenD_s^{*+}\to D_s^+\gamma} = 6340 \pm 260 \tag{54}$$

$$N^{afterNTuple}_{seenD_s^{*-}\to D_s^-\gamma} = 6310 \pm 260 \tag{55}$$

The expected and seen number of events after n-tuplizing are within each other's standard deviation and no problem is noted. Now we can calculate the conversion scales as follows:

$$S_{D_s^+ con} = \frac{N^{afterNTuple}_{seenD_s^{*+}\to D_s^+\gamma}}{N^{afterNTuple}_{ConversionsD_s^+}} \tag{56}$$

$$S_{D_s^- con} = \frac{N^{afterNTuple}_{seenD_s^{*-}\to D_s^-\gamma}}{N^{afterNTuple}_{ConversionsD_s^-}} \tag{57}$$

$$\Delta S_{D_s^+ con} = S_{D_s^+ con}\sqrt{\left(\frac{\Delta N^{afterNTuple}_{seenD_s^{*+}\to D_s^+\gamma}}{N^{afterNTuple}_{seenD_s^{*+}\to D_s^+\gamma}}\right)^2 + \frac{1}{N^{afterNTuple}_{ConversionsD_s^+}}} \tag{58}$$

$$\Delta S_{D_s^- con} = S_{D_s^- con}\sqrt{\left(\frac{\Delta N^{afterNTuple}_{seenD_s^{*-}\to D_s^-\gamma}}{N^{afterNTuple}_{seenD_s^{*-}\to D_s^-\gamma}}\right)^2 + \frac{1}{N^{afterNTuple}_{ConversionsD_s^-}}} \tag{59}$$

So now, we can calculate:

$$S_{D_s^+ con} = \frac{6340 \pm 260}{106893} = 0.059 \pm 0.003 \tag{60}$$

$$S_{D_s^- con} = \frac{6310 \pm 260}{115969} = 0.054 \pm 0.002 \tag{61}$$

We use the scale factors for the conversion background samples derived in Equations 60 for the rest of the document.

Table 32: Maximum likelihood fit parameters for the *MC shape* in m_{BC} distribution.

Fit Parameters	Value
p_0	-3.91135e+02
p_1	1.91233e+02

Table 33: Maximum likelihood fit parameters for the *data shape* in m_{BC} distribution.

Fit Parameters	Value
p_0	-2.79836e+02
p_1	1.38607e+02

12.1 Determining the Shape of the m_{BC} Distribution

The distribution of m_{BC} in the data and Monte Carlo are added up for all modes and presented in Fig. 129. The Monte Carlo is fitted to the function 62 between 2.060 GeV and 2.155 GeV. It is depicted in the figure as a black curve and shall be called the *MC shape*. The data is also fitted to the same function, but between the disconnected domains of 2.060 to 2.100 GeV and 2.124 to 2.155 GeV. It is depicted in the figure as a magenta curve and shall be referred to as the *data shape*. Each sideband region, it may be noted, is separated from the signal region by half the width of the signal region. This is done in order to avoid contaminating the sideband region with signal.

$$y = (p_0 + p_1 x)\sqrt{2.155 - x}/GeV \tag{62}$$

The maximum likelihood fit parameters of the *MC shape* and *data shape* are tabulated in Tables 32 33, respectively.

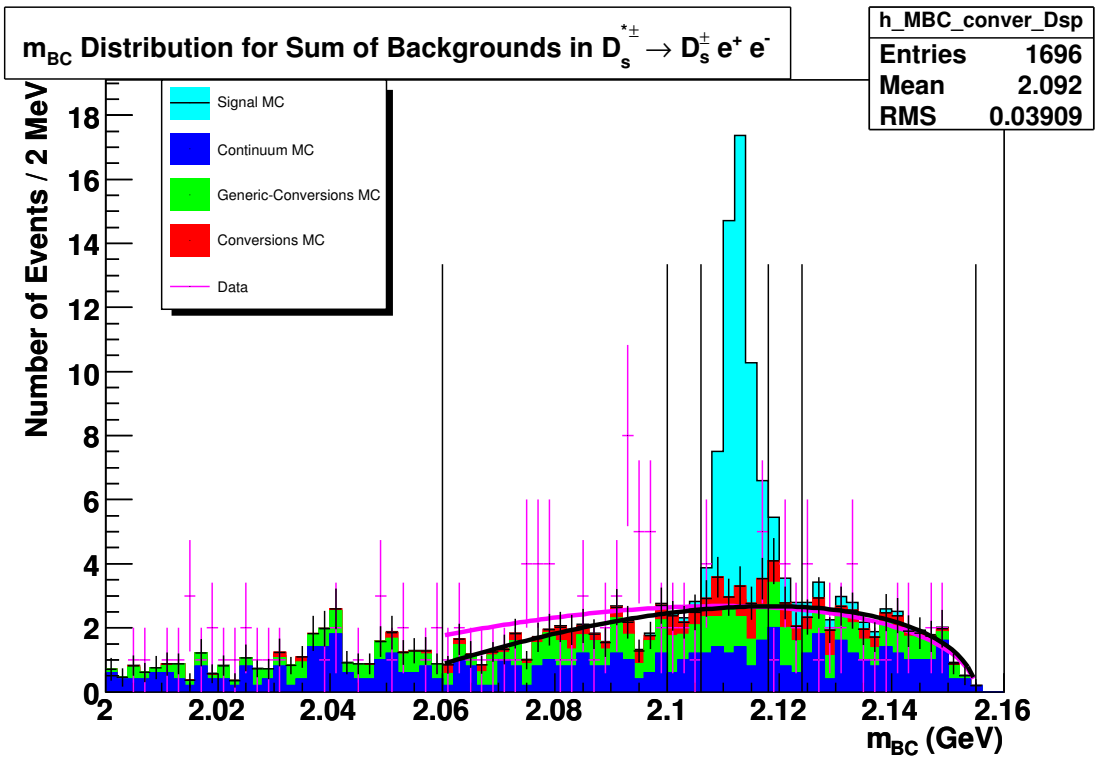

Figure 129: Distributions of m_{BC} in Monte Carlo and data. The blue region is distribution of m_{BC} in Continuum MC. On top of that, in green, is stacked the Generic MC with Conversion type events vetoed. The Conversion MC is stacked on top of that in red. The black curve is fitted to the sum of the aforementioned background distributions. The Signal MC is stacked on top of the background MC to show roughly what expect to see when we unblind data. Data points, blinded in the signal region, are overlaid in magenta. The magenta curve is fitted to the data in the sideband regions, as described in the text.

Table 34: Maximum likelihood fit parameters for the *MC shape* in δm distribution.

Fit Parameters	Value
p_0	-2.45787e+03
p_1	6.02306e+03
p_2	-2.39666e+03
p_3	1.65951e+03

Table 35: Maximum likelihood fit parameters for the *Data shape* in δm distribution.

Fit Parameters	Value
p_0	2.38215e+03
p_1	-8.89072e+03
p_2	2.35325e+03
p_3	-2.76871e+03

12.2 Determining the Shape of the δm Distribution

As we have done in the case of the m_{BC} distribution, the distribution of δm in the data and Monte Carlo are added up for all modes and presented in Fig. 130. However, to further increase the sample sizes, the width of the m_{BC} cuts for each of the modes have been doubled. The Monte Carlo is fitted to a third order Chebyshev polynomial 63 between 0.100 GeV and 0.250 GeV. It is depicted in the figure as a black curve and shall be called the *MC shape*. The data is also fitted to the same function, but between the disconnected domains of 0.1000 to 0.1298 GeV and 0.1578 to 0.2500 GeV. It is depicted in the figure as a magenta curve and shall be referred to as the *data shape*. Each sideband region, it may be noted, is separated from the signal region by half the width of the signal region.

$$y = p_0 + p_1 T_1 + p_2 T_2 + p_3 T_3 \tag{63}$$

The maximum likelihood fit parameters of the *MC shape* and *data shape* are tabulated in Tables 34 35, respectively.

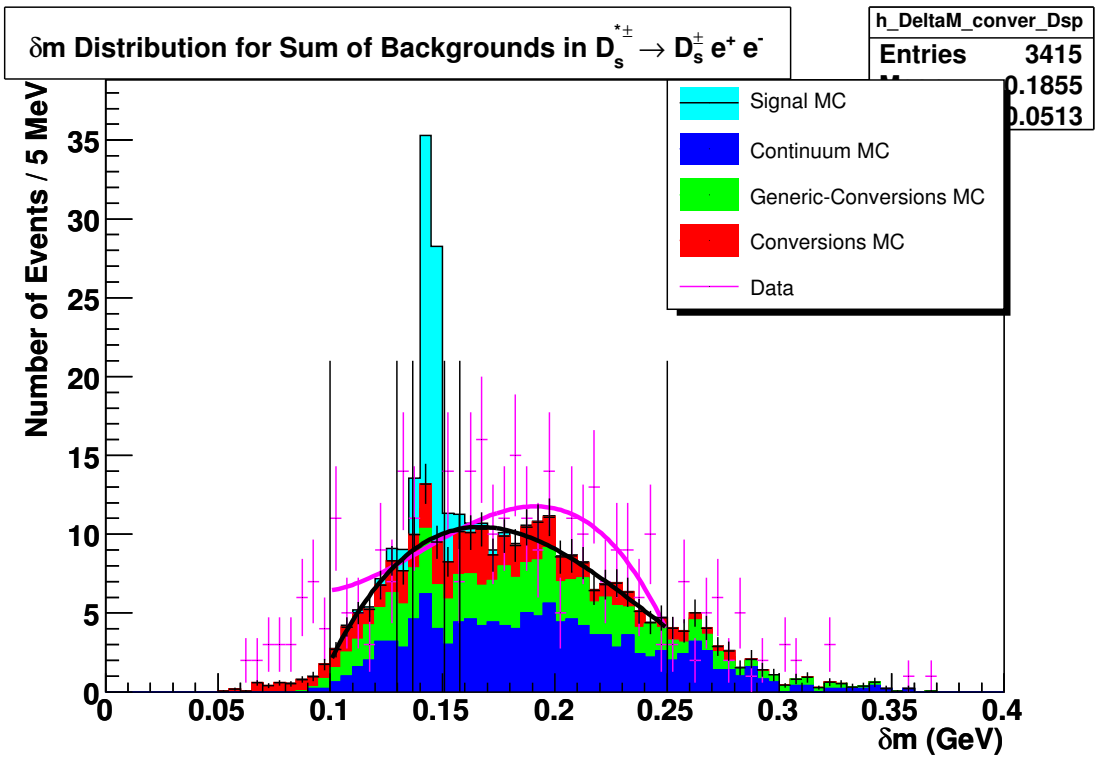

Figure 130: Distributions of δm in Monte Carlo and data. The blue region is distribution of δm in Continuum MC. On top of that, in green, is stacked the Generic MC with Conversion type events vetoed. The Conversion MC is stacked on top of that in red. The black curve is fitted to the sum of the aforementioned background distributions. The Signal MC is stacked on top of the background MC to show roughly what expect to see when we unblind data. Data points, blinded in the signal region, are overlaid in magenta. The magenta curve is fitted to the data in the sideband regions, as described in the text.

12.3 Estimating the Background in the $D_s^+ \to K^+K^-\pi^+$ Mode

Having found the generic *MC shape* and *data shape* in the m_{BC} distribution in Section 12.1, we now proceed to scale those shapes to fit data in the sideband regions of the $D_s^+ \to K^+K^-\pi^+$ mode. The signal region is centered at 2.112 GeV with a width of 0.008 GeV. The sideband regions are separated from the signal region by half the width of the signal region. The sideband regions extend from 2.060 to 2.104 GeV and 2.120 to 2.155 GeV. The maximum likelihood fits are displayed in Fig. 131 and the values for the scale parameters are presented in Table 36.

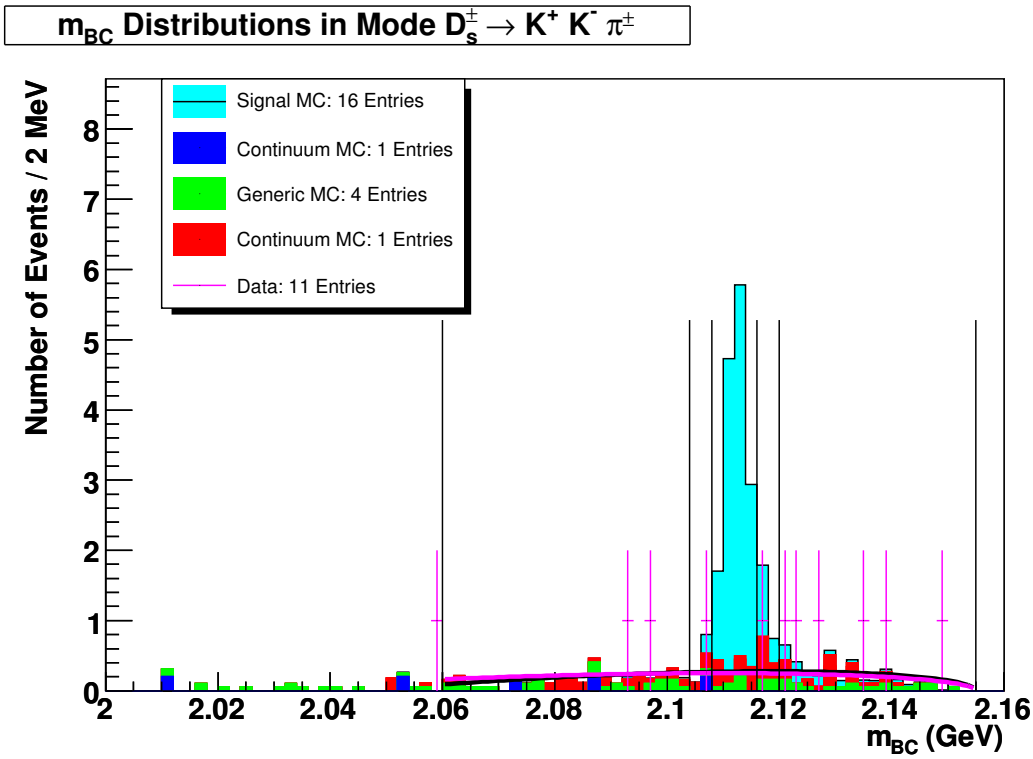

Figure 131: The various backgrounds and signal MC expected in the vicinity of the signal region in m_{BC} distribution of the $D_s^+ \to K^+K^-\pi^+$ mode. The data, blinded in the signal region, is overlaid in magenta points. The black and magenta curves are *MC* and *data shapes* scaled by maximum likelihood to the points of data in the sideband regions.

Also, having found the generic *MC* and *data shapes* in the δm distribution in Section 12.2, we can now scale those to fit data in the sideband regions of δm in the $D_s^+ \to K^+K^-\pi^+$ mode. The signal region is centered at 0.1438 GeV with a width of 0.012 GeV. The sideband regions are separated from the signal region by half the width of the signal region. The sideband regions extend from 0.1000 to 0.1318 GeV and 0.1558 to 0.2500 GeV. The maximum likelihood fits are displayed in Fig. 132 and the values for the scale parameters are presented in Table 36.

Table 36: Maximum likelihood fit parameters to estimate background in the $D_s^+ \to K^+K^-\pi^+$ mode

Scale for Shape	Value
m_{BC} *MC shape*	1.03798e-01
δm *MC shape*	9.35684e-02
m_{BC} *data shape*	7.75452e-02
δm *data shape*	6.54773e-02

Table 37: Estimates of the background in the signal region of the $D_s^+ \to K^+K^-\pi^+$ mode using four fits outlined above.

Mode	m_{BC}		δm	
	MC shape	*data shape*	*MC shape*	*data shape*
$K^+K^-\pi^+$	1.10 ± 0.39	1.00 ± 0.35	2.06 ± 0.49	1.61 ± 0.38

The four different fits give us four estimates of the background in the signal region. These are tabulated in Table 37. The uncertainties noted in the table are statistical and are estimated by assuming Poisson statistics on the number of data points in the sidebands. It is calculated as given in Eq. 64 where b is the estimated number of background events and $N_{\texttt{side}}$ is the number of events observed in the data sidebands.

$$\Delta b = \frac{b}{\sqrt{N_{\texttt{side}}}} \tag{64}$$

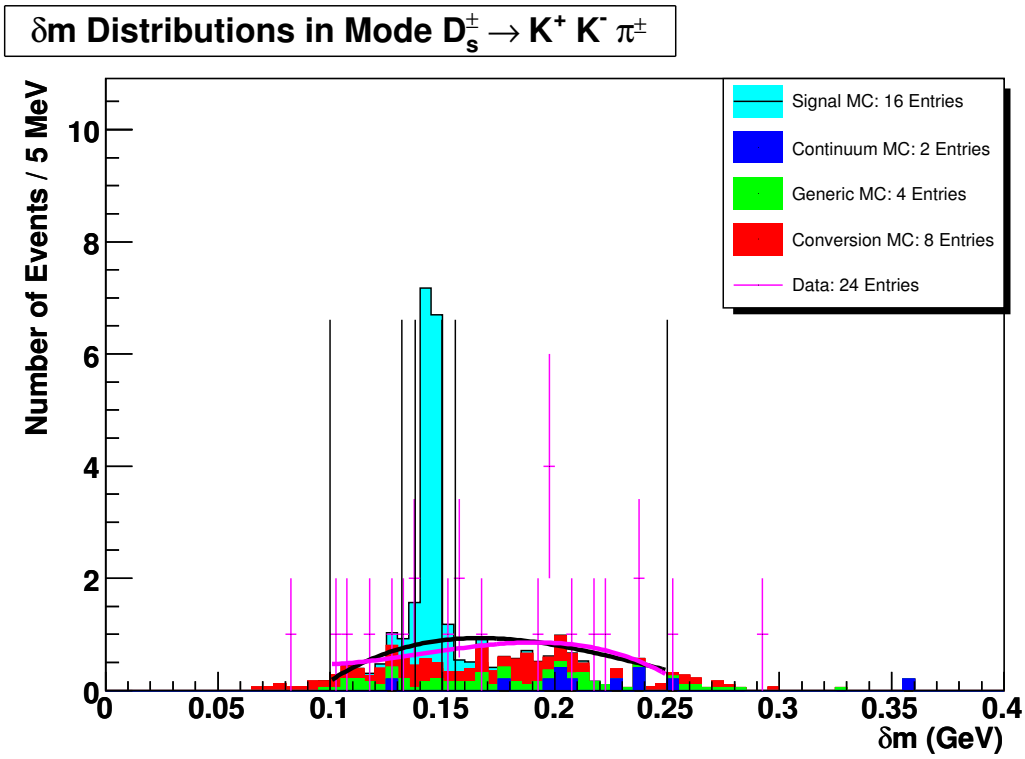

Figure 132: The various backgrounds and signal MC expected in the vicinity of the signal region in δm distribution of the $D_s^+ \to K^+K^-\pi^+$ mode. The data, blinded in the signal region, is overlaid in magenta points. The black and magenta curves are *MC* and *data shapes* scaled by maximum likelihood to the points of data in the sideband regions.

12.4 Estimating the Background in the $D_s^+ \to K_S K^+$ Mode

The signal region in the m_{BC} distribution of this mode is centered at 2.112 GeV with a width of 0.014 GeV. The sideband regions extend from 2.060 to 2.098 GeV and 2.126 to 2.155 GeV. The maximum likelihood fits are displayed in Fig. 133 and the values for the scale parameters are presented in Table 38.

The signal region in the δm distribution is centered at 0.1438 GeV with a width of 0.012 GeV. The sideband regions extend from 0.1000 to 0.1318 GeV and 0.1558 to 0.2500 GeV. The maximum likelihood fits are displayed in Fig. 134 and the values for the scale parameters are presented in Table 38.

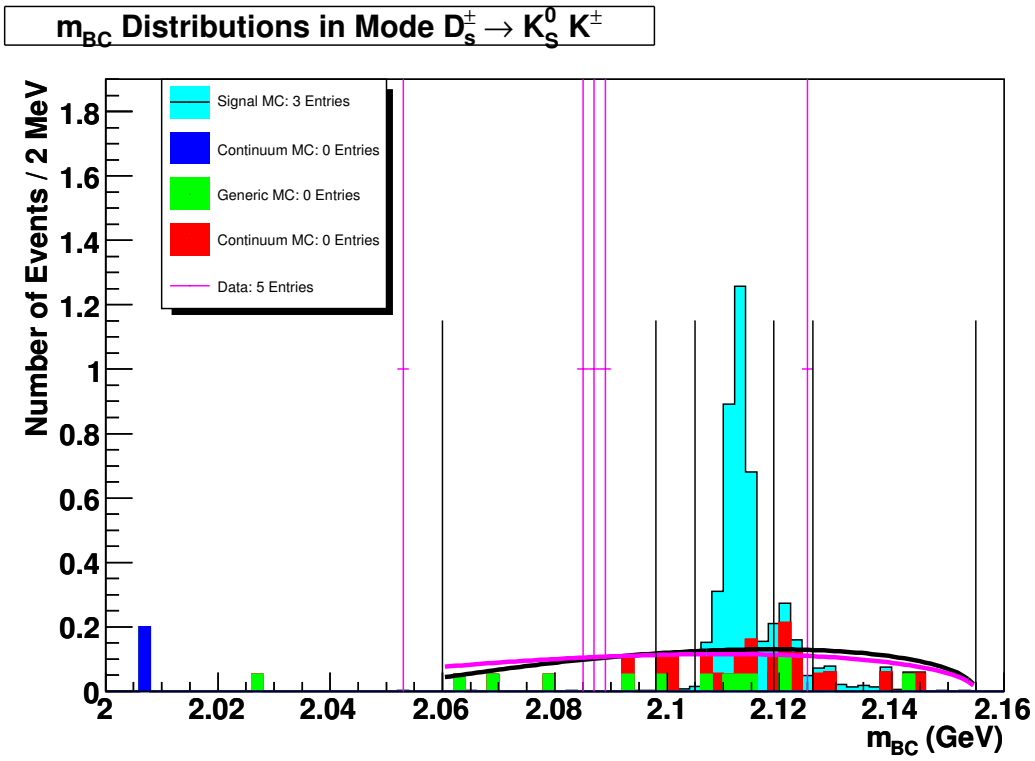

Figure 133: The various backgrounds and signal MC expected in the vicinity of the signal region in m_{BC} distribution of the $D_s^+ \to K_S K^+$ mode. The data, blinded in the signal region, is overlaid in magenta points. The black and magenta curves are *MC* and *data shapes* scaled by maximum likelihood to the points of data in the sideband regions.

The four different fits give us four estimates of the background in the signal region. These are tabulated in Table 39.

Table 38: Maximum likelihood fit parameters to estimate background in the $D_s^+ \to K_S K^+$ mode

Scale for Shape	Value
m_{BC} *MC shape*	4.86292e-02
δm *MC shape*	4.29587e-02
m_{BC} *data shape*	5.25423e-03
δm *data shape*	4.28206e-03

Table 39: Estimates of the background in the signal region of the $D_s^+ \to K_S K^+$ mode using four fits outlined above.

Mode	m_{BC}		δm	
	MC shape	*data shape*	*MC shape*	*data shape*
$K_S K^+$	0.90 ± 0.45	0.80 ± 0.40	0.12 ± 0.12	0.10 ± 0.10

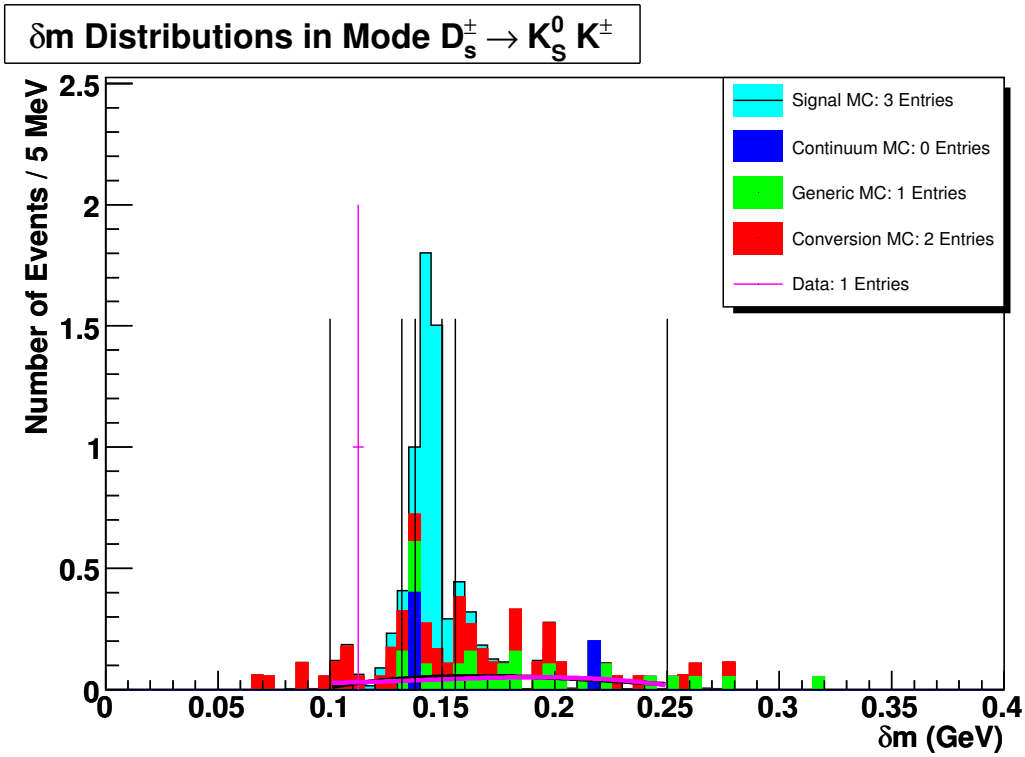

Figure 134: The various backgrounds and signal MC expected in the vicinity of the signal region in δm distribution of the $D_s^+ \to K_S K^+$ mode. The data, blinded in the signal region, is overlaid in magenta points. The black and magenta curves are *MC* and *data shapes* scaled by maximum likelihood to the points of data in the sideband regions.

12.5 Estimating the Background in the $D_s^+ \to \eta\pi^+; \eta \to \gamma\gamma$ Mode

The signal region in the m_{BC} distribution of this mode is centered at 2.112 GeV with a width of 0.016 GeV. The sideband regions extend from 2.060 to 2.096 GeV and 2.128 to 2.155 GeV. The maximum likelihood fits are displayed in Fig. 135 and the values for the scale parameters are presented in Table 40.

The signal region in the δm distribution of this mode is centered at 0.1438 GeV with a width of 0.016 GeV. The sideband regions extend from 0.1000 to 0.1278 GeV and 0.1598 to 0.2500 GeV. The maximum likelihood fits are displayed in Fig. 136 and the values for the scale parameters are presented in Table 40.

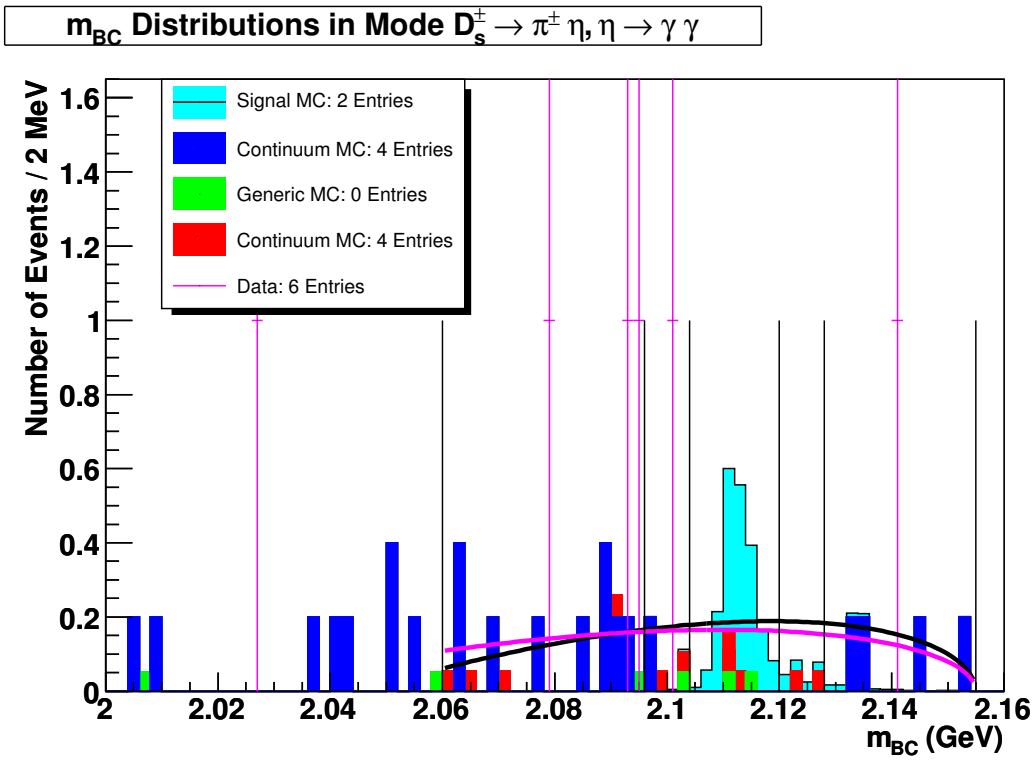

Figure 135: The various backgrounds and signal MC expected in the vicinity of the signal region in m_{BC} distribution of the $D_s^+ \to \eta\pi^+; \eta \to \gamma\gamma$ mode. The data, blinded in the signal region, is overlaid in magenta points. The black and magenta curves are *MC* and *data shapes* scaled by maximum likelihood to the points of data in the sideband regions.

The four different fits give us four estimates of the background in the signal region. These are tabulated in Table 41.

Table 40: Maximum likelihood fit parameters to estimate background in the $D_s^+ \to \eta\pi^+; \eta \to \gamma\gamma$ mode

Scale for Shape	Value
m_{BC} *MC shape*	7.05486e-02
δm *MC shape*	6.18039e-02
m_{BC} *data shape*	3.33356e-02
δm *data shape*	2.68789e-02

Table 41: Estimates of the background in the signal region of the $D_s^+ \to \eta\pi^+; \eta \to \gamma\gamma$ mode using four fits outlined above.

Mode	m_{BC}		δm	
	MC shape	*data shape*	*MC shape*	*data shape*
$\eta\pi^+$	1.48 ± 0.74	1.32 ± 0.66	1.02 ± 0.39	0.79 ± 0.30

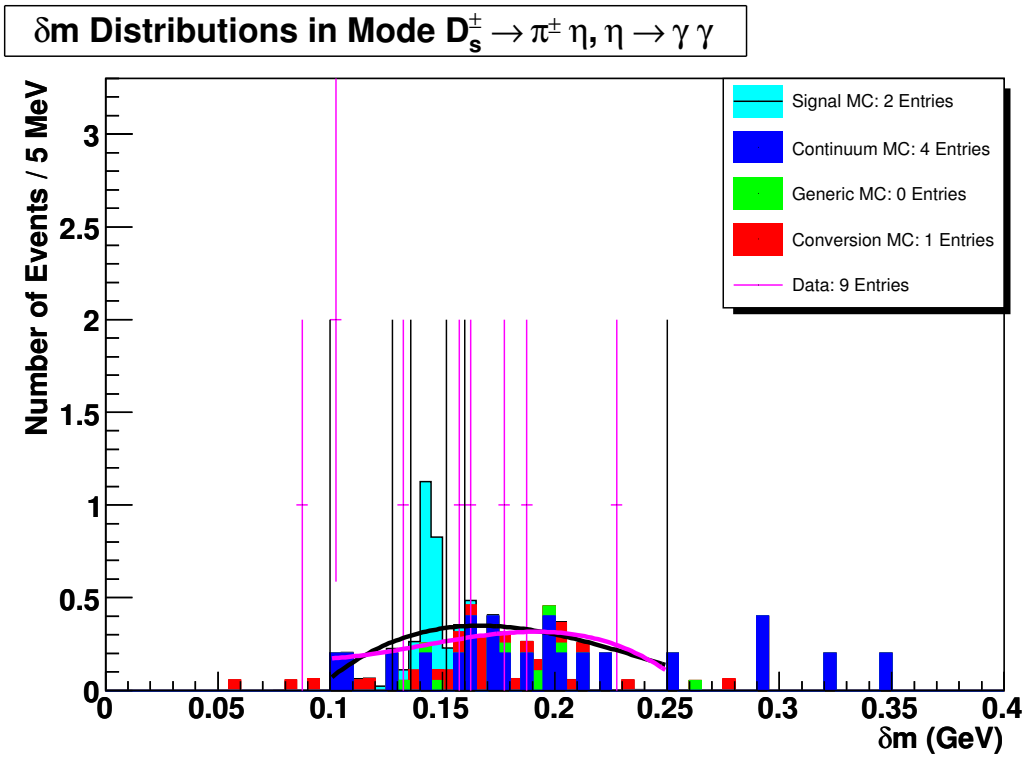

Figure 136: The various backgrounds and signal MC expected in the vicinity of the signal region in δm distribution of the $D_s^+ \to \eta\pi^+; \eta \to \gamma\gamma$ mode. The data, blinded in the signal region, is overlaid in magenta points. The black and magenta curves are *MC* and *data shapes* scaled by maximum likelihood to the points of data in the sideband regions.

12.6 Estimating the Background in the $D_s^+ \to \eta'\pi^+; \eta' \to \pi^+\pi^-\eta; \eta \to \gamma\gamma$ Mode

The signal region in the m_{BC} distribution of this mode is centered at 2.112 GeV with a width of 0.022 GeV. The sideband regions extend from 2.060 to 2.090 GeV and 2.134 to 2.155 GeV. The maximum likelihood fits are displayed in Fig. 137 and since no data point fell within our sideband region, no fit could be made.

The signal region in the δm distribution of this mode is centered at 0.1438 GeV with a width of 0.026 GeV. The sideband regions extend from 0.1000 to 0.1178 GeV and 0.1698 to 0.2500 GeV. The maximum likelihood fits are displayed in Fig. 138.

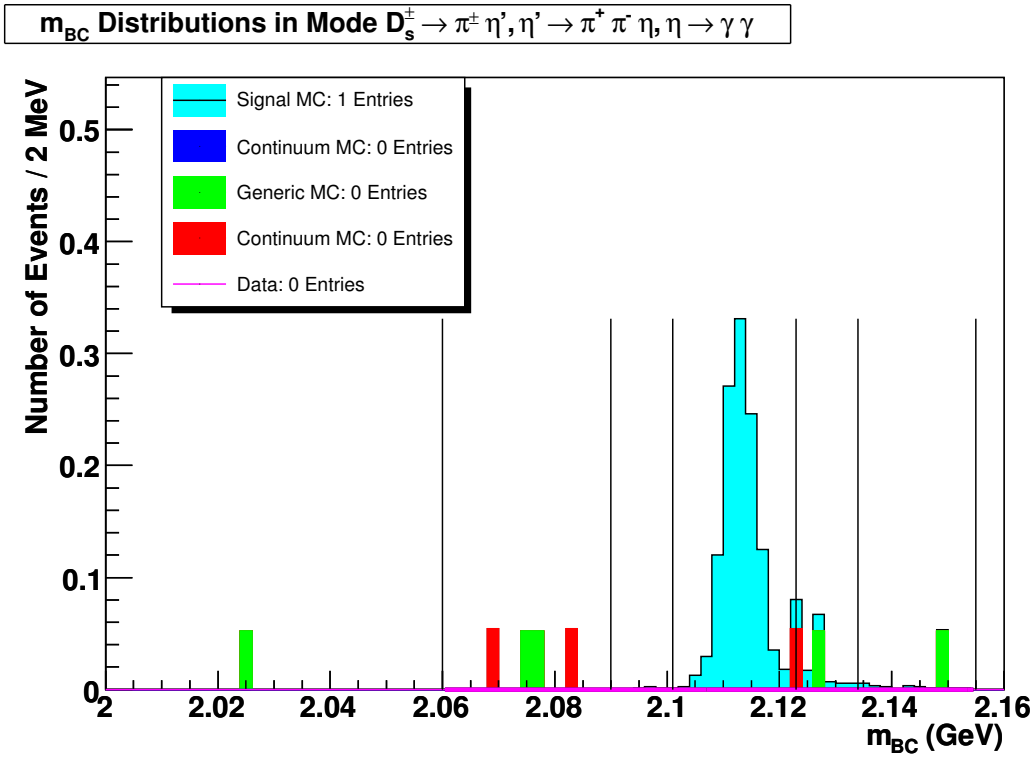

Figure 137: The various backgrounds and signal MC expected in the vicinity of the signal region in m_{BC} distribution of the $D_s^+ \to \eta'\pi^+; \eta' \to \pi^+\pi^-\eta; \eta \to \gamma\gamma$ mode. The data, blinded in the signal region, is overlaid in magenta points. The black and magenta curves are *MC* and *data shapes* scaled by maximum likelihood to the points of data in the sideband regions.

Not much could be estimated of the background expected in the signal region. This is tabulated in Table 42.

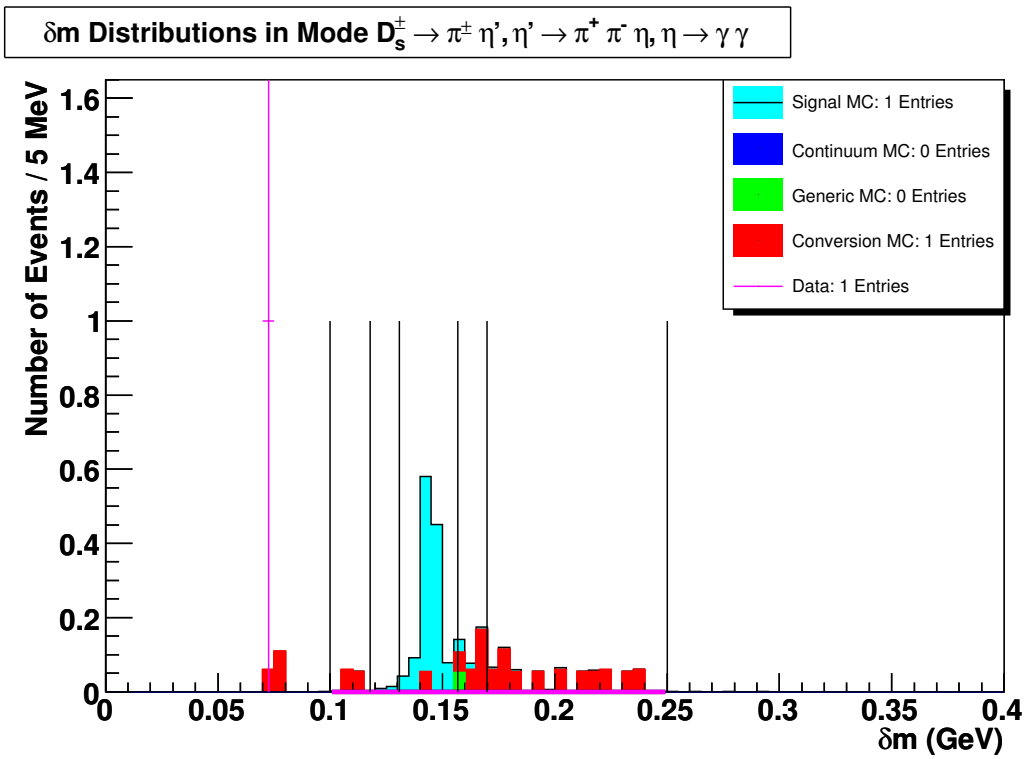

Figure 138: The various backgrounds and signal MC expected in the vicinity of the signal region in δm distribution of the $D_s^+ \to \eta'\pi^+; \eta' \to \pi^+\pi^-\eta; \eta \to \gamma\gamma$ mode. The data, blinded in the signal region, is overlaid in magenta points. The black and magenta curves are *MC* and *data shapes* scaled by maximum likelihood to the points of data in the sideband regions.

Table 42: Estimates of the background in the signal region of the $D_s^+ \to \eta'\pi^+; \eta' \to \pi^+\pi^-\eta; \eta \to \gamma\gamma$ mode using four fits outlined above.

Mode	m_{BC}		δm	
	MC shape	*data shape*	*MC shape*	*data shape*
$\eta'\pi^+$	0.00 + 0.68	0.00 + 0.59	0.00 + 0.34	0.00 + 0.26

Table 43: Maximum likelihood fit parameters to estimate background in the $D_s^+ \to K^+K^-\pi^+\pi^0$ mode

Scale for Shape	Value
m_{BC} *MC shape*	1.68672e-01
δm *MC shape*	1.52049e-01
m_{BC} *data shape*	1.10339e-01
δm *data shape*	8.99227e-02

Table 44: Estimates of the background in the signal region of the $D_s^+ \to K^+K^-\pi^+\pi^0$ mode using four fits outlined above.

Mode	m_{BC}		δm	
	MC shape	*data shape*	*MC shape*	*data shape*
$K^+K^-\pi^+\pi^0$	1.78 ± 0.49	1.63 ± 0.45	2.54 ± 0.54	1.99 ± 0.43

12.7 Estimating the Background in the $D_s^+ \to K^+K^-\pi^+\pi^0$ Mode

The signal region in the m_{BC} distribution of this mode is centered at 2.112 GeV with a width of 0.008 GeV. The sideband regions extend from 2.060 to 2.104 GeV and 2.120 to 2.155 GeV. The maximum likelihood fits are displayed in Fig. 139 and the values for the scale parameters are presented in Table 43.

The signal region in the δm distribution of this mode is centered at 0.1438 GeV with a width of 0.012 GeV. The sideband regions extend from 0.1000 to 0.1318 GeV and 0.1558 to 0.2500 GeV. The maximum likelihood fits are displayed in Fig. 140 and the values for the scale parameters are presented in Table 43.

The four different fits give us four estimates of the background in the signal region. These are tabulated in Table 44.

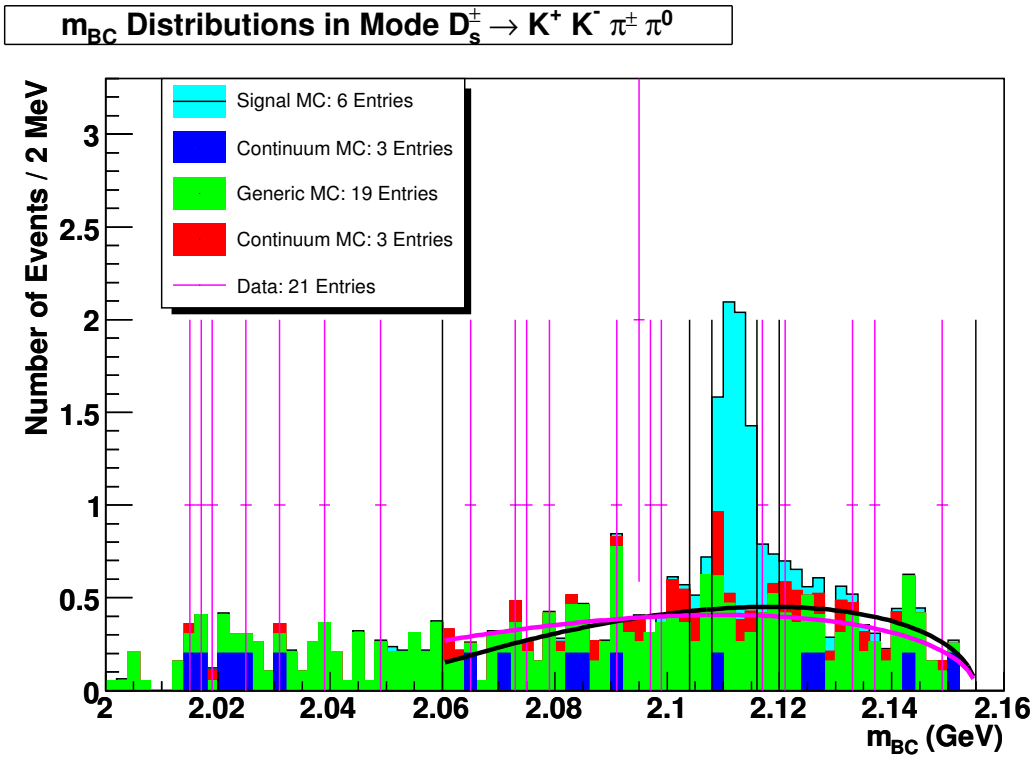

Figure 139: The various backgrounds and signal MC expected in the vicinity of the signal region in m_{BC} distribution of the $D_s^+ \to K^+K^-\pi^+\pi^0$ mode. The data, blinded in the signal region, is overlaid in magenta points. The black and magenta curves are *MC* and *data shapes* scaled by maximum likelihood to the points of data in the sideband regions.

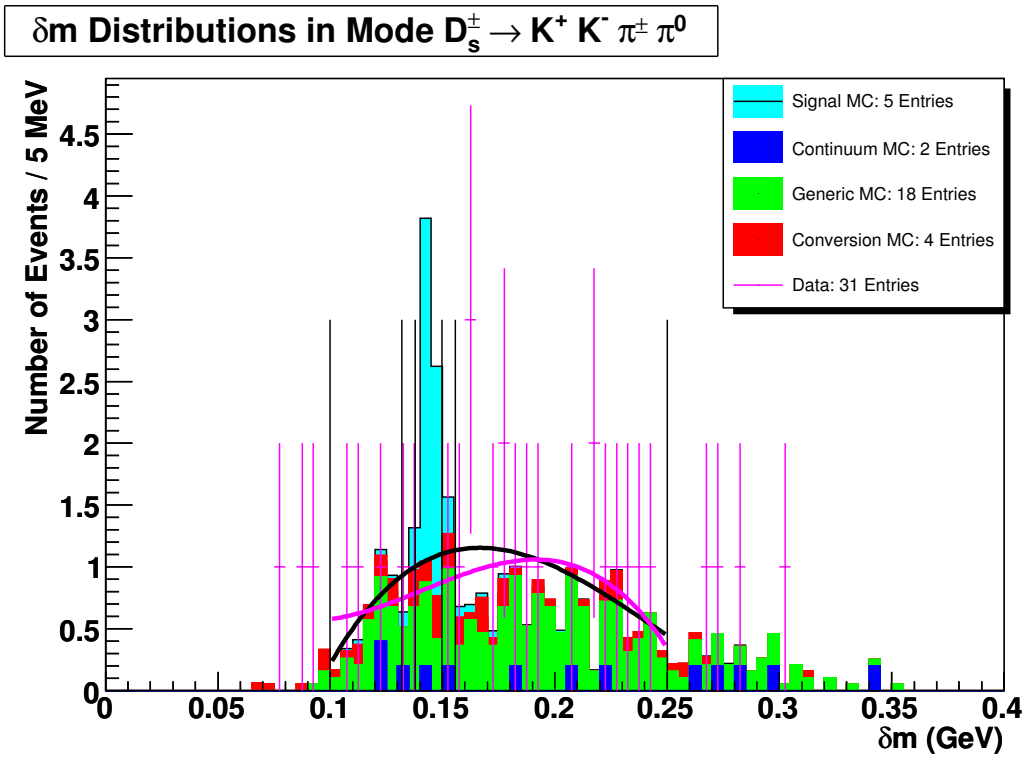

Figure 140: The various backgrounds and signal MC expected in the vicinity of the signal region in δm distribution of the $D_s^+ \to K^+K^-\pi^+\pi^0$ mode. The data, blinded in the signal region, is overlaid in magenta points. The black and magenta curves are *MC* and *data shapes* scaled by maximum likelihood to the points of data in the sideband regions.

12.8 Estimating the Background in the $D_s^+ \to \pi^+\pi^-\pi^+$ Mode

The signal region in the m_{BC} distribution of this mode is centered at 2.112 GeV with a width of 0.008 GeV. The sideband regions extend from 2.060 to 2.104 GeV and 2.120 to 2.155 GeV. The maximum likelihood fits are displayed in Fig. 141 and the values for the scale parameters are presented in Table 45.

The signal region in the δm distribution of this mode is centered at 0.1438 GeV with a width of 0.012 GeV. The sideband regions extend from 0.1000 to 0.1318 GeV and 0.1558 to 0.2500 GeV. The maximum likelihood fits are displayed in Fig. 142 and the values for the scale parameters are presented in Table 45.

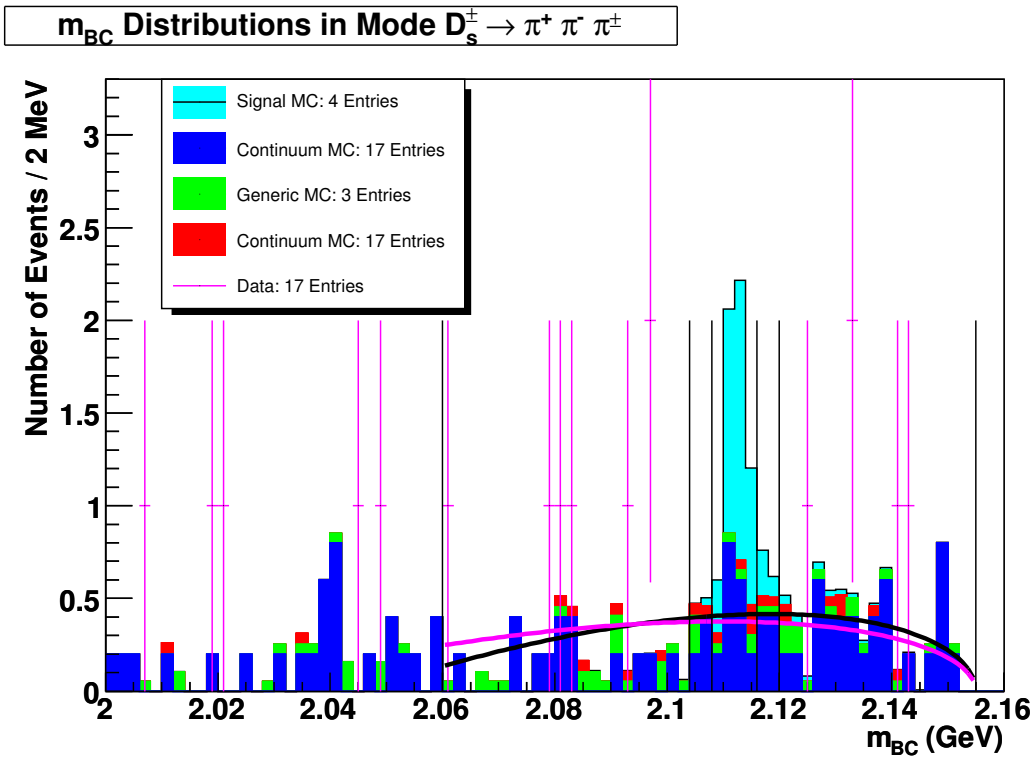

Figure 141: The various backgrounds and signal MC expected in the vicinity of the signal region in m_{BC} distribution of the $D_s^+ \to \pi^+\pi^-\pi^+$ mode. The data, blinded in the signal region, is overlaid in magenta points. The black and magenta curves are *MC* and *data shapes* scaled by maximum likelihood to the points of data in the sideband regions.

The four different fits give us four estimates of the background in the signal region. These are tabulated in Table 46.

Table 45: Maximum likelihood fit parameters to estimate background in the $D_s^+ \to \pi^+\pi^-\pi^+$ mode

Scale for Shape	Value
m_{BC} *MC shape*	1.55698e-01
δm *MC shape*	1.40353e-01
m_{BC} *data shape*	1.05085e-01
δm *data shape*	8.56409e-02

Table 46: Estimates of the background in the signal region of the $D_s^+ \to \pi^+\pi^-\pi^+$ mode using four fits outlined above.

Mode	m_{BC}		δm	
	MC shape	*data shape*	*MC shape*	*data shape*
$\pi^+\pi^-\pi^+$	1.64 ± 0.48	1.50 ± 0.43	2.42 ± 0.53	1.90 ± 0.41

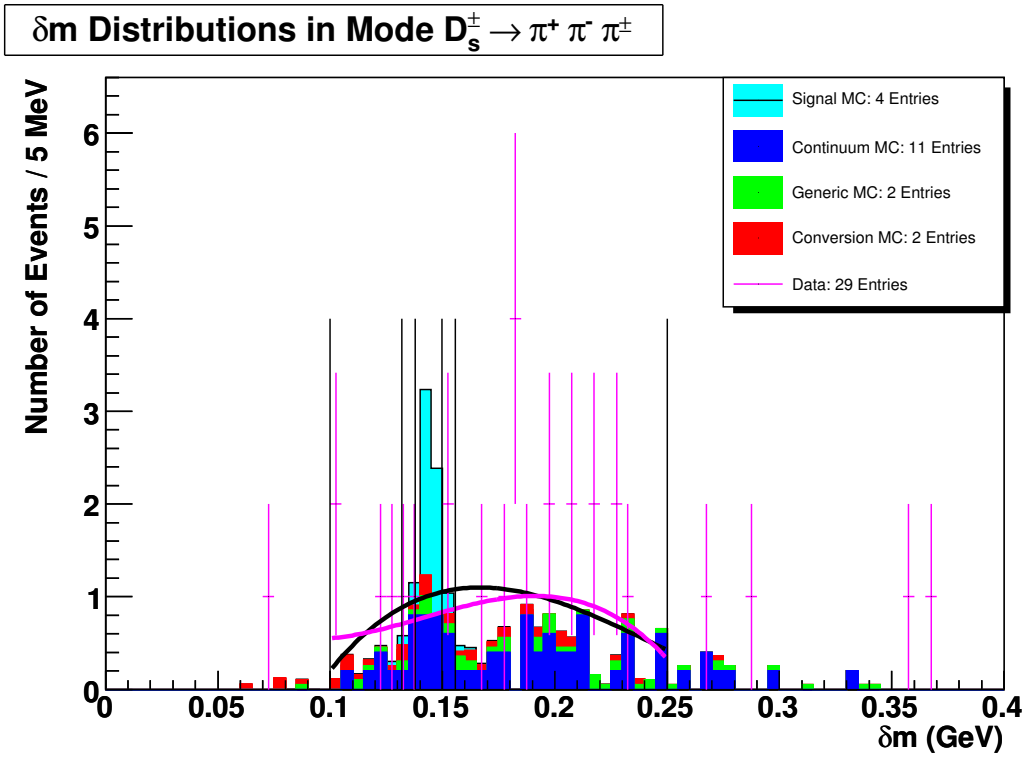

Figure 142: The various backgrounds and signal MC expected in the vicinity of the signal region in δm distribution of the $D_s^+ \to \pi^+\pi^-\pi^+$ mode. The data, blinded in the signal region, is overlaid in magenta points. The black and magenta curves are *MC* and *data shapes* scaled by maximum likelihood to the points of data in the sideband regions.

12.9 Estimating the Background in the $D_s^+ \to K^{*+}K^{*0}$ Mode

The signal region in the m_{BC} distribution of this mode is centered at 2.112 GeV with a width of 0.010 GeV. The sideband regions extend from 2.060 to 2.102 GeV and 2.122 to 2.155 GeV. The maximum likelihood fits are displayed in Fig. 143 and the values for the scale parameters are presented in Table 47.

The signal region in the δm distribution of this mode is centered at 0.1438 GeV with a width of 0.016 GeV. The sideband regions extend from 0.1000 to 0.1278 GeV and 0.1598 to 0.2500 GeV. The maximum likelihood fits are displayed in Fig. 144 and the values for the scale parameters are presented in Table 47.

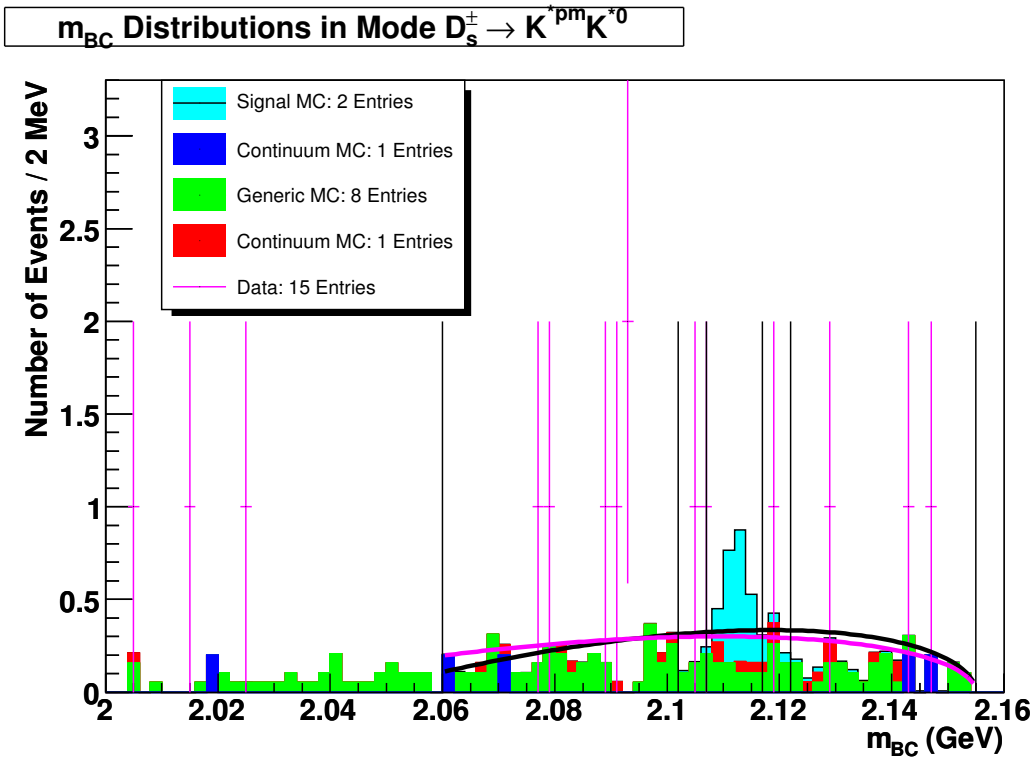

Figure 143: The various backgrounds and signal MC expected in the vicinity of the signal region in m_{BC} distribution of the $D_s^+ \to K^{*+}K^{*0}$ mode. The data, blinded in the signal region, is overlaid in magenta points. The black and magenta curves are *MC* and *data shapes* scaled by maximum likelihood to the points of data in the sideband regions.

The four different fits give us four estimates of the background in the signal region. These are tabulated in Table 48.

Table 47: Maximum likelihood fit parameters to estimate background in the $D_s^+ \to K^{*+}K^{*0}$ mode

Scale for Shape	Value
m_{BC} *MC shape*	1.25192e-01
δm *MC shape*	1.12174e-01
m_{BC} *data shape*	7.22271e-02
δm *data shape*	5.82375e-02

Table 48: Estimates of the background in the signal region of the $D_s^+ \to K^{*+}K^{*0}$ mode using four fits outlined above.

Mode	m_{BC}		δm	
	MC shape	*data shape*	*MC shape*	*data shape*
$K^{*+}K^{*0}$	1.65 ± 0.55	1.50 ± 0.50	2.21 ± 0.61	1.72 ± 0.48

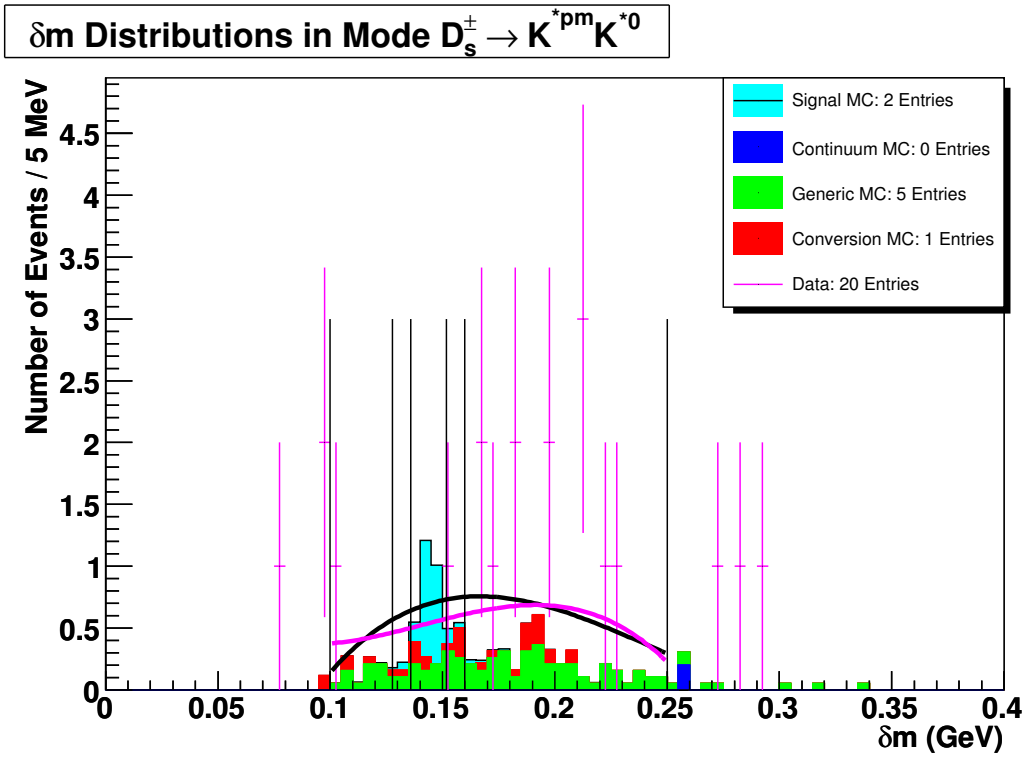

Figure 144: The various backgrounds and signal MC expected in the vicinity of the signal region in δm distribution of the $D_s^+ \to K^{*+}K^{*0}$ mode. The data, blinded in the signal region, is overlaid in magenta points. The black and magenta curves are *MC* and *data shapes* scaled by maximum likelihood to the points of data in the sideband regions.

12.10 Estimating the Background in the $D_s^+ \to \eta\rho^+; \eta \to \gamma\gamma; \rho^+ \to \pi^+\pi^0$ Mode

The signal region in the m_{BC} distribution of this mode is centered at 2.112 GeV with a width of 0.008 GeV. The sideband regions extend from 2.060 to 2.104 GeV and 2.120 to 2.155 GeV. The maximum likelihood fits are displayed in Fig. 145 and the values for the scale parameters are presented in Table 49.

The signal region in the δm distribution of this mode is centered at 0.1438 GeV with a width of 0.010 GeV. The sideband regions extend from 0.1000 to 0.1338 GeV and 0.1538 to 0.2500 GeV. The maximum likelihood fits are displayed in Fig. 146 and the values for the scale parameters are presented in Table 49.

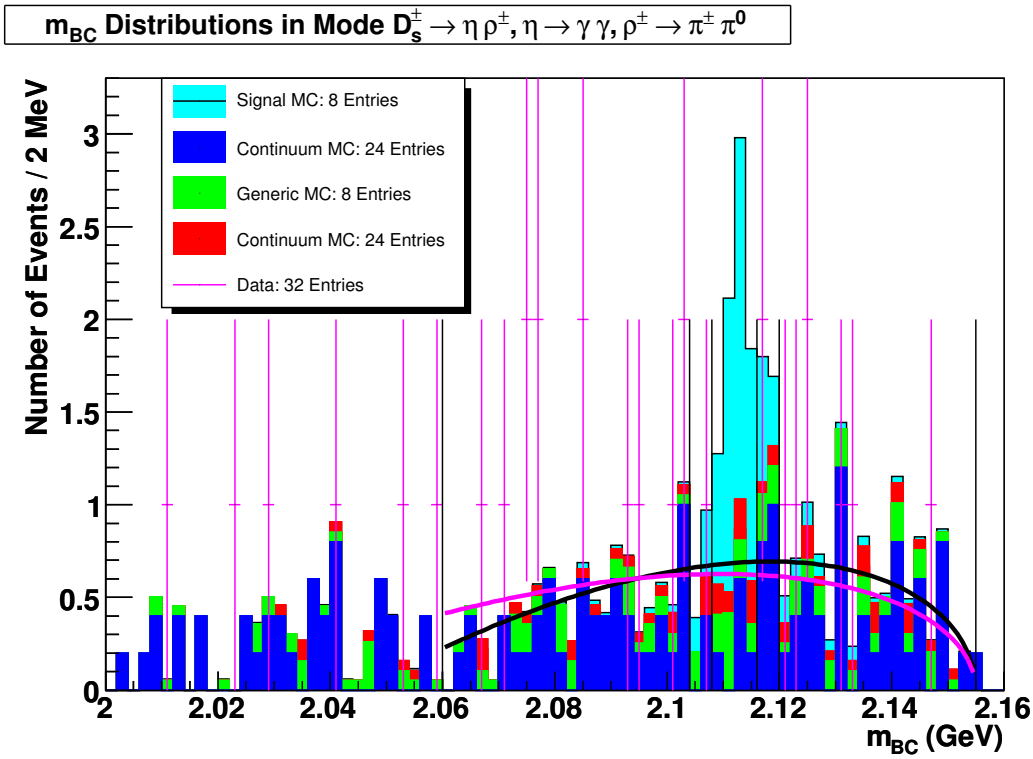

Figure 145: The various backgrounds and signal MC expected in the vicinity of the signal region in m_{BC} distribution of the $D_s^+ \to \eta\rho^+; \eta \to \gamma\gamma; \rho^+ \to \pi^+\pi^0$ mode. The data, blinded in the signal region, is overlaid in magenta points. The black and magenta curves are *MC* and *data shapes* scaled by maximum likelihood to the points of data in the sideband regions.

The four different fits give us four estimates of the background in the signal region. These are tabulated in Table 50.

Table 49: Maximum likelihood fit parameters to estimate background in the $D_s^+ \to \eta\rho^+; \eta \to \gamma\gamma; \rho^+ \to \pi^+\pi^0$ mode

Scale for Shape	Value
m_{BC} *MC shape*	2.59496e-01
δm *MC shape*	2.33921e-01
m_{BC} *data shape*	1.65995e-01
δm *data shape*	1.36454e-01

Table 50: Estimates of the background in the signal region of the $D_s^+ \to \eta\rho^+; \eta \to \gamma\gamma; \rho^+ \to \pi^+\pi^0$ mode using four fits outlined above.

Mode	m_{BC}		δm	
	MC shape	*data shape*	*MC shape*	*data shape*
$\eta\rho^+$	2.74 ± 0.61	2.50 ± 0.56	3.19 ± 0.54	2.52 ± 0.43

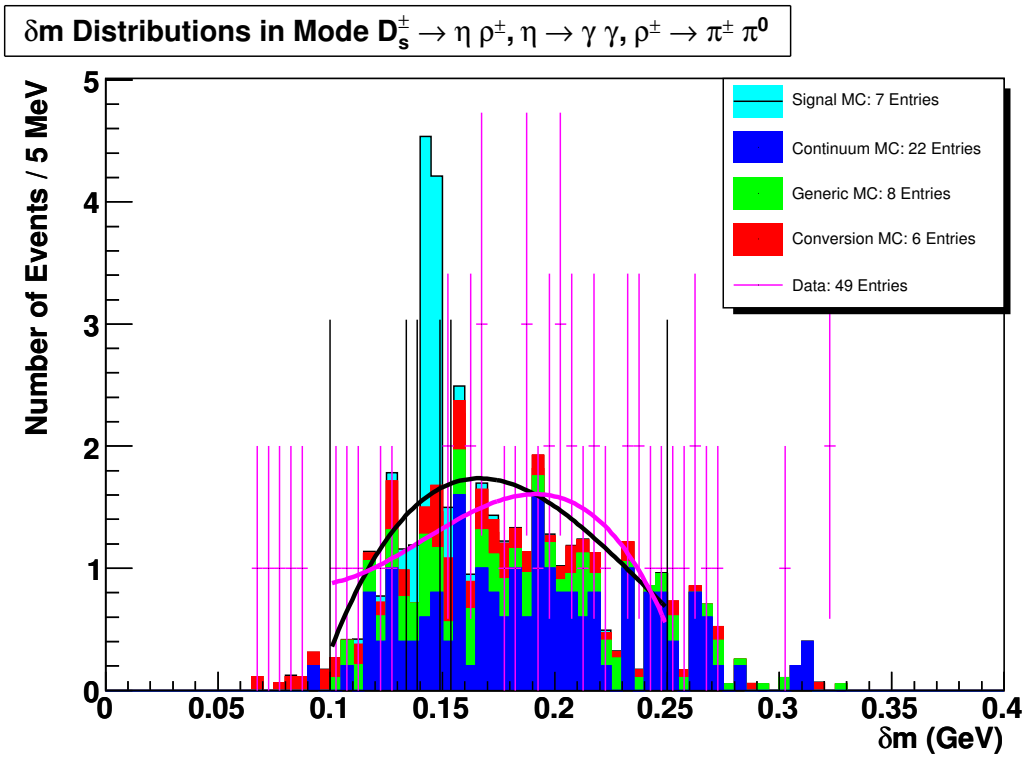

Figure 146: The various backgrounds and signal MC expected in the vicinity of the signal region in δm distribution of the $D_s^+ \to \eta\rho^+; \eta \to \gamma\gamma; \rho^+ \to \pi^+\pi^0$ mode. The data, blinded in the signal region, is overlaid in magenta points. The black and magenta curves are *MC* and *data shapes* scaled by maximum likelihood to the points of data in the sideband regions.

12.11 Estimating the Background in the $D_s^+ \to \eta'\pi^+; \eta' \to \rho^0\gamma$ Mode

The signal region in the m_{BC} distribution of this mode is centered at 2.112 GeV with a width of 0.008 GeV. The sideband regions extend from 2.060 to 2.104 GeV and 2.12 to 2.155 GeV. The maximum likelihood fits are displayed in Fig. 147 and the values for the scale parameters are presented in Table 51.

The signal region in the δm distribution of this mode is centered at 0.1438 GeV with a width of 0.014 GeV. The sideband regions extend from 0.1000 to 0.1298 GeV and 0.1578 to 0.2500 GeV. The maximum likelihood fits are displayed in Fig. 148 and the values for the scale parameters are presented in Table 51.

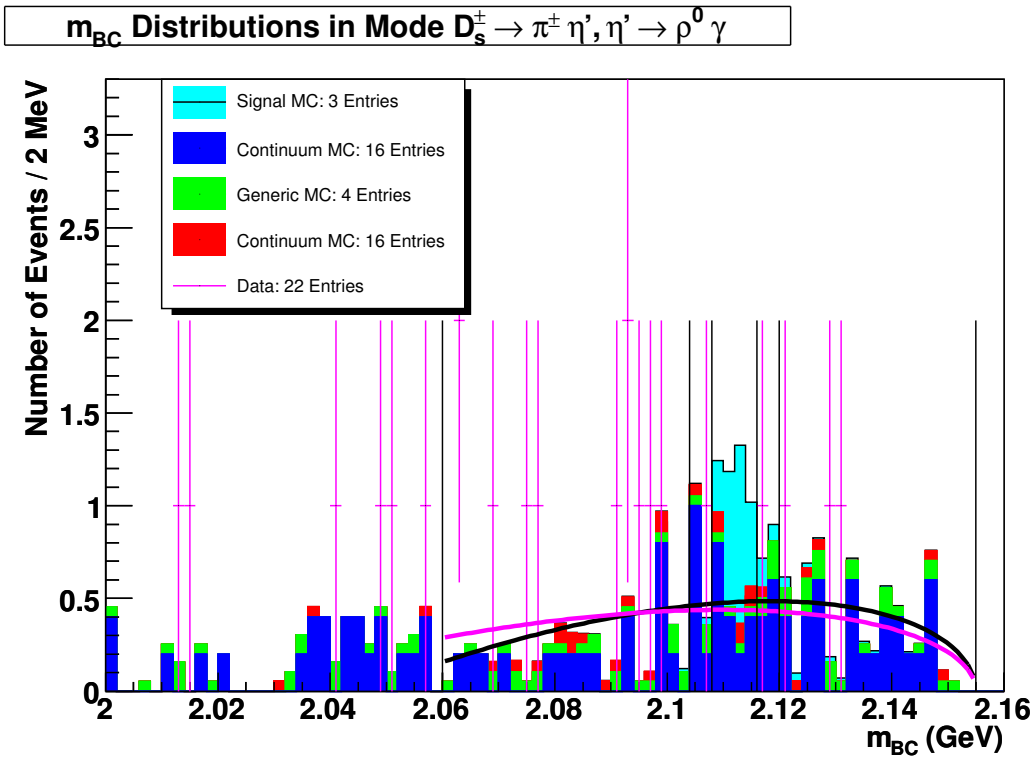

Figure 147: The various backgrounds and signal MC expected in the vicinity of the signal region in m_{BC} distribution of the $D_s^+ \to \eta'\pi^+; \eta' \to \rho^0\gamma$ mode. The data, blinded in the signal region, is overlaid in magenta points. The black and magenta curves are *MC* and *data shapes* scaled by maximum likelihood to the points of data in the sideband regions.

The four different fits give us four estimates of the background in the signal region. These are tabulated in Table 52.

Table 51: Maximum likelihood fit parameters to estimate background in the $D_s^+ \to \eta'\pi^+; \eta' \to \rho^0\gamma$ mode

Scale for Shape	Value
m_{BC} *MC shape*	1.81647e-01
δm *MC shape*	1.63745e-01
m_{BC} *data shape*	6.66708e-02
δm *data shape*	5.37577e-02

Table 52: Estimates of the background in the signal region of the $D_s^+ \to \eta'\pi^+; \eta' \to \rho^0\gamma$ mode using four fits outlined above.

Mode	m_{BC}		δm	
	MC shape	*data shape*	*MC shape*	*data shape*
$\eta'\pi^+$	1.92 ± 0.51	1.75 ± 0.47	1.79 ± 0.52	1.39 ± 0.40

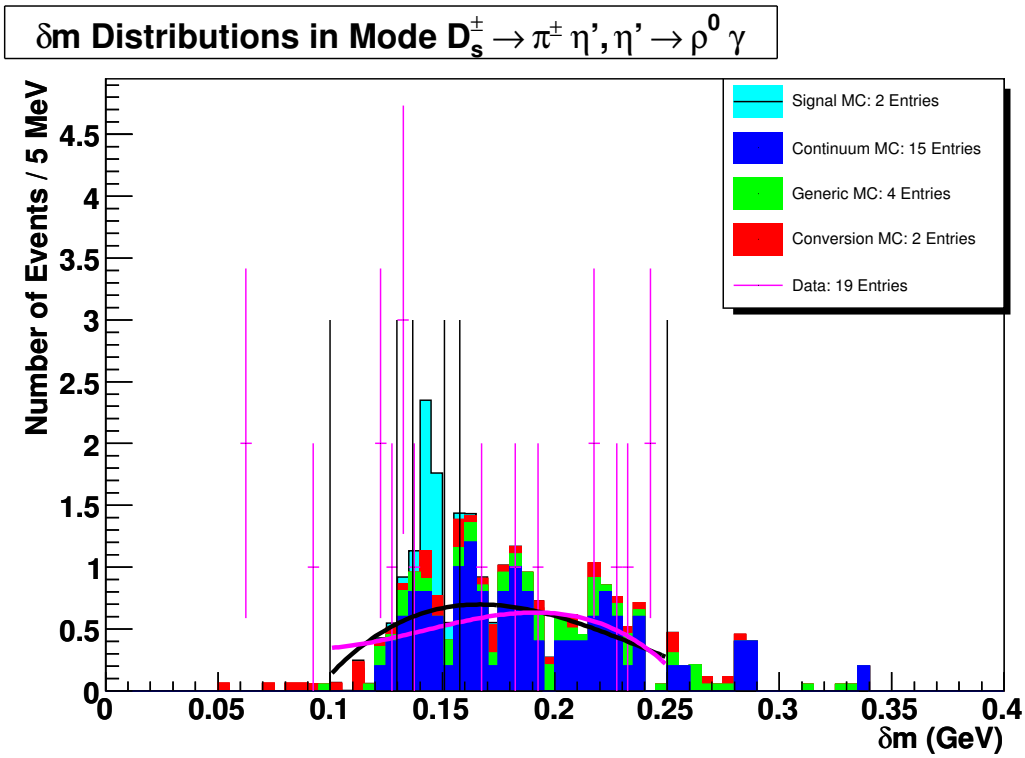

Figure 148: The various backgrounds and signal MC expected in the vicinity of the signal region in δm distribution of the $D_s^+ \to \eta'\pi^+; \eta' \to \rho^0\gamma$ mode. The data, blinded in the signal region, is overlaid in magenta points. The black and magenta curves are *MC* and *data shapes* scaled by maximum likelihood to the points of data in the sideband regions.

Table 53: Summary of the estimates for the background in the signal region for all the modes we have studied.

Mode	m_{BC}		δm		Background ± (Stat) ± (Syst)
	MC Shape	*Data Shape*	*MC Shape*	*Data Shape*	
$K^+K^-\pi^+$	1.10 ± 0.39	1.00 ± 0.35	2.06 ± 0.49	1.61 ± 0.38	1.05 ± 0.37 ± 0.79
K_SK^+	0.90 ± 0.45	0.80 ± 0.40	0.12 ± 0.12	0.10 ± 0.10	0.85 ± 0.43 ± 0.74
$\eta\pi^+$	1.48 ± 0.74	1.32 ± 0.66	1.02 ± 0.39	0.79 ± 0.30	1.40 ± 0.70 ± 0.49
$\eta'\pi^+;\eta' \to \pi^+\pi^-\eta$	0.00 + 0.68	0.00 + 0.59	0.00 + 0.34	0.00 + 0.26	0.00 + 0.63 + 0.00
$K^+K^-\pi^+\pi^0$	1.78 ± 0.49	1.63 ± 0.45	2.54 ± 0.54	1.99 ± 0.43	1.70 ± 0.47 ± 0.56
$\pi^+\pi^-\pi^+$	1.64 ± 0.48	1.50 ± 0.43	2.42 ± 0.53	1.90 ± 0.41	1.57 ± 0.45 ± 0.59
$K^{*+}K^{*0}$	1.65 ± 0.55	1.50 ± 0.50	2.21 ± 0.61	1.72 ± 0.48	1.58 ± 0.53 ± 0.40
$\eta\rho^+$	2.74 ± 0.61	2.50 ± 0.56	3.19 ± 0.54	2.52 ± 0.43	2.62 ± 0.59 ± 0.23
$\eta'\pi^+;\eta' \to \rho^0\gamma$	1.92 ± 0.51	1.75 ± 0.47	1.79 ± 0.52	1.39 ± 0.40	1.84 ± 0.49 ± 0.25

12.12 Summary of Estimated Background in the Various Modes

Given that we determined the shape of the m_{BC} distribution in Section 12.1 without loosening other cuts (as we did for the δm distribution), that the distribution itself is less peaked, and that the difference between the predictions of the *MC shape* and *data shape* is lower than in the δm distribution, we choose to use the predictions of this distribution as the primary estimate of the backgrounds in each mode.

For each mode, we quote the mean of the *MC shape* and *data shape* predictions in the m_{BC} distribution as the estimate of the background we expect in the signal region for that mode. The statistical errors from these two predictions are averaged to obtain the statistical error for this estimate. The absolute value of the difference between this estimate and the mean of the predictions from the two shapes in the δm distribution is quoted as the systematic error. This is tabulated for each mode in Table 53

12.13 Predicted Signal Significances

It is clear from our optimization and background estimation studies that we do not expect equally significant results from each of the hadronic decay modes we are studying. For instance, it is clear that the $D_s^+ \to K^+K^-\pi^+$ decay mode will contribute more significantly than any other mode due to the marked excess of expected signal yield over the estimated background in its signal region. It therefore behooves us to establish a clear measure of signal significance over estimated background, calculate what signal significance we expect in each mode based on a Monte Carlo estimate of the signal and the background we've estimated from data in section 12.12, and converge on a group of modes to unblind together in order to achieve the most significant result.

In order to establish a measure of our signal significance, we assume that the uncertainty in our estimated background is shaped as a Gaussian with a standard deviation equal to the quadrature sum of the statistical and systematic uncertainties in the estimated background.

Then we calculate the Poisson probability of such a background fluctuating to higher than the number of events we find in the signal region on unblinding. In effect, we convolute a Gaussian smeared background with a Poisson distribution to model the probability of it fluctuating to the yield we see in data. So, if we call the background estimate b with a standard deviation of σ, and unblind our data to discover n events in the signal region, we may estimate the probability for it to be a fluctuation of the background as P given in Eq. 65. We may express this probability, P, in terms of the number of standard deviations in a Gaussian that one must go out to in order to exclude a region of such probability, and we will use this number as a measure of signal significance.

$$P(b,\sigma,n) = \frac{\sum_{i=n}^{i=\infty} \int_{x=0}^{x=\infty} \frac{x^i}{i!} e^{-[x+\frac{1}{2}(\frac{x-b}{\sigma})^2]} dx}{\int_{x=0}^{x=\infty} e^{-\frac{1}{2}(\frac{x-b}{\sigma})^2} dx} \tag{65}$$

The signal significance projected for each individual hadronic decay mode of the D_s^+ is tabulated in Table 54. The uncertainty on the estimated background is the quadrature sum of the statistical and systematic uncertainties. The projected signal is estimated by Monte Carlo. As expected, the $D_s^+ \to K^+K^-\pi^+$ mode is projected to give us the highest signal significance among individual modes of 5.40. However, we notice that summing all modes can give us a significance of 6.39, which is higher than any of the individual mode. We discover that discarding $D_s^+ \to \eta'\pi^+; \eta' \to \pi^+\pi^-\eta$, the mode of lowest significance, from the sum of all modes gives us a higher total significances of 6.51. However, if we discard the next mode of lowest signal significance, the $D_s^+ \to \eta\pi^+; \eta \to \gamma\gamma$, our total signal significance begins to drop. The increase in signal significance from 6.39 to 6.51 corresponds to an decrease in probability from 1.70×10^{-10} to 7.34×10^{-11}. We decide to forgo this decrease for an already remarkably low value of probability in order to keep the yield in signal we expect to get from unblinding all modes together.

Table 54: The projected signal significance expected for each individual hadronic decay mode of the D_s^+, as well as various modes combined.

Hadronic Decay Mode	Estimated Background	Projected Signal	Signal Significance
$K^+K^-\pi^+$	$1.05 \pm 0.37 \pm 0.79$	13.65	5.40
K_SK^+	$0.85 \pm 0.43 \pm 0.74$	3.02	1.95
$\eta\pi^+$ (2)	$1.40 \pm 0.70 \pm 0.49$	1.81	1.25
$\eta'\pi^+; \eta' \to \pi^+\pi^-\eta$ (1)	$0.00 + 0.63 + 0.00$	1.20	0.98
$K^+K^-\pi^+\pi^0$	$1.70 \pm 0.47 \pm 0.56$	4.85	2.71
$\pi^+\pi^-\pi^+$	$1.57 \pm 0.45 \pm 0.59$	3.75	2.03
$K^{*+}K^{*0}$	$1.58 \pm 0.53 \pm 0.40$	1.99	1.65
$\eta\rho^+; \eta \to \gamma\gamma$	$2.62 \pm 0.59 \pm 0.23$	5.49	2.59
$\eta'\pi^+$	$1.84 \pm 0.49 \pm 0.25$	2.42	1.52
Sum of All Modes	$12.60 \pm 2.50 \pm 1.08$	38.18	6.39
Sum except (1)	$12.60 \pm 2.10 \pm 1.08$	36.98	6.51
Sum except (1) & (2)	$11.20 \pm 1.61 \pm 2.25$	35.17	6.35

12.14 Check on the Modeling of Material in the Detector

In order to make sure that the Monte Carlo simulation models the material budget of the detector that contributes towards the conversion of photons into e^+e^- pairs, we draw up a comparison between the number of conversion-type events in Monte Carlo and data. To select for conversion-type events, we look on the "wrong-side" of the Δd_0 and $\Delta\phi_0$ criteria. Such a comparison is presented in Table 55. The ratio data/MC for the conversion-type events is found to be 1.12 ± 0.19, which makes it consistent with accurate modeling of the material.

Table 55: A comparison between the numbers of conversion-type events in the Monte Carlo and data. The *Signal MC* column contains the number of events from $D_s^{*+} \to D_s^+ e^+ e^-$ MC that remain after our criteria that select out conversion-type events. *Conversion MC* contain numbers of events from $D_s^{*+} \to D_s^+ \gamma$ MC that remain. *Generic MC* contain numbers of events from Generic MC simulation where $D_s^{*+} \to D_s^+ \gamma$ events have been rejected at the level of event generation. *Continuum MC* contains numbers of light-quark phenomena that remain after our criteria. *Sum MC* is the sum of the aforementioned numbers from Monte Carlo simulations. *Data* contains the number of events left in data. The ratio of numbers of data over Monte Carlo events are summarized in the data/MC column.

Hadronic Decay Mode	Signal MC	Conversion MC	Generic MC	Continuum MC	Sum MC	Data	$\frac{\text{data}}{\text{MC}}$
$K^+K^-\pi^+$	3.1 ± 0.21	7.6 ± 0.69	1.1 ± 0.25	0 ± 0	8.8 ± 0.74	9 ± 3	1 ± 0.35
$K_S K^+$	0.65 ± 0.048	2.1 ± 0.35	0.52 ± 0.17	0 ± 0	2.7 ± 0.39	2 ± 1.4	0.75 ± 0.54
$\eta\pi^+$	0.38 ± 0.025	1.3 ± 0.27	0 ± 0	1.2 ± 0.49	2.5 ± 0.56	2 ± 1.4	0.81 ± 0.6
$\eta'\pi^+; \eta' \to \pi^+\pi^-\eta$	0.32 ± 0.023	0.96 ± 0.24	0.1 ± 0.074	0 ± 0	1.1 ± 0.25	2 ± 1.4	1.9 ± 1.4
$K^+K^-\pi^+\pi^0$	1.1 ± 0.11	2.2 ± 0.36	3.1 ± 0.42	0.8 ± 0.4	6.2 ± 0.69	10 ± 3.2	1.6 ± 0.54
$\pi^+\pi^-\pi^+$	0.78 ± 0.049	2.6 ± 0.39	0.68 ± 0.19	2.4 ± 0.69	5.7 ± 0.82	10 ± 3.2	1.8 ± 0.61
$K^{*+}K^{*0}$	0.47 ± 0.041	1.3 ± 0.28	2 ± 0.33	0.2 ± 0.2	3.5 ± 0.48	0 ± 0	$0 \pm$ nan
$\eta\rho^+$	1.1 ± 0.11	1.9 ± 0.33	1.2 ± 0.25	2.6 ± 0.72	5.7 ± 0.83	2 ± 1.4	0.35 ± 0.26
$\eta'\pi^+; \eta' \to \rho^0\gamma$	0.53 ± 0.038	1.6 ± 0.3	1.1 ± 0.25	2.4 ± 0.69	5.1 ± 0.8	0 ± 0	$0 \pm$ nan
Total	8.43 ± 0.28	21.56 ± 1.14	9.80 ± 0.74	9.60 ± 1.38	41.3 ± 1.95	37 ± 6.1	1.12 ± 0.19

Mode	Signal Selection Efficiency
$K^+K^-\pi^+$	0.0729375 ± 0.00191083
K_SK^+	0.0596716 ± 0.00172834
$\eta\pi^+$	0.0854525 ± 0.00206827
$\eta'\pi^+$	0.0530136 ± 0.00162907
$K^+K^-\pi^+\pi^0$	0.0254806 ± 0.00112941
$\pi^+\pi^-\pi^+$	0.0992191 ± 0.00222866
$K^{*+}K^{*0}$	0.0355927 ± 0.00133483
$\eta\rho^+$	0.0315879 ± 0.00125749
$\eta'\pi^+$	0.0637765 ± 0.0017868

Table 56: Selection efficiencies for reconstructing the $D_s^{*+} \to D_s^+e^+e^-$ signal in each of the decay modes of the D_s^+.

13 Efficiency of Selection Criteria for reconstructing $D_s^{*+} \to D_s^+e^+e^-$

In order to estimate the branching fraction for our signal channel, $D_s^{*+} \to D_s^+e^+e^-$, and ultimately the ratio of branching fractions:

$$K = \frac{B(D_s^{*+} \to D_s^+e^+e^-)}{B(D_s^{*+} \to D_s^+\gamma)}$$

we need to know the efficiency of our selection criteria for each of the hadronic decay modes of the D_s^+ meson. This is determined by applying our selection criteria on the Monte Carlo simulations of our signal in each of the modes. The efficiency for each mode may be calculated by dividing the number of sample events remaining within the signal region of the m_{BC} distribution, having applied all other cuts, by the number of produced sample events. Such distributions of the m_{BC} for each mode with marked signal regions are presented in Fig. 149 - 157. Measurements of these selection efficiencies are presented in Table 56.

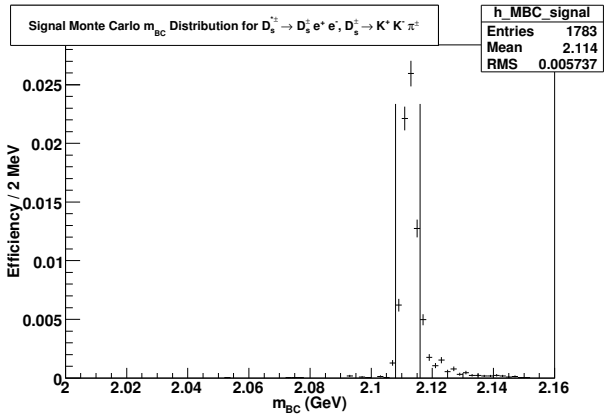

Figure 149: Signal efficiency for reconstructing $D_s^{*+} \to D_s^+ e^+ e^-$ in $D_s^+ \to K^+ K^- \pi^+$ as represented in the m_{BC} distribution.

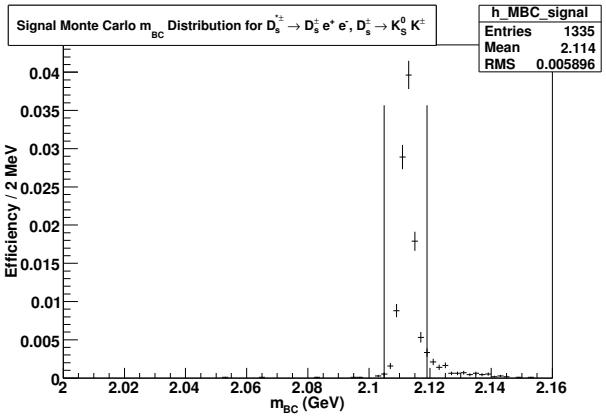

Figure 150: Signal efficiency for reconstructing $D_s^{*+} \to D_s^+ e^+ e^-$ in $D_s^+ \to K_S K^+$ as represented in the m_{BC} distribution.

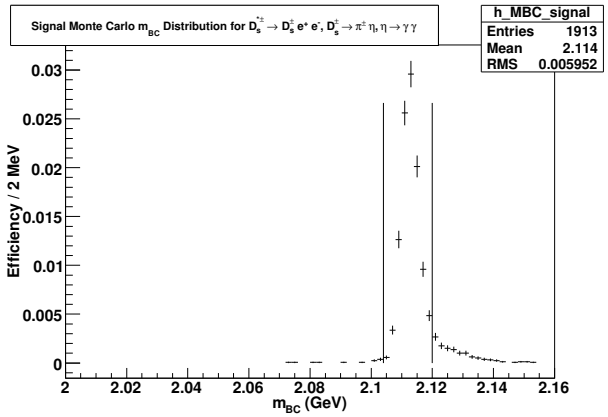

Figure 151: Signal efficiency for reconstructing $D_s^{*+} \to D_s^+ e^+ e^-$ in $D_s^+ \to \eta \pi^+$ as represented in the m_{BC} distribution.

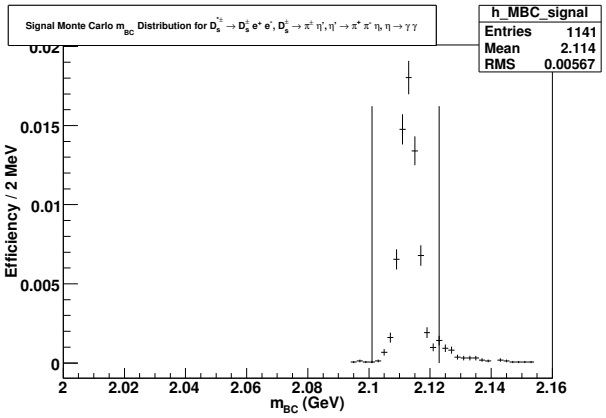

Figure 152: Signal efficiency for reconstructing $D_s^{*+} \to D_s^+ e^+ e^-$ in $D_s^+ \to \eta' \pi^+$ as represented in the m_{BC} distribution.

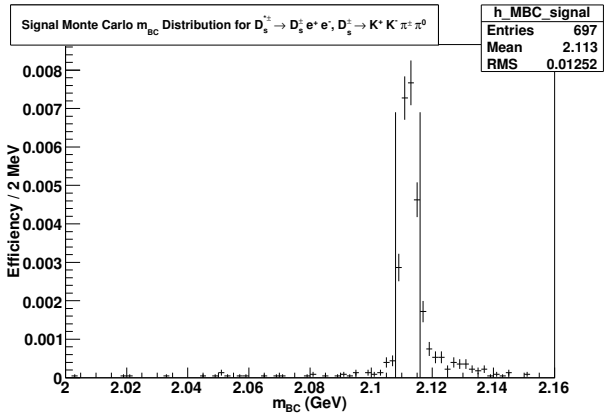

Figure 153: Signal efficiency for reconstructing $D_s^{*+} \to D_s^+ e^+ e^-$ in $D_s^+ \to K^+ K^- \pi^+ \pi^0$ as represented in the m_{BC} distribution.

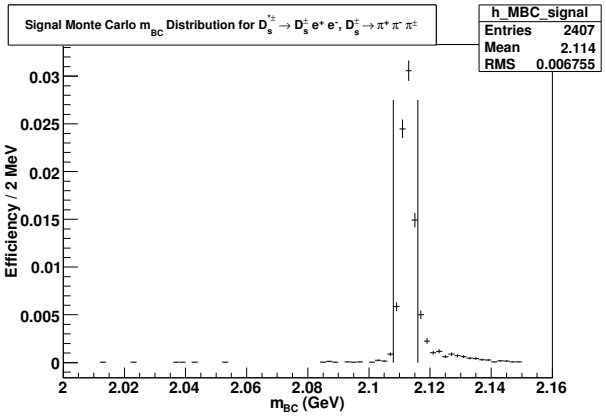

Figure 154: Signal efficiency for reconstructing $D_s^{*+} \to D_s^+ e^+ e^-$ in $D_s^+ \to \pi^+ \pi^- \pi^+$ as represented in the m_{BC} distribution.

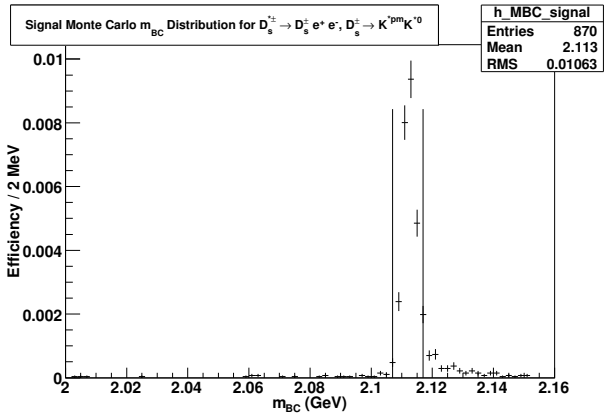

Figure 155: Signal efficiency for reconstructing $D_s^{*+} \to D_s^+ e^+ e^-$ in $D_s^+ \to K^{*+} K^{*0}$ as represented in the m_{BC} distribution.

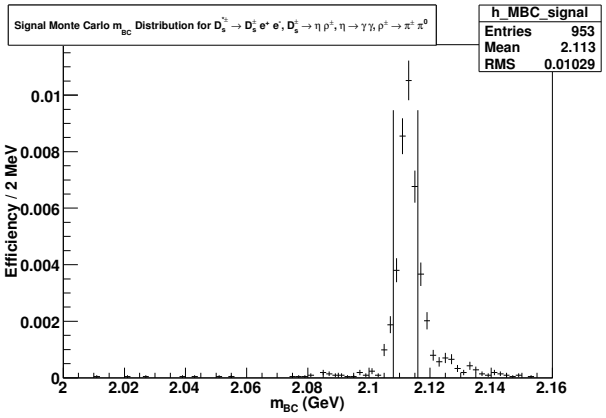

Figure 156: Signal efficiency for reconstructing $D_s^{*+} \to D_s^+ e^+ e^-$ in $D_s^+ \to \eta \rho^+$ as represented in the m_{BC} distribution.

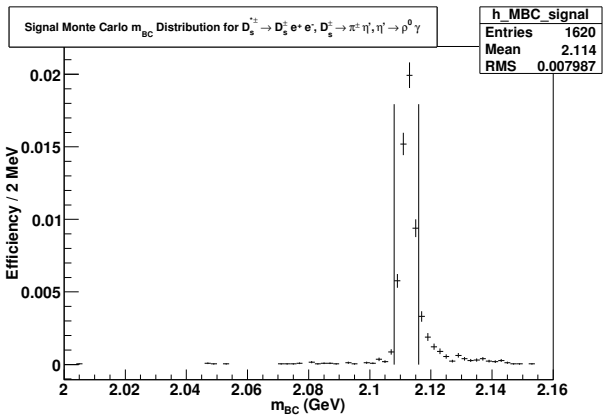

Figure 157: Signal efficiency for reconstructing $D_s^{*+} \to D_s^+ e^+ e^-$ in $D_s^+ \to \eta' \pi^+$ as represented in the m_{BC} distribution.

14 Signal Yields and Selection Efficiencies for $D_s^{*+} \to D_s^+\gamma$

In this section, we measure the selection efficiencies and yields for $D_s^{*+} \to D_s^+\gamma$ where the D_s^+ decays through the 9 hadronic decays modes we have focused on for this analysis. For all modes, we begin by generating a Monte Carlo sample of $D_s^{*+} \to D_s^+\gamma$ where the D_s^+ is forced to decay through the mode we are investigating while the D_s^- is allowed to decay generically. Selection criteria very similar to those used for the corresponding $D_s^{*+} \to D_s^+e^+e^-$ analysis are used, though with a wider δm selection criterion. The reason for this can be seen from the δm distribution of the $K^+K^-\pi^+$ channel as shown in Fig. 158. The low-end tail implies that a loss in the reconstructed energy of photons is expected. This may not be well modeled in Monte Carlo, and to avoid possible discrepancies between Monte Carlo and data in that region, a larger region containing the peak is selected. Next, we study the m_{BC} distribution of various backgrounds where the D_s^{*+} is incorrectly reconstructed using the D_s^-. These backgrounds are accounted for in data before calculating the signal yield for each mode, as summarized in Table 57 along with the signal selection efficiencies. The calculated branching fraction $B(D_s^{*+} \to D_s^+\gamma)$ does not include an estimate for the systematic uncertainty arising from the reconstruction of the D_s^+ and γ and hence is not a result we shall publish. It is presented as a check on our method of obtaining the signal yields and selection efficiencies. We expect the uncertainty from the reconstruction of the D_s^+ to cancel between $B(D_s^{*+} \to D_s^+e^+e^-)$ and $B(D_s^{*+} \to D_s^+\gamma)$ and hence report this ratio. A similar summary for the generic MC is presented in Table 58. Discrepancies between the recovered branching fractions and the value for it programmed into the Generic Monte Carlo simulation result from inconsistencies between the decay models of the D_s^+ in the Generic Monte Carlo and our signal Monte Carlo simulations. The manner in which we measure our signal selection efficiency and evaluate the various backgrounds before we estimate the signal yield is described in detail for the $K^+K^-\pi^+$ mode.

Table 57: Signal yields and efficiencies for $D_s^{*+} \to D_s^+\gamma$ from all the modes of decay of the D_s^+ relevant for our measurement of the ratio $B(D_s^{*+} \to D_s^+e^+e^-)/B(D_s^{*+} \to D_s^+\gamma)$. $B(D_s^+ \to i)$ is the known branching fraction for D_s^+ to decay via the i^{th} hadronic mode we are studying. $\epsilon^i_{D_s\gamma}$ is the efficiency of our selection criteria for the mode. $N^i_{D_s\gamma}$ is the signal yield observed for this mode. $B(D_s^{*+} \to D_s^+\gamma)$ is the branching fraction for $D_s^{*+} \to D_s^+e^+e^-$ inferred from this mode. Error [1] on the inferred branching fraction is the statistical error from the final fit. Error [2] arises from the uncertainty in the branching fraction for $D_s^+ \to i$. Error [3] encapsulates the systematic uncertainties from the signal efficiency, the integrated luminosity and the production cross section for $D_s^{*\pm}D_s^{\mp}$. Error [4] encapsulates the systematic error arising from the fit. *Disclaimer:* This estimate of the branching fraction for $D_s^{*+} \to D_s^+\gamma$ does not include systematic uncertainties from the reconstruction of the D_s^+ and γ, and therefore shall not be published as an independent result. It is presented here for a swift check on our method of obtaining the signal yields and efficiencies.

i (Decay Mode of D_s^+)	$B(D_s^+ \to i)$	$\epsilon^i_{D_s\gamma}$	$N^i_{D_s\gamma} \pm (stat) \pm (syst)$	$B(D_s^{*+} \to D_s^+\gamma)$ Inferred
$K^+K^-\pi^+$	0.055 ± 0.0028	0.339 ± 0.002	$9114 \pm 110 \pm 201$	$0.880 \pm 0.011^{[1]} \pm 0.045^{[2]} \pm 0.035^{[3]} \pm 0.019^{[4]}$
K_SK^+	0.0149 ± 0.0009	0.2573 ± 0.0004	$1902 \pm 57 \pm 45$	$0.893 \pm 0.027^{[1]} \pm 0.054^{[2]} \pm 0.035^{[3]} 0.021^{[4]}$
$D_s^+ \to \eta\pi^+; \eta \to \gamma\gamma$	0.00621 ± 0.00083	0.3310 ± 0.0015	$1037 \pm 46 \pm 37$	$0.908 \pm 0.040^{[1]} \pm 0.121^{[2]} \pm 0.036^{[3]} \pm 0.032^{[4]}$
$D_s^+ \to \eta'\pi^+; \eta' \to \pi^+\pi^-\eta; \eta \to \gamma\gamma$	0.00666 ± 0.00070	0.2101 ± 0.0013	$691 \pm 34 \pm 40$	$0.889 \pm 0.043^{[1]} \pm 0.094^{[2]} \pm 0.035^{[3]} \pm 0.052^{[4]}$
$D_s^+ \to K^+K^-\pi^+\pi^0$	0.056 ± 0.005	0.1225 ± 0.0010	$3592 \pm 118 \pm 72$	$0.943 \pm 0.031^{[1]} \pm 0.085^{[2]} \pm 0.038^{[3]} \pm 0.019^{[4]}$
$D_s^+ \to \pi^+\pi^-\pi^+$	0.0111 ± 0.0008	0.4583 ± 0.0018	$2745 \pm 93 \pm 52$	$0.971 \pm 0.033^{[1]} \pm 0.070^{[2]} \pm 0.038^{[3]} \pm 0.018^{[4]}$
$D_s^+ \to K^{*+}K^{*0}$	0.0164 ± 0.0012	0.1913 ± 0.0012	$1570 \pm 74 \pm 13$	$0.900 \pm 0.043^{[1]} \pm 0.066^{[2]} \pm 0.036^{[3]} \pm 0.007^{[4]}$
$D_s^+ \to \eta\rho^+; \eta \to \gamma\gamma; \rho^+ \to \pi^+\pi^0$	0.0348 ± 0.0031	0.1839 ± 0.0013	$3170 \pm 161 \pm 313$	$0.891 \pm 0.045^{[1]} \pm 0.080^{[2]} \pm 0.036^{[3]} \pm 0.088^{[4]}$
$D_s^+ \to \eta'\pi^+; \eta' \to \rho^0\gamma$	0.0112 ± 0.0012	0.3171 ± 0.0015	$1531 \pm 80 \pm 122$	$0.778 \pm 0.041^{[1]} \pm 0.085^{[2]} \pm 0.031^{[3]} \pm 0.062^{[4]}$

Table 58: Signal yields and efficiencies for $D_s^{*+} \to D_s^+\gamma$ from all the modes of decay of the D_s^+ relevant for our measurement of the ratio $B(D_s^{*+} \to D_s^+e^+e^-)/B(D_s^{*+} \to D_s^+\gamma)$ in Generic Monte Carlo. $B(D_s^+ \to i)$ is the known branching fraction for D_s^+ to decay via the i^{th} hadronic mode we are studying. $\epsilon^i_{D_s\gamma}$ is the efficiency of our selection criteria for the mode. $N^i_{D_s\gamma}$ is the signal yield observed for this mode. $B(D_s^{*+} \to D_s^+\gamma)$ is the branching fraction for $D_s^{*+} \to D_s^+e^+e^-$ inferred from this mode. Error [1] on the inferred branching fraction is the statistical error from the final fit. Error [2] encapsulates the systematic uncertainties from the signal efficiency and the uncertainty in the number of produced generic MC events as described in Section 7.1.

i (Mode)	$B(D_s^+ \to i)$	$\epsilon^i_{D_s\gamma}$	$N^i_{D_s\gamma}$	$B(D_s^{*+} \to D_s^+\gamma)$
$K^+K^-\pi^+$	0.0537	0.339 ± 0.002	9364 ± 40	$0.9259 \pm 0.0040^{[1]} \pm 0.0043^{[2]}$
K_SK^+	0.01465	0.25727 ± 0.00043	2006 ± 17	$0.9581 \pm 0.0083^{[1]} \pm 0.0018^{[2]}$
$D_s^+ \to \eta\pi^+; \eta \to \gamma\gamma$	0.0061	0.3310 ± 0.0015	998 ± 27	$0.8933 \pm 0.0240^{[1]} \pm 0.0043^{[2]}$
$D_s^+ \to \eta'\pi^+; \eta' \to \pi^+\pi^-\eta; \eta \to \gamma\gamma$	0.00633	0.2101 ± 0.0013	690 ± 11	$0.9341 \pm 0.0149^{[1]} \pm 0.0058^{[2]}$
$D_s^+ \to K^+K^-\pi^+\pi^0$	0.0525	0.1225 ± 0.0010	3178 ± 49	$0.8894 \pm 0.0138^{[1]} \pm 0.0073^{[2]}$
$D_s^+ \to \pi^+\pi^-\pi^+$	0.0103	0.4583 ± 0.0018	2706 ± 43	$1.0327 \pm 0.0162^{[1]} \pm 0.0041^{[2]}$
$D_s^+ \to K^{*+}K^{*0}$	0.01628	0.1913 ± 0.0012	1644 ± 22	$0.9502 \pm 0.0129^{[1]} \pm 0.0058^{[2]}$
$D_s^+ \to \eta\rho^+; \eta \to \gamma\gamma; \rho^+ \to \pi^+\pi^0$	0.0298	0.1839 ± 0.0013	2993 ± 87	$0.9829 \pm 0.0284^{[1]} \pm 0.0070^{[2]}$
$D_s^+ \to \eta'\pi^+; \eta' \to \rho^0\gamma$	0.0111	0.3171 ± 0.0015	1930 ± 45	$0.9886 \pm 0.0231^{[1]} \pm 0.0049^{[2]}$

Table 59: Selection criteria for $D_s^{*+} \to D_s^+\gamma$ events where $D_s^+ \to K^+K^-\pi^+$. The δm cut has been widened to accomodate the wider peak for the signal in this distribution.

Selection Criterion	Cut Center ± Width
$m_{D_s^+}$	1.969 ± 0.011 GeV
δm	0.140 ± 0.02 GeV
γ Shower Energy	10 MeV to 2.0 GeV
γ Hot Crystals	None
Tracks Matched to γ	None
γ E9/E25 Unfolded	99 percentile

14.1 $D_s^+ \to K^+K^-\pi^+$

We begin with a Monte Carlo signal sample of $D_s^{*+} \to D_s^+\gamma$ events where D_s^+ decays to $K^+K^-\pi^+$ and the D_s^- is allowed to decay generically. The selection criteria applied are tabulated in Table 59. Instead of the cuts on Δd_0 and $\Delta\phi_0$, which are applicable to the soft e^+e^- pair, we have some selection criteria on the γ that is kept common across all modes of decay of the D_s^+ and shall not be repeated in subsequent tables of this section. A plot of the δm distribution is presented in Fig. 158.

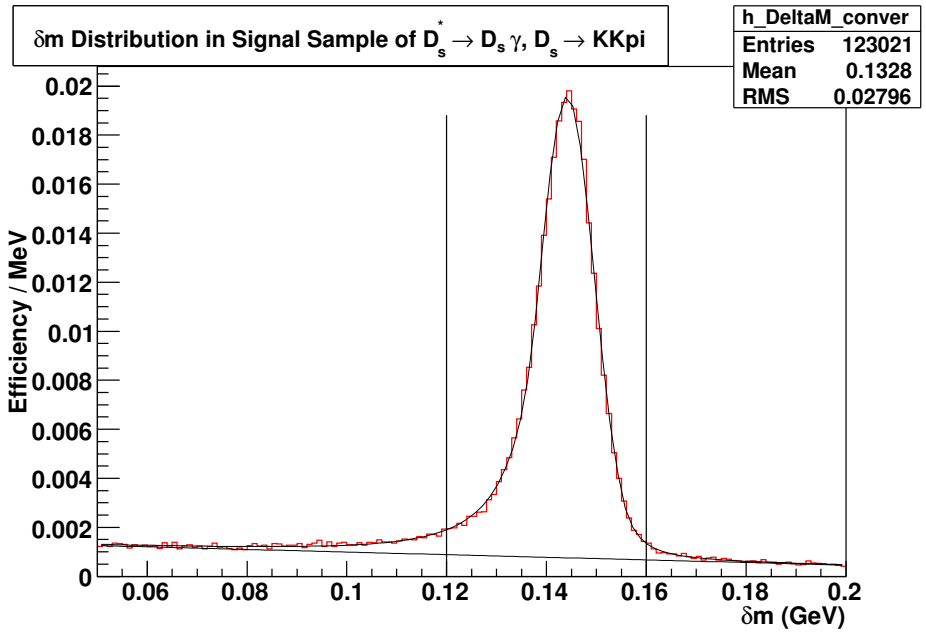

Figure 158: Distribution of δm in the signal Monte Carlo sample of $D_s^{*+} \to D_s^+\gamma$ events where $D_s^+ \to K^+K^-\pi^+$. The plot is normalized so as to directly read out the efficiency of the δm selection criterion.

To obtain the selection efficiency using the condition on m_{BC} as our last selection criterion, we produce a plot of the m_{BC} distribution of the signal sample, having applied all

other criteria, as shown in Fig. 159. For a handle on the shape of the peak in this plot, we produce one more plot – that of m_{BC} where the D_s^+ and the photon are matched to their generated counterparts in the Monte Carlo simulation. This plot, shown in Fig. 160, is fitted to a Crystal Ball function of the form given in Eq. 66 that has the power law shoulder on the higher side of the central peak and also contains a wide Gaussian on this shoulder. The shape of this peak is attenuated by a scaling factor and added to a background shape modeled by Eq. 67 to fit the m_{BC} distribution of the signal Monte Carlo between 2.08 and 2.15 GeV as shown in 159. The signal efficiency of our selection criteria is read off from this plot as the integral of the fit to the data within the marked region minus the background curve within that region.

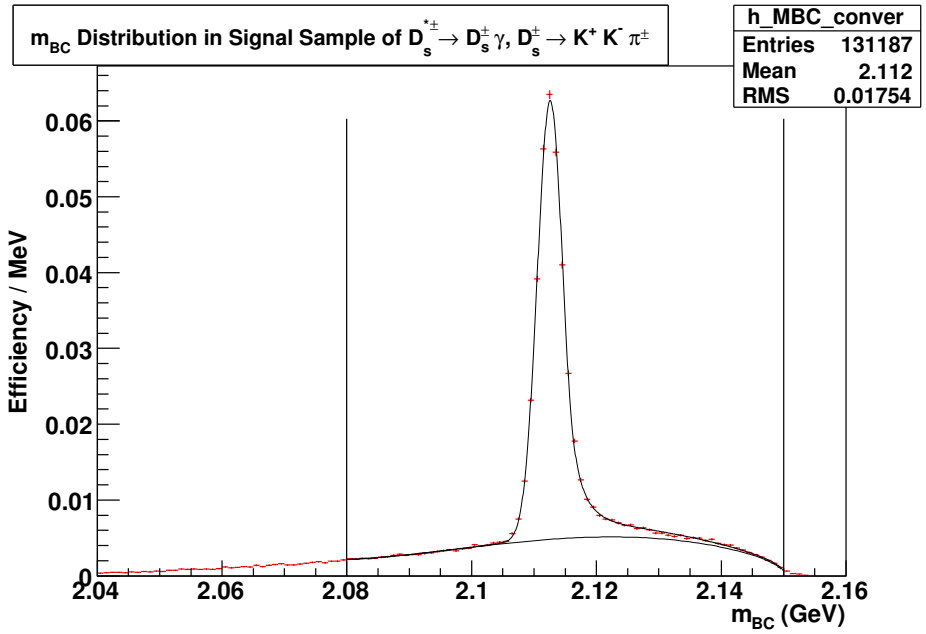

Figure 159: Distribution of m_{BC} in the signal Monte Carlo sample of $D_s^{*+} \to D_s^+\gamma$ events where $D_s^+ \to K^+K^-\pi^+$. The plot is normalized so as to directly read out the efficiency of the m_{BC} selection criterion.

$$
\begin{aligned}
f(x;\bar{x_0},\sigma_0,\alpha,n,N_0,\bar{x_1},\sigma_1,N_1) &= N_1 \exp\left(-\frac{(x-\bar{x_1})^2}{2\sigma_1^2}\right) \\
&+ N_0 \cdot \left\{ \begin{array}{ll} A\cdot\left(B+\frac{x-\bar{x_0}}{\sigma_0}\right)^{-n}, & \text{for} \quad \alpha < \frac{x-\bar{x_0}}{\sigma_0} \\ \exp\left(-\frac{(x-\bar{x_0})^2}{2\sigma_0^2}\right), & \text{for} \quad \frac{x-\bar{x_0}}{\sigma_0} \leq \alpha \end{array} \right\} \quad (66)
\end{aligned}
$$

where

$$A = \left(\frac{n}{\alpha}\right)^n \exp\left(-\frac{\alpha^2}{2}\right),$$

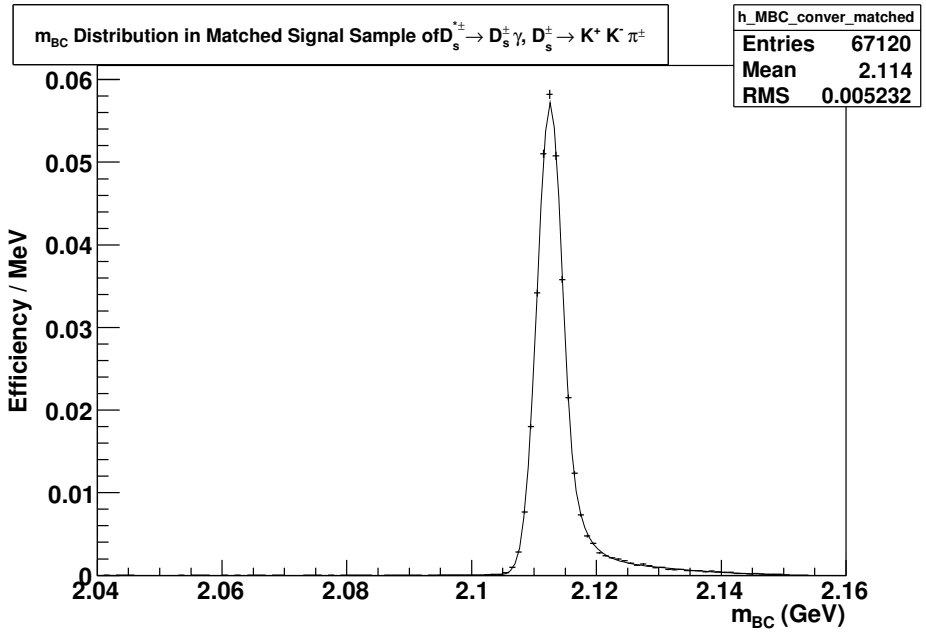

Figure 160: Distribution of m_{BC} in the signal Monte Carlo sample of $D_s^{*+} \to D_s^+\gamma$ events where $D_s^+ \to K^+K^-\pi^+$.

$$B = \frac{n}{\alpha} - \alpha$$

$$f(x; x_0, p, C_0, C_1, C_2, C_3) = (C_0 + C_1 x + C_2 x^2 + C_3 x^3)(x - x_0)^p, \quad 0 < p < 1 \tag{67}$$

The m_{BC} distribution in data contain more features than just a signal peak. A structured background emerges from events where our selection criteria reconstructs the D_s^{*+} incorrectly using the D_s^- and the γ. The D_s^- would then have been reconstructed from its decay to $K^+K^-\pi^-$. A Monte Carlo sample where the D_s^{*+} decays to $D_s^+\gamma$ but only the D_s^- is forced to decay to $K^+K^-\pi^-$ is generated to help us model this background in data. For reasons that will soon become clear, this background is decomposed into two components. The first includes cases where the D_s^- and the photon are matched to their generated counterparts in Monte Carlo. The m_{BC} distribution of these events is shown in Fig. 161. The second component includes cases where the D_s^- has been matched but the photon failed to match the photon from the D_s^{*+} decay at the generator level of the Monte Carlo simulation. These events have m_{BC} distributed as shown in Fig. 162. These two components are cleft apart and fitted separately in data because there is no reason for such combinatorial backgrounds to maintain the same ratio to one another as modeled in our privately produced Monte Carlo.

Fig. 161 is fitted to a function that contains a Crystal Ball shape with the power law on the high side, a wide Gaussian on the high side, and another Gaussian on the lower side of the center of the Crystal Ball as described by Eq. 68. The fit is restricted to 2.08 GeV $< m_{BC} <$ 2.15 GeV.

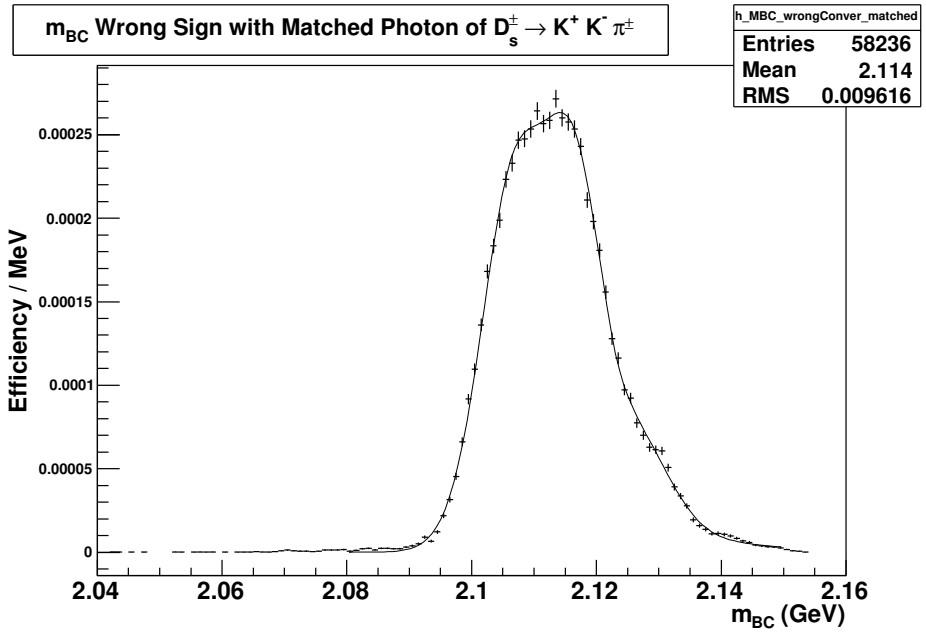

Figure 161: Combinatorial background structured in the m_{BC} distribution consisting of events where the D_s^{*+} has been reconstructed out of the D_s^- and the γ, and where both the D_s^- and the γ have been matched to their generated counterparts in the Monte Carlo simulation. This distribution has been fitted to a shape described by Eq. 68.

$$
\begin{aligned}
f(x;\bar{x_0},\sigma_0,\alpha,n,N_0,\bar{x_1},\sigma_1,N_1,\bar{x_2},\sigma_2,N_2) &= N_1 \exp\left(-\frac{(x-\bar{x_1})^2}{2\sigma_1^2}\right) \\
&+ N_0 \cdot \left\{ \begin{array}{ll} A\cdot\left(B+\frac{x-\bar{x_0}}{\sigma_0}\right)^{-n}, & \text{for} \quad \alpha < \frac{x-\bar{x_0}}{\sigma_0} \\ \exp\left(-\frac{(x-\bar{x_0})^2}{2\sigma_0^2}\right), & \text{for} \quad \frac{x-\bar{x_0}}{\sigma_0} \leq \alpha \end{array} \right\} \\
&+ N_2 \exp\left(-\frac{(x-\bar{x_2})^2}{2\sigma_2^2}\right) \qquad (68)
\end{aligned}
$$

where

$$A = \left(\frac{n}{\alpha}\right)^n \exp\left(-\frac{\alpha^2}{2}\right),$$

$$B = \frac{n}{\alpha} - \alpha$$

Fig. 162 is fitted to a function that contains a Crystal Ball centered around the higher edge of the trapezoidal shape with the power law on the higher side of the Gaussian, and continued analytically on the lower side with a straight line as described by Eq. 69. The fit

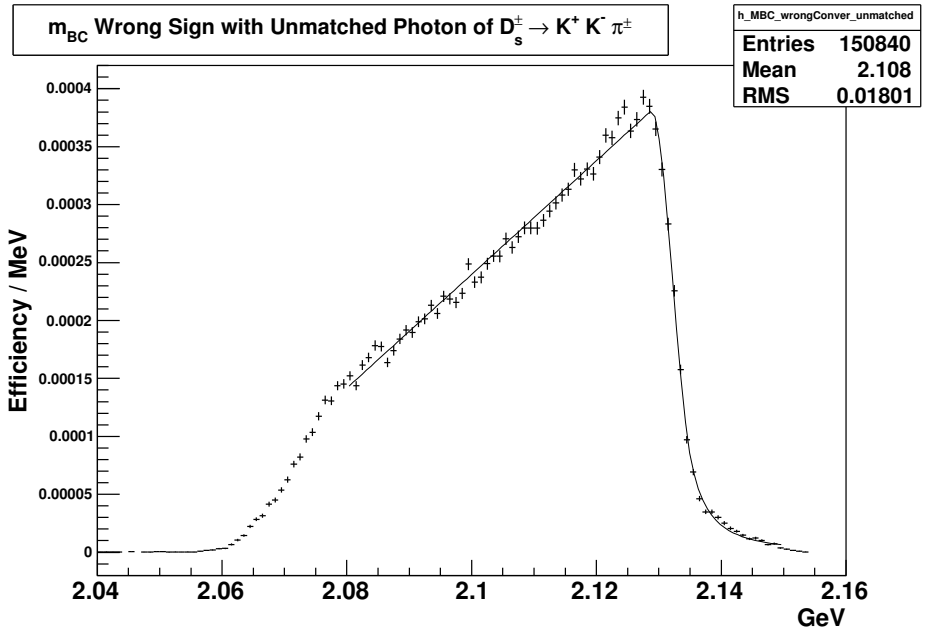

Figure 162: Combinatorial background structured in the m_{BC} distribution consisting of events where the D_s^{*+} has been reconstructed out of the D_s^- and the γ, and the D_s^- has been matched to its generated counterpart but the γ has failed to match the photon from the D_s^{*+} decay at the generator level of the Monte Carlo simulation. This distribution has been fitted to a shape described by Eq. 69.

is restricted to $2.08\text{GeV} < m_{BC} < 2.15\text{GeV}$

$$f(x;\bar{x},\sigma,\alpha,n,\beta,N) = N_0 \cdot \left\{ \begin{array}{c} A\cdot\left(B+\frac{x-\bar{x}}{\sigma}\right)^{-n}, \quad \text{for} \quad \alpha < \frac{x-\bar{x}}{\sigma} \\ \exp\left(-\frac{(x-\bar{x})^2}{2\sigma^2}\right), \quad \text{for} \quad \beta \geq \frac{x-\bar{x}}{\sigma} \leq \alpha \\ C + D\frac{x-\bar{x}}{\sigma}, \quad \text{for} \quad \frac{x-\bar{x}}{\sigma} < \beta \end{array} \right\} \tag{69}$$

where

$$A = \left(\frac{n}{\alpha}\right)^n \exp\left(-\frac{\alpha^2}{2}\right),$$

$$B = \frac{n}{\alpha} - \alpha,$$

$$C = \left(1+\frac{\beta^2}{\sigma^2}\right)\exp\left(-\frac{\beta^2}{2\sigma^2}\right),$$

$$D = \frac{-\beta}{\sigma^2}\exp\left(-\frac{\beta^2}{2\sigma^2}\right)$$

Having established the shapes of the signal and various backgrounds, we first study the m_{BC} distribution of the Generic Monte Carlo sample to see how well our fits fare in reproducing the branching fraction for $B(D_s^{*+} \to D_s^+\gamma)$ that had been programmed into the

simulation. The plot of m_{BC} and the fits of the signal and various backgrounds to it are presented in Fig. 163. The lowest curve is a function of the form given in Eq. 67 that models the continuum and featureless combinatorial backgrounds. The curve above that is a scaled version of the shape fitted to the plot in Fig. 161. Above that is a scaled version of the shape fitted to the plot in Fig. 162. On top of these backgrounds lies the signal peak, which is a scaled version of the shape fitted to Fig. 160. The fit is restricted to the range 2.08GeV $< m_{BC} <$ 2.15GeV. The signal yield is measured by the integral of the highest curve that includes the signal peak minus the integral of all the backgrounds between 2.08 and 2.15 GeV. This may be combined with the efficiency of our selection criteria $\epsilon^i_{D_s\gamma}$, the integrated luminosity of data being used L, the cross section for producing $D_s^{*\pm}D_s^{\mp}$ (values given in Section 7) and the value for $B(D_s^+ \to K^+K^-\pi^+)$ programmed into the simulation to give us an estimate for $B(D_s^{*+} \to D_s^+\gamma$ as tabulated in Table 60. We find the thus estimated value for $B(D_s^{*+} \to D_s^+\gamma)$ equal to 0.9259 ± 0.0058 to be 2.8σ away from the programmed value of 0.942 in the Monte Carlo simulation.

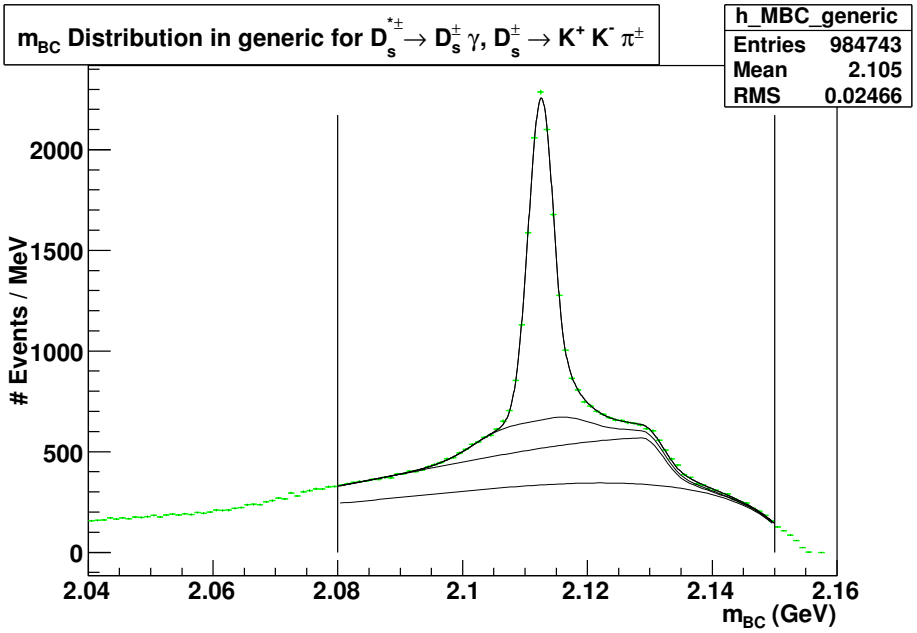

Figure 163: Distribution of m_{BC} of $D_s^{*+} \to D_s^+\gamma$ events where $D_s^+ \to K^+K^-\pi^+$ in 586 pb^{-1} of Generic Monte Carlo.

We present the distribution of m_{BC} in data in Fig. 164. It is fitted to the signal and background shapes as described in the previous paragraph. The ratio of amplitudes for the signal peak shape to the shape for the incorrectly reconstructed D_s^{*+} with the photon strictly unmatched (second curve from the top) is carried over as a constant from the fit to the generic MC. A systematic uncertainty is evaluated by repeating this fit without such constraints on the ratio. The signal yield is measured by subtracting the integral of all the backgrounds from the integral of the total fit between 2.08 and 2.15 GeV, as described earlier. This, again, may be combined with the efficiency of our selection criteria $\epsilon^i_{D_s\gamma}$, the

Table 60: $\epsilon^i_{D_s\gamma}$ is the efficiency of our selection criteria for the mode. $N^i_{D_s\gamma}$ is the signal yield observed for this mode. $B(D_s^{*+} \to D_s^+\gamma)$ is the branching fraction for $D_s^{*+} \to D_s^+e^+e^-$ inferred from this mode. Error [1] on the inferred branching fraction is the statistical error from the final fit. Error [2] encapsulates the systematic uncertainties from the signal efficiency and the uncertainty in the number of produced generic MC events.

i (Decay Mode of D_s^+)	$B(D_s^+ \to i)$	$\epsilon^i_{D_s\gamma}$	$N^i_{D_s\gamma}$	$B(D_s^{*+} \to D_s^+\gamma)$ Inferred
$K^+K^-\pi^+$	0.0537	0.339 ± 0.002	9364 ± 40	$0.9259 \pm 0.0040^{[1]} \pm 0.0043^{[2]}$

integrated luminosity of data being used L, the cross section for producing $D_s^{*\pm}D_s^{\mp}$ and the currently accepted value for $B(D_s^+ \to K^+K^-\pi^+)$ from the Review of Particle Physics 2008 [2] to give us an estimate for $B(D_s^{*+} \to D_s^+\gamma)$ as tabulated in Table 61. We find the estimated value for $B(D_s^{*+} \to D_s^+\gamma)$ equal to 0.880 ± 0.060 to be roughly 1σ away from the currently accepted value of 0.942 ± 0.007. We shall not, however, publish this measurement of $B(D_s^{*+} \to D_s^+\gamma)$ as it is not what we set out to do. We expect systematic uncertainties arising from the reconstruction of the D_s^+ to cancel between measurements of $B(D_s^{*+} \to D_s^+e^+e^-)$ and $B(D_s^{*+} \to D_s^+\gamma)$, which is why we set out to report the ratio of branching fractions $B(D_s^{*+} \to D_s^+e^+e^-)/B(D_s^{*+} \to D_s^+\gamma)$. Arriving at a result for this ratio will only require us to report the signal yields and efficiencies for $D_s^{*+} \to D_s^+\gamma$ for each of the decay modes of the D_s^+.

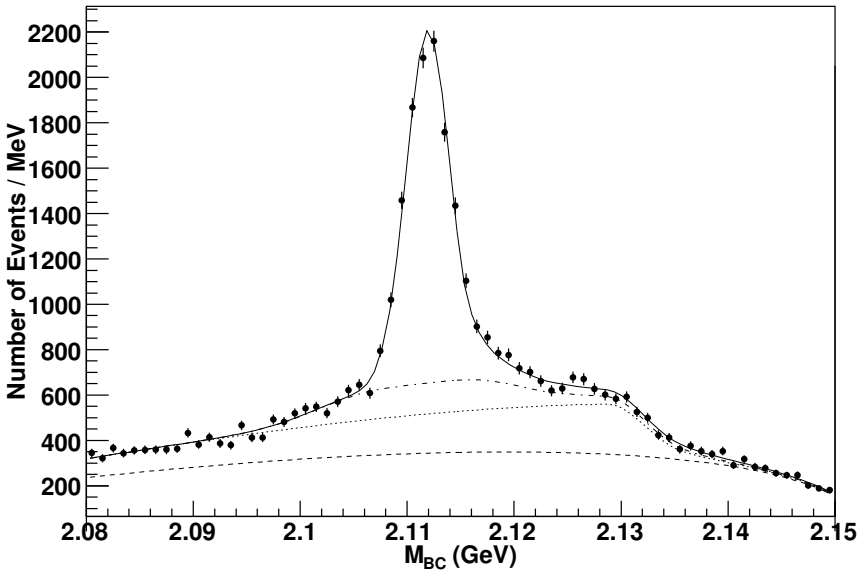

Figure 164: Distribution of m_{BC} of $D_s^{*+} \to D_s^+\gamma$ events where $D_s^+ \to K^+K^-\pi^+$ in 586 pb^{-1} of data.

Table 61: $\epsilon^i_{D_s\gamma}$ is the efficiency of our selection criteria for the mode. $N^i_{D_s\gamma}$ is the signal yield observed for this mode. $B(D_s^{*+} \to D_s^+\gamma)$ is the branching fraction for $D_s^{*+} \to D_s^+e^+e^-$ inferred from this mode. Error [1] on the inferred branching fraction is the statistical error from the final fit. Error [2] arises from the uncertainty in the branching fraction for $D_s^+ \to i$. Error [3] encapsulates the systematic uncertainties from the signal efficiency, the integrated luminosity and the production cross section for $D_s^{*\pm}D_s^{\mp}$. Error [4] encapsulates the systematic error arising from the fit.

i (Decay Mode of D_s^+)	$B(D_s^+ \to i)$	$\epsilon^i_{D_s\gamma}$	$N^i_{D_s\gamma} \pm (stat) \pm (syst)$	$B(D_s^{*+} \to D_s^+\gamma)$ Inferred
$K^+K^-\pi^+$	0.055 ± 0.0028	0.339 ± 0.002	$9114 \pm 110 \pm 201$	$0.880 \pm 0.011^{[1]} \pm 0.045^{[2]} \pm 0.035^{[3]} \pm 0.019^{[4]}$

Table 62: Selection criteria for $D_s^{*+} \to D_s^+\gamma$ events where $D_s^+ \to K_S K^+$. The δm cut has been widened to accomodate the wider peak for the signal in this distribution.

Selection Criterion	Cut Center ± Width
$m_{D_s^+}$	1.969 ± 0.008 GeV
δm	0.140 ± 0.02 GeV

14.2 $D_s^+ \to K_S K^+$

We begin with a Monte Carlo signal sample of $D_s^{*+} \to D_s^+\gamma$ events where $D_s^+ \to K_S K^+$ and the D_s^- is allowed to decay generically. The selection criteria applied are tabulated in Table 62. Fig. 165 depicts the δm distribution of this signal sample and the region selected by our criterion.

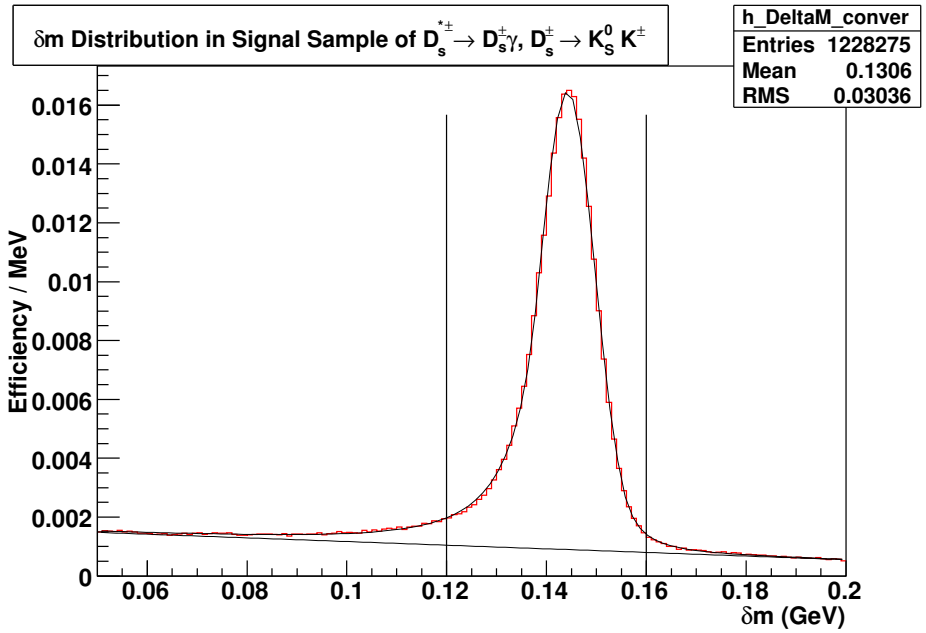

Figure 165: Distribution of δm in the signal Monte Carlo sample of $D_s^{*+} \to D_s^+\gamma$ events where $D_s^+ \to K_S K^+$. The plot is normalized so as to directly read out the efficiency of the δm selection criterion.

To obtain the selection efficiency using the condition on m_{BC} as our last selection criterion, we produce a plot of the m_{BC} distribution of the signal sample, having applied all other criteria, as shown in Fig. 166. We extract the shape of the peak from the plot of m_{BC} where the D_s^+ and the photon are matched to their generated counterparts in the Monte Carlo simulation as shown in Fig. 167. The equations that parameterize all fits and the range they are fitted in are identical to those used in the $K^+K^-\pi^+$ mode.

Structured backgrounds arising from incorrectly reconstructed D_s^{*+} are simulated as done previously for the $K^+K^-\pi^+$ mode. Fig. 168 shows the structure of the D_s^- matched and

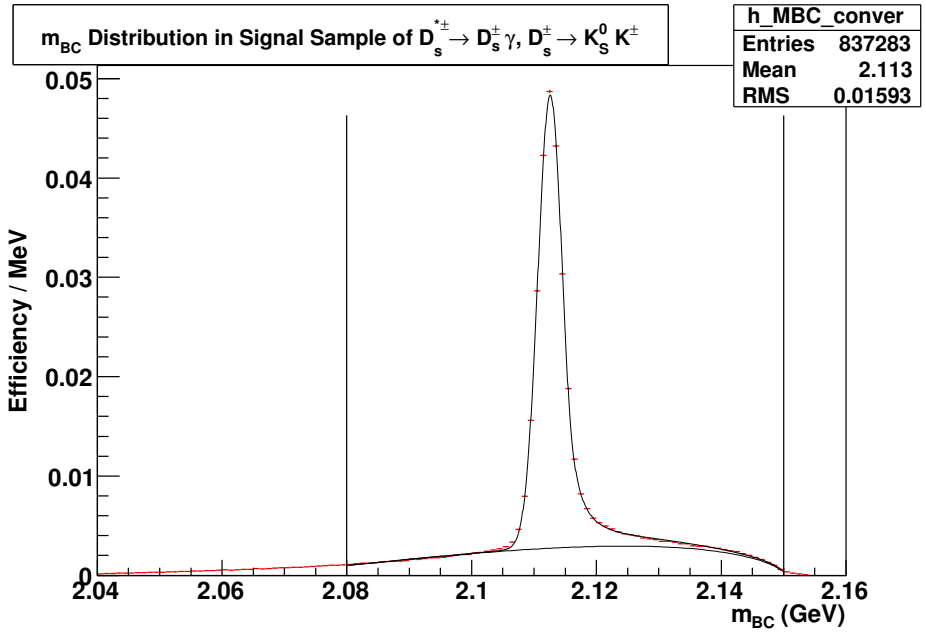

Figure 166: Distribution of m_{BC} in the signal Monte Carlo sample of $D_s^{*+} \to D_s^+\gamma$ events where $D_s^+ \to K_S K^+$. The plot is normalized so as to directly read out the efficiency of the m_{BC} selection criterion.

Table 63: $\epsilon^i_{D_s\gamma}$ is the efficiency of our selection criteria for the mode. $N^i_{D_s\gamma}$ is the signal yield observed for this mode. $B(D_s^{*+} \to D_s^+\gamma)$ is the branching fraction for $D_s^{*+} \to D_s^+e^+e^-$ inferred from this mode. Error [1] on the inferred branching fraction is the statistical error from the final fit. Error [2] encapsulates the systematic uncertainties from the signal efficiency and the uncertainty in the number of produced generic MC events.

i (Decay Mode of D_s^+)	$B(D_s^+ \to i)$	$\epsilon^i_{D_s\gamma}$	$N^i_{D_s\gamma}$	$B(D_s^{*+} \to D_s^+\gamma)$ Inferred
$K_S K^+$	0.01465	0.25727 ± 0.00043	2006 ± 17	$0.9581 \pm 0.0083^{[1]} \pm 0.0018^{[2]}$

photon matched background, and our fit to parameterize this shape. The background with the D_s^- matched and a photon that failed matching is shown in Fig. 169 along with our fit to parameterize the shape.

As a check on how well our background and signal estimation performs, we present the overall fit to generic MC, as described for the $K^+K^-\pi^+$ mode, in Fig. 170. Our measurement of the signal selection efficiency and the signal yield is presented in Table 63. We find the thus estimated value for $B(D_s^{*+} \to D_s^+\gamma)$ equal to 0.9616 ± 0.0085 to be 2.3σ away from the programmed value of 0.942 in the Monte Carlo simulation.

We present the distribution of m_{BC} in data and our fits to estimate the signal yield over the backgrounds, as described for the $K^+K^-\pi^+$ mode, in Fig. 164. Our measurements of the signal efficiency and signal yield are presented in Table 64. We find the estimated value for $B(D_s^{*+} \to D_s^+\gamma)$ equal to 0.893 ± 0.073 to be roughly 0.7σ away from the currently

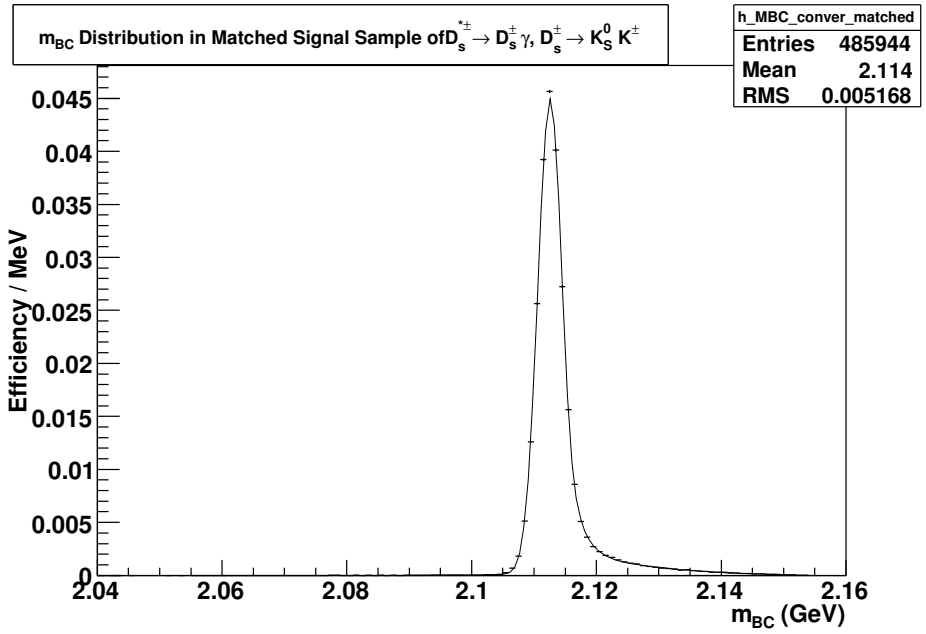

Figure 167: Distribution of m_{BC} in the signal Monte Carlo sample of $D_s^{*+} \to D_s^+\gamma$ events where $D_s^+ \to K_S K^+$.

accepted value of 0.942 ± 0.007.

Table 64: $\epsilon^i_{D_s\gamma}$ is the efficiency of our selection criteria for the mode. $N^i_{D_s\gamma}$ is the signal yield observed for this mode. $B(D_s^{*+} \to D_s^+\gamma)$ is the branching fraction for $D_s^{*+} \to D_s^+ e^+ e^-$ inferred from this mode. Error [1] on the inferred branching fraction is the statistical error from the final fit. Error [2] arises from the uncertainty in the branching fraction for $D_s^+ \to i$. Error [3] encapsulates the systematic uncertainties from the signal efficiency, the integrated luminosity and the production cross section for $D_s^{*\pm} D_s^{\mp}$. Error [4] encapsulates the systematic error arising from the fit.

i (Decay Mode of D_s^+)	$B(D_s^+ \to i)$	$\epsilon^i_{D_s\gamma}$	$N^i_{D_s\gamma}$	$B(D_s^{*+} \to D_s^+\gamma)$ Inferred
$K_S K^+$	0.0149 ± 0.0009	0.2573 ± 0.0004	$1902 \pm 57 \pm 45$	$0.893 \pm 0.027^{[1]} \pm 0.054^{[2]} \pm 0.035^{[3]} 0.021^{[4]}$

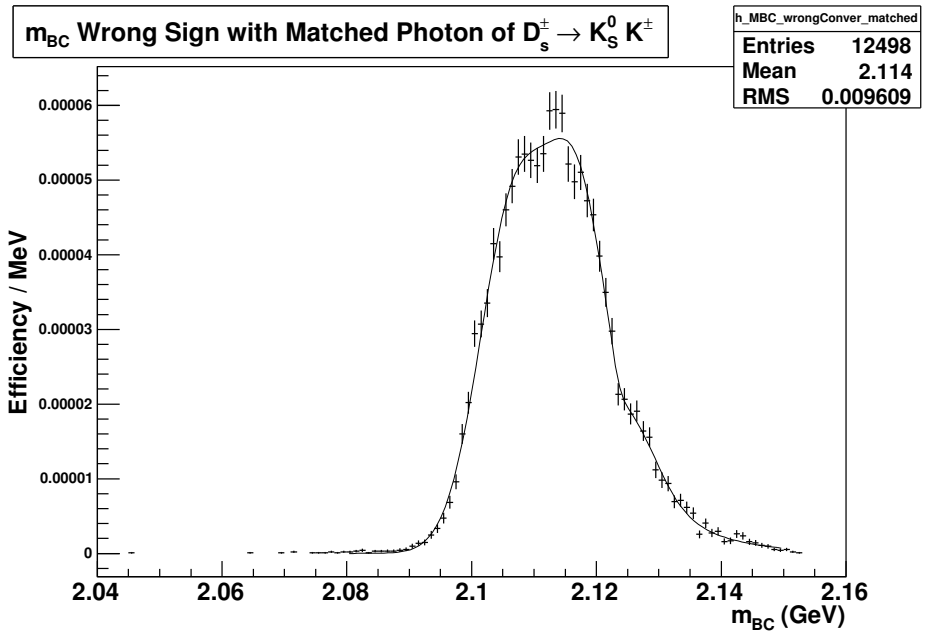

Figure 168: Combinatorial background in the m_{BC} distribution consisting of events where the D_s^{*+} has been reconstructed out of the D_s^- and the γ, and where both the D_s^- and the γ have been matched to their generated counterparts in the Monte Carlo simulation. This distribution has been fitted to a shape described by Eq. 68.

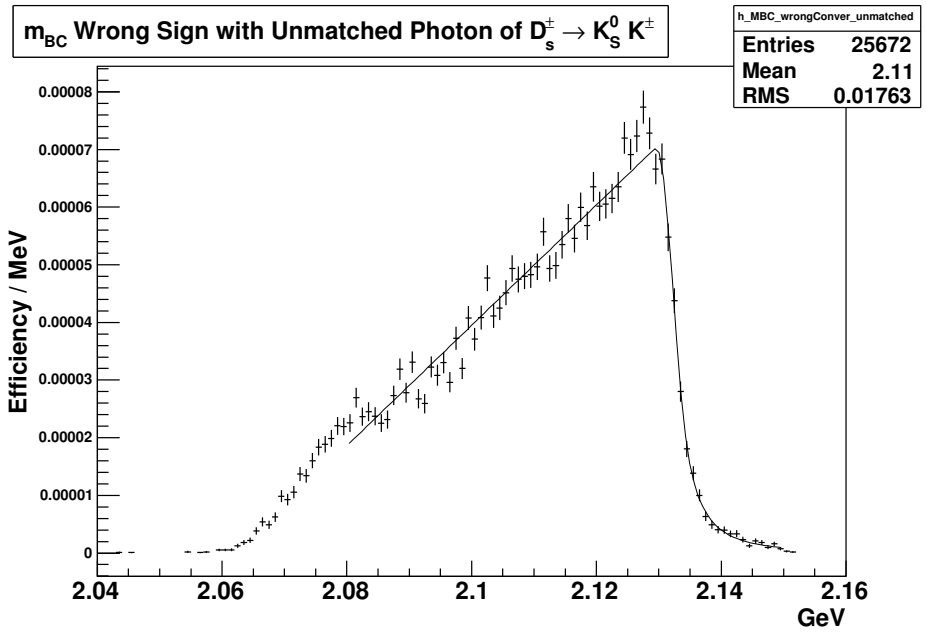

Figure 169: Combinatorial background structured in the m_{BC} distribution consisting of events where the D_s^{*+} has been reconstructed out of the D_s^- and the γ, and the D_s^- has been matched to its generated counterpart but the γ has failed to match the photon from the D_s^{*+} decay at the generator level of the Monte Carlo simulation. This distribution has been fitted to a shape described by Eq. 69.

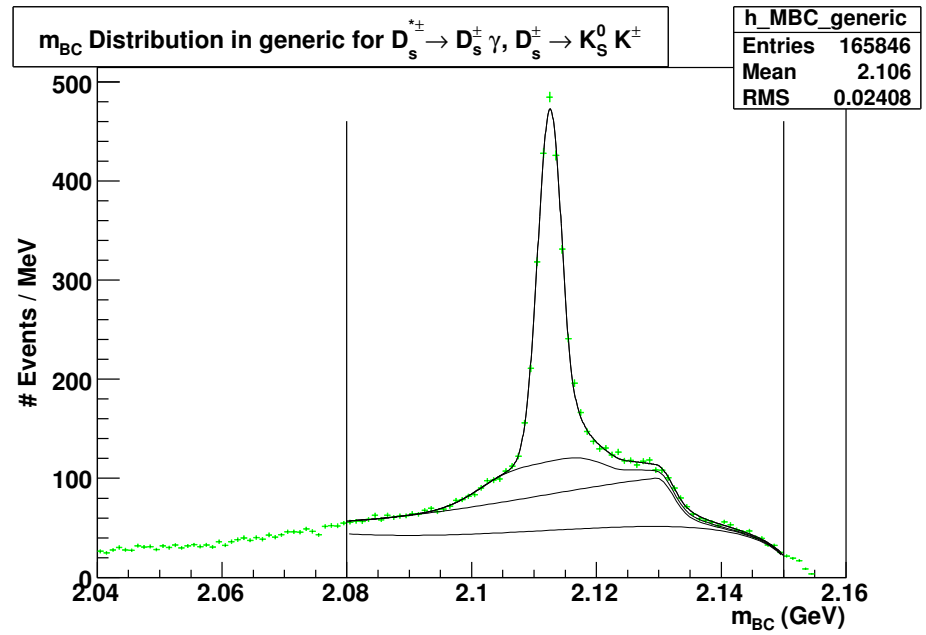

Figure 170: Distribution of m_{BC} of $D_s^{*+} \to D_s^+\gamma$ events where $D_s^+ \to K_S K^+$ in 586 pb^{-1} of Generic Monte Carlo.

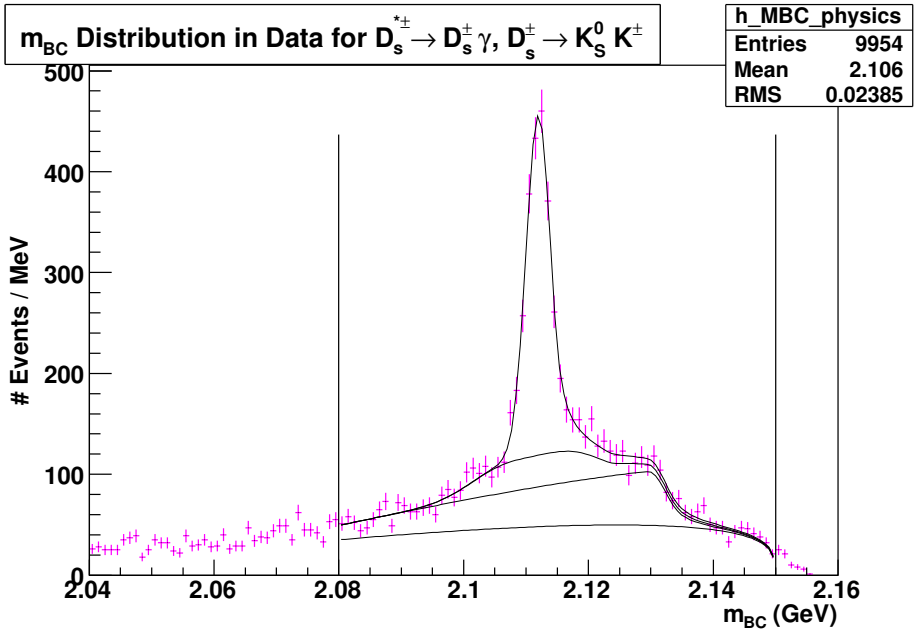

Figure 171: Distribution of m_{BC} of $D_s^{*+} \to D_s^+\gamma$ events where $D_s^+ \to K_S K^+$ in 586 pb^{-1} of data.

Table 65: Selection criteria for $D_s^{*+} \to D_s^+\gamma$ events where $D_s^+ \to \eta\pi^+; \eta \to \gamma\gamma$. The δm cut has been widened to accomodate the wider peak for the signal in this distribution.

Selection Criterion	Cut Center ± Width
$m_{D_s^+}$	1.969 ± 0.016 GeV
δm	0.140 ± 0.02 GeV

14.3 $D_s^+ \to \eta\pi^+; \eta \to \gamma\gamma$

We begin with a Monte Carlo signal sample of $D_s^{*+} \to D_s^+\gamma$ events where $D_s^+ \to \eta\pi^+; \eta \to \gamma\gamma$ and the D_s^- is allowed to decay generically. The selection criteria applied are tabulated in Table 65. Fig. 172 depicts the δm distribution of this signal sample and the region selected by our criterion.

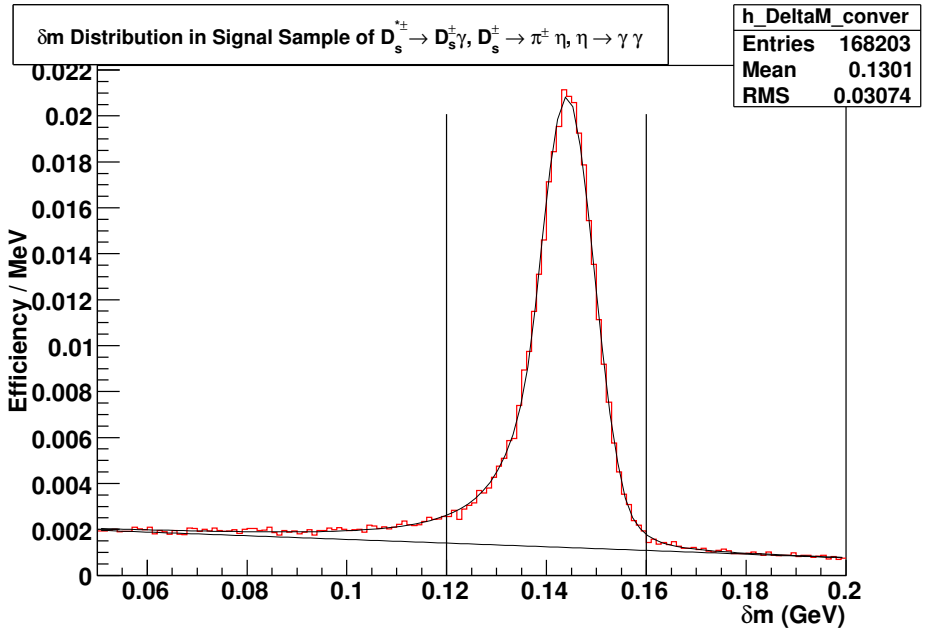

Figure 172: Distribution of δm in the signal Monte Carlo sample of $D_s^{*+} \to D_s^+\gamma$ events where $D_s^+ \to \eta\pi^+; \eta \to \gamma\gamma$. The plot is normalized so as to directly read out the efficiency of the δm selection criterion.

To obtain the selection efficiency using the condition on m_{BC} as our last selection criterion, we produce a plot of the m_{BC} distribution of the signal sample, having applied all other criteria, as shown in Fig. 173. We extract the shape of the peak from the plot of m_{BC} where the D_s^+ and the photon are matched to their generated counterparts in the Monte Carlo simulation as shown in Fig. 174. The equations that parameterize all fits and the range they are fitted in are identical to those used in the $K^+K^-\pi^+$ mode.

Structured backgrounds arising from incorrectly reconstructed D_s^{*+} are simulated as done previously for the $K^+K^-\pi^+$ mode. Fig. 175 shows the structure of the D_s^- matched and

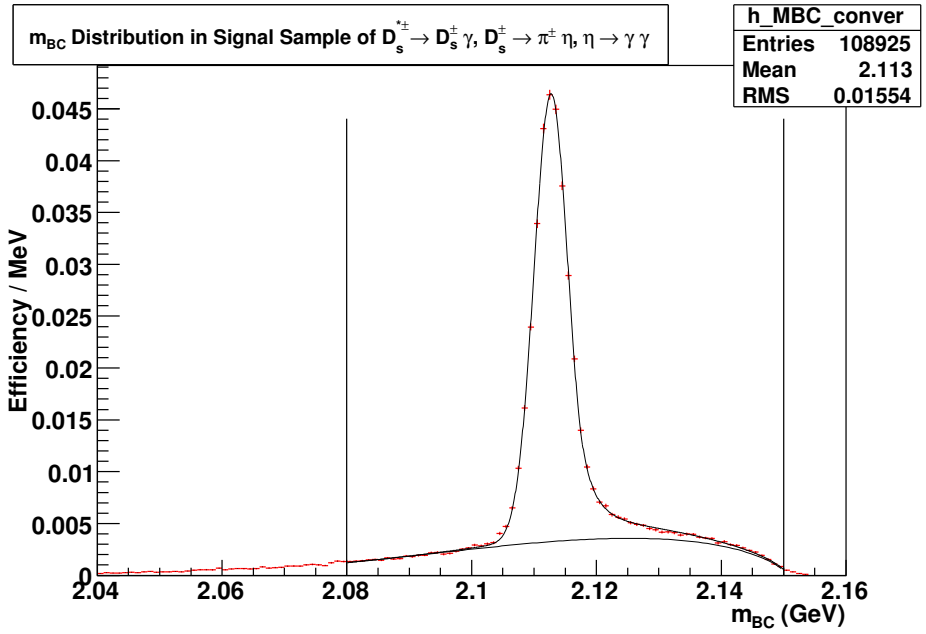

Figure 173: Distribution of m_{BC} in the signal Monte Carlo sample of $D_s^{*+} \to D_s^+\gamma$ events where $D_s^+ \to \eta\pi^+; \eta \to \gamma\gamma$. The plot is normalized so as to directly read out the efficiency of the m_{BC} selection criterion from the area under the fit within the signal region.

Table 66: $\epsilon^i_{D_s\gamma}$ is the efficiency of our selection criteria for the mode. $N^i_{D_s\gamma}$ is the signal yield observed for this mode. $B(D_s^{*+} \to D_s^+\gamma)$ is the branching fraction for $D_s^{*+} \to D_s^+e^+e^-$ inferred from this mode. Error [1] on the inferred branching fraction is the statistical error from the final fit. Error [2] encapsulates the systematic uncertainties from the signal efficiency, the integrated luminosity and the production cross section for $D_s^{*\pm}D_s^{\mp}$.

i (Decay Mode of D_s^+)	$B(D_s^+ \to i)$	$\epsilon^i_{D_s\gamma}$	$N^i_{D_s\gamma}$	$B(D_s^{*+} \to D_s^+\gamma)$ Inferred
$D_s^+ \to \eta\pi^+; \eta \to \gamma\gamma$	0.0061	0.3310 ± 0.0015	998 ± 27	$0.8933 \pm 0.0240^{[1]} \pm 0.0043^{[2]}$

photon matched background, and our fit to parameterize this shape. The background with the D_s^- matched and a photon that failed matching is shown in Fig. 176 along with our fit to parameterize the shape.

As a check on how well our background and signal estimation performs, we present the overall fit to generic MC, as described for the $K^+K^-\pi^+$ mode, in Fig. 177. Our measurement of the signal selection efficiency and the signal yield is presented in Table 66. We find the thus estimated value for $B(D_s^{*+} \to D_s^+\gamma)$ equal to 0.893 ± 0.024 to be 2σ away from the programmed value of 0.942 in the Monte Carlo simulation.

We present the distribution of m_{BC} in data and our fits to estimate the signal yield over the backgrounds, as described for the $K^+K^-\pi^+$ mode, in Fig. 178. Our measurements of the signal efficiency and signal yield are presented in Table 67. We find the estimated value for $B(D_s^{*+} \to D_s^+\gamma)$ equal to 0.908 ± 0.136 to be roughly 0.25σ away from the currently

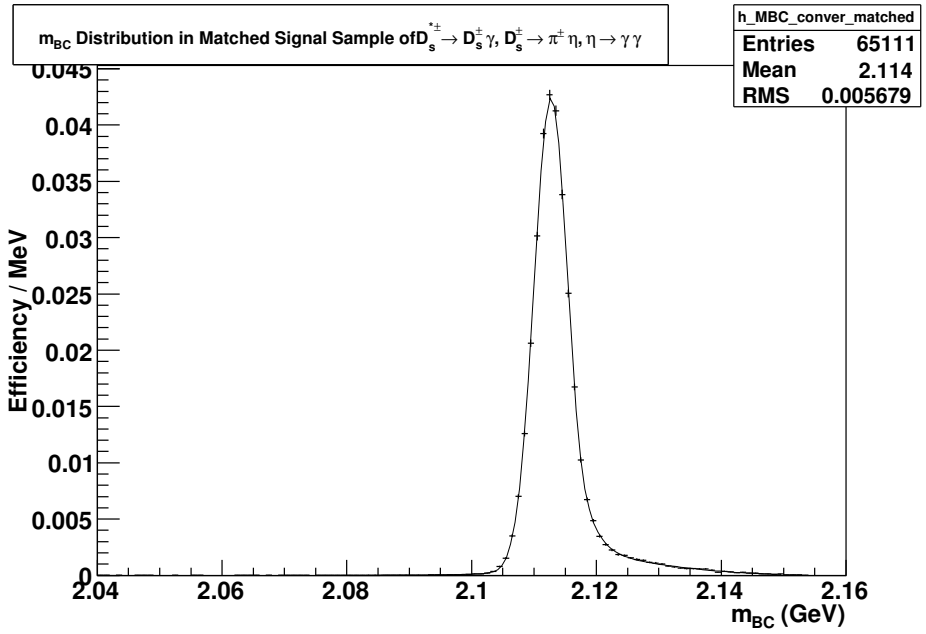

Figure 174: Distribution of m_{BC} in the signal Monte Carlo sample of $D_s^{*+} \to D_s^+\gamma$ events where $D_s^+ \to \eta\pi^+; \eta \to \gamma\gamma$.

accepted value of 0.942 ± 0.007.

Table 67: $\epsilon^i_{D_s\gamma}$ is the efficiency of our selection criteria for the mode. $N^i_{D_s\gamma}$ is the signal yield observed for this mode. $B(D_s^{*+} \to D_s^+\gamma)$ is the branching fraction for $D_s^{*+} \to D_s^+e^+e^-$ inferred from this mode. Error [1] on the inferred branching fraction is the statistical error from the final fit. Error [2] arises from the uncertainty in the branching fraction for $D_s^+ \to i$. Error [3] encapsulates the systematic uncertainties from the signal efficiency, the integrated luminosity and the production cross section for $D_s^{*\pm}D_s^{\mp}$. Error [4] encapsulates the systematic error arising from the fit.

i (Decay Mode of D_s^+)	$B(D_s^+ \to i)$	$\epsilon^i_{D_s\gamma}$	$N^i_{D_s\gamma}$	$B(D_s^{*+} \to D_s^+\gamma)$ Inferred
$D_s^+ \to \eta\pi^+; \eta \to \gamma\gamma$	0.00621 ± 0.00083	0.3310 ± 0.0015	$1037 \pm 46 \pm 37$	$0.908 \pm 0.040^{[1]} \pm 0.121^{[2]} \pm 0.036^{[3]} \pm 0.032^{[4]}$

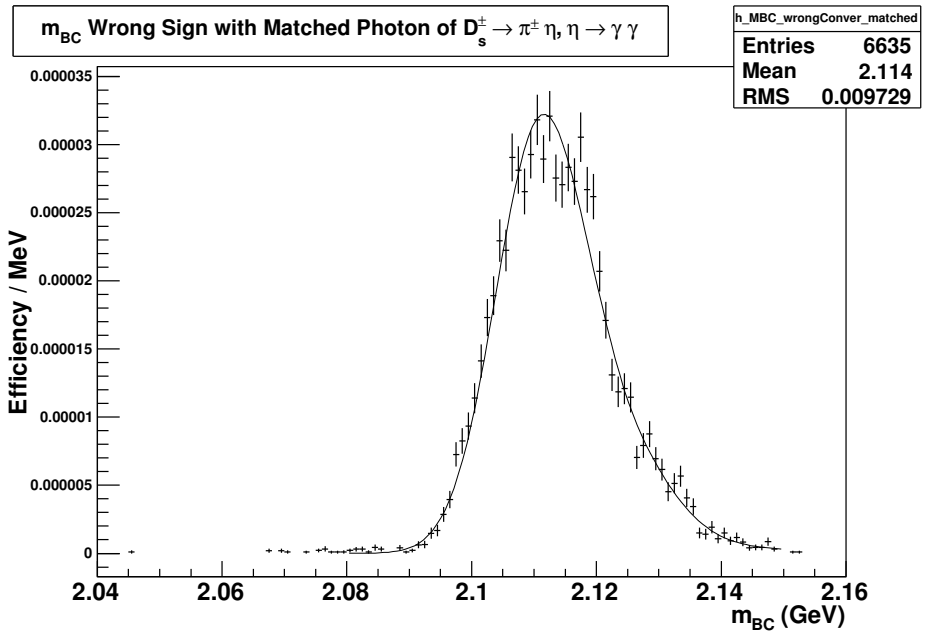

Figure 175: Combinatorial background in the m_{BC} distribution consisting of events where the D_s^{*+} has been reconstructed out of the D_s^- and the γ, and where both the D_s^- and the γ have been matched to their generated counterparts in the Monte Carlo simulation. This distribution has been fitted to a shape described by Eq. 68.

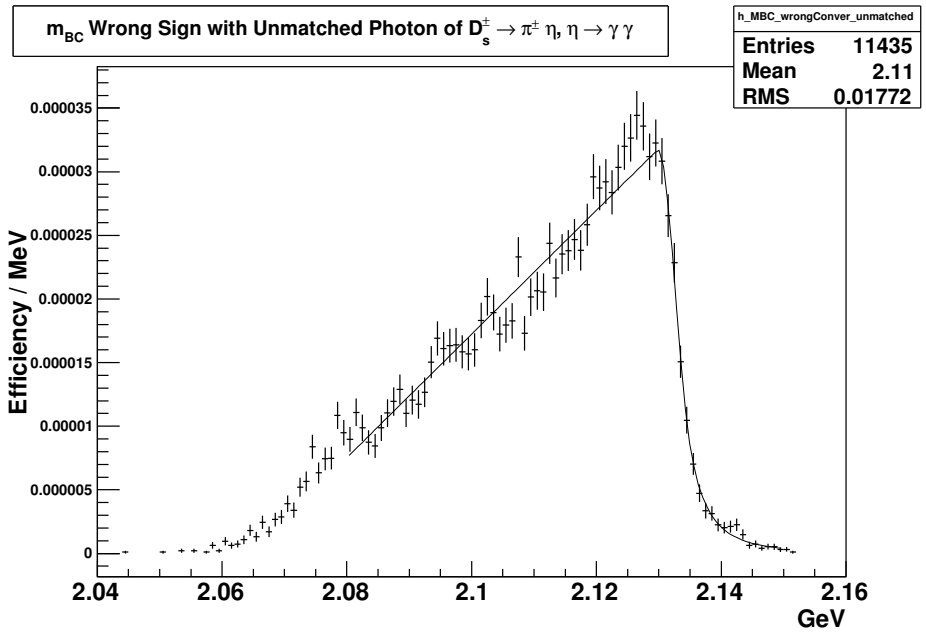

Figure 176: Combinatorial background structured in the m_{BC} distribution consisting of events where the D_s^{*+} has been reconstructed out of the D_s^- and the γ, and the D_s^- has been matched to its generated counterpart but the γ has failed to match the photon from the D_s^{*+} decay at the generator level of the Monte Carlo simulation. This distribution has been fitted to a shape described by Eq. 69.

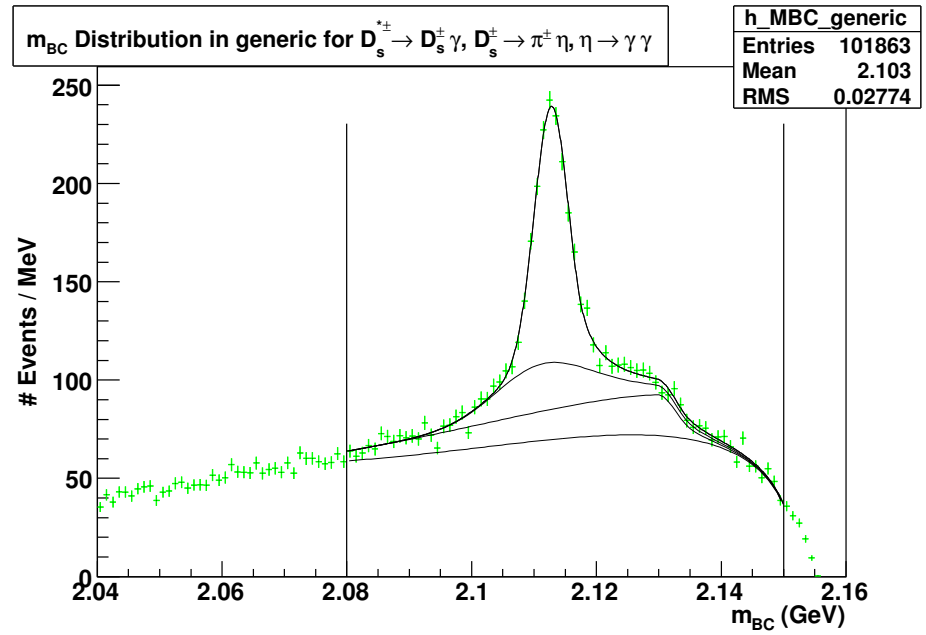

Figure 177: Distribution of m_{BC} of $D_s^{*+} \to D_s^+\gamma$ events where $D_s^+ \to \eta\pi^+; \eta \to \gamma\gamma$ in 586 pb^{-1} of Generic Monte Carlo.

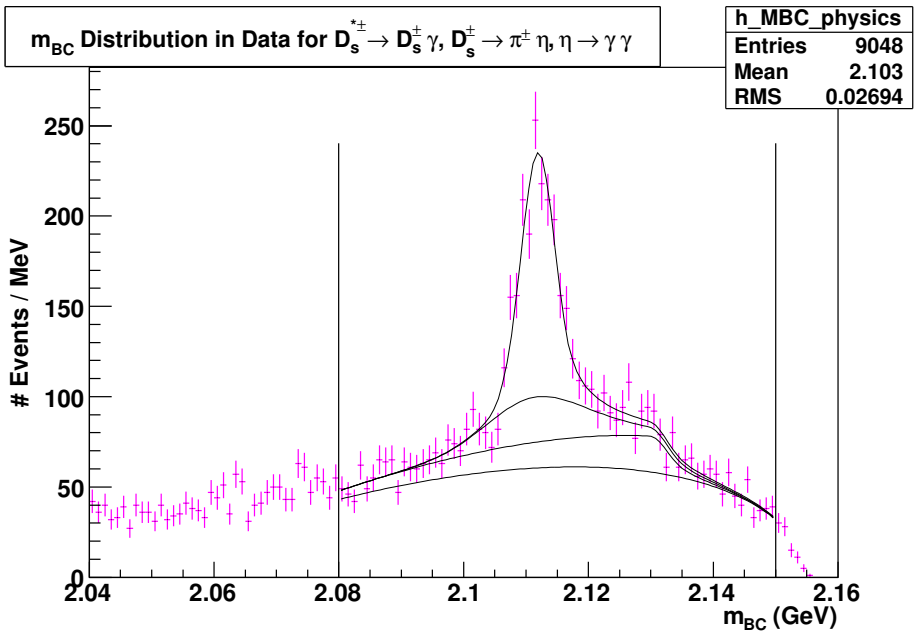

Figure 178: Distribution of m_{BC} of $D_s^{*+} \to D_s^+\gamma$ events where $D_s^+ \to \eta\pi^+; \eta \to \gamma\gamma$ in 586 pb^{-1} of data.

Table 68: Selection criteria for $D_s^{*+} \to D_s^+\gamma$ events where $D_s^+ \to \eta'\pi^+; \eta' \to \pi^+\pi^-\eta; \eta \to \gamma\gamma$. The δm cut has been widened to accomodate the wider peak for the signal in this distribution.

Selection Criterion	Cut Center ± Width
$m_{D_s^+}$	1.969 ± 0.011 GeV
δm	0.140 ± 0.020 GeV

14.4 $D_s^+ \to \eta'\pi^+; \eta' \to \pi^+\pi^-\eta; \eta \to \gamma\gamma$

We begin with a Monte Carlo signal sample of $D_s^{*+} \to D_s^+\gamma$ events where $D_s^+ \to \eta'\pi^+; \eta' \to \pi^+\pi^-\eta; \eta \to \gamma\gamma$ and the D_s^- is allowed to decay generically. The selection criteria applied are tabulated in Table 68. Fig. 179 depicts the δm distribution of this signal sample and the region selected by our criterion.

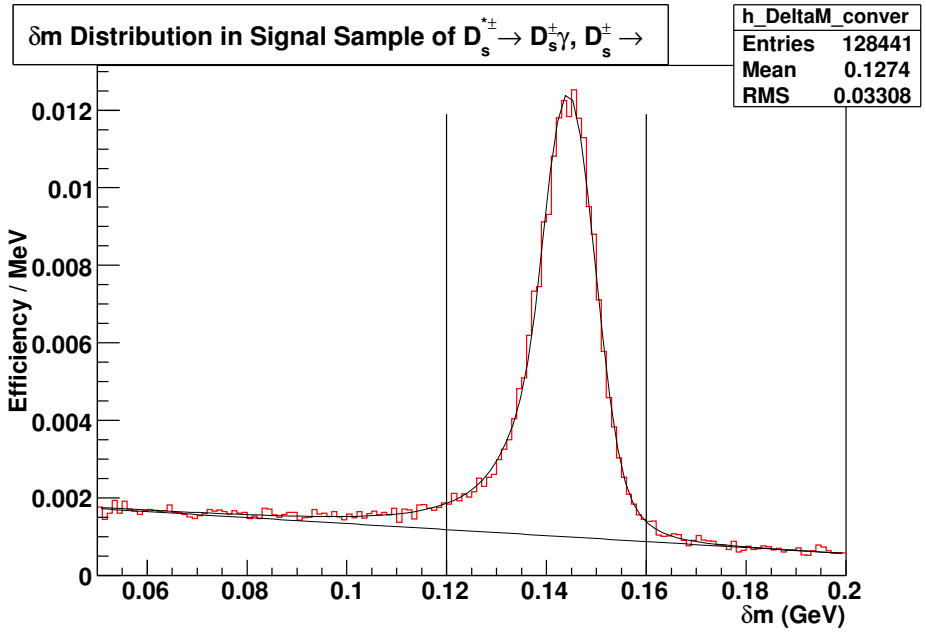

Figure 179: Distribution of δm in the signal Monte Carlo sample of $D_s^{*+} \to D_s^+\gamma$ events where $D_s^+ \to \eta'\pi^+; \eta' \to \pi^+\pi^-\eta; \eta \to \gamma\gamma$. The plot is normalized so as to directly read out the efficiency of the δm selection criterion.

To obtain the selection efficiency using the condition on m_{BC} as our last selection criterion, we produce a plot of the m_{BC} distribution of the signal sample, having applied all other criteria, as shown in Fig. 180. We extract the shape of the peak from the plot of m_{BC} where the D_s^+ and the photon are matched to their generated counterparts in the Monte Carlo simulation as shown in Fig. 181. The equations that parameterize all fits and the range they are fitted in are identical to those used in the $K^+K^-\pi^+$ mode.

Structured backgrounds arising from incorrectly reconstructed D_s^{*+} are simulated as done previously for the $K^+K^-\pi^+$ mode. Fig. 182 shows the structure of the D_s^- matched and

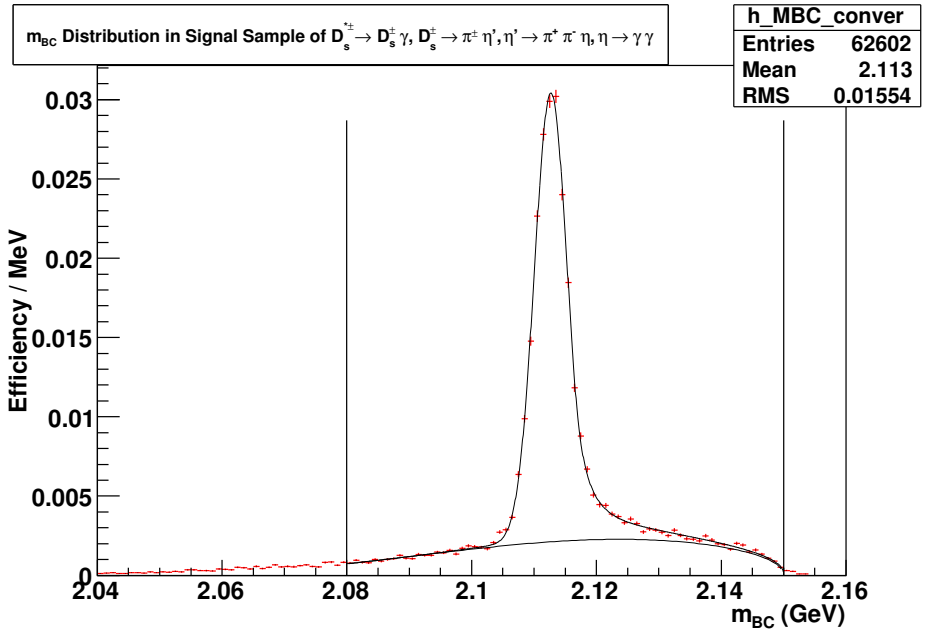

Figure 180: Distribution of m_{BC} in the signal Monte Carlo sample of $D_s^{*+} \to D_s^+\gamma$ events where $D_s^+ \to \eta'\pi^+; \eta' \to \pi^+\pi^-\eta; \eta \to \gamma\gamma$. The plot is normalized so as to directly read out the efficiency of the m_{BC} selection criterion from the area under the fit within the signal region.

photon matched background, and our fit to parameterize this shape. The background with the D_s^- matched and a photon that failed matching is shown in Fig. 183 along with our fit to parameterize the shape.

As a check on how well our background and signal estimation performs, we present the overall fit to generic MC, as described for the $K^+K^-\pi^+$ mode, in Fig. 184. Our measurement of the signal selection efficiency and the signal yield is presented in Table 69. We find the thus estimated value for $B(D_s^{*+} \to D_s^+\gamma)$ equal to 0.934 ± 0.016 to be 0.5σ away from the programmed value of 0.942 in the Monte Carlo simulation.

We present the distribution of m_{BC} in data and our fits to estimate the signal yield over the backgrounds, as described for the $K^+K^-\pi^+$ mode, in Fig. 185. Our measurements of

Table 69: $\epsilon^i_{D_s\gamma}$ is the efficiency of our selection criteria for the mode. $N^i_{D_s\gamma}$ is the signal yield observed for this mode. $B(D_s^{*+} \to D_s^+\gamma)$ is the branching fraction for $D_s^{*+} \to D_s^+e^+e^-$ inferred from this mode. Error [1] on the inferred branching fraction is the statistical error from the final fit. Error [2] encapsulates the systematic uncertainties from the signal efficiency, the integrated luminosity and the production cross section for $D_s^{*\pm}D_s^{\mp}$.

i (Decay Mode of D_s^+)	$B(D_s^+ \to i)$	$\epsilon^i_{D_s\gamma}$	$N^i_{D_s\gamma}$	$B(D_s^{*+} \to D_s^+\gamma)$ Inferred
$D_s^+ \to \eta'\pi^+; \eta' \to \pi^+\pi^-\eta; \eta \to \gamma\gamma$	0.00633	0.2101 ± 0.0013	690 ± 11	$0.9341 \pm 0.0149^{[1]} \pm 0.0058^{[2]}$

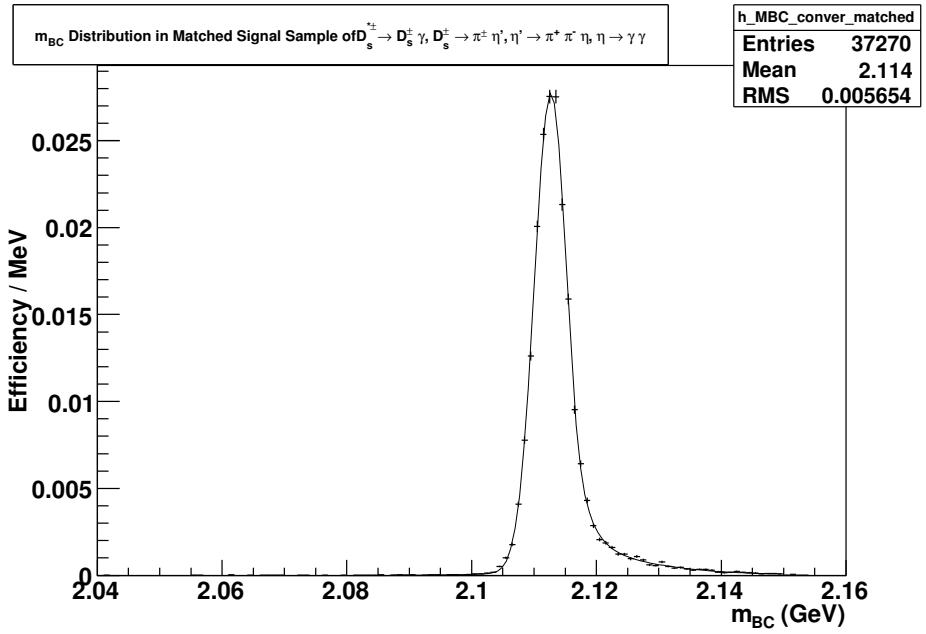

Figure 181: Distribution of m_{BC} in the signal Monte Carlo sample of $D_s^{*+} \to D_s^+\gamma$ events where $D_s^+ \to \eta'\pi^+; \eta' \to \pi^+\pi^-\eta; \eta \to \gamma\gamma$.

the signal efficiency and signal yield are presented in Table 70. We find the estimated value for $B(D_s^{*+} \to D_s^+\gamma)$ equal to 0.889 ± 0.121 to be roughly 0.44σ away from the currently accepted value of 0.942 ± 0.007.

Table 70: $\epsilon^i_{D_s\gamma}$ is the efficiency of our selection criteria for the mode. $N^i_{D_s\gamma}$ is the signal yield observed for this mode. $B(D_s^{*+} \to D_s^+\gamma)$ is the branching fraction for $D_s^{*+} \to D_s^+e^+e^-$ inferred from this mode. Error [1] on the inferred branching fraction is the statistical error from the final fit. Error [2] arises from the uncertainty in the branching fraction for $D_s^+ \to i$. Error [3] encapsulates the systematic uncertainties from the signal efficiency, the integrated luminosity and the production cross section for $D_s^{*\pm}D_s^{\mp}$. Error [4] encapsulates the systematic error arising from the fit.

i (Decay Mode of D_s^+)	$B(D_s^+ \to i)$	$\epsilon^i_{D_s\gamma}$	$N^i_{D_s\gamma}$	$B(D_s^{*+} \to D_s^+\gamma)$ Inferred
$D_s^+ \to \eta'\pi^+; \eta' \to \pi^+\pi^-\eta; \eta \to \gamma\gamma$	0.00666 ± 0.00070	0.2101 ± 0.0013	$691 \pm 34 \pm 40$	$0.889 \pm 0.043^{[1]} \pm 0.094^{[2]} \pm 0.035^{[3]} \pm 0.052^{[4]}$

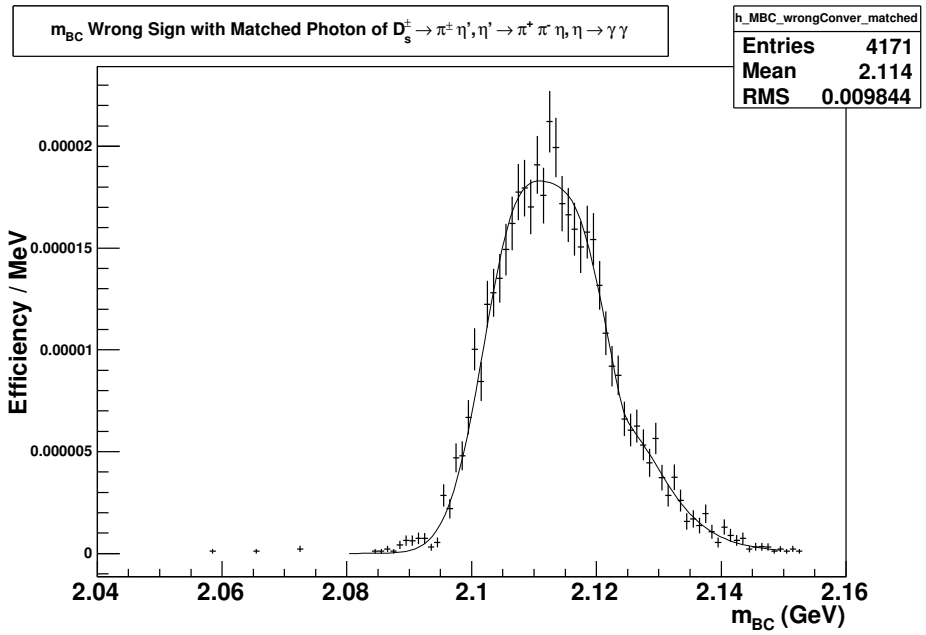

Figure 182: Combinatorial background in the m_{BC} distribution consisting of events where the D_s^{*+} has been reconstructed out of the D_s^- and the γ, and where both the D_s^- and the γ have been matched to their generated counterparts in the Monte Carlo simulation. This distribution has been fitted to a shape described by Eq. 68.

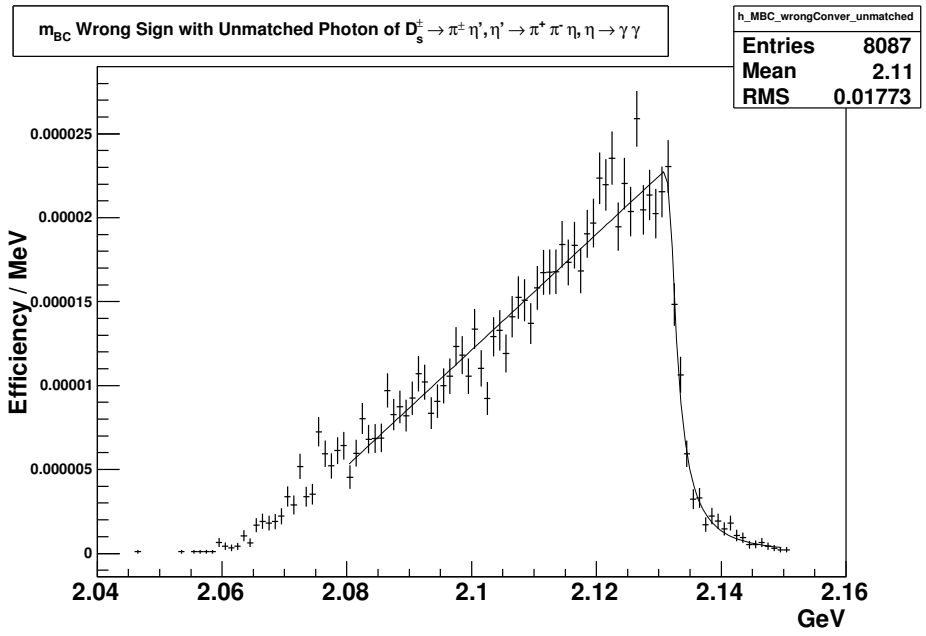

Figure 183: Combinatorial background structured in the m_{BC} distribution consisting of events where the D_s^{*+} has been reconstructed out of the D_s^- and the γ, and the D_s^- has been matched to its generated counterpart but the γ has failed to match the photon from the D_s^{*+} decay at the generator level of the Monte Carlo simulation. This distribution has been fitted to a shape described by Eq. 69.

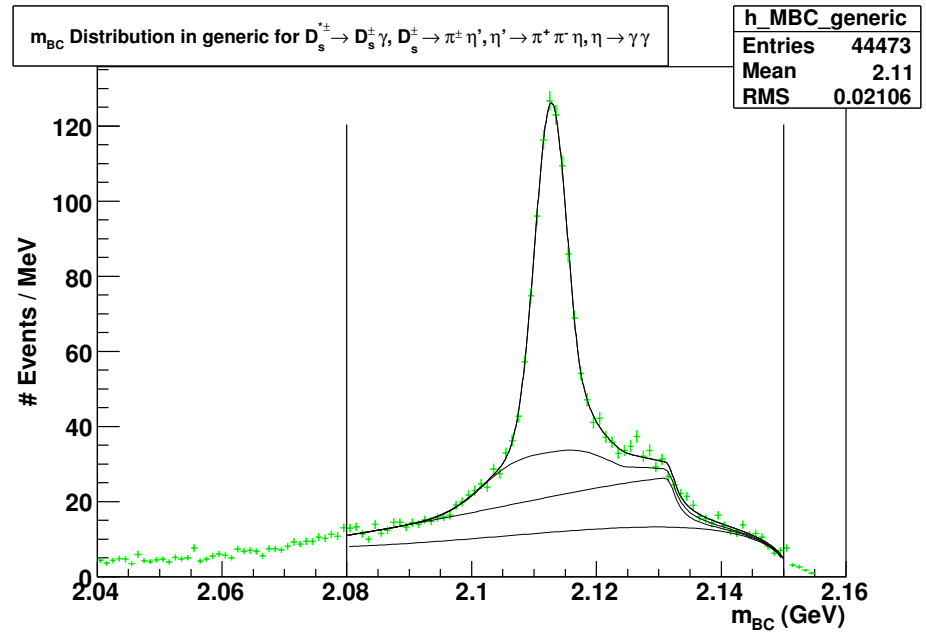

Figure 184: Distribution of m_{BC} of $D_s^{*+} \to D_s^+\gamma$ events where $D_s^+ \to \eta'\pi^+; \eta' \to \pi^+\pi^-\eta; \eta \to \gamma\gamma$ in 586 pb^{-1} of Generic Monte Carlo.

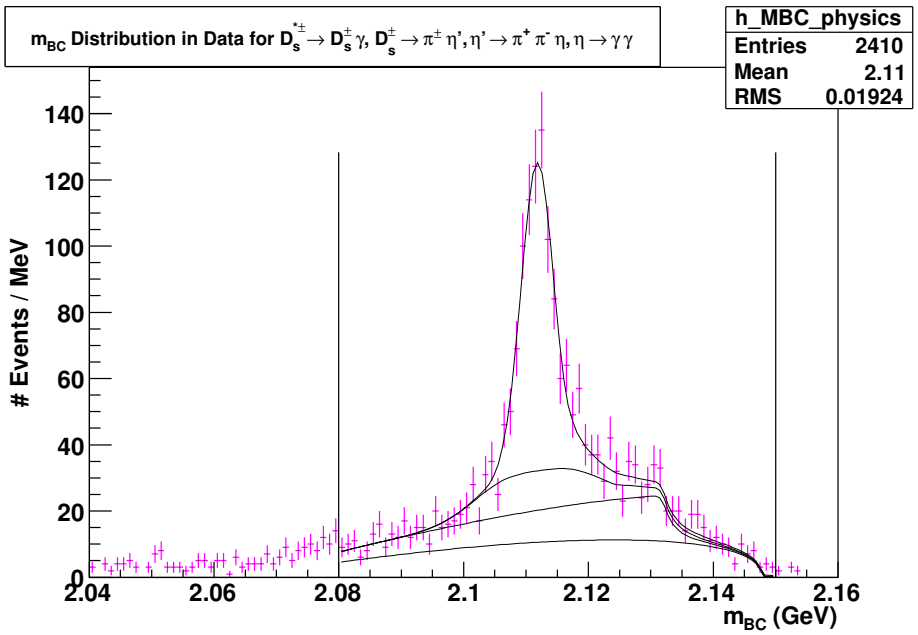

Figure 185: Distribution of m_{BC} of $D_s^{*+} \to D_s^+\gamma$ events where $D_s^+ \to \eta'\pi^+; \eta' \to \pi^+\pi^-\eta; \eta \to \gamma\gamma$ in 586 pb^{-1} of data.

Table 71: Selection criteria for $D_s^{*+} \to D_s^+\gamma$ events where $D_s^+ \to K^+K^-\pi^+\pi^0$. The δm cut has been widened to accomodate the wider peak for the signal in this distribution.

Selection Criterion	Cut Center ± Width
$m_{D_s^+}$	1.969 ± 0.010 GeV
δm	0.140 ± 0.020 GeV

14.5 $D_s^+ \to K^+K^-\pi^+\pi^0$

We begin with a Monte Carlo signal sample of $D_s^{*+} \to D_s^+\gamma$ events where $D_s^+ \to K^+K^-\pi^+\pi^0$ and the D_s^- is allowed to decay generically. The selection criteria applied are tabulated in Table 71. Fig. 186 depicts the δm distribution of this signal sample and the region selected by our criterion.

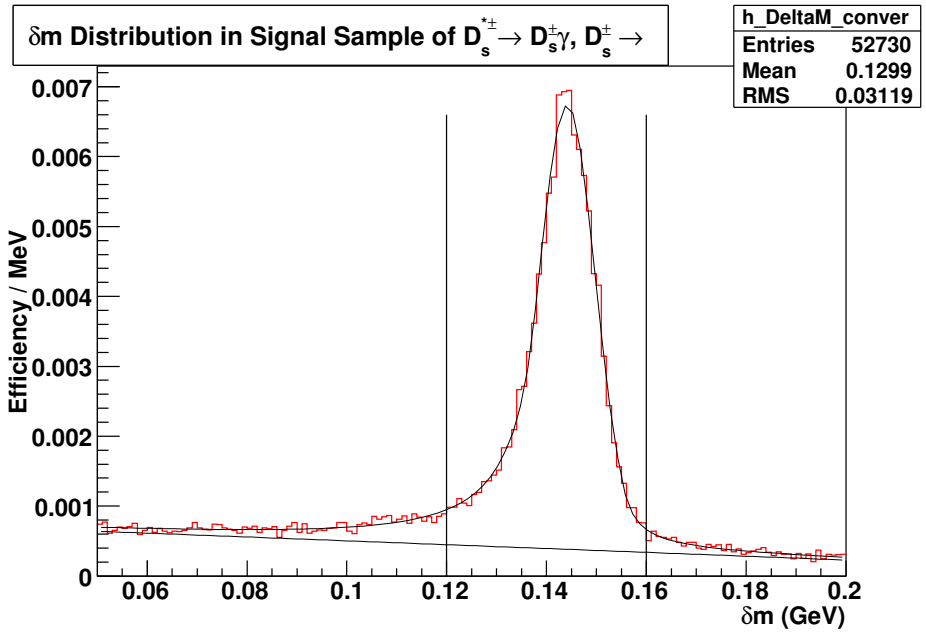

Figure 186: Distribution of δm in the signal Monte Carlo sample of $D_s^{*+} \to D_s^+\gamma$ events where $D_s^+ \to K^+K^-\pi^+\pi^0$. The plot is normalized so as to directly read out the efficiency of the δm selection criterion.

To obtain the selection efficiency using the condition on m_{BC} as our last selection criterion, we produce a plot of the m_{BC} distribution of the signal sample, having applied all other criteria, as shown in Fig. 187. We extract the shape of the peak from the plot of m_{BC} where the D_s^+ and the photon are matched to their generated counterparts in the Monte Carlo simulation as shown in Fig. 188. The equations that parameterize all fits and the range they are fitted in are identical to those used in the $K^+K^-\pi^+$ mode.

Structured backgrounds arising from incorrectly reconstructed D_s^{*+} are simulated as done previously for the $K^+K^-\pi^+$ mode. Fig. 189 shows the structure of the D_s^- matched and

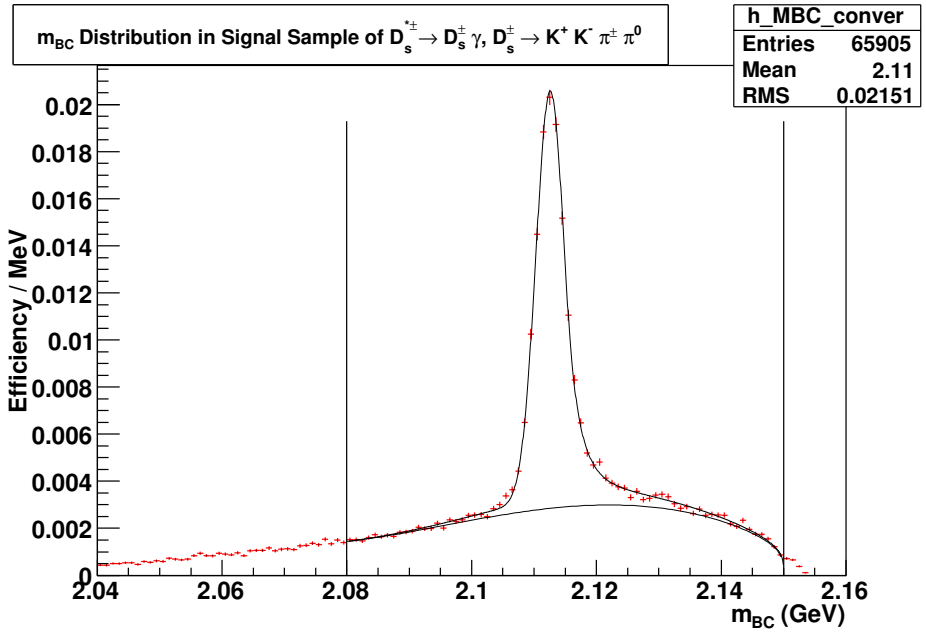

Figure 187: Distribution of m_{BC} in the signal Monte Carlo sample of $D_s^{*+} \to D_s^+\gamma$ events where $D_s^+ \to K^+K^-\pi^+\pi^0$. The plot is normalized so as to directly read out the efficiency of the m_{BC} selection criterion from the area under the fit within the signal region.

Table 72: $\epsilon^i_{D_s\gamma}$ is the efficiency of our selection criteria for the mode. $N^i_{D_s\gamma}$ is the signal yield observed for this mode. $B(D_s^{*+} \to D_s^+\gamma)$ is the branching fraction for $D_s^{*+} \to D_s^+e^+e^-$ inferred from this mode. Error [1] on the inferred branching fraction is the statistical error from the final fit. Error [2] encapsulates the systematic uncertainties from the signal efficiency, the integrated luminosity and the production cross section for $D_s^{*\pm}D_s^{\mp}$.

i (Decay Mode of D_s^+)	$B(D_s^+ \to i)$	$\epsilon^i_{D_s\gamma}$	$N^i_{D_s\gamma}$	$B(D_s^{*+} \to D_s^+\gamma)$ Inferred
$D_s^+ \to K^+K^-\pi^+\pi^0$	0.0525	0.1225 ± 0.0010	3178 ± 49	$0.8894 \pm 0.0138^{[1]} \pm 0.0073^{[2]}$

photon matched background, and our fit to parameterize this shape. The background with the D_s^- matched and a photon that failed matching is shown in Fig. 190 along with our fit to parameterize the shape.

As a check on how well our background and signal estimation performs, we present the overall fit to generic MC, as described for the $K^+K^-\pi^+$ mode, in Fig. 191. Our measurement of the signal selection efficiency and the signal yield is presented in Table 72. We find the thus estimated value for $B(D_s^{*+} \to D_s^+\gamma)$ equal to 0.889 ± 0.016 to be 3.3σ away from the programmed value of 0.942 in the Monte Carlo simulation.

We present the distribution of m_{BC} in data and our fits to estimate the signal yield over the backgrounds, as described for the $K^+K^-\pi^+$ mode, in Fig. 192. Our measurements of the signal efficiency and signal yield are presented in Table 73. We find the estimated value for $B(D_s^{*+} \to D_s^+\gamma)$ equal to 0.943 ± 0.100 to be roughly 0.01σ away from the currently

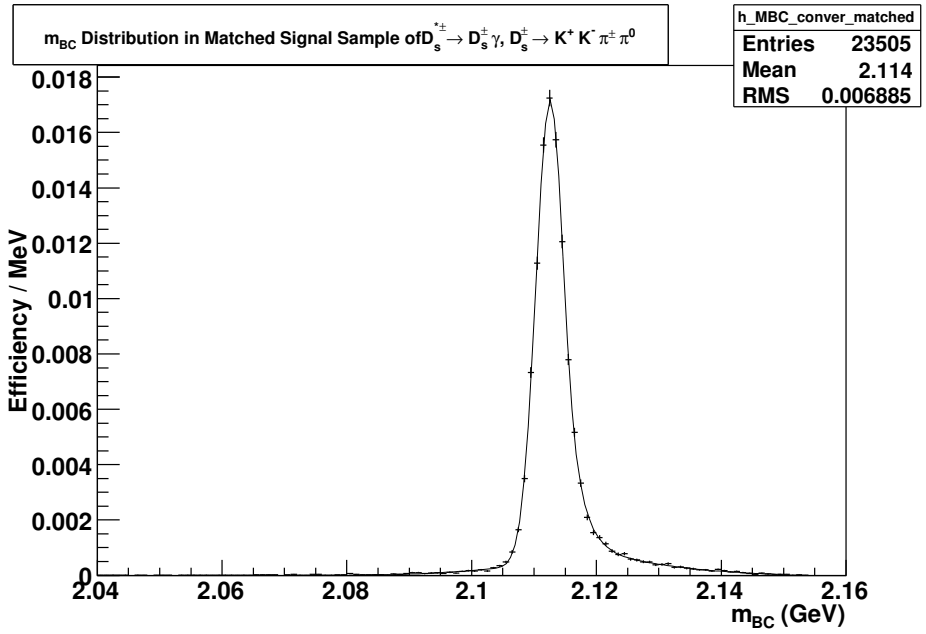

Figure 188: Distribution of m_{BC} in the signal Monte Carlo sample of $D_s^{*+} \to D_s^+\gamma$ events where $D_s^+ \to K^+K^-\pi^+\pi^0$.

accepted value of 0.942 ± 0.007.

Table 73: $\epsilon^i_{D_s\gamma}$ is the efficiency of our selection criteria for the mode. $N^i_{D_s\gamma}$ is the signal yield observed for this mode. $B(D_s^{*+} \to D_s^+\gamma)$ is the branching fraction for $D_s^{*+} \to D_s^+e^+e^-$ inferred from this mode. Error [1] on the inferred branching fraction is the statistical error from the final fit. Error [2] arises from the uncertainty in the branching fraction for $D_s^+ \to i$. Error [3] encapsulates the systematic uncertainties from the signal efficiency, the integrated luminosity and the production cross section for $D_s^{*\pm}D_s^{\mp}$. Error [4] encapsulates the systematic error arising from the fit.

i (Decay Mode of D_s^+)	$B(D_s^+ \to i)$	$\epsilon^i_{D_s\gamma}$	$N^i_{D_s\gamma}$	$B(D_s^{*+} \to D_s^+\gamma)$ Inferred
$D_s^+ \to K^+K^-\pi^+\pi^0$	0.056 ± 0.005	0.1225 ± 0.0010	$3592 \pm 118 \pm 72$	$0.943 \pm 0.031^{[1]} \pm 0.085^{[2]} \pm 0.038^{[3]} \pm 0.019^{[4]}$

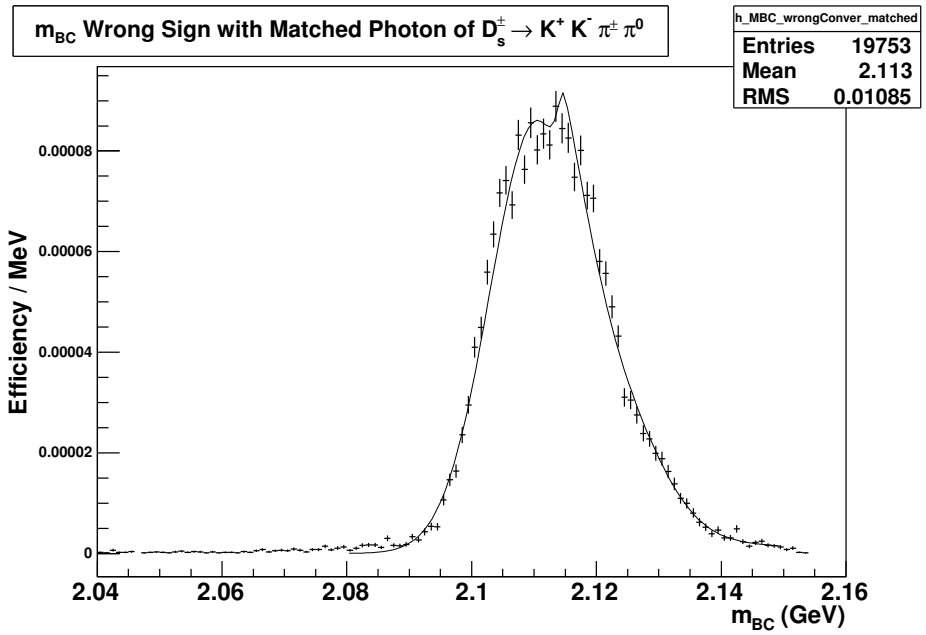

Figure 189: Combinatorial background in the m_{BC} distribution consisting of events where the D_s^{*+} has been reconstructed out of the D_s^- and the γ, and where both the D_s^- and the γ have been matched to their generated counterparts in the Monte Carlo simulation. This distribution has been fitted to a shape described by Eq. 68.

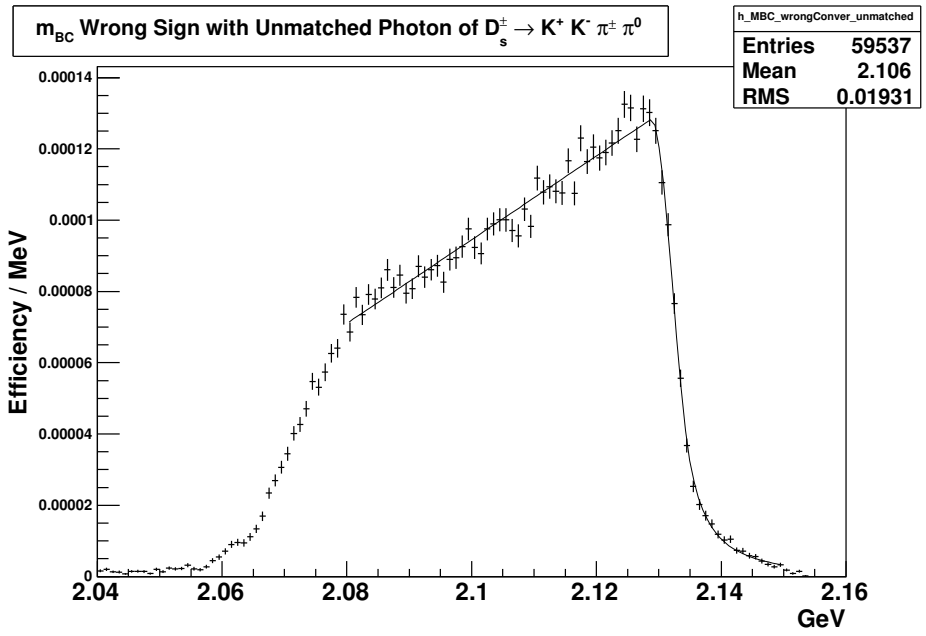

Figure 190: Combinatorial background structured in the m_{BC} distribution consisting of events where the D_s^{*+} has been reconstructed out of the D_s^- and the γ, and the D_s^- has been matched to its generated counterpart but the γ has failed to match the photon from the D_s^{*+} decay at the generator level of the Monte Carlo simulation. This distribution has been fitted to a shape described by Eq. 69.

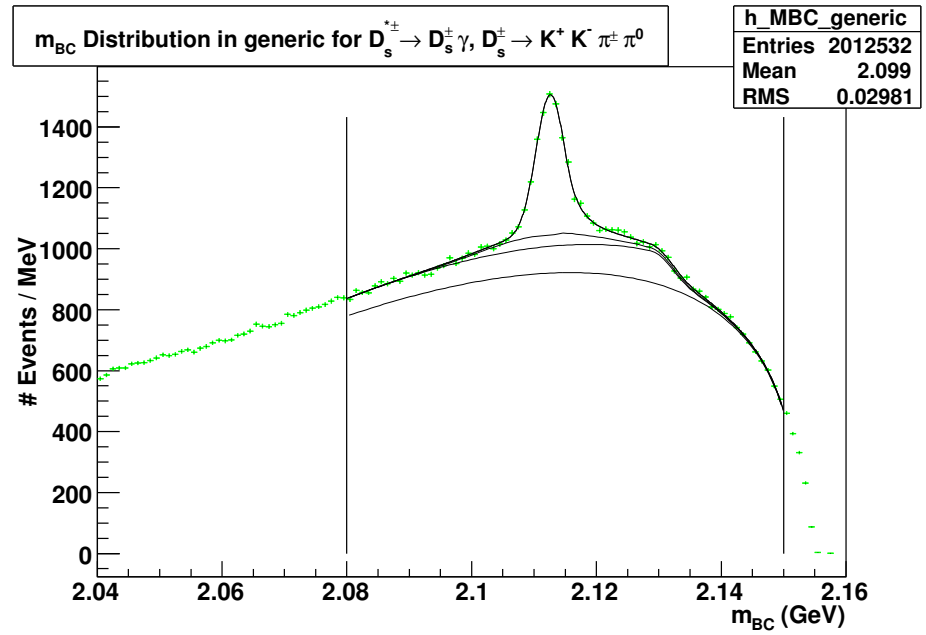

Figure 191: Distribution of m_{BC} of $D_s^{*+} \to D_s^+\gamma$ events where $D_s^+ \to K^+K^-\pi^+\pi^0$ in 586 pb^{-1} of Generic Monte Carlo.

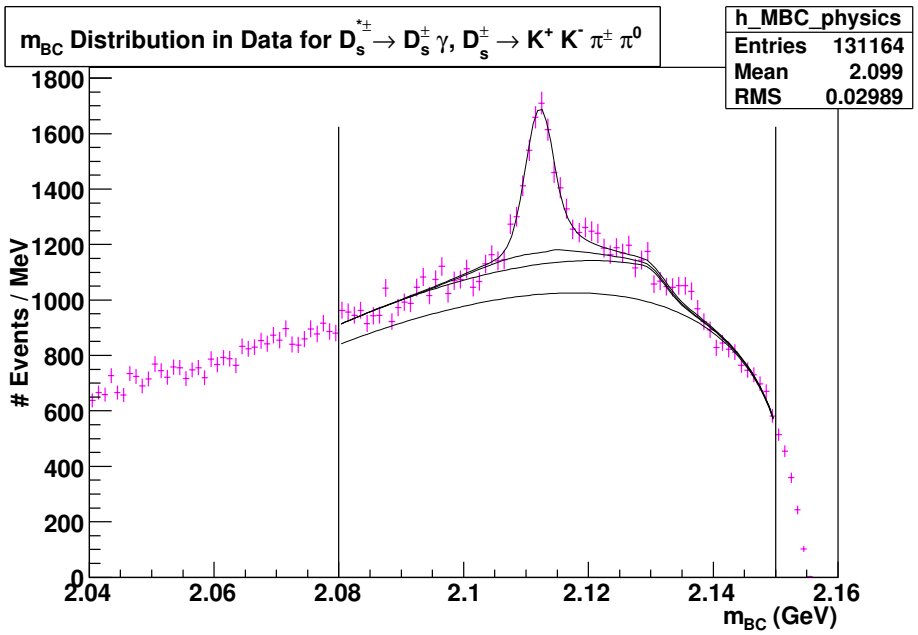

Figure 192: Distribution of m_{BC} of $D_s^{*+} \to D_s^+\gamma$ events where $D_s^+ \to K^+K^-\pi^+\pi^0$ in 586 pb^{-1} of data.

Table 74: Selection criteria for $D_s^{*+} \to D_s^+\gamma$ events where $D_s^+ \to \pi^+\pi^-\pi^+$. The δm cut has been widened to accomodate the wider peak for the signal in this distribution.

Selection Criterion	Cut Center ± Width
$m_{D_s^+}$	1.969 ± 0.012 GeV
δm	0.140 ± 0.020 GeV

14.6 $D_s^+ \to \pi^+\pi^-\pi^+$

We begin with a Monte Carlo signal sample of $D_s^{*+} \to D_s^+\gamma$ events where $D_s^+ \to \pi^+\pi^-\pi^+$ and the D_s^- is allowed to decay generically. The selection criteria applied are tabulated in Table 74. Fig. 193 depicts the δm distribution of this signal sample and shows why the corresponding selection criterion had to be widened relative to the $D_s^{*+} \to D_s^+e^+e^-$ signal selection.

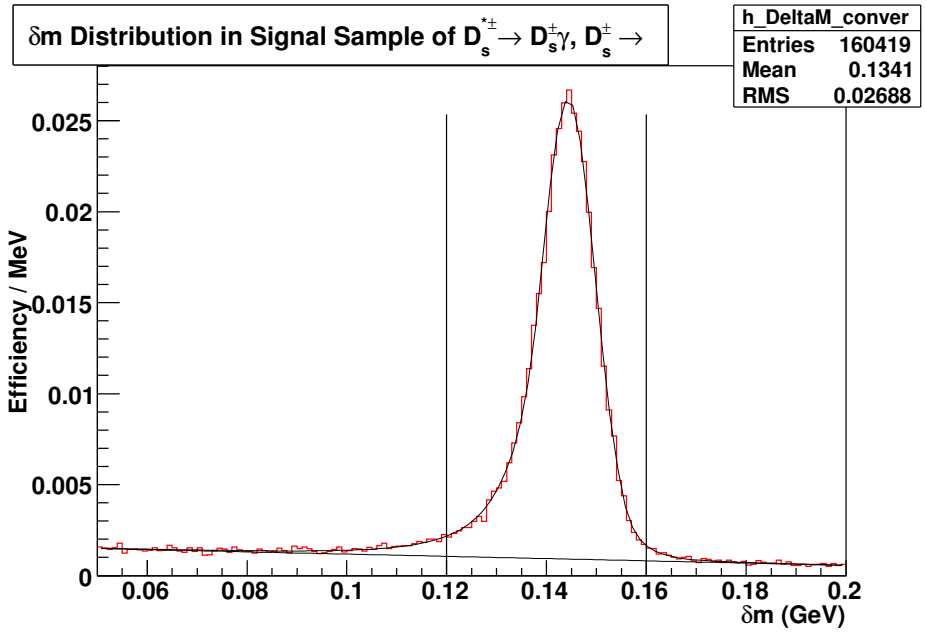

Figure 193: Distribution of δm in the signal Monte Carlo sample of $D_s^{*+} \to D_s^+\gamma$ events where $D_s^+ \to \pi^+\pi^-\pi^+$. The plot is normalized so as to directly read out the efficiency of the δm selection criterion.

To obtain the selection efficiency using the condition on m_{BC} as our last selection criterion, we produce a plot of the m_{BC} distribution of the signal sample, having applied all other criteria, as shown in Fig. 194. We extract the shape of the peak from the plot of m_{BC} where the D_s^+ and the photon are matched to their generated counterparts in the Monte Carlo simulation as shown in Fig. 195. The equations that parameterize all fits and the range they are fitted in are identical to those used in the $K^+K^-\pi^+$ mode.

Structured backgrounds arising from incorrectly reconstructed D_s^{*+} are simulated as done

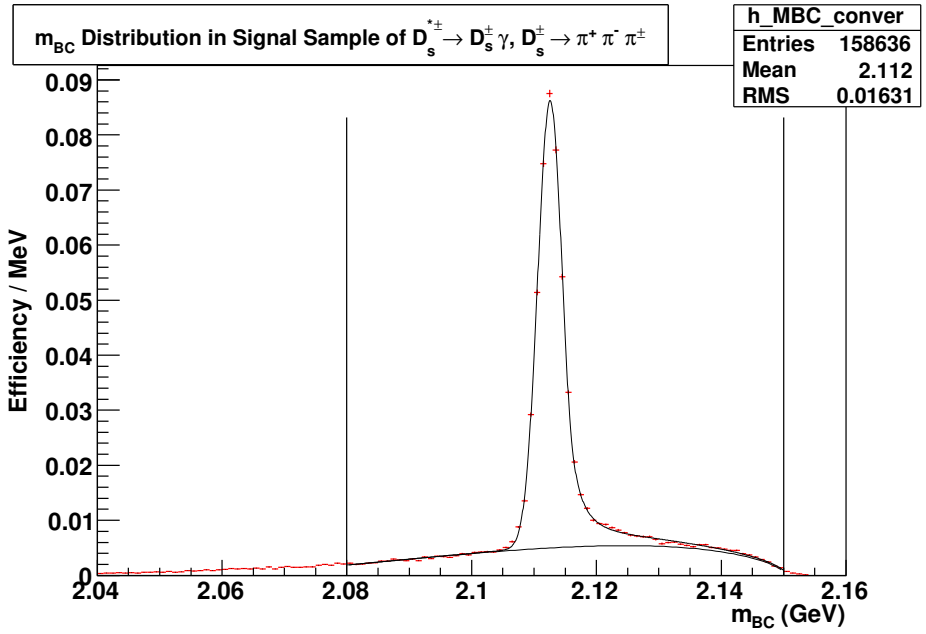

Figure 194: Distribution of m_{BC} in the signal Monte Carlo sample of $D_s^{*+} \to D_s^+\gamma$ events where $D_s^+ \to \pi^+\pi^-\pi^+$. The plot is normalized so as to directly read out the efficiency of the m_{BC} selection criterion from the area under the fit within the signal region.

Table 75: $\epsilon^i_{D_s\gamma}$ is the efficiency of our selection criteria for the mode. $N^i_{D_s\gamma}$ is the signal yield observed for this mode. $B(D_s^{*+} \to D_s^+\gamma)$ is the branching fraction for $D_s^{*+} \to D_s^+e^+e^-$ inferred from this mode. Error [1] on the inferred branching fraction is the statistical error from the final fit. Error [2] encapsulates the systematic uncertainties from the signal efficiency, the integrated luminosity and the production cross section for $D_s^{*\pm}D_s^{\mp}$.

i (Decay Mode of D_s^+)	$B(D_s^+ \to i)$	$\epsilon^i_{D_s\gamma}$	$N^i_{D_s\gamma}$	$B(D_s^{*+} \to D_s^+\gamma)$ Inferred
$D_s^+ \to \pi^+\pi^-\pi^+$	0.0103	0.4583 ± 0.0018	2706 ± 43	$1.0327 \pm 0.0162^{[1]} \pm 0.0041^{[2]}$

previously for the $K^+K^-\pi^+$ mode. Fig. 196 shows the structure of the D_s^- matched and photon matched background, and our fit to parameterize this shape. The background with the D_s^- matched and a photon that failed matching is shown in Fig. 197 along with our fit to parameterize the shape.

As a check on how well our background and signal estimation performs, we present the overall fit to generic MC, as described for the $K^+K^-\pi^+$ mode, in Fig. 198. Our measurement of the signal selection efficiency and the signal yield is presented in Table 75. We find the thus estimated value for $B(D_s^{*+} \to D_s^+\gamma)$ equal to 1.0327 ± 0.0167 to be 5.4σ away from the programmed value of 0.942 in the Monte Carlo simulation.

We present the distribution of m_{BC} in data and our fits to estimate the signal yield over the backgrounds, as described for the $K^+K^-\pi^+$ mode, in Fig. 199. Our measurements of the signal efficiency and signal yield are presented in Table 76. We find the estimated value

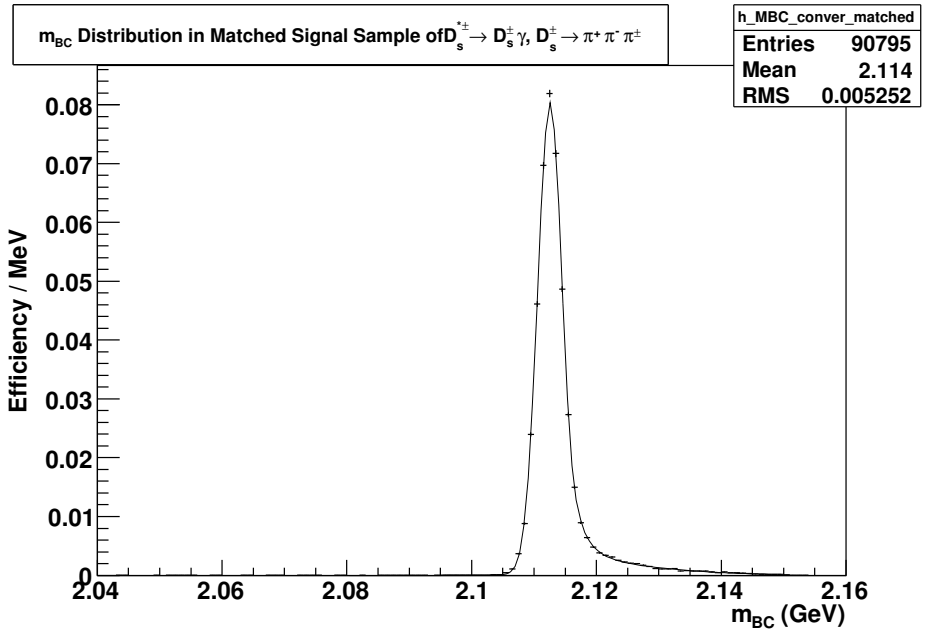

Figure 195: Distribution of m_{BC} in the signal Monte Carlo sample of $D_s^{*+} \to D_s^+\gamma$ events where $D_s^+ \to \pi^+\pi^-\pi^+$.

for $B(D_s^{*+} \to D_s^+\gamma)$ equal to 0.971 ± 0.088 to be roughly 0.3σ away from the currently accepted value of 0.942 ± 0.007.

Table 76: $\epsilon^i_{D_s\gamma}$ is the efficiency of our selection criteria for the mode. $N^i_{D_s\gamma}$ is the signal yield observed for this mode. $B(D_s^{*+} \to D_s^+\gamma)$ is the branching fraction for $D_s^{*+} \to D_s^+e^+e^-$ inferred from this mode. Error [1] on the inferred branching fraction is the statistical error from the final fit. Error [2] arises from the uncertainty in the branching fraction for $D_s^+ \to i$. Error [3] encapsulates the systematic uncertainties from the signal efficiency, the integrated luminosity and the production cross section for $D_s^{*\pm}D_s^{\mp}$. Error [4] encapsulates the systematic error arising from the fit.

i (Decay Mode of D_s^+)	$B(D_s^+ \to i)$	$\epsilon^i_{D_s\gamma}$	$N^i_{D_s\gamma}$	$B(D_s^{*+} \to D_s^+\gamma)$ Inferred
$D_s^+ \to \pi^+\pi^-\pi^+$	0.0111 ± 0.0008	0.4583 ± 0.0018	$2745 \pm 93 \pm 52$	$0.971 \pm 0.033^{[1]} \pm 0.070^{[2]} \pm 0.038^{[3]} \pm 0.018^{[4]}$

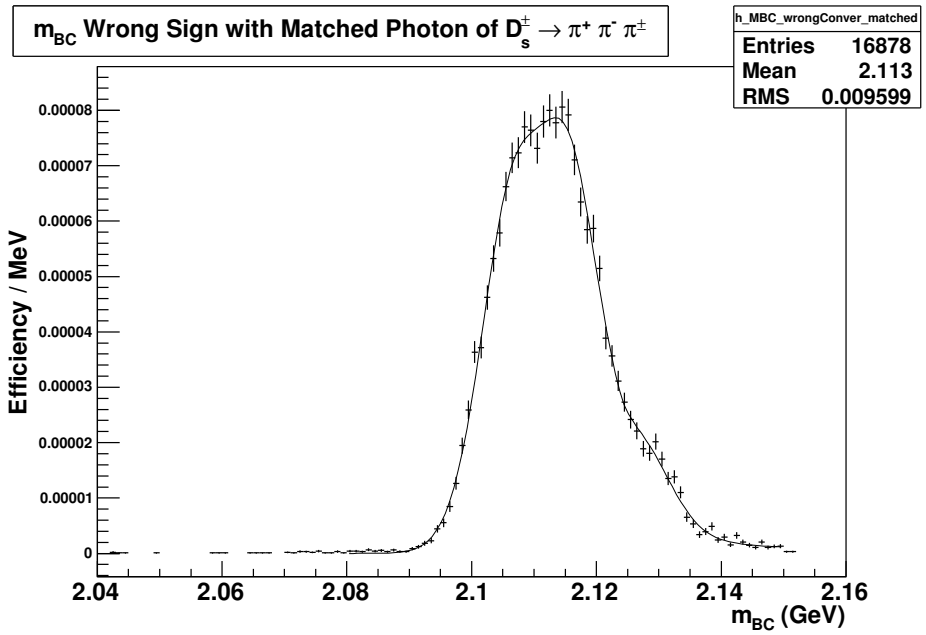

Figure 196: Combinatorial background in the m_{BC} distribution consisting of events where the D_s^{*+} has been reconstructed out of the D_s^- and the γ, and where both the D_s^- and the γ have been matched to their generated counterparts in the Monte Carlo simulation. This distribution has been fitted to a shape described by Eq. 68.

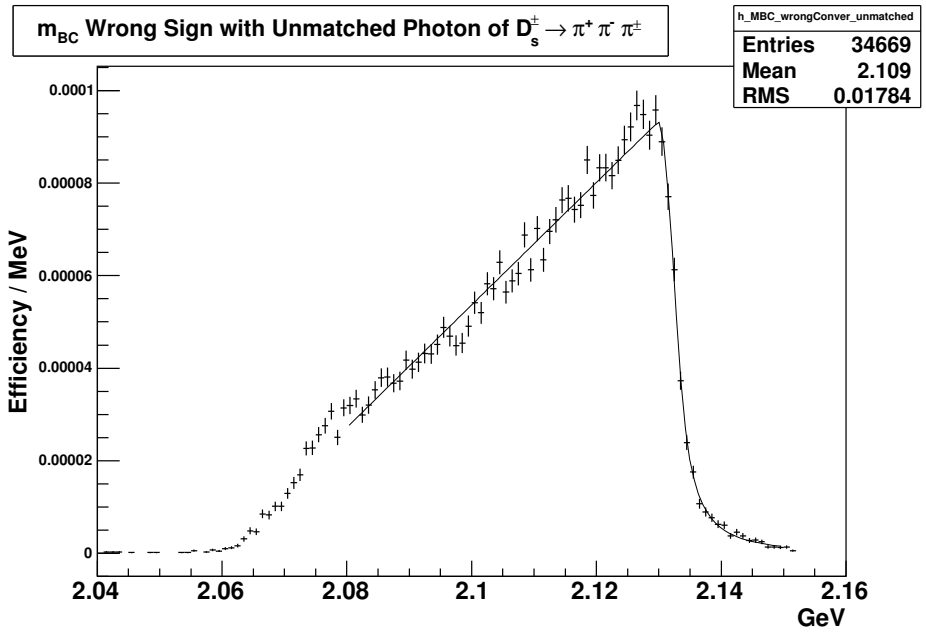

Figure 197: Combinatorial background structured in the m_{BC} distribution consisting of events where the D_s^{*+} has been reconstructed out of the D_s^- and the γ, and the D_s^- has been matched to its generated counterpart but the γ has failed to match the photon from the D_s^{*+} decay at the generator level of the Monte Carlo simulation. This distribution has been fitted to a shape described by Eq. 69.

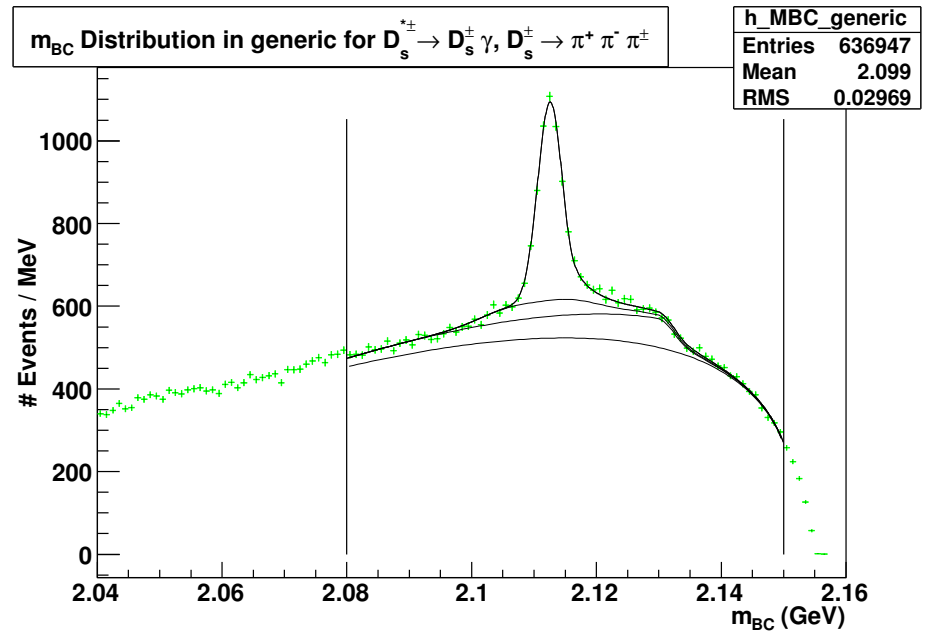

Figure 198: Distribution of m_{BC} of $D_s^{*+} \to D_s^+\gamma$ events where $D_s^+ \to \pi^+\pi^-\pi^+$ in 586 pb^{-1} of Generic Monte Carlo.

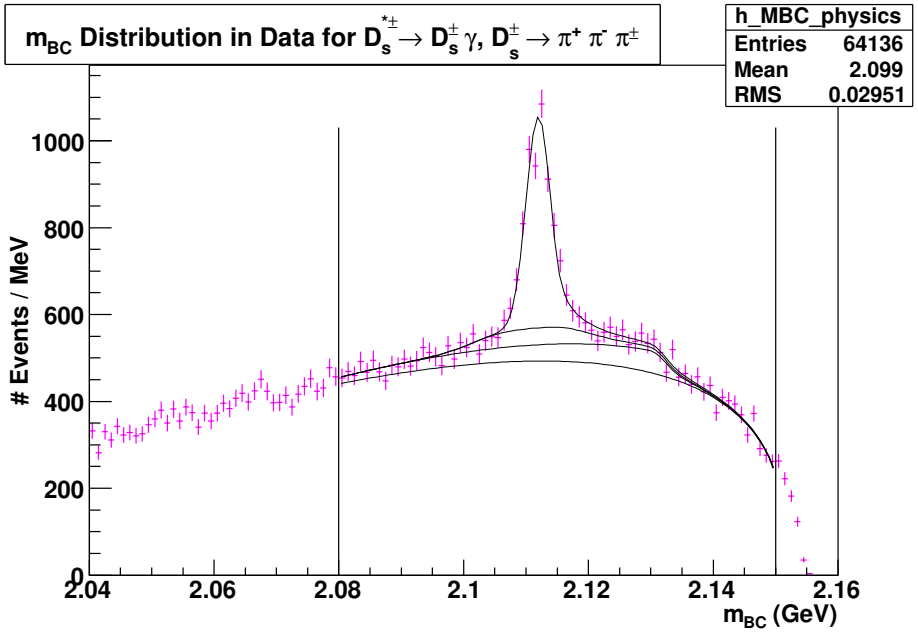

Figure 199: Distribution of m_{BC} of $D_s^{*+} \to D_s^+\gamma$ events where $D_s^+ \to \pi^+\pi^-\pi^+$ in 586 pb^{-1} of data.

Table 77: Selection criteria for $D_s^{*+} \to D_s^+\gamma$ events where $D_s^+ \to K^{*+}K^{*0}$. The δm cut has been widened to accomodate the wider peak for the signal in this distribution.

Selection Criterion	Cut Center ± Width
$m_{D_s^+}$	1.969 ± 0.006 GeV
m_{BC}	2.112 ± 0.005 GeV
δm	0.140 ± 0.020 GeV

14.7 $D_s^+ \to K^{*+}K^{*0}$

We begin with a Monte Carlo signal sample of $D_s^{*+} \to D_s^+\gamma$ events where $D_s^+ \to K^{*+}K^{*0}$ and the D_s^- is allowed to decay generically. The selection criteria applied are tabulated in Table 77. Fig. 200 depicts the δm distribution of this signal sample and shows why the corresponding selection criterion had to be widened relative to the $D_s^{*+} \to D_s^+e^+e^-$ signal selection.

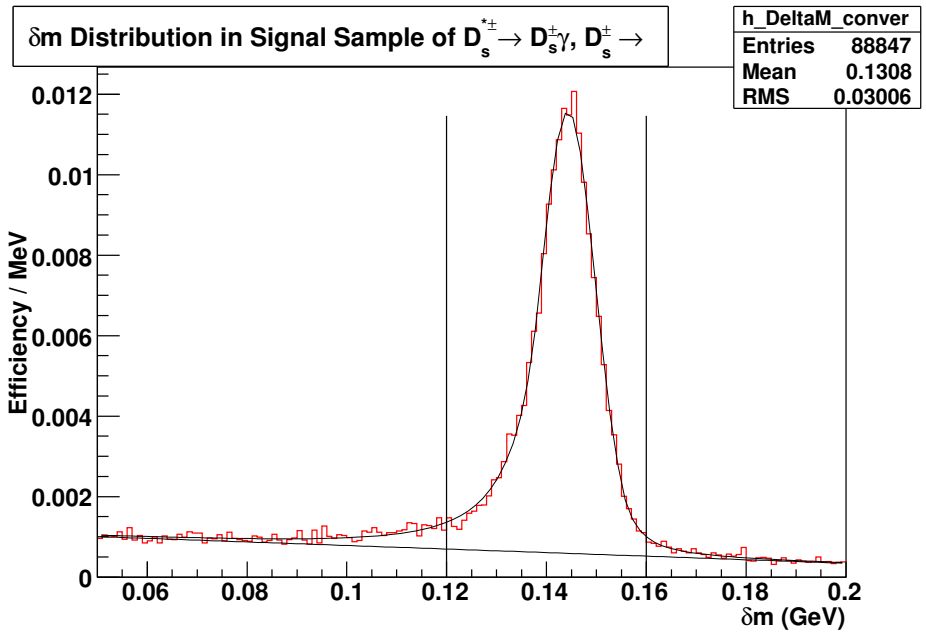

Figure 200: Distribution of δm in the signal Monte Carlo sample of $D_s^{*+} \to D_s^+\gamma$ events where $D_s^+ \to K^{*+}K^{*0}$. The plot is normalized so as to directly read out the efficiency of the δm selection criterion.

To obtain the selection efficiency using the condition on m_{BC} as our last selection criterion, we produce a plot of the m_{BC} distribution of the signal sample, having applied all other criteria, as shown in Fig. 201. We extract the shape of the peak from the plot of m_{BC} where the D_s^+ and the photon are matched to their generated counterparts in the Monte Carlo simulation as shown in Fig. 202. The equations that parameterize all fits and the range they are fitted in are identical to those used in the $K^+K^-\pi^+$ mode.

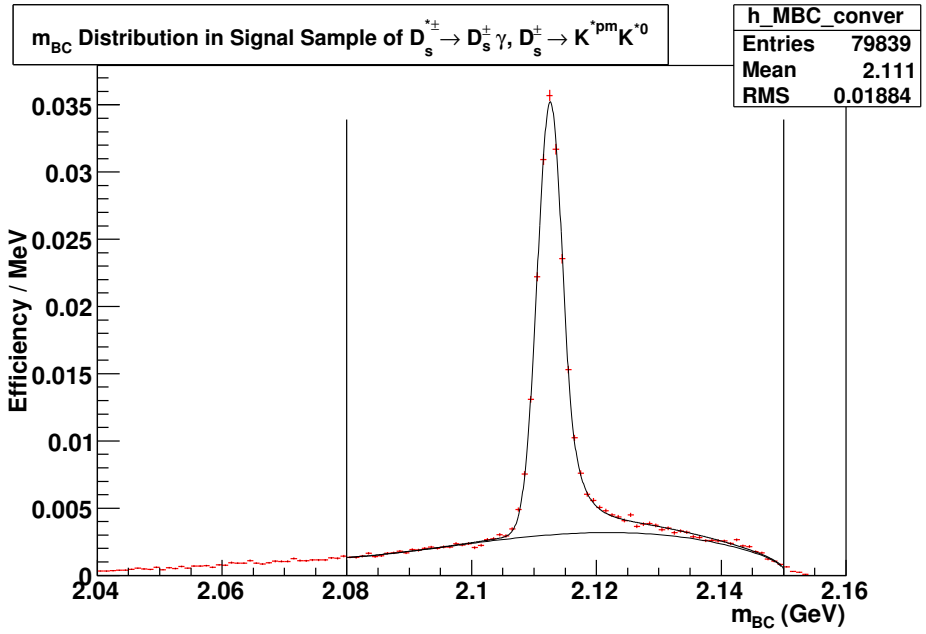

Figure 201: Distribution of m_{BC} in the signal Monte Carlo sample of $D_s^{*+} \to D_s^+\gamma$ events where $D_s^+ \to K^{*+}K^{*0}$. The plot is normalized so as to directly read out the efficiency of the m_{BC} selection criterion from the area under the fit within the signal region.

Table 78: $\epsilon^i_{D_s\gamma}$ is the efficiency of our selection criteria for the mode. $N^i_{D_s\gamma}$ is the signal yield observed for this mode. $B(D_s^{*+} \to D_s^+\gamma)$ is the branching fraction for $D_s^{*+} \to D_s^+e^+e^-$ inferred from this mode. Error [1] on the inferred branching fraction is the statistical error from the final fit. Error [2] encapsulates the systematic uncertainties from the signal efficiency, the integrated luminosity and the production cross section for $D_s^{*\pm}D_s^{\mp}$.

i (Decay Mode of D_s^+)	$B(D_s^+ \to i)$	$\epsilon^i_{D_s\gamma}$	$N^i_{D_s\gamma}$	$B(D_s^{*+} \to D_s^+\gamma)$ Inferred
$D_s^+ \to K^{*+}K^{*0}$	0.01628	0.1913 ± 0.0012	1644 ± 22	$0.9502 \pm 0.0129^{[1]} \pm 0.0058^{[2]}$

Structured backgrounds arising from incorrectly reconstructed D_s^{*+} are simulated as done previously for the $K^+K^-\pi^+$ mode. Fig. 203 shows the structure of the D_s^- matched and photon matched background, and our fit to parameterize this shape. The background with the D_s^- matched and a photon that failed matching is shown in Fig. 204 along with our fit to parameterize the shape.

As a check on how well our background and signal estimation performs, we present the overall fit to generic MC, as described for the $K^+K^-\pi^+$ mode, in Fig. 205. Our measurement of the signal selection efficiency and the signal yield is presented in Table 78. We find the thus estimated value for $B(D_s^{*+} \to D_s^+\gamma)$ equal to 0.950 ± 0.014 to be 0.6σ away from the programmed value of 0.942 in the Monte Carlo simulation.

We present the distribution of m_{BC} in data and our fits to estimate the signal yield over the backgrounds, as described for the $K^+K^-\pi^+$ mode, in Fig. 206. Our measurements of

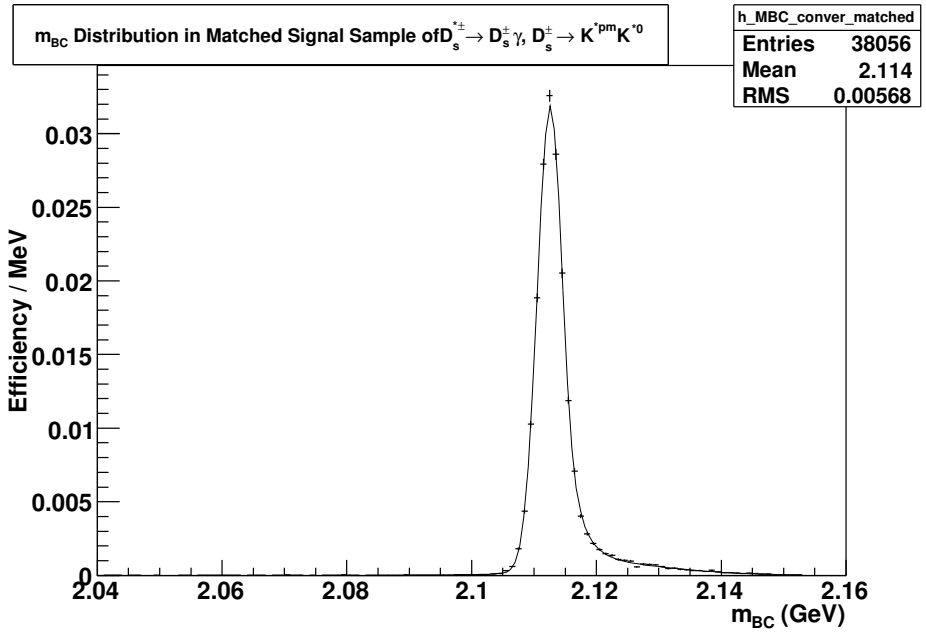

Figure 202: Distribution of m_{BC} in the signal Monte Carlo sample of $D_s^{*+} \to D_s^+\gamma$ events where $D_s^+ \to K^{*+}K^{*0}$.

the signal efficiency and signal yield are presented in Table 79. We find the estimated value for $B(D_s^{*+} \to D_s^+\gamma)$ equal to 0.900 ± 0.087 to be roughly 0.5σ away from the currently accepted value of 0.942 ± 0.007.

Table 79: $\epsilon^i_{D_s\gamma}$ is the efficiency of our selection criteria for the mode. $N^i_{D_s\gamma}$ is the signal yield observed for this mode. $B(D_s^{*+} \to D_s^+\gamma)$ is the branching fraction for $D_s^{*+} \to D_s^+e^+e^-$ inferred from this mode. Error [1] on the inferred branching fraction is the statistical error from the final fit. Error [2] arises from the uncertainty in the branching fraction for $D_s^+ \to i$. Error [3] encapsulates the systematic uncertainties from the signal efficiency, the integrated luminosity and the production cross section for $D_s^{*\pm}D_s^{\mp}$. Error [4] encapsulates the systematic error arising from the fit.

i (Decay Mode of D_s^+)	$B(D_s^+ \to i)$	$\epsilon^i_{D_s\gamma}$	$N^i_{D_s\gamma}$	$B(D_s^{*+} \to D_s^+\gamma)$ Inferred
$D_s^+ \to K^{*+}K^{*0}$	0.0164 ± 0.0012	0.1913 ± 0.0012	$1570 \pm 74 \pm 13$	$0.900 \pm 0.043^{[1]} \pm 0.066^{[2]} \pm 0.036^{[3]} \pm 0.007^{[4]}$

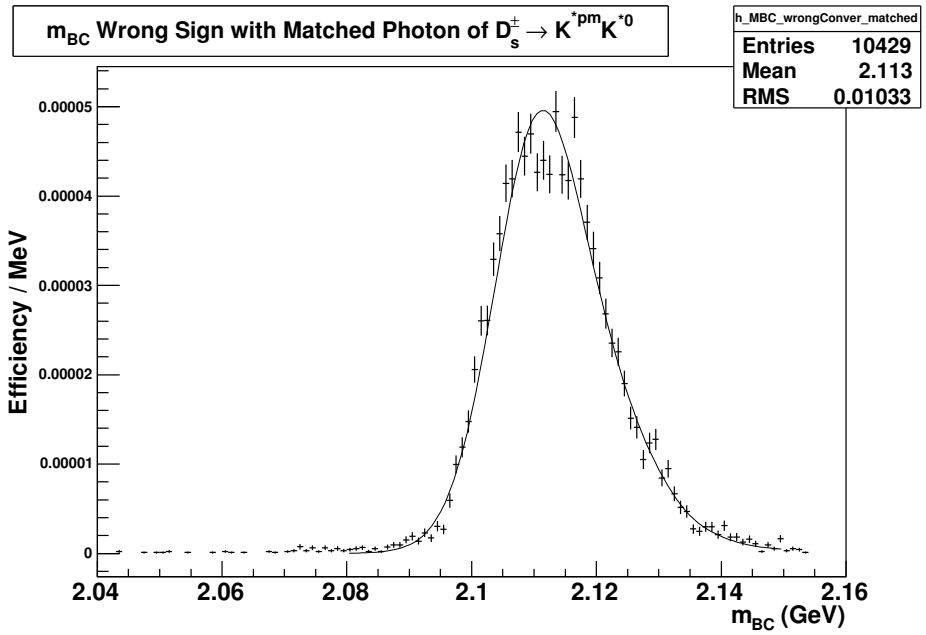

Figure 203: Combinatorial background in the m_{BC} distribution consisting of events where the D_s^{*+} has been reconstructed out of the D_s^- and the γ, and where both the D_s^- and the γ have been matched to their generated counterparts in the Monte Carlo simulation. This distribution has been fitted to a shape described by Eq. 68.

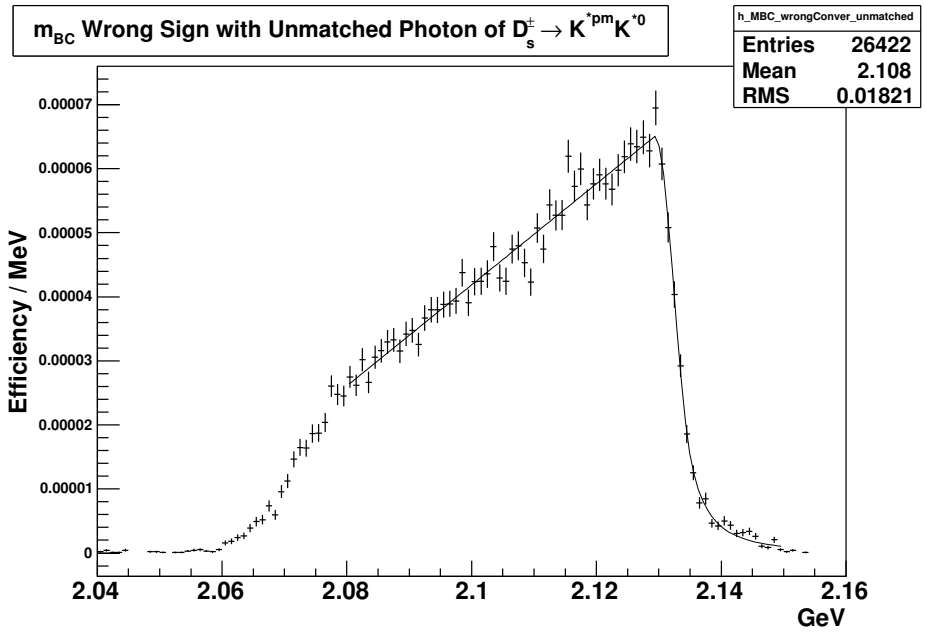

Figure 204: Combinatorial background structured in the m_{BC} distribution consisting of events where the D_s^{*+} has been reconstructed out of the D_s^- and the γ, and the D_s^- has been matched to its generated counterpart but the γ has failed to match the photon from the D_s^{*+} decay at the generator level of the Monte Carlo simulation. This distribution has been fitted to a shape described by Eq. 69.

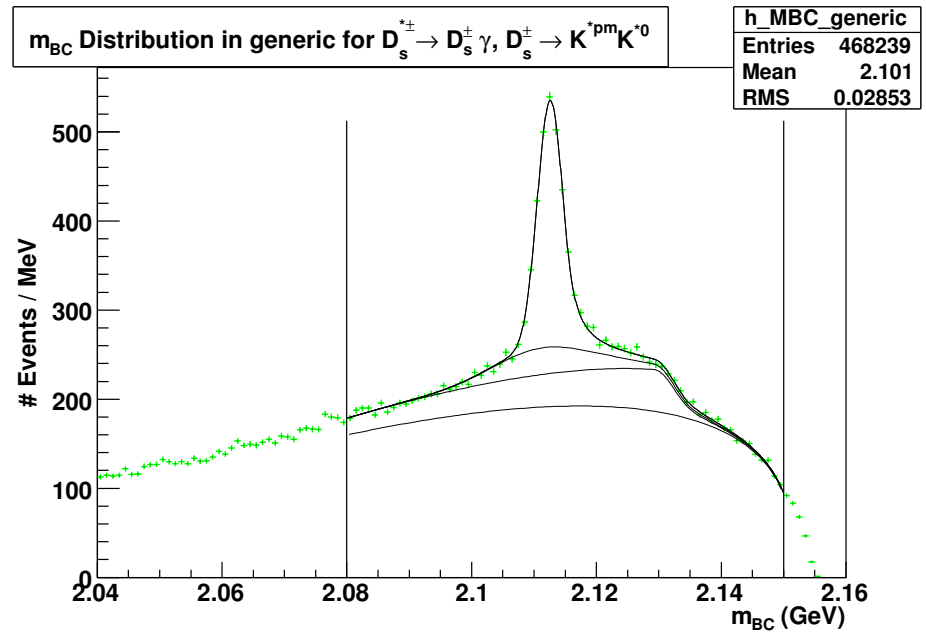

Figure 205: Distribution of m_{BC} of $D_s^{*+} \to D_s^+\gamma$ events where $D_s^+ \to K^{*+}K^{*0}$ in 586 pb^{-1} of Generic Monte Carlo.

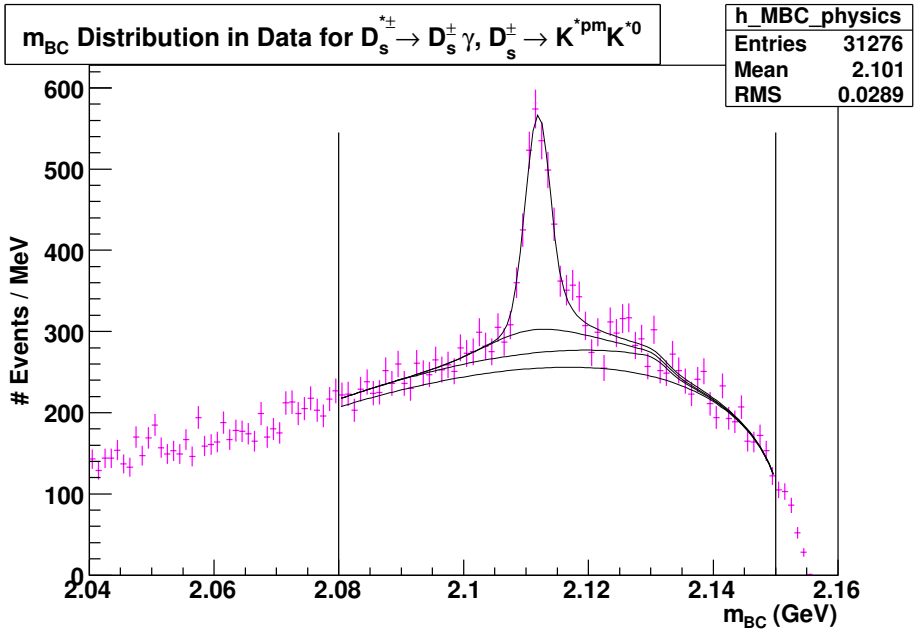

Figure 206: Distribution of m_{BC} of $D_s^{*+} \to D_s^+\gamma$ events where $D_s^+ \to K^{*+}K^{*0}$ in 586 pb^{-1} of data.

Table 80: Selection criteria for $D_s^{*+} \to D_s^+\gamma$ events where $D_s^+ \to \eta\rho^+$. The δm cut has been widened to accomodate the wider peak for the signal in this distribution.

Selection Criterion	Cut Center ± Width
$m_{D_s^+}$	1.969 ± 0.015 GeV
δm	0.140 ± 0.020 GeV

14.8 $D_s^+ \to \eta\rho^+; \eta \to \gamma\gamma; \rho^+ \to \pi^+\pi^0$

We begin with a Monte Carlo signal sample of $D_s^{*+} \to D_s^+\gamma$ events where $D_s^+ \to \eta\rho^+; \eta \to \gamma\gamma; \rho^+ \to \pi^+\pi^0$ and the D_s^- is allowed to decay generically. The selection criteria applied are tabulated in Table 80. Fig. 207 depicts the δm distribution of this signal sample and shows why the corresponding selection criterion had to be widened relative to the $D_s^{*+} \to D_s^+e^+e^-$ signal selection.

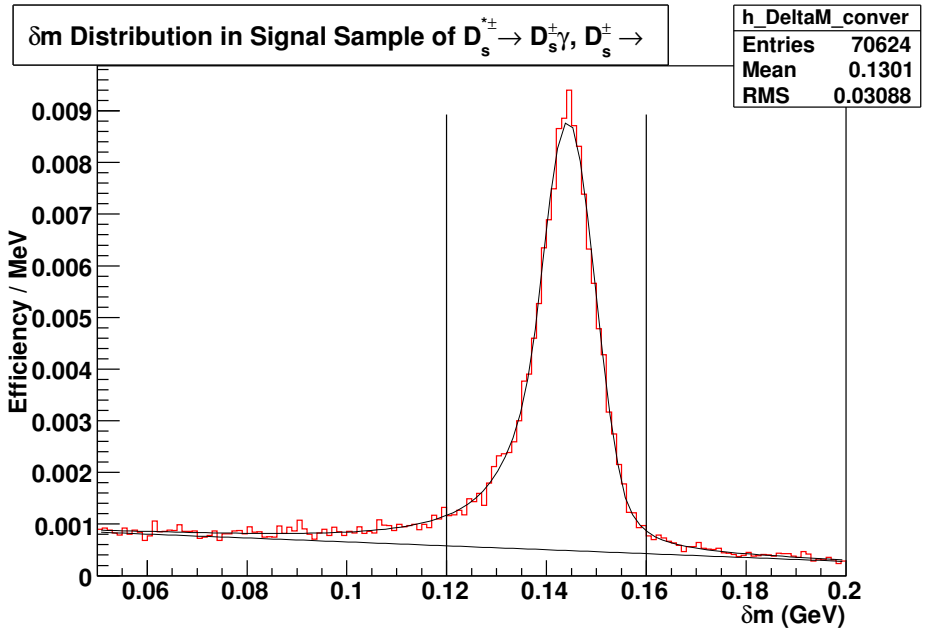

Figure 207: Distribution of δm in the signal Monte Carlo sample of $D_s^{*+} \to D_s^+\gamma$ events where $D_s^+ \to \eta\rho^+$. The plot is normalized so as to directly read out the efficiency of the δm selection criterion.

To obtain the selection efficiency using the condition on m_{BC} as our last selection criterion, we produce a plot of the m_{BC} distribution of the signal sample, having applied all other criteria, as shown in Fig. 208. We extract the shape of the peak from the plot of m_{BC} where the D_s^+ and the photon are matched to their generated counterparts in the Monte Carlo simulation as shown in Fig. 209. The equations that parameterize all fits and the range they are fitted in are identical to those used in the $K^+K^-\pi^+$ mode.

Structured backgrounds arising from incorrectly reconstructed D_s^{*+} are simulated as done

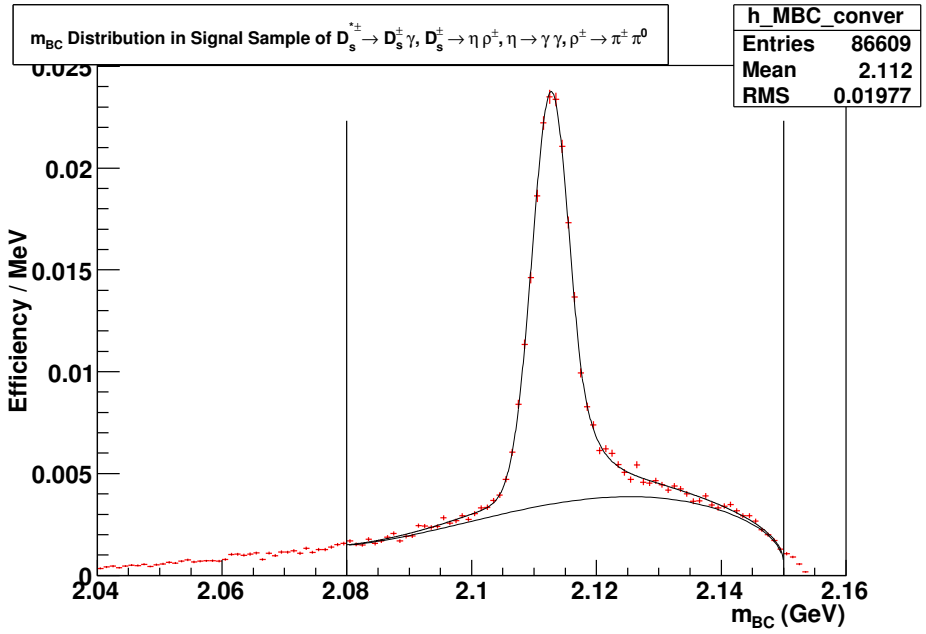

Figure 208: Distribution of m_{BC} in the signal Monte Carlo sample of $D_s^{*+} \to D_s^+\gamma$ events where $D_s^+ \to \eta\rho^+; \eta \to \gamma\gamma; \rho^+ \to \pi^+\pi^0$. The plot is normalized so as to directly read out the efficiency of the m_{BC} selection criterion from the area under the fit within the signal region.

Table 81: $\epsilon^i_{D_s\gamma}$ is the efficiency of our selection criteria for the mode. $N^i_{D_s\gamma}$ is the signal yield observed for this mode. $B(D_s^{*+} \to D_s^+\gamma)$ is the branching fraction for $D_s^{*+} \to D_s^+e^+e^-$ inferred from this mode. Error [1] on the inferred branching fraction is the statistical error from the final fit. Error [2] encapsulates the systematic uncertainties from the signal efficiency, the integrated luminosity and the production cross section for $D_s^{*\pm}D_s^{\mp}$.

i (Decay Mode of D_s^+)	$B(D_s^+ \to i)$	$\epsilon^i_{D_s\gamma}$	$N^i_{D_s\gamma}$	$B(D_s^{*+} \to D_s^+\gamma)$ Inferred
$D_s^+ \to \eta\rho^+; \eta \to \gamma\gamma; \rho^+ \to \pi^+\pi^0$	0.0298	0.1839 ± 0.0013	2993 ± 87	$0.9829 \pm 0.0284^{[1]} \pm 0.0070^{[2]}$

previously for the $K^+K^-\pi^+$ mode. Fig. 210 shows the structure of the D_s^- matched and photon matched background, and our fit to parameterize this shape. The background with the D_s^- matched and a photon that failed matching is shown in Fig. 211 along with our fit to parameterize the shape.

As a check on how well our background and signal estimation performs, we present the overall fit to generic MC, as described for the $K^+K^-\pi^+$ mode, in Fig. 212. Our measurement of the signal selection efficiency and the signal yield is presented in Table 81. We find the thus estimated value for $B(D_s^{*+} \to D_s^+\gamma)$ equal to $0.983 \pm 0.029$to be 1.4σ away from the programmed value of 0.942 in the Monte Carlo simulation.

We present the distribution of m_{BC} in data and our fits to estimate the signal yield over the backgrounds, as described for the $K^+K^-\pi^+$ mode, in Fig. 213. Our measurements of the signal efficiency and signal yield are presented in Table 82. We find the estimated value

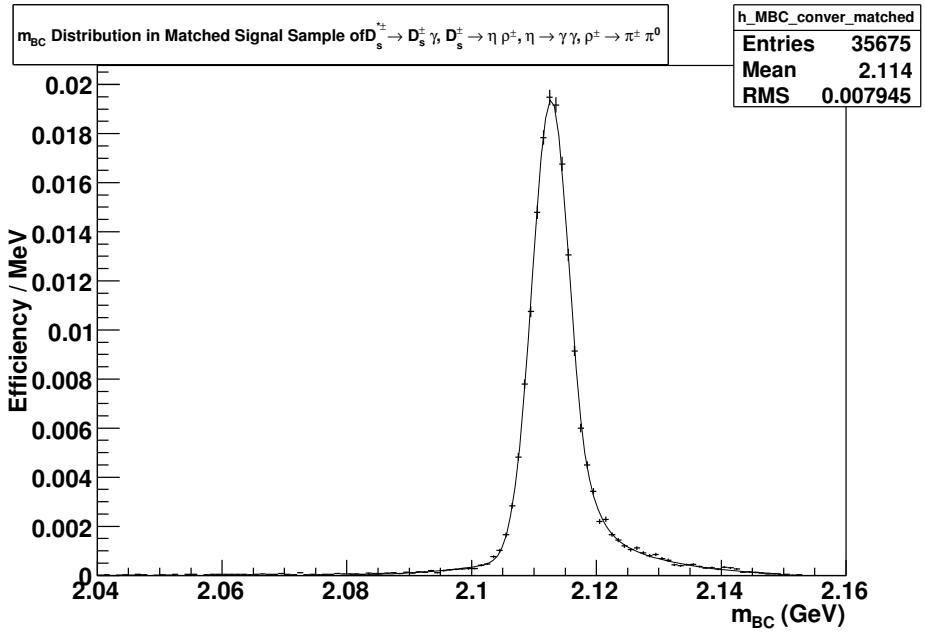

Figure 209: Distribution of m_{BC} in the signal Monte Carlo sample of $D_s^{*+} \to D_s^+\gamma$ events where $D_s^{*+} \to D_s^+\gamma$ events where $D_s^+ \to \eta\rho^+; \eta \to \gamma\gamma; \rho^+ \to \pi^+\pi^0$.

for $B(D_s^{*+} \to D_s^+\gamma)$ equal to 0.891 ± 0.132 to be roughly 0.4σ away from the currently accepted value of 0.942 ± 0.007.

Table 82: $\epsilon^i_{D_s\gamma}$ is the efficiency of our selection criteria for the mode. $N^i_{D_s\gamma}$ is the signal yield observed for this mode. $B(D_s^{*+} \to D_s^+\gamma)$ is the branching fraction for $D_s^{*+} \to D_s^+e^+e^-$ inferred from this mode. Error [1] on the inferred branching fraction is the statistical error from the final fit. Error [2] arises from the uncertainty in the branching fraction for $D_s^+ \to i$. Error [3] encapsulates the systematic uncertainties from the signal efficiency, the integrated luminosity and the production cross section for $D_s^{*\pm}D_s^{\mp}$. Error [4] encapsulates the systematic error arising from the fit.

i (Decay Mode of D_s^+)	$B(D_s^+ \to i)$	$\epsilon^i_{D_s\gamma}$	$N^i_{D_s\gamma}$	$B(D_s^{*+} \to D_s^+\gamma)$ Inferred
$D_s^+ \to \eta\rho^+; \eta \to \gamma\gamma; \rho^+ \to \pi^+\pi^0$	0.0348 ± 0.0031	0.1839 ± 0.0013	$3170 \pm 161 \pm 313$	$0.891 \pm 0.045^{[1]} \pm 0.080^{[2]} \pm 0.036^{[3]} \pm 0.088^{[4]}$

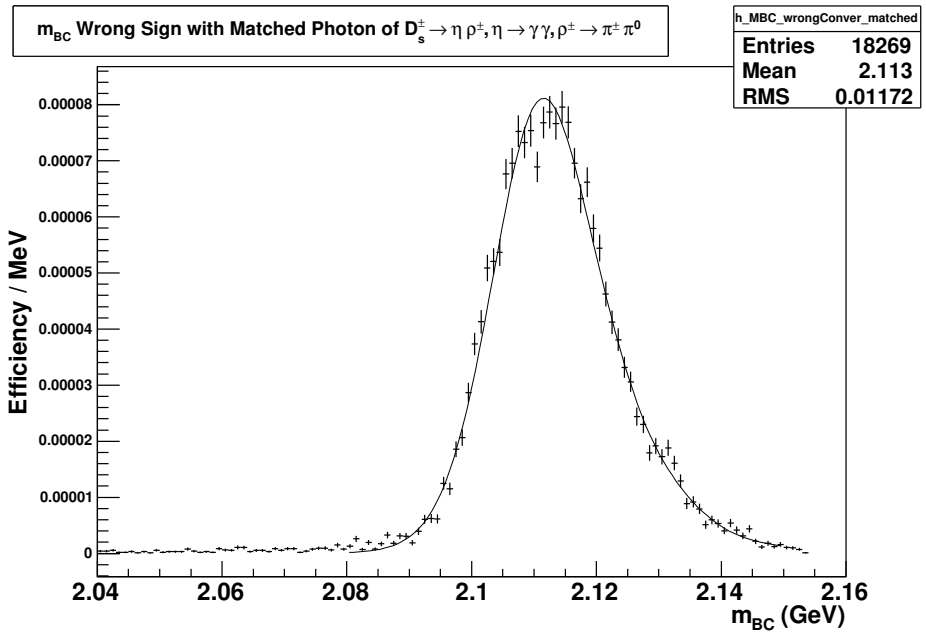

Figure 210: Combinatorial background in the m_{BC} distribution consisting of events where the D_s^{*+} has been reconstructed out of the D_s^- and the γ, and where both the D_s^- and the γ have been matched to their generated counterparts in the Monte Carlo simulation. This distribution has been fitted to a shape described by Eq. 68.

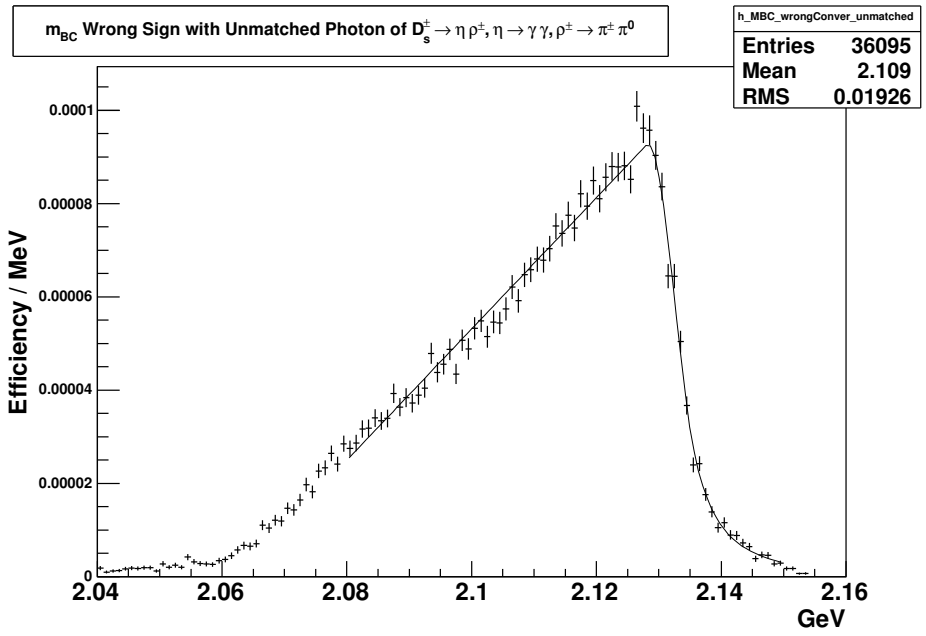

Figure 211: Combinatorial background structured in the m_{BC} distribution consisting of events where the D_s^{*+} has been reconstructed out of the D_s^- and the γ, and the D_s^- has been matched to its generated counterpart but the γ has failed to match the photon from the D_s^{*+} decay at the generator level of the Monte Carlo simulation. This distribution has been fitted to a shape described by Eq. 69.

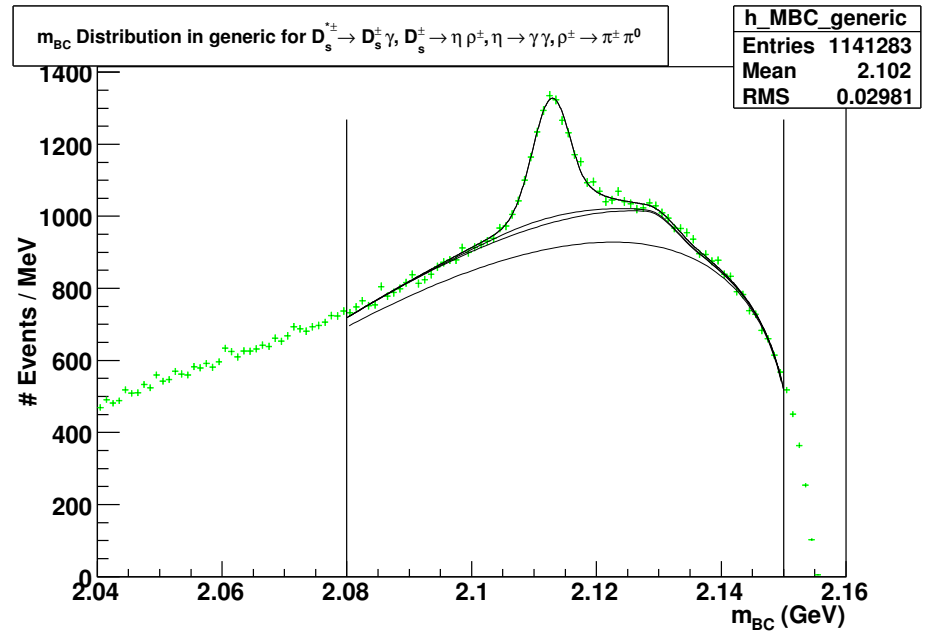

Figure 212: Distribution of m_{BC} of $D_s^{*+} \to D_s^+\gamma$ events where $D_s^+ \to \eta\rho^+; \eta \to \gamma\gamma; \rho^+ \to \pi^+\pi^0$ in 586 pb^{-1} of Generic Monte Carlo.

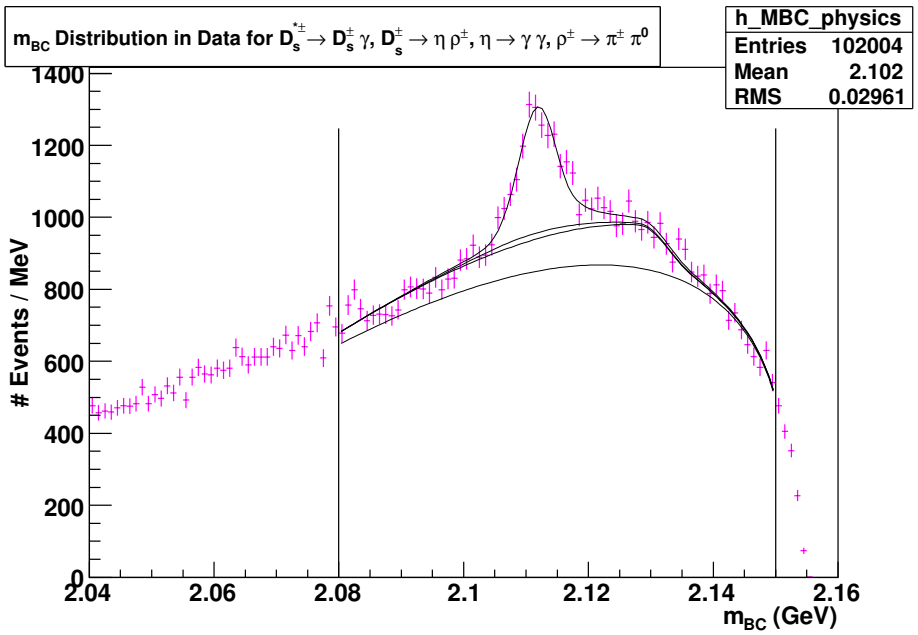

Figure 213: Distribution of m_{BC} of $D_s^{*+} \to D_s^+\gamma$ events where $D_s^+ \to \eta\rho^+; \eta \to \gamma\gamma; \rho^+ \to \pi^+\pi^0$ in 586 pb^{-1} of data.

Table 83: Selection criteria for $D_s^{*+} \to D_s^+\gamma$ events where $D_s^+ \to \eta'\pi^+; \eta' \to \rho^0\gamma$. The δm cut has been widened to accomodate the wider peak for the signal in this distribution.

Selection Criterion	Cut Center ± Width
$m_{D_s^+}$	1.969 ± 0.012 GeV
δm	0.140 ± 0.020 GeV

14.9 $D_s^+ \to \eta'\pi^+; \eta' \to \rho^0\gamma$

We begin with a Monte Carlo signal sample of $D_s^+ \to \eta'\pi^+; \eta' \to \rho^0\gamma$ and the D_s^- is allowed to decay generically. The selection criteria applied are tabulated in Table 83. Fig. 214 depicts the δm distribution of this signal sample and shows why the corresponding selection criterion had to be widened relative to the $D_s^{*+} \to D_s^+ e^+ e^-$ signal selection.

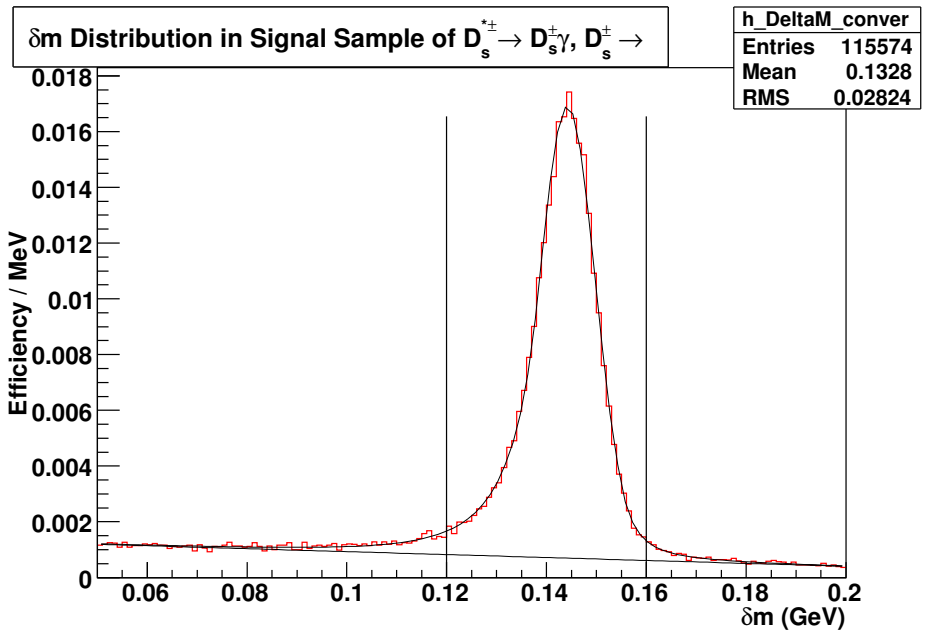

Figure 214: Distribution of δm in the signal Monte Carlo sample of $D_s^{*+} \to D_s^+\gamma$ events where $D_s^+ \to \eta'\pi^+; \eta' \to \rho^0\gamma$. The plot is normalized so as to directly read out the efficiency of the δm selection criterion.

To obtain the selection efficiency using the condition on m_{BC} as our last selection criterion, we produce a plot of the m_{BC} distribution of the signal sample, having applied all other criteria, as shown in Fig. 215. We extract the shape of the peak from the plot of m_{BC} where the D_s^+ and the photon are matched to their generated counterparts in the Monte Carlo simulation as shown in Fig. 216. The equations that parameterize all fits and the range they are fitted in are identical to those used in the $K^+K^-\pi^+$ mode.

Structured backgrounds arising from incorrectly reconstructed D_s^{*+} are simulated as done previously for the $K^+K^-\pi^+$ mode. Fig. 217 shows the structure of the D_s^- matched and

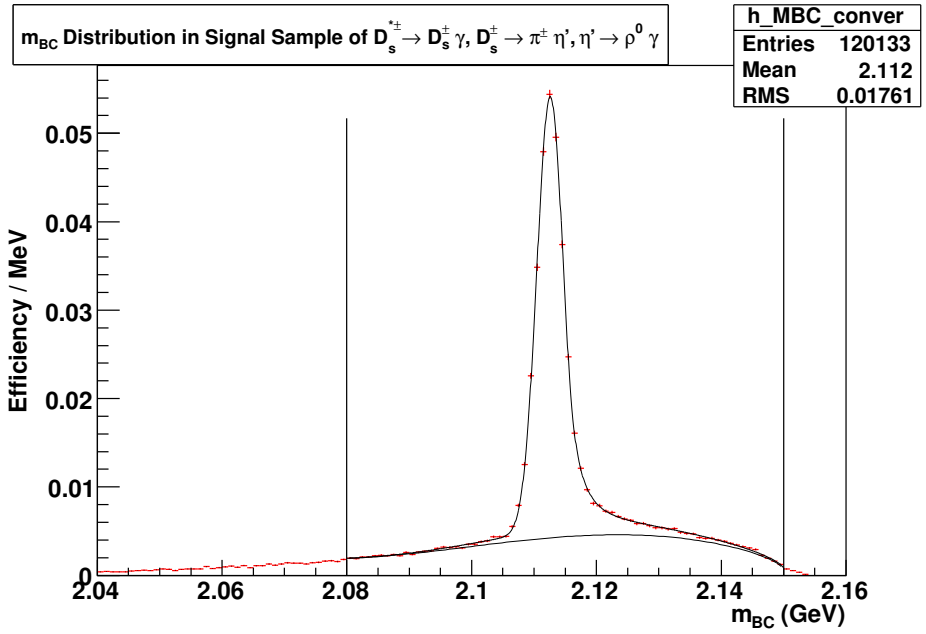

Figure 215: Distribution of m_{BC} in the signal Monte Carlo sample of $D_s^{*+} \to D_s^+\gamma$ events where $D_s^+ \to \eta'\pi^+; \eta' \to \rho^0\gamma$. The plot is normalized so as to directly read out the efficiency of the m_{BC} selection criterion from the area under the fit within the signal region.

Table 84: $\epsilon^i_{D_s\gamma}$ is the efficiency of our selection criteria for the mode. $N^i_{D_s\gamma}$ is the signal yield observed for this mode. $B(D_s^{*+} \to D_s^+\gamma)$ is the branching fraction for $D_s^{*+} \to D_s^+e^+e^-$ inferred from this mode. Error [1] on the inferred branching fraction is the statistical error from the final fit. Error [2] encapsulates the systematic uncertainties from the signal efficiency, the integrated luminosity and the production cross section for $D_s^{*\pm}D_s^{\mp}$.

i (Decay Mode of D_s^+)	$B(D_s^+ \to i)$	$\epsilon^i_{D_s\gamma}$	$N^i_{D_s\gamma}$	$B(D_s^{*+} \to D_s^+\gamma)$ Inferred
$D_s^+ \to \eta'\pi^+; \eta' \to \rho^0\gamma$	0.0111	0.3171 ± 0.0015	1930 ± 45	$0.9886 \pm 0.0231^{[1]} \pm 0.0049^{[2]}$

photon matched background, and our fit to parameterize this shape. The background with the D_s^- matched and a photon that failed matching is shown in Fig. 218 along with our fit to parameterize the shape.

As a check on how well our background and signal estimation performs, we present the overall fit to generic MC, as described for the $K^+K^-\pi^+$ mode, in Fig. 219. Our measurement of the signal selection efficiency and the signal yield is presented in Table 84. We find the thus estimated value for $B(D_s^{*+} \to D_s^+\gamma)$ equal to 0.989 ± 0.024 to be about 2σ away from the programmed value of 0.942 in the Monte Carlo simulation.

We present the distribution of m_{BC} in data and our fits to estimate the signal yield over the backgrounds, as described for the $K^+K^-\pi^+$ mode, in Fig. 220. Our measurements of the signal efficiency and signal yield are presented in Table 85. We find the estimated value for $B(D_s^{*+} \to D_s^+\gamma)$ equal to 0.778 ± 0.117 to be roughly 1.4σ away from the currently

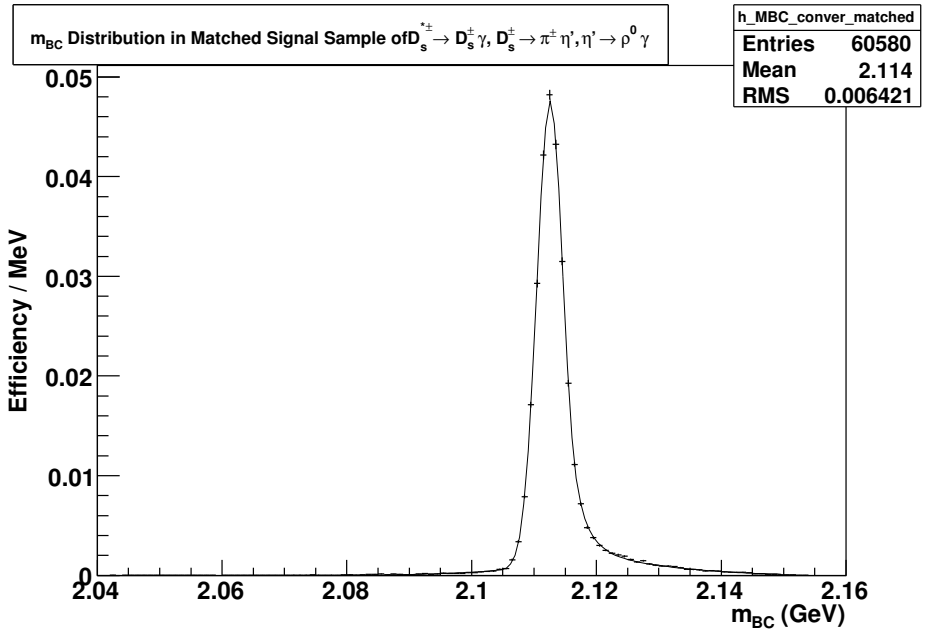

Figure 216: Distribution of m_{BC} in the signal Monte Carlo sample of $D_s^{*+} \to D_s^+\gamma$ events where $D_s^{*+} \to D_s^+\gamma$ events where $D_s^+ \to \eta'\pi^+; \eta' \to \rho^0\gamma$.

accepted value of 0.942 ± 0.007.

Table 85: $\epsilon^i_{D_s\gamma}$ is the efficiency of our selection criteria for the mode. $N^i_{D_s\gamma}$ is the signal yield observed for this mode. $B(D_s^{*+} \to D_s^+\gamma)$ is the branching fraction for $D_s^{*+} \to D_s^+e^+e^-$ inferred from this mode. Error [1] on the inferred branching fraction is the statistical error from the final fit. Error [2] arises from the uncertainty in the branching fraction for $D_s^+ \to i$. Error [3] encapsulates the systematic uncertainties from the signal efficiency, the integrated luminosity and the production cross section for $D_s^{*\pm}D_s^{\mp}$. Error [4] encapsulates the systematic error arising from the fit.

i (Decay Mode of D_s^+)	$B(D_s^+ \to i)$	$\epsilon^i_{D_s\gamma}$	$N^i_{D_s\gamma}$	$B(D_s^{*+} \to D_s^+\gamma)$ Inferred
$D_s^+ \to \eta'\pi^+; \eta' \to \rho^0\gamma$	0.0112 ± 0.0012	0.3171 ± 0.0015	$1531 \pm 80 \pm 122$	$0.778 \pm 0.041^{[1]} \pm 0.085^{[2]} \pm 0.031^{[3]} \pm 0.062^{[4]}$

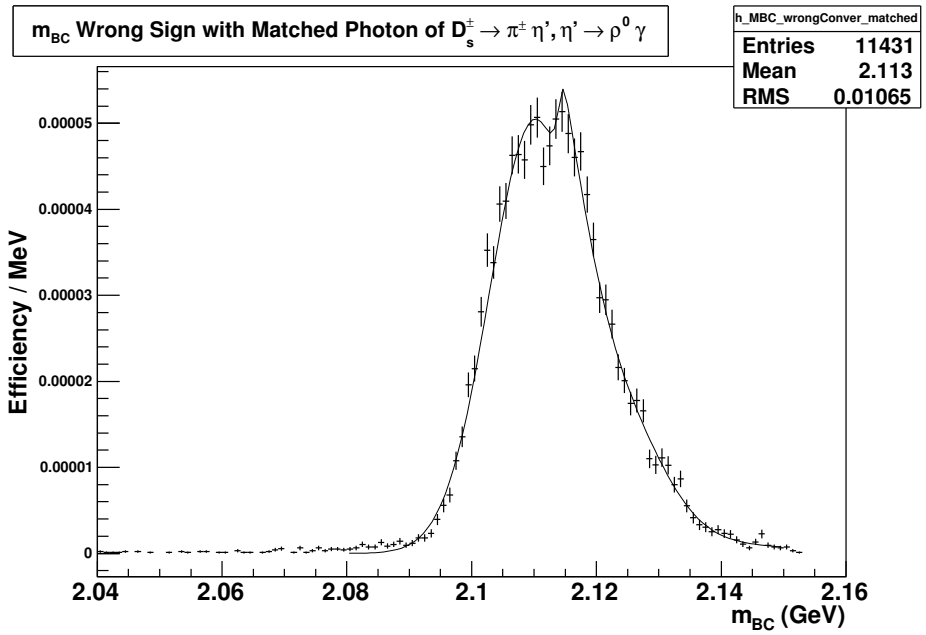

Figure 217: Combinatorial background in the m_{BC} distribution consisting of events where the D_s^{*+} has been reconstructed out of the D_s^- and the γ, and where both the D_s^- and the γ have been matched to their generated counterparts in the Monte Carlo simulation. This distribution has been fitted to a shape described by Eq. 68.

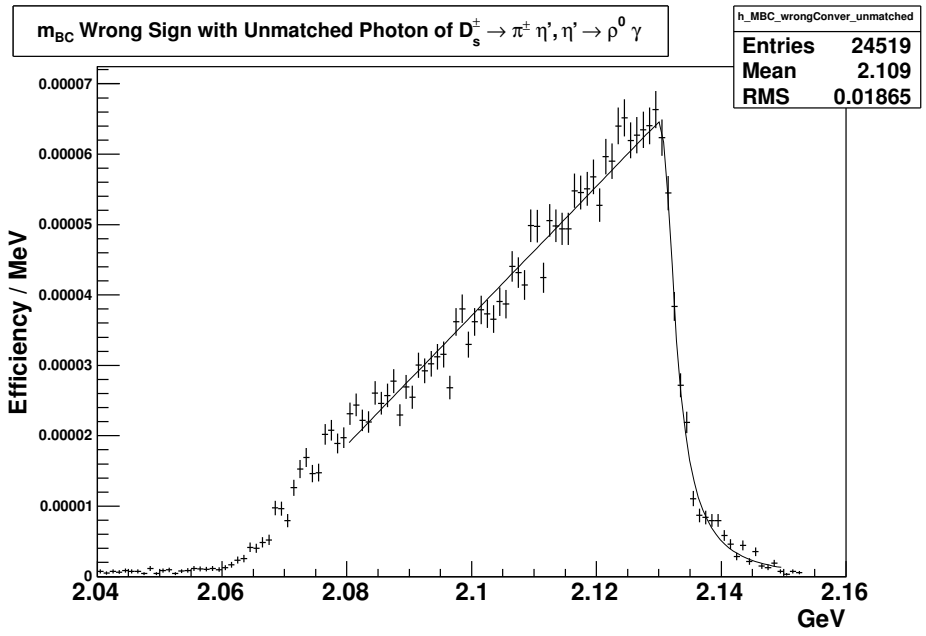

Figure 218: Combinatorial background structured in the m_{BC} distribution consisting of events where the D_s^{*+} has been reconstructed out of the D_s^- and the γ, and the D_s^- has been matched to its generated counterpart but the γ has failed to match the photon from the D_s^{*+} decay at the generator level of the Monte Carlo simulation. This distribution has been fitted to a shape described by Eq. 69.

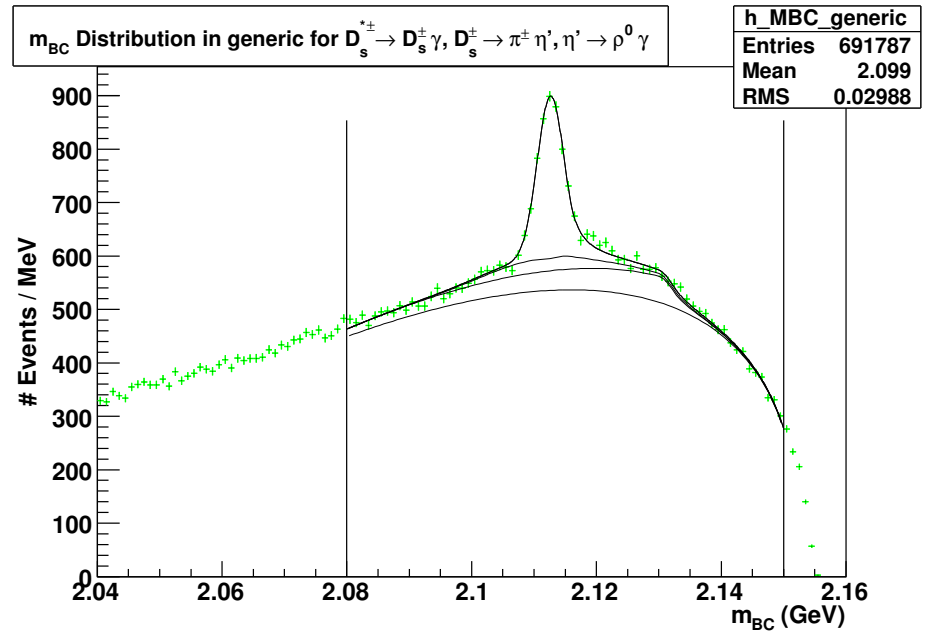

Figure 219: Distribution of m_{BC} of $D_s^{*+} \to D_s^+\gamma$ events where $D_s^+ \to \eta'\pi^+; \eta' \to \rho^0\gamma$ in 586 pb^{-1} of Generic Monte Carlo.

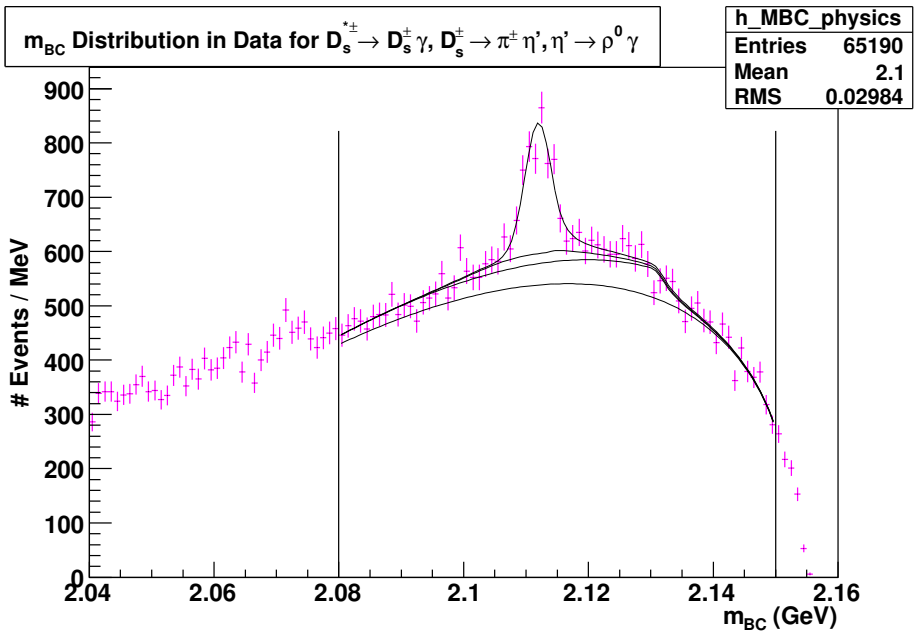

Figure 220: Distribution of m_{BC} of $D_s^{*+} \to D_s^+\gamma$ events where $D_s^+ \to \eta'\pi^+; \eta' \to \rho^0\gamma$ in 586 pb^{-1} of data.

Table 86: Data and estimated backgrounds in the signal region used to estimate the numbers of signal events found in each mode and the corresponding significance of the signal. Expected numbers of signal events from Monte Carlo simulations also listed.

Mode i	Yield Found in the Signal Region $Y^i_{e^+e^-}$	Estimated Background $B^i_{e^+e^-}$ ± stat ± syst	Background Subtracted Yield in Signal Region $N^i_{e^+e^-}$ ± stat ± syst	Expected Signal Yield from Monte Carlo ± stat	Signal Significance
$K^+K^-\pi^+$	14	1.05 ± 0.37 ± 0.79	12.95 ± 3.76 ± 0.79	13.65 ± 0.65	5.13
K_SK^+	1	0.85 ± 0.43 ± 0.74	0.15 ± 1.09 ± 0.74	3.02 ± 0.15	0.73
$\eta\pi^+$	4	1.40 ± 0.70 ± 0.49	2.60 ± 2.12 ± 0.49	1.81 ± 0.08	1.66
$\eta'\pi^+;\eta'\to\pi^+\pi^-\eta$	4	0.00 + 0.63 + 0.00	4.00 ± 2.10 ± 0.00	1.20 ± 0.06	2.68
$K^+K^-\pi^+\pi^0$	6	1.70 ± 0.47 ± 0.56	4.30 ± 2.49 ± 0.56	4.85 ± 0.29	2.34
$\pi^+\pi^-\pi^+$	7	1.57 ± 0.45 ± 0.59	5.43 ± 2.68 ± 0.59	3.75 ± 0.17	2.79
$K^{*+}K^{*0}$	4	1.58 ± 0.53 ± 0.40	2.42 ± 2.07 ± 0.40	1.99 ± 0.11	1.65
$\eta\rho^+$	7	2.62 ± 0.59 ± 0.23	4.38 ± 2.71 ± 0.23	5.49 ± 0.31	2.23
$\eta'\pi^+;\eta'\to\rho^0\gamma$	4	1.84 ± 0.49 ± 0.25	2.16 ± 2.06 ± 0.25	2.42 ± 0.12	1.52
Sum of all modes	51	12.61 ± 2.50 ± 1.08	38.39 ± 7.32 ± 1.53	38.18 ± 0.83	6.39

15 Un-blinding Data and Results

Having estimated, for each decay mode of the D_s^+, the background levels in the signal region for the reconstruction of $D_s^{*+}\to D_s^+e^+e^-$ (Section 12), the efficiency of our selection criteria in reconstructing the $D_s^{*+}\to D_s^+e^+e^-$, and the yields and efficiencies of our selection criteria in reconstructing the $D_s^{*+}\to D_s^+\gamma$, we are now in a position to unblind our data and observe the yield in the signal region of $D_s^{*+}\to D_s^+e^+e^-$. We unblind our data in the m_{BC} kinematic variable, as that is the variable we obtained our primary estimate of the background from. We count the yield in the signal region and subtract off the estimated background to determine the background subtrated yield. This is tabulated in Table 86, along with the signal significance of observing such a signal over the background and the number of signal events expected from Monte Carlo simulations. The unblinded plots for the individual modes are presented in the following sub-sections.

The statistical and systematic uncertainties in the estimated backgrounds have been derived in Section 12. The systematic uncertainties from the estimated backgrounds simply carry over as the systematic uncertainties in the estimated number of signal events. The statistical uncertainties in the estimated number of signal events is the quadrature sum, denoted by the symbol $\oplus$, of the statistical uncertainties in the estimated background and one standard deviation of the Poisson distribution with mean equal to the yields. That is,

$$\Delta N^i_{e^+e^-}(\text{stat}) = \Delta B^i_{e^+e^-}(\text{stat}) \oplus \Delta Y^i_{e^+e^-}$$

where,

- i refers to a hadronic decay mode of the D_s^+,
- $\Delta Y^i_{e^+e^-} = \sqrt{Y^i_{e^+e^-}}$ is the statistical uncertainty in the yield of data found in the signal region for the i^{th} mode,

- $\Delta B^i_{e^+e^-}$(stat) is the statistical uncertainty in the number of background events to $D_s^{*+} \to D_s^+ e^+ e^-$ we expect in the signal region for the i^{th} mode,
- $N^i_{e^+e^-}$(stat) is the statistical uncertainty in the background subtracted yield in our signal region for the i^{th} mode.

The efficiencies for our selection criteria in each of the modes have been tabulated in Table 56 in Section 13. Using the relation:

$$L\sigma B(D_s^{*+} \to D_s^+ e^+ e^-) B(D_s \to i) \epsilon^i_{D_s^+ e^+ e^-} = N^i_{e^+e^-}$$

we can compute the absolute branching fraction $B(D_s^{*+} \to D_s^+ e^+ e^-)$ with each and all modes using the number of signal events for each channel tabulated in Table 86 and Eq. 70 & 71. Values for the absolute branching fraction computed thus are tabulated in Table 87.

$$B(D_s^{*+} \to D_s^+ e^+ e^-) = \frac{N^i_{e^+e^-}}{L\sigma B(D_s \to i)\epsilon^i_{D_s^+ e^+ e^-}} \tag{70}$$

$$B(D_s^{*+} \to D_s^+ e^+ e^-) = \frac{\Sigma_i N^i_{e^+e^-}}{L\sigma \sum_i B(D_s \to i)\epsilon^i_{D_s^+ e^+ e^-}} \tag{71}$$

Additional symbols in these equations are described as follows.

- L is the integrated luminosity of data, 586 ± 6 pb^{-1}, we are studying,
- σ is the production cross section of $D_s^{\pm} D_s^{*\mp}$ at 4170 MeV e^+e^- collisions,
- $B(D_s^+ \to i)$ is the branching fraction of the D_s^+ decaying to the i^{th} mode,
- $\epsilon^i_{D_s^+ e^+ e^-}$ the selection efficiency for the $D_s^{*+} \to D_s^+ e^+ e^-$ selection criteria, for the i^{th} mode of D_s^+ decay,

The statistical uncertainty in the selection efficiencies are calculated by assuming Poisson statistics for Monte Carlo simulation events that pass the selection criteria. The statistical and systematic uncertainties in the absolute branching fraction for a given mode are calculated using Eq. 72 and Eq. 73.

$$\frac{\Delta B(D_s^{*+} \to D_s^+ e^+ e^-)(\text{stat})}{B(D_s^{*+} \to D_s^+ e^+ e^-)} = \frac{\Delta N^i_{e^+e^-}(\text{stat})}{N^i_{e^+e^-}} \tag{72}$$

$$\begin{aligned} \frac{\Delta B(D_s^{*+} \to D_s^+ e^+ e^-)(\text{syst})}{B(D_s^{*+} \to D_s^+ e^+ e^-)} &= \frac{\Delta L}{L} \oplus \frac{\Delta \sigma}{\sigma} \oplus \frac{\Delta N^i_{e^+e^-}(\text{syst})}{N^i_{e^+e^-}} \\ &\oplus \frac{\Delta \epsilon^i_{D_s^+ e^+ e^-}}{\epsilon^i_{D_s^+ e^+ e^-}} \oplus \frac{\Delta B(D_s^+ \to i)}{B(D_s^+ \to i)} \end{aligned} \tag{73}$$

Table 87: Absolute branching fractions for $D_s^{*+} \to D_s^+ e^+ e^-$ inferred from the signal yields and efficiencies of each and all modes.

D_s^+ Decay Mode i	$B(D_s^+ \to i)$	Background Subtracted Yield in Signal Region $N^i_{e^+e^-}$ ± stat ± syst	Selection Efficiency from Monte Carlo $\epsilon^i_{D_s^+e^+e^-}$ ± stat	$B(D_s^{*+} \to D_s^+ e^+ e^-)$ ± stat ± syst
$K^+K^-\pi^+$	0.0550 ± 0.0028	12.95 ± 3.76 ± 0.79	0.0730 ± 0.0019	0.0058 ± 0.0017 ± 0.0005
$K_S K^+$	0.0149 ± 0.0009	0.15 ± 1.09 ± 0.74	0.0597 ± 0.0017	0.0003 ± 0.0022 ± 0.0015
$\eta\pi^+; \eta \to \gamma\gamma$	0.00621 ± 0.00083	2.60 ± 2.12 ± 0.49	0.0855 ± 0.0021	0.0088 ± 0.0072 ± 0.0021
$\eta'\pi^+; \eta' \to \pi^+\pi^-\eta; \eta \to \gamma\gamma$	0.00666 ± 0.00070	4.00 ± 2.10 ± 0.00	0.0530 ± 0.0016	0.0204 ± 0.0107 ± 0.0024
$K^+K^-\pi^+\pi^0$	0.056 ± 0.005	4.30 ± 2.49 ± 0.56	0.0255 ± 0.0011	0.0054 ± 0.0031 ± 0.0009
$\pi^+\pi^-\pi^+$	0.0111 ± 0.0008	5.43 ± 2.68 ± 0.59	0.0992 ± 0.0022	0.0089 ± 0.0044 ± 0.0012
$K^{*+}K^{*0}$	0.0164 ± 0.0012	2.42 ± 2.07 ± 0.40	0.0356 ± 0.0013	0.0075 ± 0.0064 ± 0.0014
$\eta\rho^+; \eta \to \gamma\gamma; \rho^+ \to \pi^+\pi^0$	0.0348 ± 0.0031	4.38 ± 2.71 ± 0.23	0.0316 ± 0.0013	0.0072 ± 0.0044 ± 0.0009
$\eta'\pi^+; \eta' \to \rho^0\gamma$	0.0112 ± 0.0012	2.16 ± 2.06 ± 0.25	0.064 ± 0.0018	0.0055 ± 0.0052 ± 0.0009
Sum of all modes		38.39 ± 7.32 ± 1.53		0.0065 ± 0.0012 ± 0.0004

Statistical and systematic uncertainties in the absolute branching fraction for the sum of all modes are calculated using Eq. 74 and Eq. 75.

$$\frac{\Delta B(D_s^{*+} \to D_s^+ e^+ e^-)(\text{stat})}{B(D_s^{*+} \to D_s^+ e^+ e^-)} = \frac{\sqrt{\sum_i (\Delta N^i_{e^+e^-})^2(\text{stat})}}{\sum_i N^i_{e^+e^-}} \tag{74}$$

$$\left(\frac{\Delta B(D_s^{*+} \to D_s^+ e^+ e^-)(\text{syst})}{B(D_s^{*+} \to D_s^+ e^+ e^-)}\right)^2 = \left(\frac{\Delta L}{L}\right)^2 + \left(\frac{\Delta\sigma}{\sigma}\right)^2 + \frac{\sum_i \left(\Delta N^i_{e^+e^-}\right)^2 (\text{syst})}{\left(\sum_i N^i_{e^+e^-}\right)^2}$$
$$+ \frac{\sum_i (\epsilon^i_{D_s^+e^+e^-} B(D_s^+ \to i))^2 ((\Delta\epsilon^i_{D_s^+e^+e^-}/\epsilon^i_{D_s^+e^+e^-})^2 + (\Delta B(D_s^+ \to i)/B(D_s^+ \to i))^2)}{(\sum_i \epsilon^i_{D_s^+e^+e^-} B(D_s^+ \to i))^2} \tag{75}$$

Now, using the numbers for $D_s^{*+} \to D_s^+ e^+ e^-$ tabulated in Table 87 in conjuction with the numbers for $D_s^{*+} \to D_s^+ \gamma$ tabulated in Table 57, we compute and tabulate the ratio of branching fractions

$$K = \frac{B(D_s^{*+} \to D_s^+ e^+ e^-)}{B(D_s^{*+} \to D_s^+ \gamma)}$$

in Table 88. This is done for each mode using Eq. 76 and with all modes using Eq. 77.

$$K = \left(\frac{N^i_{e^+e^-}}{N^i_\gamma}\right)\left(\frac{\epsilon^i_{D_s^+\gamma}}{\epsilon^i_{D_s^+e^+e^-}}\right) \tag{76}$$

$$K = \left(\frac{\sum_i N^i_{e^+e^-}}{\sum_i N^i_\gamma}\right)\left(\frac{\sum_i \epsilon^i_{D_s^+\gamma} B(D_s^+ \to i)}{\sum_i \epsilon^i_{D_s^+e^+e^-} B(D_s^+ \to i)}\right) \tag{77}$$

where,

- K is the aforementioned ratio of branching fractions we're trying to measure,

- N^i_γ is the background subtracted yield of $D_s^{*+} \to D_s^+\gamma$ events we find in our signal region for the i^{th} mode of D_s^+ decay, and
- $\epsilon^i_{D_s^+\gamma}$ encodes the detection and selection efficiency for the $D_s^{*+} \to D_s^+\gamma$ selection criteria, for the i^{th} mode of D_s^+ decay.

Uncertainties in the ratio of branching fractions, K, are calculated for each mode using Eq. 78 and Eq. 79.

$$\left(\frac{\Delta K(\text{stat})}{K}\right)^2 = \left(\frac{\Delta N^i_{e^+e^-}(\text{stat})}{N^i_{e^+e^-}}\right)^2 + \left(\frac{\Delta N^i_\gamma}{N_\gamma}\right)^2 \tag{78}$$

$$\left(\frac{\Delta K(\text{syst})}{K}\right)^2 = \left(\frac{\Delta N^i_{e^+e^-}(\text{syst})}{N^i_{e^+e^-}}\right)^2 + \left(\frac{\Delta \epsilon^i_{D_s^+e^+e^-}}{\epsilon^i_{D_s^+e^+e^-}}\right)^2 + \left(\frac{\Delta \epsilon^i_{D_s^+\gamma}}{\epsilon^i_{D_s^+\gamma}}\right)^2 \tag{79}$$

Uncertainties in the ratio of branching fractions, K, are calculated using the sum of all modes as follows. The statistical uncertainty depends solely on the statistical uncertainties associated with the signal yields, $N^i_{e^+e^-}$ and N^i_γ. These statistical uncertainties for each mode are tabulated in Table 88. Therefore, the statistical uncertainty in K is calculated using Eq. 80.

$$\left(\frac{\Delta K(\text{stat})}{K}\right)^2 = \frac{\sum_i (\Delta N^i_{e^+e^-}(\text{stat}))^2}{(\sum_i N^i_{e^+e^-})^2} + \frac{\sum_i (\Delta N^i_\gamma)^2}{(\sum_i N_\gamma)^2} \tag{80}$$

For an estimate of the systematic error, we decompose Eq. 77 as

$$K = \left(\frac{\sum_i N^i_{e^+e^-}}{\sum_i N^i_\gamma}\right)\left(\frac{\epsilon_\gamma}{\epsilon_{e^+e^-}}\right)\left(\frac{\sum_i \epsilon^i_{D_s^+} B(D_s^+ \to i)}{\sum_i \epsilon^i_{D_s^+} B(D_s^+ \to i)}\right) \tag{81}$$

where ϵ_γ and $\epsilon_{e^+e^-}$ are the reconstruction efficiencies for the photon and the e^+e^- which are common to all modes of the D_s^+ decay, and the $\epsilon^i_{D_s^+}$ is the reconstruction efficiency of the D_s^+ as it decays into the i^{th} hadronic decay mode. This can be simplified to

$$K = \left(\frac{\sum_i N^i_{e^+e^-}}{\sum_i N^i_\gamma}\right)\left(\frac{\epsilon_\gamma}{\epsilon_{e^+e^-}}\right) \tag{82}$$

Therefore, we may estimate the systematic uncertainty in K as given in Eq. 83.

$$\left(\frac{\Delta K(\text{syst})}{K}\right)^2 = \frac{\sum_i (\Delta N^i_{e^+e^-}(\text{syst}))^2}{(\sum_i N^i_{e^+e^-})^2} \oplus \frac{\sum_i (\Delta N^i_\gamma(\text{syst}))^2}{(\sum_i N^i_\gamma)^2} \oplus \left(\frac{\Delta(\epsilon_\gamma/\epsilon_{e^+e^-})}{\epsilon_\gamma/\epsilon_{e^+e^-}}\right)^2 \tag{83}$$

A plot of the unblinded data in the m_{BC} and δm kinematic variables, summed over all modes, are presented in Fig. 221 and Fig. 222. The data points are marked by magenta points with error bars. The data-driven estimated backgrounds are marked by the black and magenta curves. The cyan histograms mark the expected signal yield. The agreement

Table 88: The ratio of branching fractions $B(D_s^{*+} \to D_s^+ e^+ e^-)/B(D_s^{*+} \to D_s^+ \gamma)$ inferred from the signal yields and efficiencies of each and all modes.

D_s^+ Decay Mode i	$B(D_s^+ \to i)$	$D_s^{*+} \to D_s^+ e^+ e^-$		$D_s^{*+} \to D_s^+ \gamma$		$K = \frac{B(D_s^{*+} \to D_s^+ e^+ e^-)}{B(D_s^{*+} \to D_s^+ \gamma)}$
		Signal Events $N^i_{e^+e^-}$	Selection Efficiency $\epsilon^i_{D_s^+ e^+ e^-}$	Signal Events N^i_γ	Selection Efficiency $\epsilon^i_{D_s^+ \gamma}$	
		± stat ± syst		± stat ± syst		± stat ± syst
$K^+K^-\pi^+$	0.0550 ± 0.0028	12.95 ± 3.76 ± 0.79	0.0730 ± 0.0019	9114 ± 110 ± 201	0.339 ± 0.002	0.0066 ± 0.0019 ± 0.0005
$K_S K^+$	0.0149 ± 0.0009	0.15 ± 1.09 ± 0.74	0.0597 ± 0.0017	1902 ± 57 ± 45	0.2573 ± 0.0004	0.0003 ± 0.0025 ± 0.0017
$\eta\pi^+; \eta \to \gamma\gamma$	0.0062 ± 0.0008	2.60 ± 2.12 ± 0.49	0.0855 ± 0.0021	1037 ± 46 ± 37	0.3310 ± 0.0015	0.0097 ± 0.0079 ± 0.0019
$\eta'\pi^+; \eta' \to \pi^+\pi^-\eta; \eta \to \gamma\gamma$	0.0067 ± 0.0007	4.00 ± 2.10 ± 0.00	0.0530 ± 0.0016	691 ± 34 ± 40	0.2101 ± 0.0013	0.023 ± 0.0123 ± 0.0015
$K^+K^-\pi^+\pi^0$	0.056 ± 0.005	4.30 ± 2.49 ± 0.56	0.0255 ± 0.0011	3592 ± 118 ± 72	0.1225 ± 0.0010	0.0058 ± 0.0033 ± 0.0008
$\pi^+\pi^-\pi^+$	0.0111 ± 0.0008	5.43 ± 2.68 ± 0.59	0.0992 ± 0.0022	2745 ± 93 ± 52	0.4583 ± 0.0018	0.0091 ± 0.0045 ± 0.0010
$K^{*+}K^{*0}$	0.0164 ± 0.0012	2.42 ± 2.07 ± 0.40	0.0356 ± 0.0013	1570 ± 74 ± 13	0.1913 ± 0.0012	0.0083 ± 0.0071 ± 0.0014
$\eta\rho^+; \eta \to \gamma\gamma; \rho^+ \to \pi^+\pi^0$	0.0298 ± 0.0051	4.38 ± 2.71 ± 0.23	0.0316 ± 0.0013	3170 ± 161 ± 313	0.1839 ± 0.0013	0.0080 ± 0.0050 ± 0.0010
$\eta'\pi^+; \eta' \to \rho^0\gamma$	0.0112 ± 0.0012	2.16 ± 2.06 ± 0.25	0.064 ± 0.0018	1531 ± 80 ± 122	0.3171 ± 0.0015	0.0070 ± 0.0067 ± 0.0010
Sum of all modes		38.39 ± 7.32 ± 1.53		25351.03 ± 280.93		0.0072 ± 0.0014 ± 0.0003

with data is remarkable. Histograms of unblinded data in each of the individual modes are presented in the following subsections.

Table 86 summarizes the signal yield observed in all modes and their significances. The total signal yield of 51 events carries a significance of 6.39 σ. The signal yields and efficiencies for $D_s^{*+} \to D_s^+ e^+ e^-$ that we just unblinded and $D_s^{*+} \to D_s^+ \gamma$ discussed in Section 14 are tabulated together in Table 86. The ratio of branching fractions $B(D_s^{*+} \to D_s^+ e^+ e^-)/B(D_s^{*+} \to D_s^+ \gamma)$ are calculated from each mode and with all modes combined. The measurement of this ratio using the combination of all modes is given in Eq. 84. However, the systematic uncertainty in K has been estimated only using the systematic uncertainties in the signal yields for $D_s^{*+} \to D_s^+ e^+ e^-$ and $D_s^{*+} \to D_s^+ \gamma$. We must also include the systematic uncertainty arising from the reconstruction of soft e^+e^- pairs and the γ as indicated in Eq. 83 for a complete result.

$$K = \frac{B(D_s^{*+} \to D_s^+ e^+ e^-)}{B(D_s^{*+} \to D_s^+ \gamma)} = (0.72 \pm 0.14(\text{stat}) \pm 0.03(\text{syst}))\% \tag{84}$$

This last source of systematic uncertainty is estimated in Section 16. There we measure this fractional uncertainty to be 6.51%. 6.51% of 0.72% is 0.047% and therefore, our final result stands to be:

$$\boxed{K = \frac{B(D_s^{*+} \to D_s^+ e^+ e^-)}{B(D_s^{*+} \to D_s^+ \gamma)} = (0.72 \pm 0.14(\text{stat}) \pm 0.06(\text{syst}))\%} \tag{85}$$

where

- (stat) is the statistical uncertainty arising from the limited signal yields of $D_s^{*+} \to D_s^+ e^+ e^-$ and $D_s^{*+} \to D_s^+ \gamma$. Larger datasets will decrease this error.
- (syst) is the systematic uncertainty arising from systematic uncertainties in the estimated background for the $D_s^{*+} \to D_s^+ e^+ e^-$ signal, systematic uncertainties in the signal yield for $D_s^{*+} \to D_s^+ \gamma$, and the systematic uncertainty arising from the e^+e^- and γ reconstruction efficiencies in the energy range relevant for this analysis.

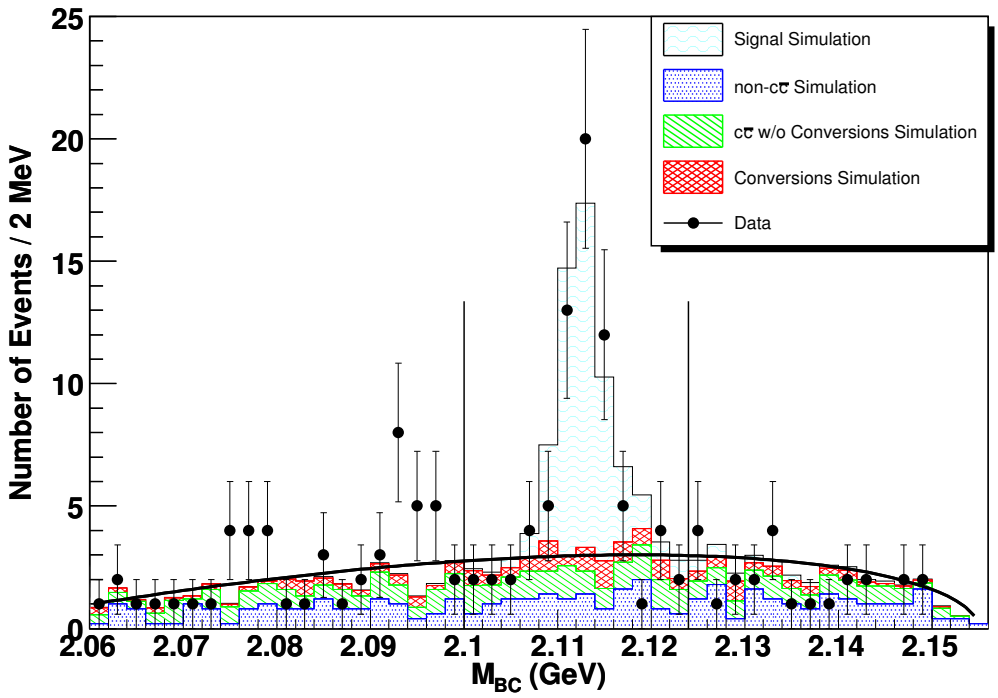

Figure 221: Distribution of m_{BC} in data after unblinding.

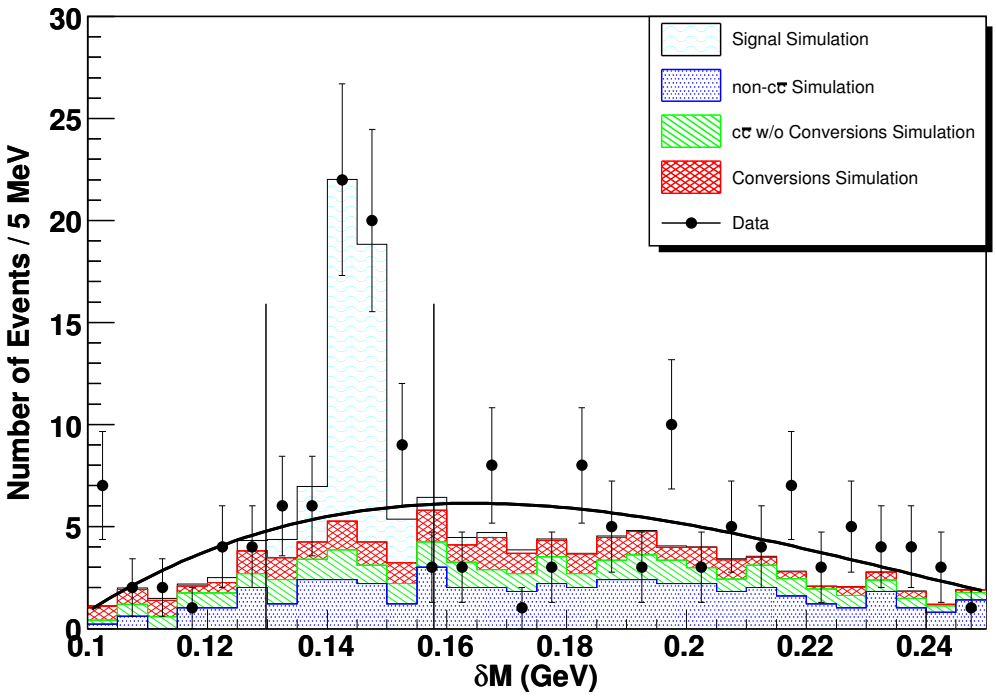

Figure 222: Distribution of δm in data after unblinding.

15.1 $D_s^+ \to K^+K^-\pi^+$

The distributions of m_{BC} and δm in data after unblinding are presented overlaid with Monte Carlo in Fig. 223 and 224. A mean of 14.7 events were expected from Monte Carlo simulations and 14 events were observed. The significance for this observation is 5.13 σ.

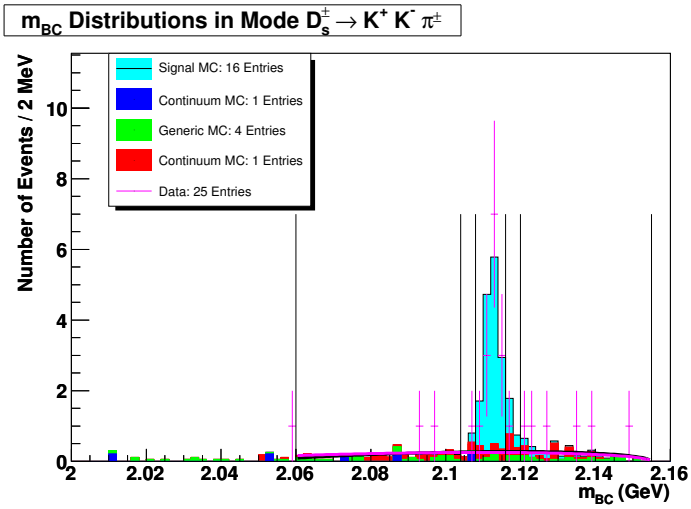

Figure 223: Distribution of m_{BC} in data after unblinding overlaid with prediction from Monte Carlo.

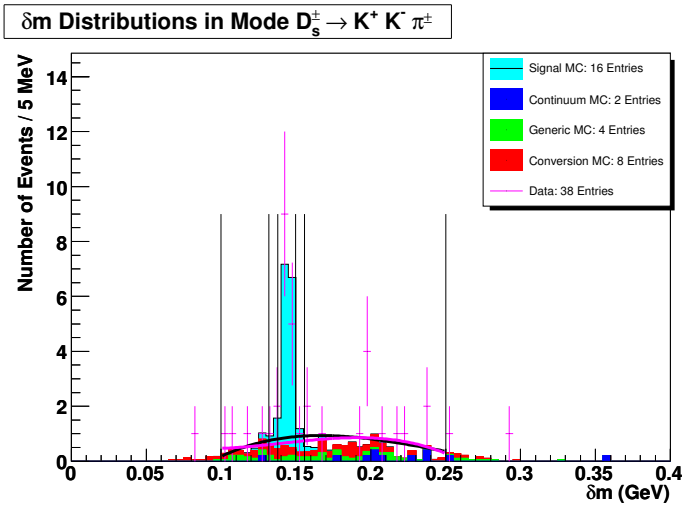

Figure 224: Distribution of δm in data after unblinding overlaid with prediction from Monte Carlo.

15.2 $D_s^+ \to K_S K^+$

The distributions of m_{BC} and δm in data after unblinding are presented overlaid with Monte Carlo in Fig. 225 and 226. A mean of 3.87 events were expected from Monte Carlo simulations and 1 events was observed. The significance for this observation is 0.73 σ.

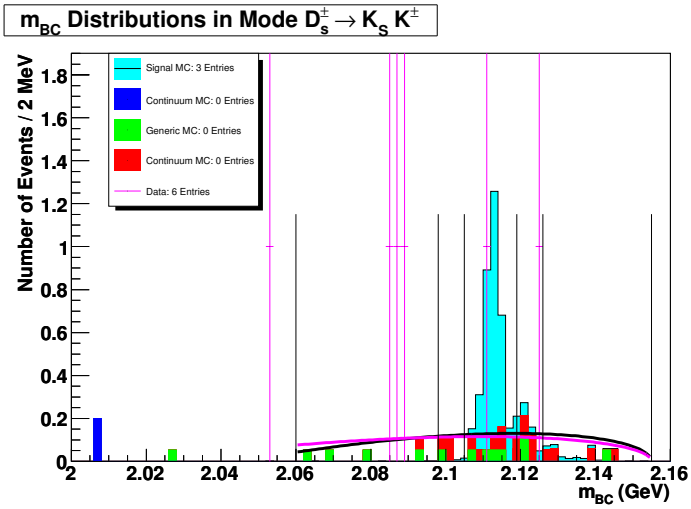

Figure 225: Distribution of m_{BC} in data after unblinding overlaid with prediction from Monte Carlo.

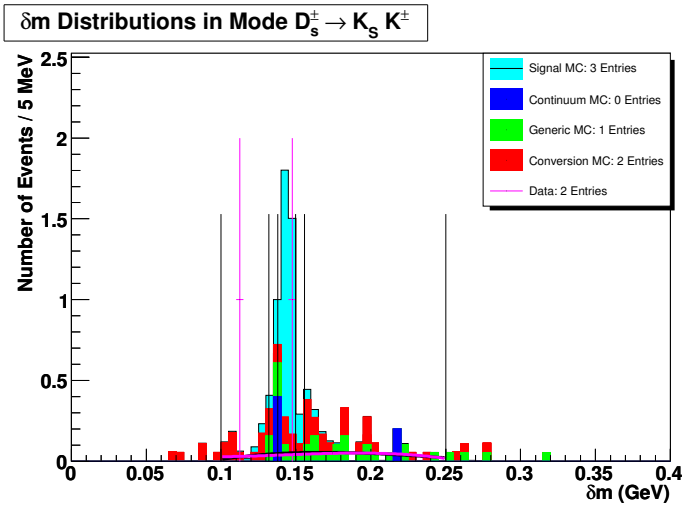

Figure 226: Distribution of δm in data after unblinding overlaid with prediction from Monte Carlo.

15.3 $D_s^+ \to \eta\pi^+; \eta \to \gamma\gamma$

The distributions of m_{BC} and δm in data after unblinding are presented overlaid with Monte Carlo in Fig. 227 and 228. A mean of 3.21 events were expected from Monte Carlo simulations and 4 events were observed. The significance for this observation is 1.66 σ.

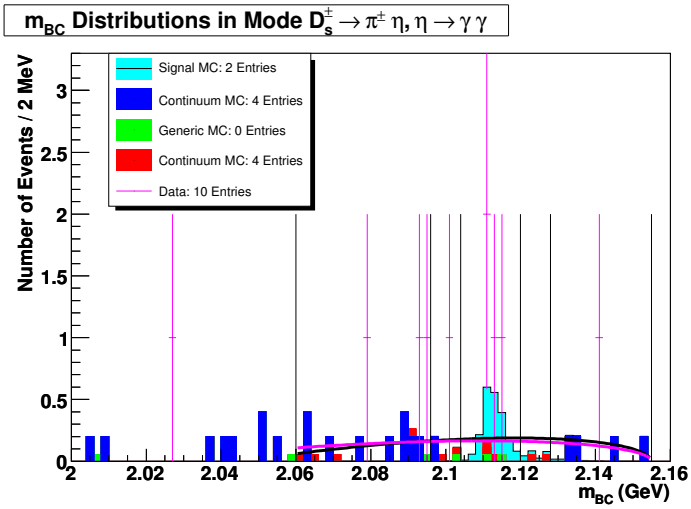

Figure 227: Distribution of m_{BC} in data after unblinding overlaid with prediction from Monte Carlo.

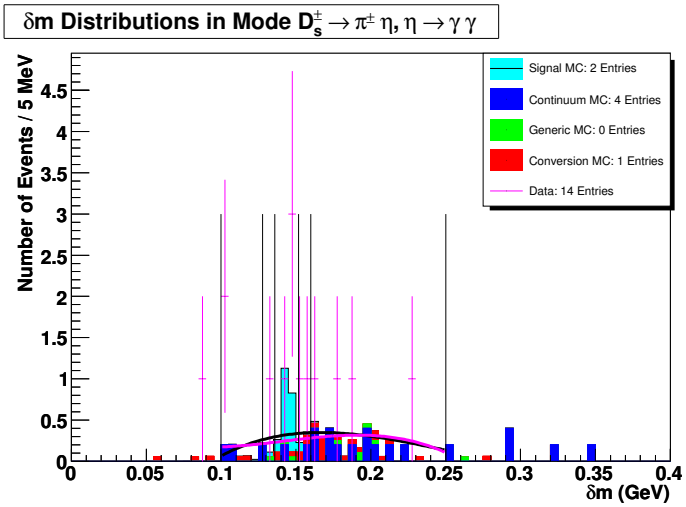

Figure 228: Distribution of δm in data after unblinding overlaid with prediction from Monte Carlo.

15.4 $D_s^+ \to \eta'\pi^+; \eta' \to \pi^+\pi^-\eta; \eta \to \gamma\gamma$

The distributions of m_{BC} and δm in data after unblinding are presented overlaid with Monte Carlo in Fig. 229 and 230. 1.20 events were expected from Monte Carlo simulations and 4 events were observed. The significance for this observation is 2.68 σ.

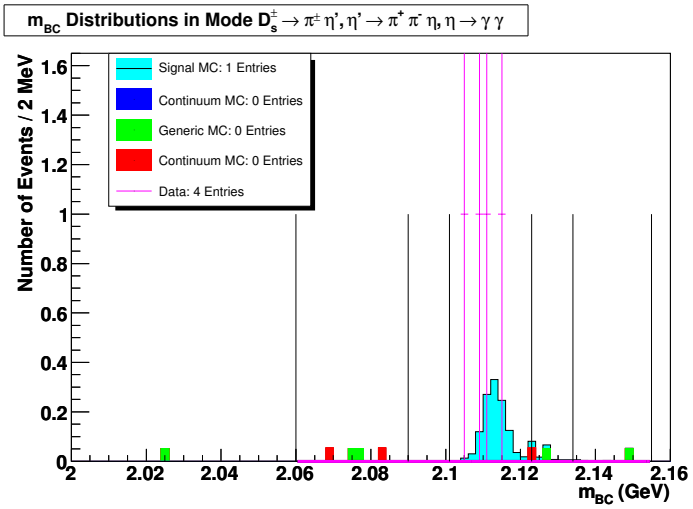

Figure 229: Distribution of m_{BC} in data after unblinding overlaid with prediction from Monte Carlo.

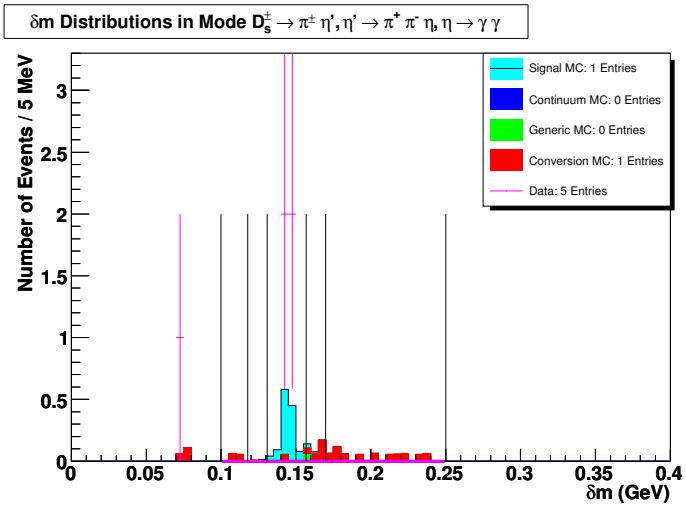

Figure 230: Distribution of δm in data after unblinding overlaid with prediction from Monte Carlo.

15.5 $D_s^+ \to K^+K^-\pi^+\pi^0$

The distributions of m_{BC} and δm in data after unblinding are presented overlaid with Monte Carlo in Fig. 231 and 232. 6.55 events were expected from Monte Carlo simulations and 6 events were observed. The significance for this observation is 2.34 σ.

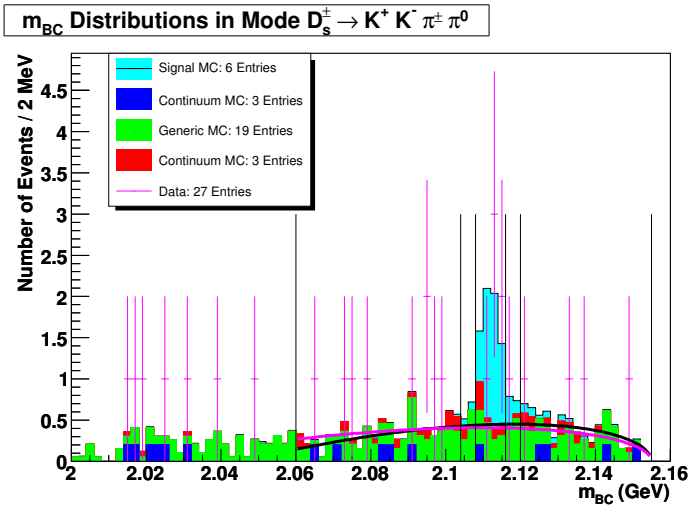

Figure 231: Distribution of m_{BC} in data after unblinding overlaid with prediction from Monte Carlo.

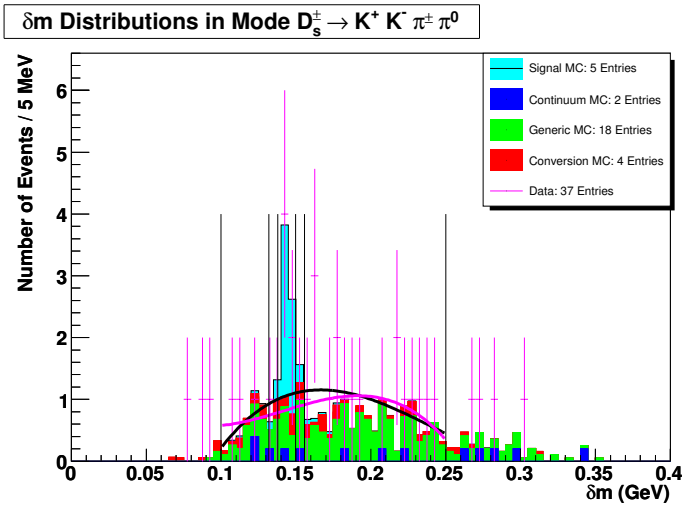

Figure 232: Distribution of δm in data after unblinding overlaid with prediction from Monte Carlo.

15.6 $D_s^+ \to \pi^+\pi^-\pi^+$

The distributions of m_{BC} and δm in data after unblinding are presented overlaid with Monte Carlo in Fig. 233 and 234. 5.32 events were expected from Monte Carlo simulations and 7 events were observed. The significance for this observation is 2.79 σ.

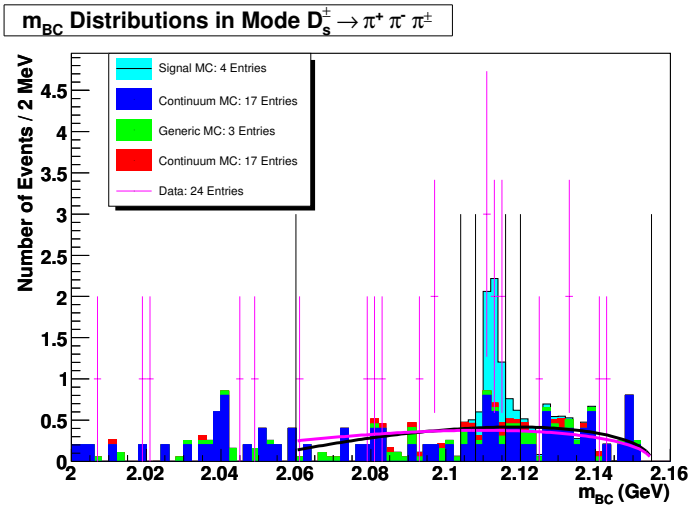

Figure 233: Distribution of m_{BC} in data after unblinding overlaid with prediction from Monte Carlo.

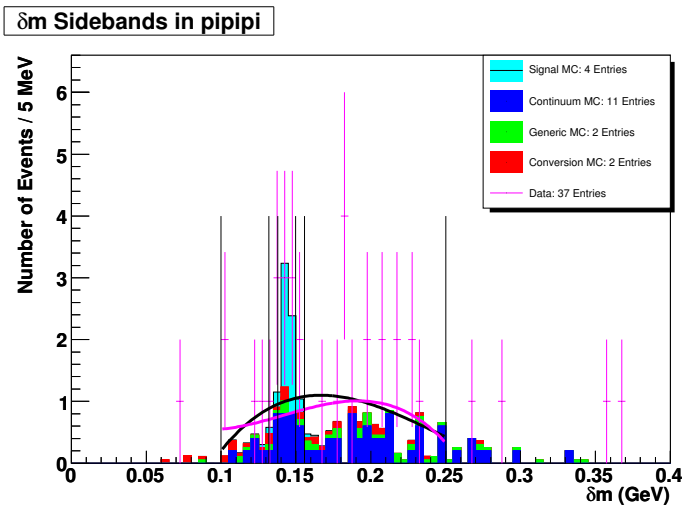

Figure 234: Distribution of δm in data after unblinding overlaid with prediction from Monte Carlo.

15.7 $D_s^+ \to K^{*+}K^{*0}$

The distributions of m_{BC} and δm in data after unblinding are presented overlaid with Monte Carlo in Fig. 235 and 236. 3.57 events were expected from Monte Carlo simulations and 4 events were observed. The significance for this observation is 1.65 σ.

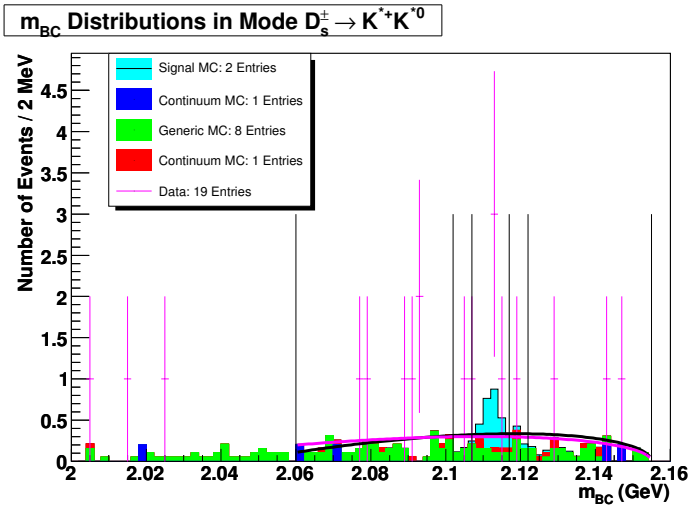

Figure 235: Distribution of m_{BC} in data after unblinding overlaid with prediction from Monte Carlo.

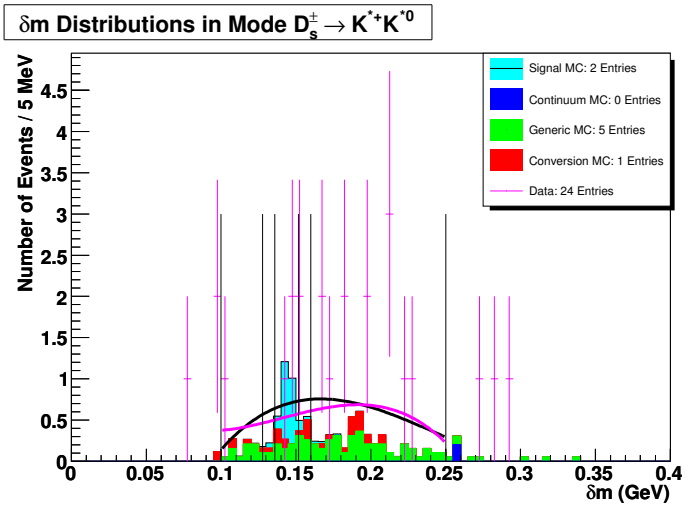

Figure 236: Distribution of δm in data after unblinding overlaid with prediction from Monte Carlo.

15.8 $D_s^+ \to \eta\rho^+; \eta \to \gamma\gamma; \rho^+ \to \pi^+\pi^0$

The distributions of m_{BC} and δm in data after unblinding are presented overlaid with Monte Carlo in Fig. 237 and 238. 8.11 events were expected from Monte Carlo simulations and 7 events were observed. The significance for this observation is 2.23 σ.

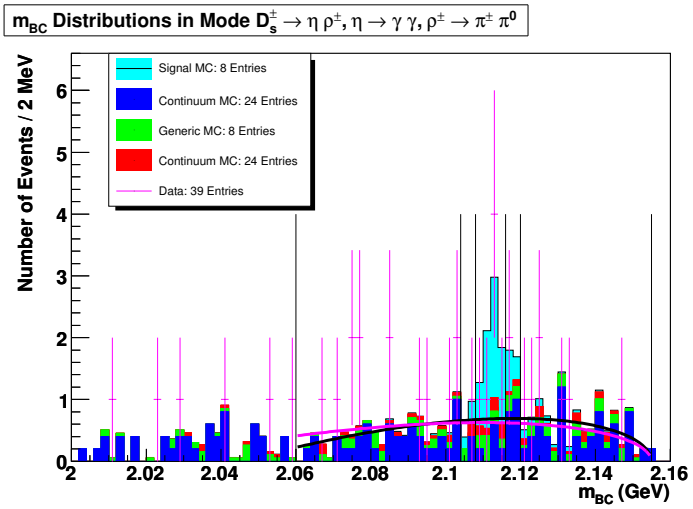

Figure 237: Distribution of m_{BC} in data after unblinding overlaid with prediction from Monte Carlo.

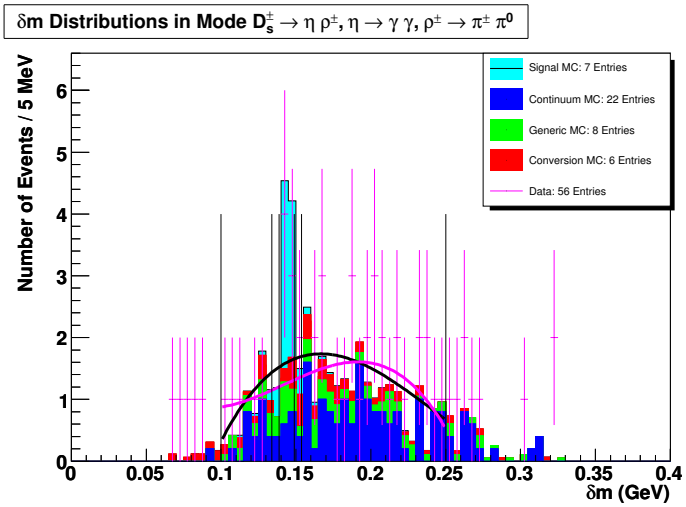

Figure 238: Distribution of δm in data after unblinding overlaid with prediction from Monte Carlo.

15.9 $D_s^+ \to \eta'\pi^+; \eta' \to \rho^0\gamma$

The distributions of m_{BC} and δm in data after unblinding are presented overlaid with Monte Carlo in Fig. 239 and 240. 4.26 events were expected from Monte Carlo simulations and 4 events were observed. The significance for this observation is 1.52 σ.

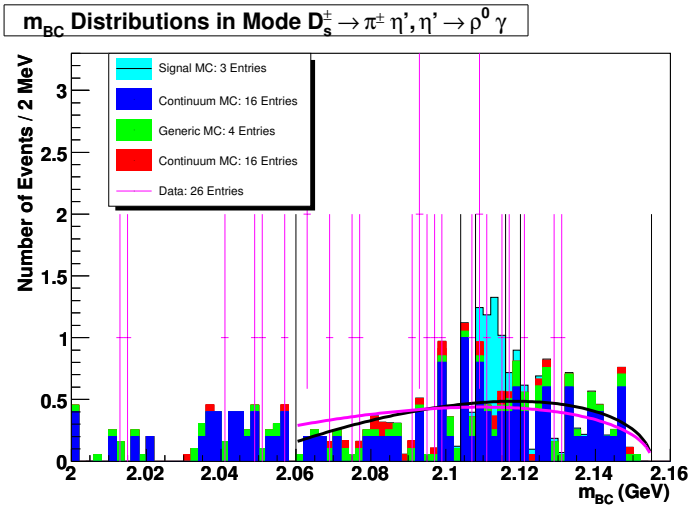

Figure 239: Distribution of m_{BC} in data after unblinding overlaid with prediction from Monte Carlo.

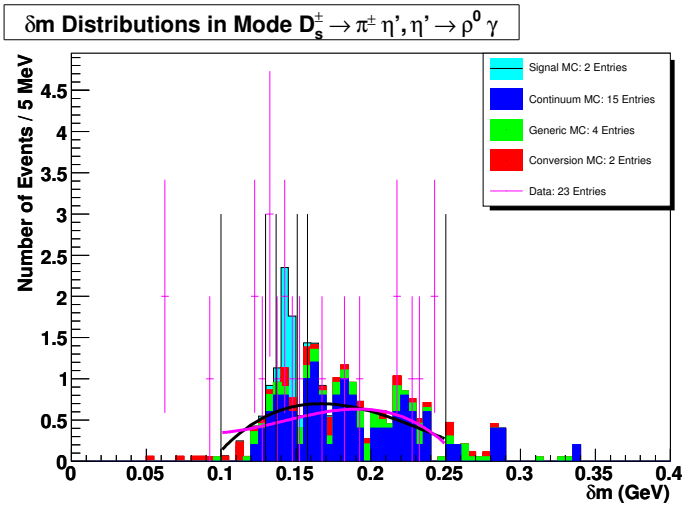

Figure 240: Distribution of δm in data after unblinding overlaid with prediction from Monte Carlo.

15.10 Comparison of $m_{e^+e^-}$ between Data and Monte Carlo Simulation

Fig. 241 shows the distribution of the invariant mass of the e^+e^- in the 51 data points uncovered when compared to the general shape predicted by our Monte Carlo simulations. It must be noted that we did not depend on the numbers from Monte Carlo for our estimation of the backgrounds. This plot is presented as a rough check. The Kolmogorov probability for the data and Monte Carlo points to have come from the same distribution is found to be 0.86.

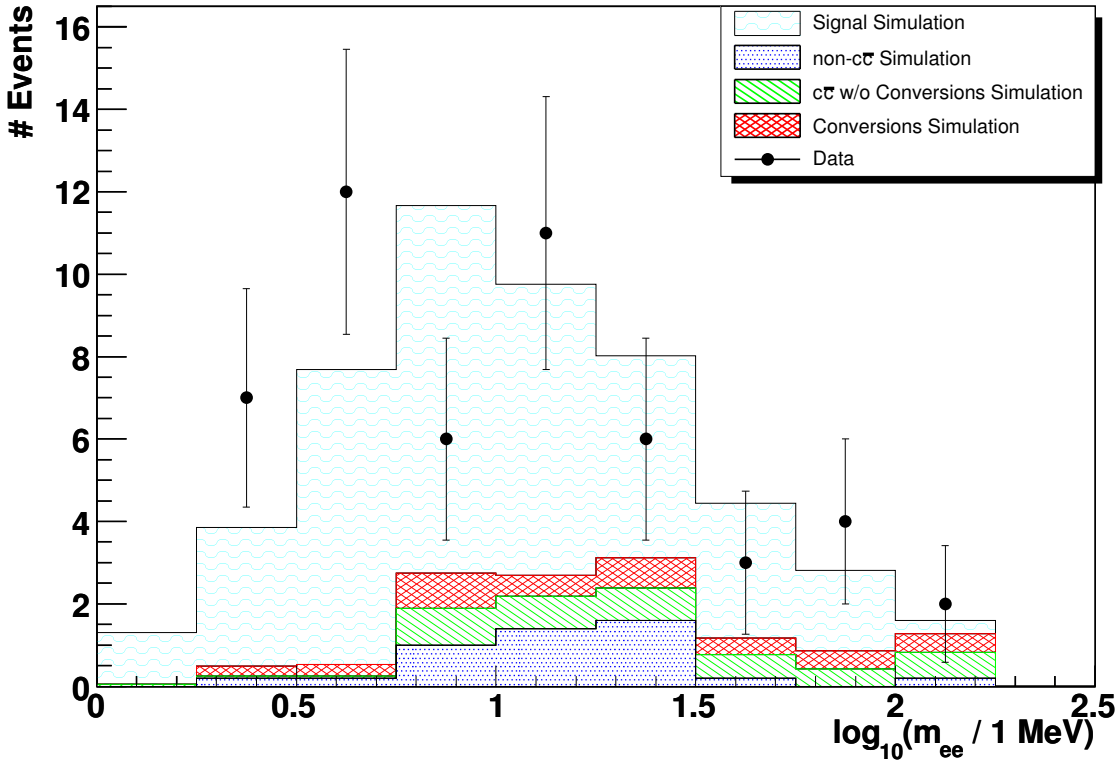

Figure 241: Distribution of $m_{e^+e^-}$ in data after unblinding overlaid with prediction from Monte Carlo.

15.11 A Re-evaluation of All D_s^{*+} Branching Fractions

Now that we have a measurement of the ratio of the branching fractions $B(D_s^{*+} \to D_s^+ e^+ e^-)/B(D_s^{*+} \to D_s^+\gamma)$, we may combine it with the measurement of $B(D_s^{*+} \to D_s^+\pi^0)/B(D_s^{*+} \to D_s^+\gamma)$ as measured by the BABAR collaboration [3] to re-evaluate the absolute branching fractions $B(D_s^{*+} \to D_s^+\gamma)$, $B(D_s^{*+} \to D_s^+\pi^0)$ and $B(D_s^{*+} \to D_s^+ e^+ e^-)$. For notational convenience, we shall denote $B(D_s^{*+} \to D_s^+\gamma)$ by b_γ, $B(D_s^{*+} \to D_s^+\pi^0)$ by b_{π^0} and $B(D_s^{*+} \to D_s^+ e^+ e^-)$ by $b_{e^+e^-}$. If we call our measurements of the ratios m_1 and m_2 as indicated in Eq. 86 & 87,

$$m_1 = \frac{b_{\pi^0}}{b_\gamma} = 0.062 \pm 0.005 \pm 0.006 \tag{86}$$

$$m_2 = \frac{b_{e^+e^-}}{b_\gamma} = 0.0072 \pm 0.0014 \pm 0.0006 \tag{87}$$

and have the absolute branching fractions add up to unity, we may write

$$b_\gamma = \frac{1}{1 + m_1 + m_2} \tag{88}$$

$$\Delta b_\gamma = \frac{\partial b_\gamma}{\partial m_1}\Delta m_1 \oplus \frac{\partial b_\gamma}{\partial m_2}\Delta m_2 \tag{89}$$

where

$$\frac{\partial b_\gamma}{\partial m_1} = \frac{\partial b_\gamma}{\partial m_2} = \frac{-1}{(1 + m_1 + m_2)^2}$$

In a similar vein, one may write the solutions for b_{π^0} and $b_{e^+e^-}$ as follows.

$$b_{\pi^0} = \frac{m_1}{1 + m_1 + m_2} \tag{90}$$

$$\Delta b_{\pi^0} = \frac{\partial b_{\pi^0}}{\partial m_1}\Delta m_1 \oplus \frac{\partial b_{\pi^0}}{\partial m_2}\Delta m_2 \tag{91}$$

where

$$\frac{\partial b_{\pi^0}}{\partial m_1} = \frac{1 + m_2}{(1 + m_1 + m_2)^2}\frac{\partial b_{\pi^0}}{\partial m_2} = \frac{-m_1}{(1 + m_1 + m_2)^2}$$

and

$$b_{e^+e^-} = \frac{m_2}{1 + m_1 + m_2} \tag{92}$$

$$\Delta b_{e^+e^-} = \frac{\partial b_{e^+e^-}}{\partial m_1}\Delta m_1 \oplus \frac{\partial b_{e^+e^-}}{\partial m_2}\Delta m_2 \tag{93}$$

where

$$\frac{\partial b_{e^+e^-}}{\partial m_1} = \frac{-m_2}{(1 + m_1 + m_2)^2}\frac{\partial b_{e^+e^-}}{\partial m_2} = \frac{1 + m_1}{(1 + m_1 + m_2)^2}$$

We evaluate these derivatives using the central values of the measurements m_1 and m_2 and propagate the statistical and systematic errors independently to give us absolute measures for the branching fractions of the D_s^{*+} thus far discovered.

$$B(D_s^{*+} \to D_s^+ \gamma) = (93.5 \pm 0.5 \pm 0.5)\% \quad (94)$$

$$B(D_s^{*+} \to D_s^+ \pi^0) = (5.8 \pm 0.4 \pm 0.5)\% \quad (95)$$

$$B(D_s^{*+} \to D_s^+ e^+ e^-) = (0.67 \pm 0.13 \pm 0.05)\% \quad (96)$$

16 Systematic Uncertainties from the Tracking of Soft Electrons and Photons

As reported in Section 15, systematic errors in the measurement of $\epsilon_{e^+e^-}/\epsilon_\gamma$ will contribute to the systematic uncertainty in our measurement of the ratio of branching fractions $B(D_s^{*+} \to D_s^+ e^+ e^-)\ B(D_s^{*+} \to D_s^+ \gamma)$. In this section, we seek to estimate the fractional systematic error associated with the measurement of $\epsilon_{e^+e^-}/\epsilon_\gamma$ in the energy range relevant for our analysis by studying the decay of $\psi(2S)$ mesons to $J/\psi\pi^0\pi^0$. We estimate this systematic error by restricting the e^+e^- energy to that found in $D_s^{*+} \to D_s^+ e^+ e^-$ and measuring the ratio of the numbers of events where one of the π^0 decays to $\gamma e^+ e^-$ to the number of events where both π^0 decay to $\gamma\gamma$ and comparing this to the ratio expected from currently accepted branching fractions for $\pi^0 \to \gamma e^+ e^-$ and $\pi^0 \to \gamma\gamma$.

Dataset 42, which contains 53 pb^{-1} of data taken at the $\psi(2S)$ resonance, was used for this study. Since soft electrons from the Dalitz decay of the π^0 would also suffer from the systematic deviation in their energy and other track parameters if their tracks are pion-fitted, we reprocessed this dataset to include electron-fits. This has been described in Section 8.

We tried to estimate e^+e^- reconstruction efficiency using the method of missing mass. This effort failed as the invariant mass of an electron is indistinguishable from that of a photon at our scale of energies and this makes it impossible for us to distinguish between efficient and inefficient events. In the following paragraphs, we describe a method that completely reconstructs the $\psi(2S)$ from its decay into $J/\psi\pi^0\pi^0$ in order to estimate our systematic error in the measurement of $\epsilon_{e^+e^-}/\epsilon_\gamma$.

For our convenience, events where one of the π^0 Dalitz decays to $e^+e^-\gamma$ will be called events of Type I. Events where both π^0 decay to $\gamma\gamma$ will be called events of Type II. The latest fit in the Review of Particle Physics 2010 establishes the ratio $B(\pi^0 \to \gamma e^+ e^-)/B(\pi^0 \to \gamma\gamma)$ to be $(1.188 \pm 0.034) \times 10^{-2}$ [7].

In our method, we obtain a measurement of this ratio from data. The deviation of this measurement from the currently accepted value of the branching fraction translates to the systematic uncertainty in our measurement of $\epsilon_{e^+e^-}/\epsilon_\gamma$:

$$\frac{\Delta\epsilon_{e^+e^-}/\epsilon_\gamma}{\epsilon_{e^+e^-}/\epsilon_\gamma} = \frac{\Delta(B(\pi^0 \to \gamma e^+ e^-)/B(\pi^0 \to \gamma\gamma))}{B(\pi^0 \to \gamma e^+ e^-)/B(\pi^0 \to \gamma\gamma)} \tag{97}$$

Our method reconstructs the $\psi(2S)$ through events of Type I ($\psi(2S) \to J/\psi\pi^0\pi^0; \pi^0 \to \gamma\gamma; \pi^0 \to e^+e^-\gamma$) and events of Type II ($\psi(2S) \to J/\psi\pi^0\pi^0; \pi^0 \to \gamma\gamma; \pi^0 \to \gamma\gamma$). We estimate the reconstruction efficiencies for both types of events using Monte Carlo samples. First, we establish a set of criteria to reconstruct Type I events in our data. To illustrate our method, we shall call the efficiency of selecting Type I events from an MC sample of Type I events ϵ_s. The efficiency of keeping Type II events in the signal region of these criteria from an MC sample of Type II events shall be called ϵ_c. For n_I produced Type I and n_{II} produced Type II events, we can expect an yield of y events after applying this set of selection criteria

to our data as expressed in Eq. 98.

$$n_I \epsilon_s + n_{II} \epsilon_c = y \tag{98}$$

Using the currently accepted ratio of n_I/n_{II} from Eq. **??**, we may calculate n_I, the number of Type I events in our data, from this.

Hereafter, we construct a set of selection criteria to reconstruct Type II events in our data. Using Type II MC, we find out the reconstruction efficiency ϵ_γ for this set of criteria. Then we may estimate the number of produced Type II events in our data with this method as n_{II} using

$$n_{II} \epsilon_\gamma = y_\gamma \tag{99}$$

where y_γ is the yield of our set of criteria on data to isolate Type II events.

Having estimated the number of Type I and II events in our data, we may estimate the branching fraction $B(\pi^0 \to e^+e^-\gamma)$ using

$$B(\pi^0 \to e^+e^-\gamma) = \frac{B(\pi^0 \to \gamma\gamma)}{2} \frac{n_I}{n_{II}}. \tag{100}$$

.

In order to establish a systematic uncertainty in our measurement of $B(\pi^0 \to e^+e^-\gamma)$, we implement a second method for measuring this branching fraction. In this method, we use Type I and Type II events in our data that are most likely conversion events, events where one of the photons from the π^0 converts to a e^+e^- in material, in combination with Eq. 98 to estimate the total number of Type I and Type II events in the data. In order to select events that are most likely to be conversion events, we select events that are rejected by the Δd_0 and $\Delta\phi_0$ criteria on the tracks of the e^+e^- pair. These selection criteria have been described in Sections 5.5 and 5.6. The efficiency of selecting such conversion-type events from a MC sample of Type I events shall be called ϵ'_s. The efficiency of selecting such events from a MC sample of Type II events shall be called ϵ'_c. Thus, upon the application of our selection criteria (that inverts the standard Δd_0 and $\delta\phi_0$ requirements), the yield in data may be denoted by y' as expressed in Eq. 101.

$$n_I \epsilon'_s + n_{II} \epsilon'_c = y' \tag{101}$$

Solving Equations 98 and 99 simultaneously gives us the number of Type I events in the data. The number of Type II events is used as deduced earlier from the selection of Type II events. This ratio, n_I/n_{II}, is plugged into Equation 100 to give us a second estimate for the π^0 Dalitz decay branching fraction.

Now we shall discuss the details of implementation of the two methods.

16.1 Method 1

First, we shall describe the selection criteria used to select events from data in our first method.

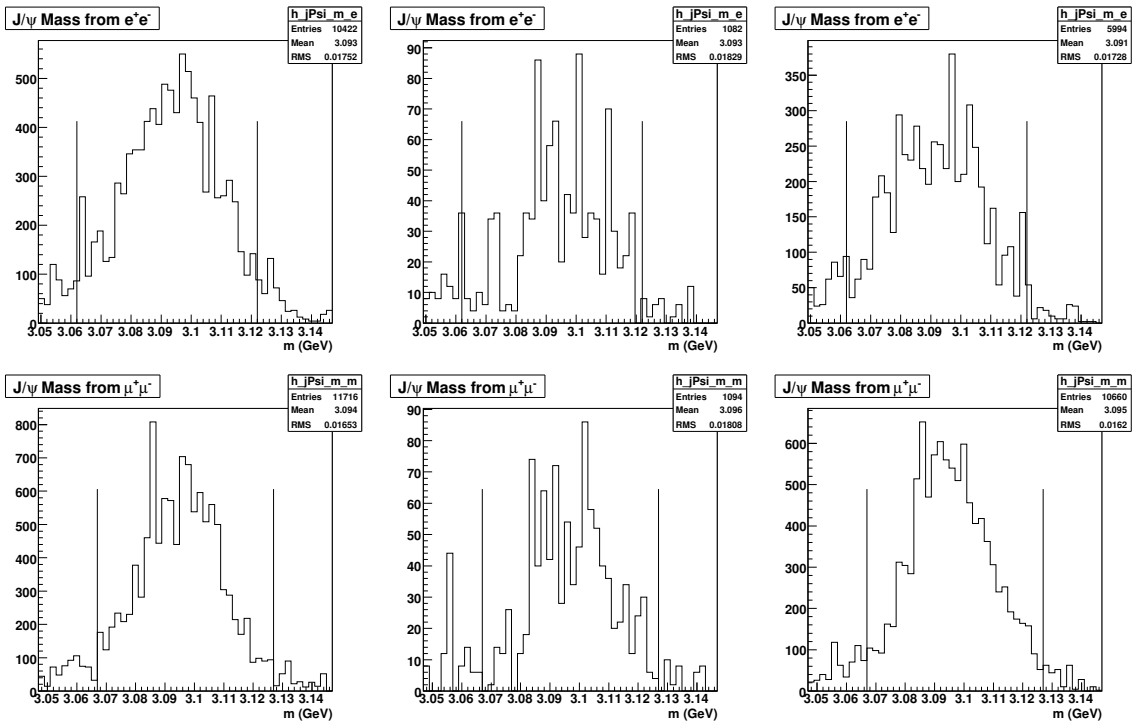

Figure 242: Invariant mass of the J/ψ reconstructed from its decay to e^+e^- (top plots) and $\mu^+\mu^-$ (bottom plots). The column on the left is from signal MC of Type I events. The column at the center is from signal MC of Type II events. The column on the right is from data.

The J/ψ is reconstructed from its decays to e^+e^- and $\mu^-\mu^+$. The tracks of these leptons are fitted with the Kalman fitter using electron and muon mass hypotheses respectively. 50% of the expected number of hits on a track are required to be present. The momentum of each track is required to be between 500 MeV and 10 GeV. They may be reconstructed upto a $\cos\theta$ of 0.93. The track parameter d_0 must be less than 5 mm and z_0 must be less than 5 cm. The dE/dx of electron and muon tracks are required to be within 3 σ of their expected values. The J/ψ has a mass of 3096.92 $\pm$ 0.001 MeV and a full natural width of 93.2 $\pm$ 2.1 keV. In our study, we require the invariant mass of the e^+e^- pair to be within 30 MeV of 3.09200 GeV, and the invariant mass of the $\mu^-\mu^+$ pair to be within 30 MeV of 3.09692 GeV as depicted in Fig 242.

The first π^0 in Type I events is reconstructed from its decay to two photons. The photons must not have showered in known noisy crystals and must not have tracks matched to them. Each of their shower energies are required to be between 10 Mev and 2 Gev. The E9E25 unfolded [*] cut is required to be less than 1.0. The pull mass of the π^0 is required to be within $\pm$ 2.5 σ. This is shown in Fig. 243.

The second π^0 in Type II events is reconstructed from its decay to a photon and a soft e^+e^- pair. Requirements on the photon are identical to those of the photons from the first

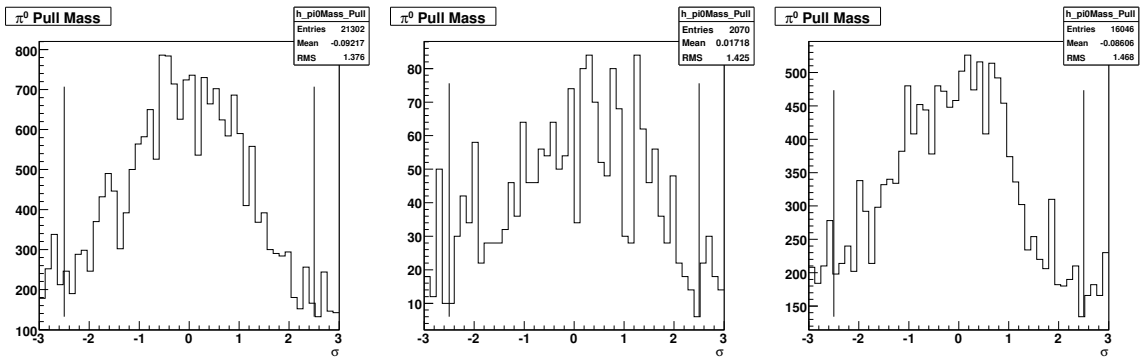

Figure 243: The invariant mass of the first π^0. The column on the left is from signal MC of Type I events. The column at the center is from MC of Type II events. The column on the right is from data.

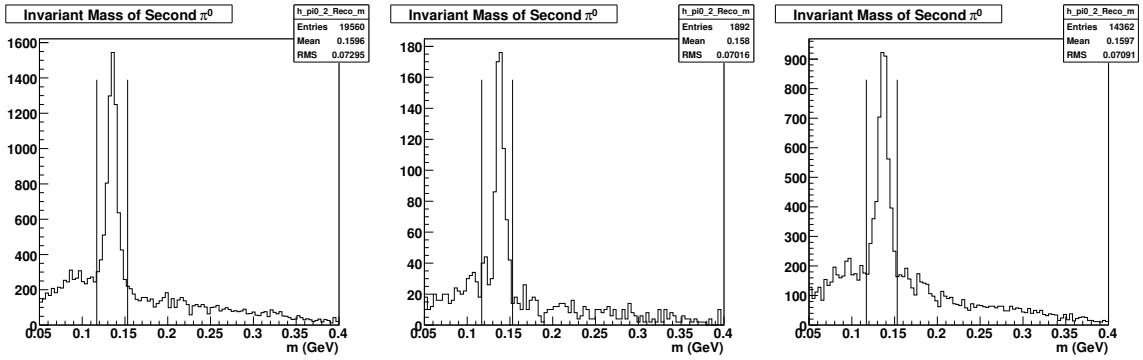

Figure 244: The invariant mass of the second π^0. The column on the left is from signal MC of Type I events. The column at the center is from MC of Type II events. The column on the right is from data.

π^0. The electron is Kalman fitted using the electron mass hypothesis and is required to have a momentum between 10 Mev and 2 GeV. It must be reconstructed within an angle of $\cos(\theta) = 0.93$. The track parameter d_0 must be less than 5 mm and z_0 must be less than 5 cm. The dE/dx of the track is required to be within 3 σ of the value expected of an electron. The invariant mass of the $\gamma e^+ e^-$ is required to be within 18 MeV of the nominal mass of the π^0 which is 134.9766 MeV. The distribution of this invariant mass and the selection range is shown in Fig. 244.

The electron and the positron are each required to have an energy less than 144 MeV as indicated in Fig. 245. This is the range of energies of the positron and the electron from the decay $D_s^{*+} \to D_s^+ e^+ e^-$.

Next, we combine the four-momenta of the J/ψ and two π^0 to get the four-momentum of the $\psi(2S)$ meson. This must be close to the four-momentum of the colliding e^+e^- pair at the center of the CLEO-c detector. Hence, we apply selection criteria constraining each component of the momentum of the $\psi(2S)$ to be within 40 MeV of that of the collision

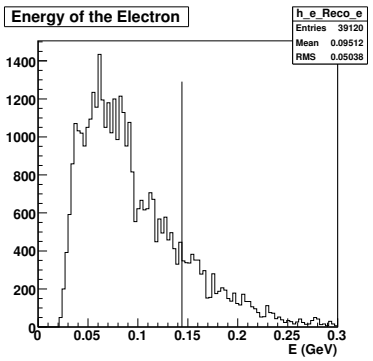

Figure 245: The distribution of energy of the positron and the electron from the Dalitz decay of the π^0 in the MC. Events containing positron and electrons with energy less than 144 MeV, as indicated, are accepted.

momentum. This is shown in Fig. 246.

We select events where the difference between the invariant masses of the reconstructed $\psi(2S)$ candidate and the J/ψ candidate is within 30 MeV of the nominal difference in masses. This is depicted in Fig. 247.

A background to the selection of Type I events are Type II events where one of the photons from a π^0 converts in material to produce an e^+e^- pair. We reject this background using the $\Delta d_0 > -5mm$ and $\Delta\phi_0 < 0.12$ criteria used in our $D_s^{*+} \to D_s^+ e^+ e^-$ analysis. This is shown in Fig. 248 and 249.

The aforementioned selection criteria are found to accept 1,069 Type I events out of a Monte Carlo sample of 299,794. Thus, we record the efficiency $\epsilon_s = 0.0357 \pm 0.0011$ as applicable in Eq. 98. They are also found to accept 10 Type II events out of a Monte Carlo sample of 149,888 and thus we may write $\epsilon_c = 2/149,888 = (1.33 \pm 0.94) \times 10^{-5}$. When these selection criteria are applied to our data, we get an yield of $y = 306$ events.

Assuming the established ratio of Type I to Type II events detailed in Eq. **??** to hold true, we may solve Eq. 98 for n_I. The solution is given in Eq. 102 and 103. The $\oplus$ symbol is used to denote addition in quadrature. This gives us $n_I = 8447 \pm 554$.

$$n_I = \frac{y}{\epsilon_s + \epsilon_c / r} \tag{102}$$

$$\frac{\Delta n_I}{n_I} = \frac{\Delta y}{y} \oplus \frac{\Delta\epsilon_s \oplus (\epsilon_c/r)(\Delta\epsilon_c/\epsilon_c \oplus \Delta r/r)}{\epsilon_s + \epsilon_c/r} \tag{103}$$

Having calculated the number of Type I events in our data, we may now estimate the number of Type II events present in the data sample. The reconstruction of Type II events is similar to the reconstruction of Type I events. The second π^0 is reconstructed from photons with the same selection criteria as the first π^0. The Δd_0 and $\Delta\phi_0$ cuts are not used as they are clearly inapplicable. A signal MC for Type II events was generated to calculate the signal efficiency of our criteria. Distributions of the J/ψ mass, the pull masses of the two

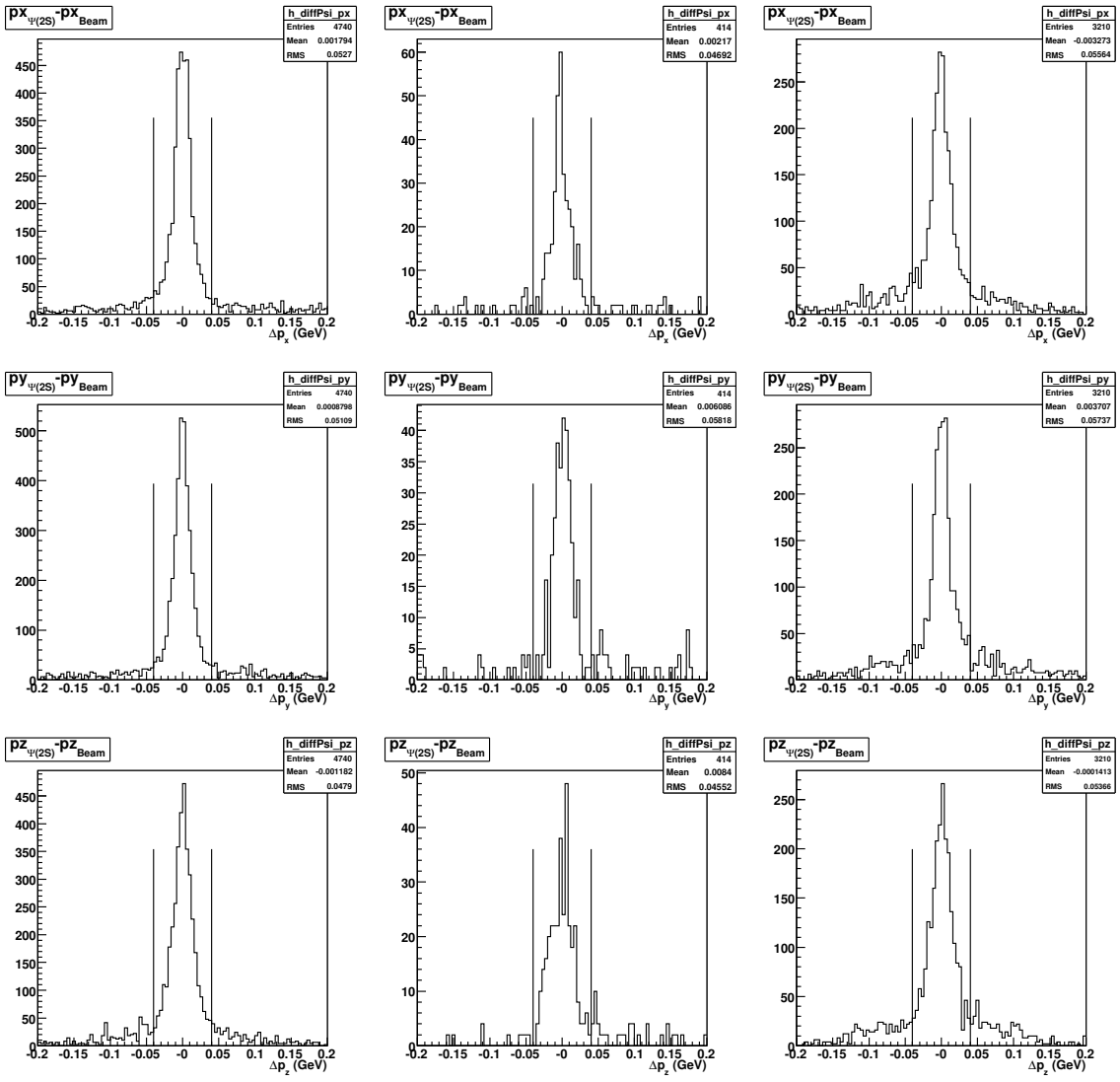

Figure 246: Four momenta of $\psi(2S)$ relative to the e^+e^- collision four momenta. The column on the left is from signal MC of Type I events. The column at the center is from MC of Type II events. The column on the right is from data.

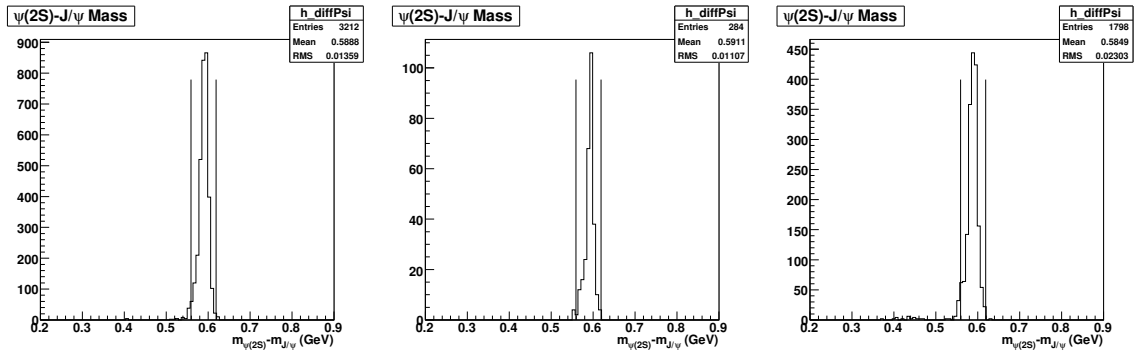

Figure 247: Difference between the invariant masses of the $\psi(2S)$ and the J/ψ. The column on the left is from signal MC of Type I events. The column at the center is from MC of Type II events. The column on the right is from data.

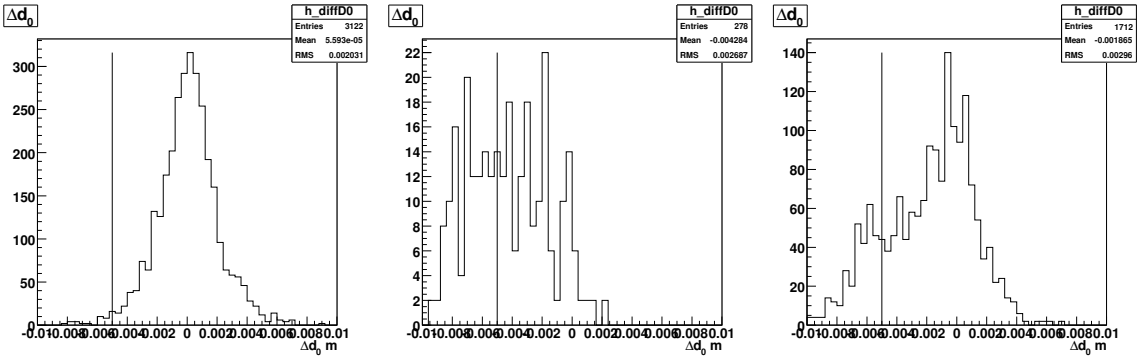

Figure 248: The Δd_0 between the e^+e^- pair from the second π^0. The column on the left is from signal MC of Type I events. The column at the center is from MC of Type II events. The column on the right is from data.

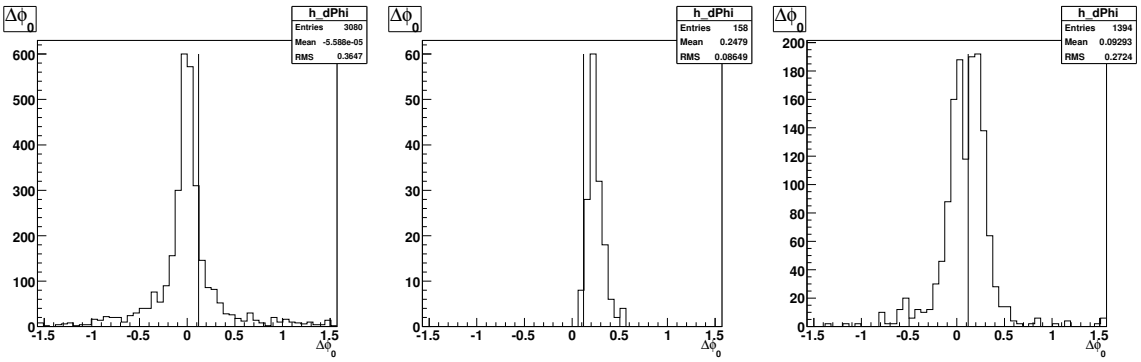

Figure 249: The $\Delta\phi_0$ between the e^+e^- pair from the second π^0. The column on the left is from signal MC of Type I events. The column at the center is from MC of Type II events. The column on the right is from data.

π^0, the momentum of the $\psi(2S)$ relative to the collision momentum and the mass difference between the $\psi(2S)$ and the J/ψ are presented in Fig. 250, 251, 252, 253 and 254.

25,713 events out of 149,888 signal MC events were seen to be accepted by our criteria. This gives a signal efficiency $\epsilon_\gamma = 0.1716 \pm 0.0011$. We find the yield in data to be $y_{II} = 58,602$ events. Using Eq. 99 we infer that the number of Type II events is our data is $n_{II} = 341,607 \pm 2,555$.

Now, we may calculate the ratio of branching fractions $B(\pi^0 \to e^+e^-\gamma)/B(\pi^0 \to \gamma\gamma)$ from the ratio of Type I to Type II events thus:

$$\frac{B(\pi^0 \to e^+e^-\gamma)}{B(\pi^0 \to \gamma\gamma)} = \frac{n_I}{2n_{II}} = 0.5 \times \frac{8447 \pm 554}{341607 \pm 2555} = 0.01237 \pm 0.00082. \quad (104)$$

In order to establish a systematic uncertainty in this measurement, we use a second method to estimate the ratio $B(\pi^0 \to e^+e^-\gamma)/B(\pi^0 \to \gamma\gamma)$.

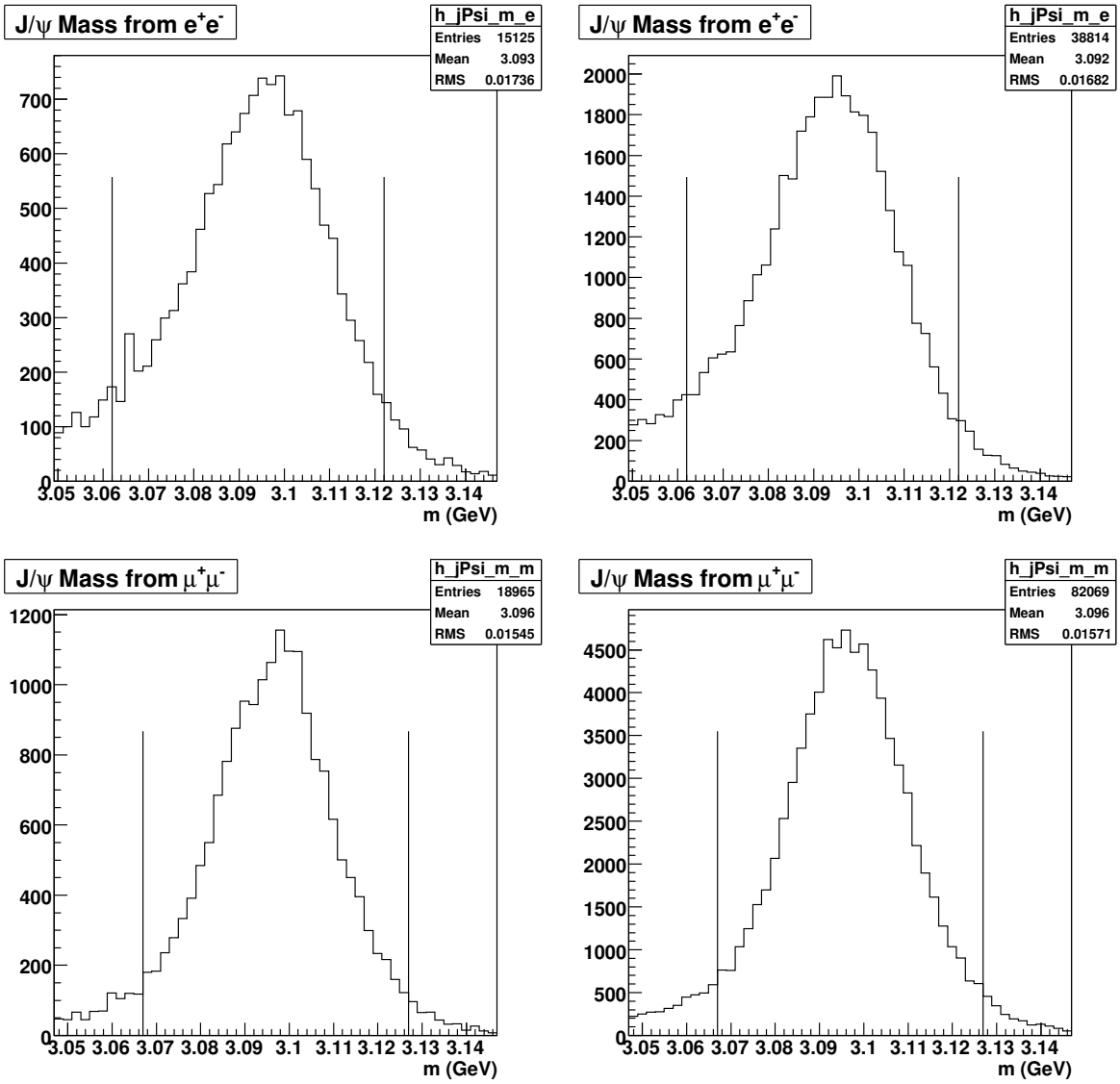

Figure 250: Invariant mass of the J/ψ reconstructed from its decay to e^+e^- (top plots) and $\mu^+\mu^-$ (bottom plots). The column on the left is from signal MC of Type II events. The column on the right is from data.

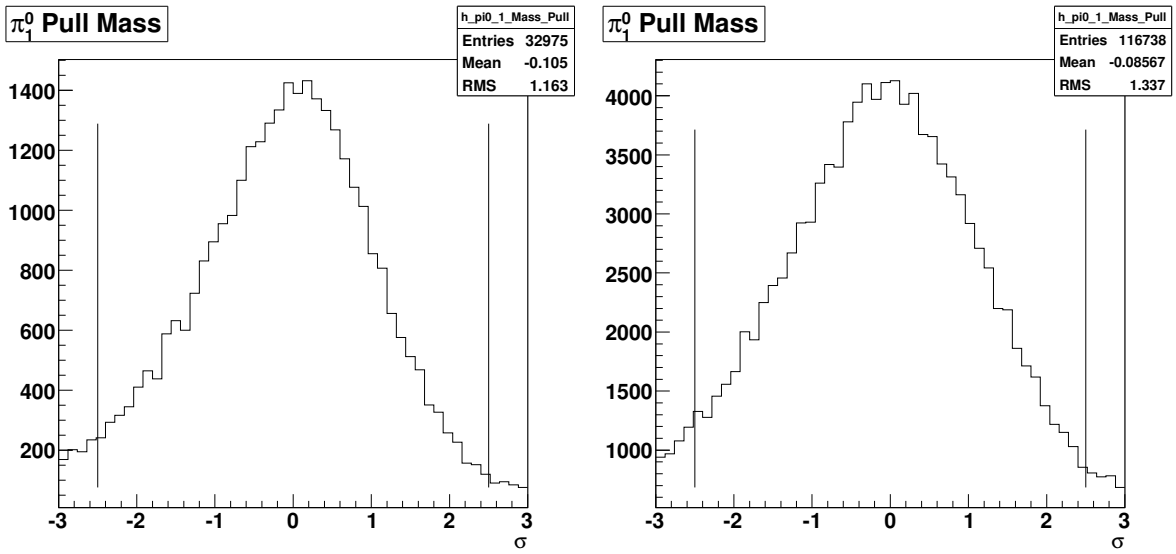

Figure 251: The invariant mass of the first π^0. The column on the left is from signal MC of Type II events. The column on the right is from data.

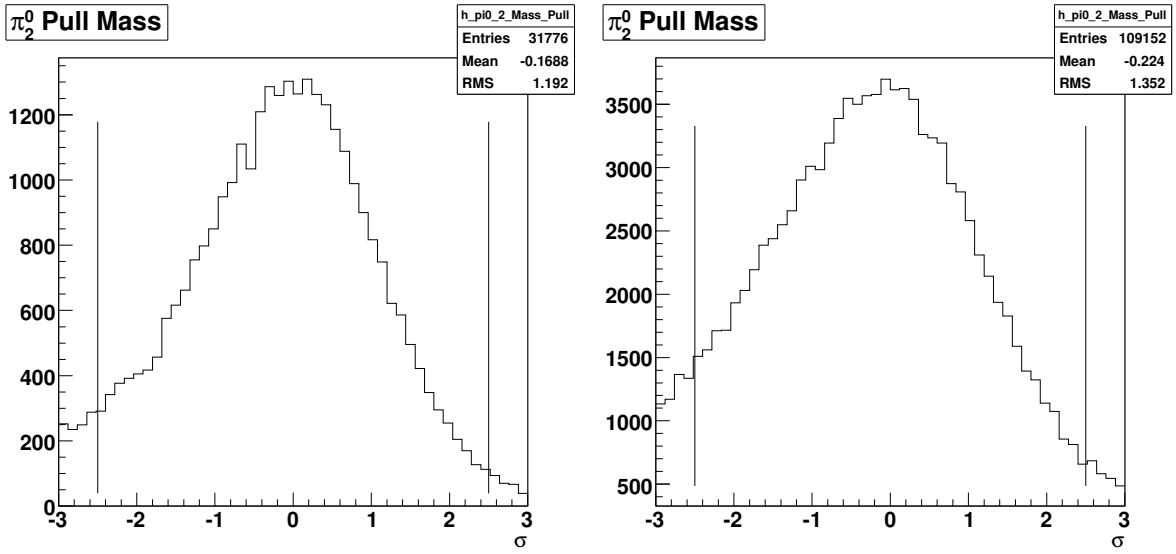

Figure 252: The invariant mass of the second π^0. The column on the left is from signal MC of Type II events. The column on the right is from data.

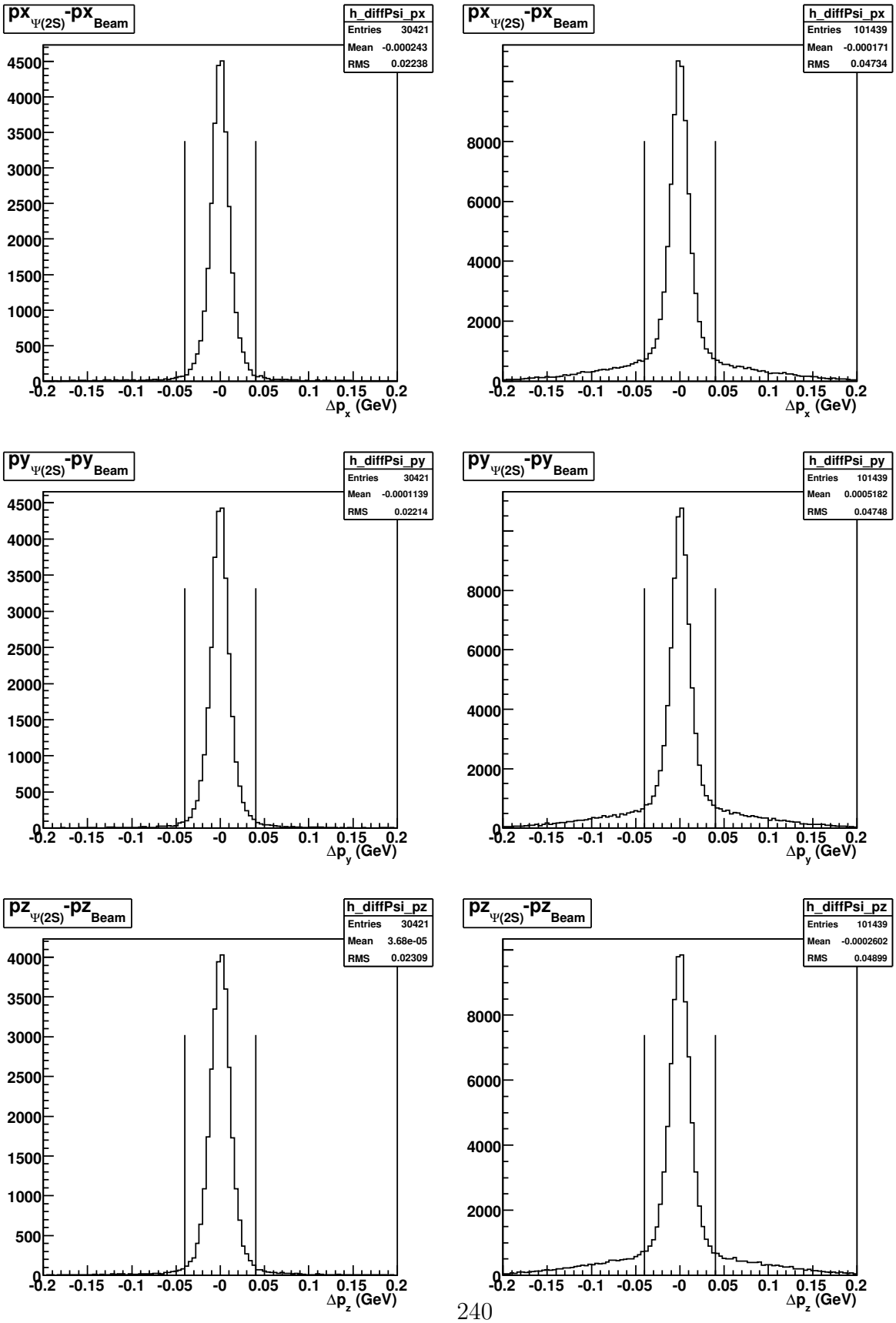

Figure 253: Four momenta of $\psi(2S)$ relative to the e^+e^- collision four momenta. The column on the left is from signal MC of Type II events. The column on the right is from data.

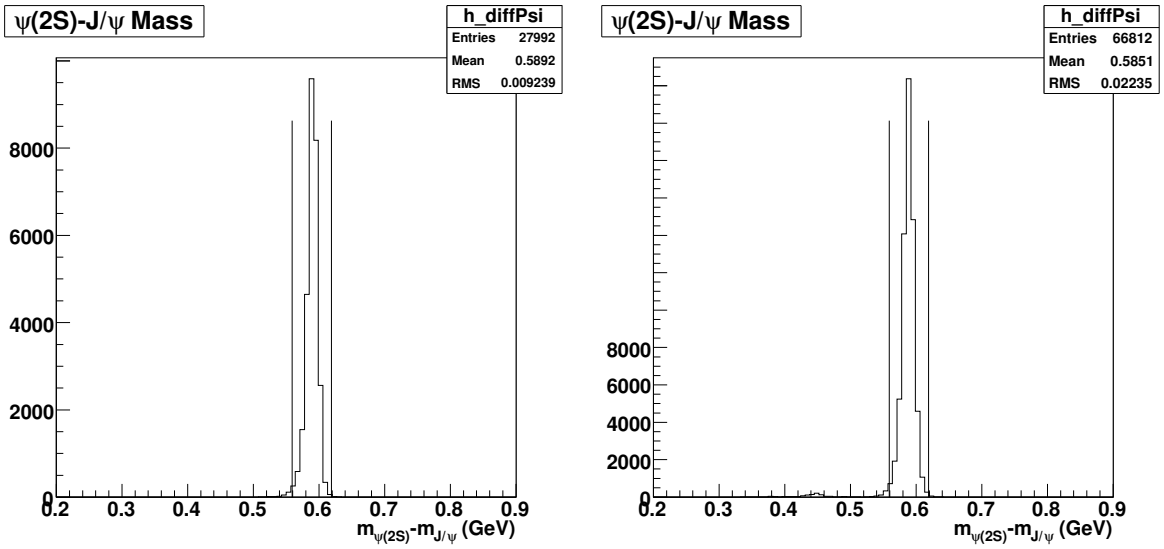

Figure 254: Difference between the invariant masses of the $\psi(2S)$ and the J/ψ. The column on the left is from signal MC of Type II events. The column on the right is from data.

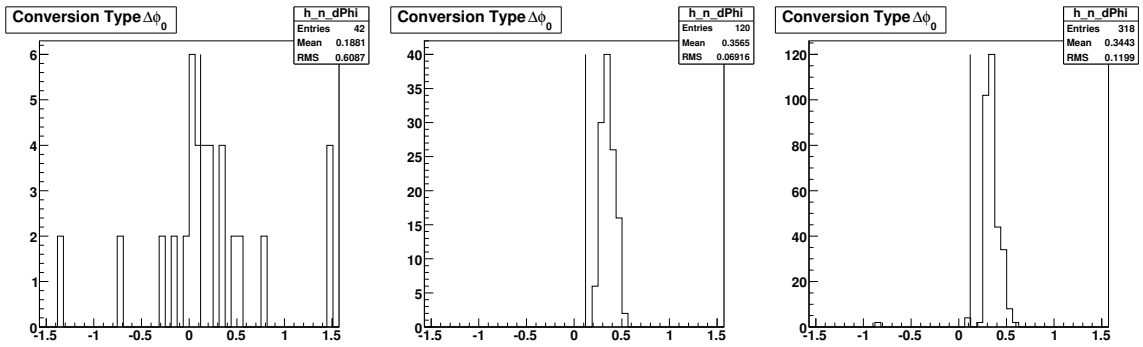

Figure 255: The $\Delta\phi_0$ between the e^+e^- pair. Now we accept events with $\Delta\phi_0$ greater than 0.12. These were previously rejected as likely to be conversion-type events. The column on the left is from signal MC of Type I events. The column at the center is from MC of Type II events. The column on the right is from data.

16.2 Method 2

Our second method for estimating $B(\pi^0 \to e^+e^-\gamma)$ uses conversion-type events found in data. Conversion-type events are those where both π^0 decay to $\gamma\gamma$ but at least one photon converts in material to form a e^+e^- pair. We select for such events by requiring all the criteria on J/ψ and the invariant masses of the π^0 used to select Type I events, except now we look at the "wrong side" of the Δd_0 and $\Delta\phi_0$ criteria. In other words, we keep events which were previously being rejected by both the Δd_0 and the $\Delta\phi_0$ criteria. The distribution of Δd_0 is the same as Fig. 248 since all preceding criteria are identical. The distribution of $\Delta\phi_0$ after having accepted tracks on the "wrong side" of Δd_0 is presented in Fig. 255 respectively.

The efficiency of such a set of selection criteria for Type I events is found to be $\epsilon'_s = 10/29,974 = (3.34 \pm 1.1(\text{stat})) \times 10^{-4}$. The efficiency for Type II events is found to be $\epsilon'_c = 54/149,888 = (3.60 \pm 0.49(\text{stat})) \times 10^{-4}$. On applying these selection criteria to our data, we are left with an yield of $y' = 141$ events. These values may be plugged into Eq. 101 and solved simultaneously with Eq. 98 to get $n_I = 8437 \pm 342$. The solution for n_I is given in Eq. 105 and 106.

$$n_I = \frac{y\epsilon'_c - y'\epsilon_c}{\epsilon_s\epsilon'_c - \epsilon_c\epsilon'_s} \tag{105}$$

$$\Delta n_I = \frac{\delta n_I}{\delta y}\Delta y \oplus \frac{\delta n_I}{\delta y'}\Delta y' \oplus \frac{\delta n_I}{\delta \epsilon_c}\Delta\epsilon_c \oplus \frac{\delta n_I}{\delta \epsilon_s}\Delta\epsilon_s \oplus \frac{\delta n_I}{\delta \epsilon'_c}\Delta\epsilon'_c \oplus \frac{\delta n_I}{\delta \epsilon'_s}\Delta\epsilon'_s \tag{106}$$

where

$$\frac{\delta n_I}{\delta y} = \epsilon'_c$$

$$\frac{\delta n_I}{\delta y'} = -\epsilon_c$$

$$\frac{\delta n_I}{\delta \epsilon_c} = \frac{-y}{\epsilon_s\epsilon'_c - \epsilon_c\epsilon'_s} + \frac{y\epsilon'_c - y'\epsilon_c}{(\epsilon_s\epsilon'_c - \epsilon_c\epsilon'_s)^2}\epsilon'_s$$

$$\frac{\delta n_I}{\delta \epsilon_s} = -\frac{y\epsilon'_c - y'\epsilon_c}{(\epsilon_s\epsilon'_c - \epsilon_c\epsilon'_s)^2}\epsilon'_c$$

$$\frac{\delta n_I}{\delta \epsilon'_c} = \frac{y}{\epsilon_s\epsilon'_c - \epsilon_c\epsilon'_s} - \frac{y\epsilon'_c - y'\epsilon_c}{(\epsilon_s\epsilon'_c - \epsilon_c\epsilon'_s)^2}\epsilon_s$$

$$\frac{\delta n_I}{\delta \epsilon'_s} = \frac{y\epsilon'_c - y'\epsilon_c}{(\epsilon_s\epsilon'_c - \epsilon_c\epsilon'_s)^2}\epsilon_c$$

Now, we may calculate the ratio of Type I to Type II events in our data as n_I/n_{II} and from that estimate the ratio of branching fraction $B(\pi^0 \to \gamma e^+e^-)/B(\pi^0 \to \gamma\gamma)$ thus:

$$\frac{B(\pi^0 \to e^+e^-\gamma)}{B(\pi^0 \to \gamma\gamma)} = \frac{n_I}{2n_{II}} = 0.5 \times \frac{8437 \pm 342}{341607 \pm 2555} = 0.01235 \pm 0.00051. \tag{107}$$

Now, we may combine our results from the two methods to establish a systematic error. Result from method 1: $B(\pi^0 \to e^+e^-\gamma)/B(\pi^0 \to \gamma\gamma) = 0.01237 \pm 0.00082$(stat). Result from method 2: $B(\pi^0 \to e^+e^-\gamma)/B(\pi^0 \to \gamma\gamma) = 0.01235 \pm 0.00051$(stat). The result of method 2 has the smaller uncertainty and will, therefore, be quoted as the central value of our measurement. The systematic uncertainty, calculated as the difference between the two central values, is 0.00002. Hence, we report $B(\pi^0 \to e^+e^-\gamma)/B(\pi^0 \to \gamma\gamma) = 0.01235 \pm 0.00051(\text{stat}) \pm 0.00002(\text{syst})$.

The current world average for this quantity is 0.01188 ± 0.00034 [7]. So, our deviation is 0.00047, which does not warrant a correction given the other errors. We add this deviation in quadrature with 0.00051 and 0.00034 to obtain 0.00077. Thus, the fractional uncertainty we set out to estimate is found to be $0.00077/0.01188 = 6.50\%$.

$$\frac{\Delta\epsilon_{e^+e^-}/\epsilon_\gamma}{\epsilon_{e^+e^-}/\epsilon_\gamma} = \frac{\Delta(B(\pi^0 \to \gamma e^+e^-)/B(\pi^0 \to \gamma\gamma))}{B(\pi^0 \to \gamma e^+e^-)/B(\pi^0 \to \gamma\gamma)} = \frac{0.077\%}{1.188\%} = 6.50\% \tag{108}$$

References

[1] J. P. Alexander et al. Absolute Measurement of Hadronic Branching Fractions of the D_s^+ Meson. *Phys. Rev. Lett.*, 100:161804, 2008.

[2] C. Amsler et al. Review of particle physics. *Physics Letters B*, 667(1-5):1 – 6, 2008. Review of Particle Physics.

[3] Bernard Aubert et al. Measurement of the branching ratios $\Gamma(D_s^{*+} \to D_s^+\pi^0)/\Gamma(D_s^{*+} \to D_s^+\gamma)$ and $\Gamma(D^{*0} \to D^0\pi^0)/\Gamma(D^{*0} \to D^0\gamma)$. *Phys. Rev.*, D72:091101, 2005.

[4] D. Cronin-Hennessy et al. Measurement of Charm Production Cross Sections in e^+e^- Annihilation at Energies between 3.97 and 4.26 GeV. *Phys. Rev. D*, 80:072001, 2009.

[5] Brian K. Heltsley. FitEvt: A User-Friendly C++ Interface for Kinematic Fitting. *CBX 06-28*, 2006.

[6] Rob Kutschke. How and Why Wonder Book of CLEO Tracking Conventions. *CSN 94-334*, 1996.

[7] K. Nakamura et al. *J. Phys. G*, 37:075021, 2010.

[8] Peter Onyisi and Werner Sun. Developments in $D_{(s)}$-Tagging. *CBX 06-11*, 2006.